



**EVALUATION AND OPTIMIZATION OF A STAND-ALONE SOLAR DRIVEN  
MEMBRANE FILTRATION SYSTEM FOR SURFACE WATER TREATMENT**

---

**by**

**TATENDA ALFRED KAJAU**

**Dissertation in fulfilment of the requirement for the degree**

**MASTER OF SCIENCE**

**in**

**CHEMISTRY**

**in the**

**COLLEGE OF SCIENCE, ENGINEERING AND TECHNOLOGY**

**of the**

**UNIVERSITY OF SOUTH AFRICA**

**Supervisor : Dr. MACHAWE M. MOTSA**

**Co-supervisors : Dr. NOMCEBO. H. MTHOMBENI**

**Prof. BHEKIE B. MAMBA**

**Prof. ARNE R. D. VERLIEFDE**

**February 2022**

## DECLARATION

---

Name: Tatenda Alfred Kajau

Student number: 67684041

Degree: Master of Science: Chemistry

Exact wording of the title of the thesis as appearing on the electronic copy submitted for examination:

---

## EVALUATION AND OPTIMIZATION OF A STAND-ALONE SOLAR DRIVEN

## MEMBRANE FILTRATION SYSTEM FOR SURFACE WATER TREATMENT.

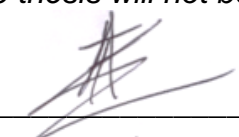
---

I declare that the above thesis is my own work and that all the sources that I have used or quoted have been indicated and acknowledged by means of complete references.

I further declare that I submitted the thesis to originality checking software and that it falls within the accepted requirements for originality.

I further declare that I have not previously submitted this work, or part of it, for examination at Unisa for another qualification or at any other higher education institution.

*(The thesis will not be examined unless this statement has been submitted.)*

  
\_\_\_\_\_  
SIGNATURE

15 July 2022  
DATE

## DEDICATION

---

This work is dedicated to my parents, **Mr Freddy Tichafa Kajau** and **Mrs Jane Kajau**. They instilled in me a sense of direction, discipline and focus to do my work diligently and pursue my passions. My father always encouraged me to follow my instincts, be inquisitive of how things work and believe in myself, while my mother nurtured in me, values of respect, honesty, and integrity in my conduct. These principles have guided me thus far.

I also dedicate this work to my son,

**Tatenda Alfred Kajau Jnr.**

This young man inspires me to be a better human being and has brought so much joy in my life.

And to my loving wife

**Ms. Mildred Marau**

She has been my pillar of strength throughout this study.

## PUBLICATIONS AND PRESENTATIONS

---

### Peer-reviewed Publications:

- Kajau, T. A., Motsa, M. M., Mamba, B. B., Mahlangu, O. T. (2021). Leaching of CuO Nanoparticles from PES Ultrafiltration Membranes. *ACS Omega* 2021, 6 (47), 31797-31809, <https://doi.org/10.1021/acsomega.1c04431>
- Kajau, T. A., Mamba, B. B., Mthombeni, N. H., Motsa, M. M. Analysis of the thermo-pneumatic properties of copper oxide-based nanofluids for pressure generation during membrane filtration. *Thermal Science and Engineering Progress*, <https://doi.org/10.1016/j.tsep.2022.101371>
- Kajau, T. A., Mamba, B. B., Mthombeni, N. H., Motsa, M. M. The state of solar energy in South Africa: An emerging opportunity for pressure driven membrane processes in low-economy regions. *Sustainable Energy Technologies, and Assessments (Under Review)*.

### Other Publications

- Sanganyado, E. & Kajau, T. A. (2021). Fate of Emerging Pollutants in Aquatic Systems. In Dalu, T. & Tavengwa, N. T. (Eds) *Emerging Freshwater Pollutants: Analysis, Fate and Regulations*. Elsevier. <https://doi.org/10.1016/B978-0-12-822850-0.00002-8>

### Presentations:

Kajau T. A., Motsa, M. M., Mthombeni, N. H., Mamba, B. B., Verliefde, A. R. D. Optimization of a solar-driven hydraulic pump system for surface water purification. Flash talk presentation. RSC/SACI Young Chemists' Symposium 2021. Online, 09 July 2021.

Kajau, T. A., Mamba, B. B., Mthombeni, N. H., Verliefde, A., Motsa, M. M. (2021). Optimization of a solar-driven hydraulic pump system for surface water treatment, p156. 2<sup>nd</sup> Commonwealth Chemistry Posters – Building Networks to address the Goals September 30 – October 1, 2021. Virtual.

**Awards:**

UNISA Innovation Challenge Award 2020.

---

For project entitled, “Energy efficient hybrid filtration-adsorbent membrane system for contaminated surface water treatment in rural areas.”

## ACKNOWLEDGEMENTS

---

**This research was made possible through the accommodations, collaboration, interaction, assistance, encouragement and guidance of the following individuals and entities:**

My supervisors: **Dr. Mxolisi M. Motsa, Dr. Nomcebo H. Mthombeni, Prof. Bheki B. Mamba and Prof. Arne R. D. Verliefde** for their patience in teaching me most of what I know now and directing the research work.

The University of South Africa for the top of the range learning environment, funding and all other things that made this research possible.

The Institute for Nanotechnology and Water Sustainability (iNanoWS) for the accommodations, conferences, and funding.

Postdoctoral fellows Dr. O. T. Mahlangu, Dr. G. Mamba, and Dr. W. Moyo for their valued assistance and direction.

Mr. E. Bergh for manufacturing the solar-driven pump prototype used in this study. The College of Agriculture and Environmental Science for accommodating the field-scale solar-driven membrane filtration system at their horticulture section.

The laboratory team, Prof. H. Nyoni, Mr. K. Mokalane, and Ms. N. Magwaza, for their illustrious training sessions on equipment operation, assistance with reagents and other miscellaneous items or services, to mention but a few.

I acknowledge my family for the support, especially my loving wife, **Ms. Mildred Marau**, who gave me a shoulder to lean on during rough patches and celebrated with me in good times.

In all this, I acknowledge the **Gracious Lord** for, “The Lord bless thee, and keep thee: The Lord make his face shine upon thee and be gracious unto thee: The Lord lift up his countenance upon thee and give thee peace” (Numbers 6: 24-26).

## ABSTRACT

---

South Africa is classified as a water-stressed country and is faced with widespread water scarcity. Water scarcity is worse in rural areas of the country where a third of the population still reside. This is due to low levels of development with no water treatment systems or piping networks and most of rural areas lack access to electricity thereby hindering the installation of conventional water treatment facilities. Membrane technology presents an opportunity to bring water treatment facilities to these areas due to its compact nature, consistent water quality production and ease of maintenance. Among membrane systems, ultrafiltration uses comparably low pressures hence making it energy efficient. Solar energy has been proven to be effective in providing energy to drive membrane filtration systems and its utility in South Africa is very viable due to the abundance of solar insolation. South Africa receives an average of 2500 hours of sunshine per year and with solar radiation reaching up to 6,5kWh/m<sup>2</sup> on some days, thereby making the use of solar energy highly favourable. In this research, water production by a solar hydraulic pump was optimized. A nanofluid was developed to improve the thermal conductivity of the working fluid for the pump and a custom-made ultrafiltration membrane was adopted for use in the membrane filtration unit. Heat transfer mechanisms within the system were investigated and the membrane filtration performances on real surface water samples collected from a lake and a stream were also determined. The nanoparticles and membranes were characterized using Scanning Electron Microscopy (SEM), Atomic Force Microscopy (AFM), Fourier Transform Infrared (FTIR) spectroscopy, Zeta-potential, drop-shape analysis, dynamic light scattering, and stability tests. Laboratory-scale application of the system was then done together with real-world studies. The optimum conditions were established to be a nanofluid composition of 0,1 %w/w CuO working fluid operated within the temperature range of 25°C – 50°C and at a pH of 6. This significantly improved the net water production of the developed prototype by 13,35 % as well as the efficiency of the prototype by 21,3%.

## TABLE OF CONTENTS

---

<b>DECLARATION .....</b>	<b>i</b>
<b>DEDICATION .....</b>	<b>ii</b>
<b>PUBLICATIONS AND PRESENTATIONS .....</b>	<b>iii</b>
<b>ACKNOWLEDGEMENTS .....</b>	<b>v</b>
<b>ABSTRACT.....</b>	<b>vi</b>
<b>TABLE OF CONTENTS.....</b>	<b>vii</b>
<b>LIST OF FIGURES.....</b>	<b>xii</b>
<b>LIST OF TABLES .....</b>	<b>xix</b>
<b>LIST OF ABBREVIATIONS .....</b>	<b>xx</b>
<b>NOMENCLATURE .....</b>	<b>xxi</b>
<b>CHAPTER 1 .....</b>	<b>1</b>
<b>INTRODUCTION.....</b>	<b>1</b>
1.1 Background.....	1
1.2 Problem statement .....	2
1.3 Justification.....	3
1.4 Aim and objectives of the study .....	5
1.5 Objectives.....	5
1.6 Dissertation outline .....	6
1.6 References .....	7
<b>CHAPTER 2 .....</b>	<b>10</b>
<b>LITERATURE REVIEW.....</b>	<b>10</b>
2.1 Introduction.....	10
2.1 Drinking water challenges in low-income areas.....	10
2.2 Potable water supply and quality challenges in rural areas.....	13
2.2.1 Natural Organic Matter (NOM) .....	15
2.2.2 Inorganic substances .....	16
2.2.3 Microbiological content .....	18
2.2.4 Emerging Micropollutants (EMPs).....	19
2.3 Surface water treatment technology.....	19
2.3.1 Simple household water treatment techniques .....	20
2.4 Filtration processes .....	21
2.5 Point of Use (POU) water treatment techniques.....	21



2.5.1 Porous pot filter.....	22
2.5.2 Biosand filter .....	23
2.5.3 Activated carbon filter .....	23
2.5.4 Fabric filters .....	24
2.5.5 Solar Disinfection (SODIS) .....	24
2.6 Convectional Water Treatment.....	25
2.7.3 Membrane filtration processes .....	26
2.7 Ultrafiltration (UF) in water treatment .....	28
2.8 Application of membrane filtration/technology in SA .....	30
2.9 Application of Nanofiltration membranes/ technology in South Africa .....	32
2.10 Membrane fouling.....	33
2.10.1 Energy Sources for membrane filtration.....	36
2.11 Application of Solar energy in water treatment .....	39
2.11.1 Solar-thermal energy conversion .....	40
2.11.2 Solar energy storage.....	42
2.12 Heat transfer in systems .....	43
2.12.1 Conduction.....	43
2.12.2 Convection.....	44
2.12.3 Radiation.....	44
2.13 Thermal conductivity.....	46
2.14 Thermodynamics of heat driven systems. ....	46
2.14.1 Laws of thermodynamics .....	47
2.15 Heat engines .....	47
2.15.1 Diaphragm pump operation.....	48
2.16 Nanofluids .....	50
2.16.1 Heat transfer mechanisms in nanofluids. ....	50
2.17 Parameters influencing heat transfer in nanofluids.....	51
2.17.1 Thermal conductivity of nanofluids.....	51
2.17.2 Effect of temperature .....	52
2.17.3 Specific heat capacity of nanofluids .....	52
2.17.4 Effect of the size and shape of nanoparticles .....	53
2.17.5 Effect of volume fraction of nanoparticles .....	54
2.17.6 Effect of charge and pH of the nanoparticles .....	54
2.17.7 Stability of nanoparticles .....	55

2.18 Integration of membrane processes with pre-treatment steps and surface water treatment .....	57
2.19 Factors influencing membrane performance .....	58
2.20 References .....	58
<b>CHAPTER 3 .....</b>	<b>80</b>
<b>EXPERIMENTAL METHODOLOGY .....</b>	<b>80</b>
3.1 Introduction.....	80
3.1 Reagents and materials.....	80
3.2 Membrane preparation .....	81
3.2.1 Membrane characterization .....	82
3.2.2 Scanning Electron Microscopy.....	82
3.2.3 Atomic Force Microscopy.....	83
3.2.4 Wettability measurements.....	83
3.2.4.1 Owens-Wendt-Rabel & Kaelble (OWRK) Model .....	84
3.2.5 Thermal stability of the membranes .....	85
3.2.6 Membrane surface functionality .....	86
3.3 Membrane filtration studies .....	86
3.4 Surface water studies .....	91
3.4.1 Sampling sites and sample collection .....	91
3.4.2 Sample analyses.....	92
3.5 Membrane testing protocols.....	94
3.5.1 Membrane filtration with real and synthetic water samples.....	94
3.5.2 Membrane fouling and cleaning.....	95
3.5.3 Specific UltraViolet Absorbance (SUVA) and % Dissolved Organic Carbon (DOC) removal .....	99
3.6 Determination of the working volume of the prototype. ....	100
3.7 Synthesis of copper oxide nanoparticles.....	100
3.7.1 Characterization of nanoparticles.....	104
3.8 References .....	107
<b>CHAPTER 4 .....</b>	<b>108</b>
EVALUATION OF A NANOPARTICLE FREE, HIGH PERFORMANCE ULTRAFILTRATION MEMBRANE AND COMMERCIAL NANOFILTRATION MEMBRANE (NF270) IN A SOLAR INDUCED PRESSURE-DRIVEN SYSTEM USED FOR SURFACE WATER TREATMENT. ....	108

4.1 Introduction.....	108
4.2 Experimental .....	108
4.2.1 Materials and methods.....	108
4.2.2 Membrane preparation and characterization .....	109
4.2.3 Water analysis .....	109
4.2.4 Membrane fouling and testing protocols .....	109
4.3 Results and Discussion .....	112
4.3.1 Membrane preparation and characterization. ....	112
4.3.2 Real water sample analysis.....	122
4.3.3 Correlation between %DOC removal and filtration time .....	128
4.3.4: Comparison between %DOC removal and SUVA for the UF and NF membranes .....	129
4.3.4 Removal of metallic ions by UF and NF270 membranes. ....	131
4.3.5 Physico-chemical properties of the membrane permeate. ....	132
4.5 Membrane testing protocols .....	134
4.5.1 Membrane pure water flux and permeability coefficient .....	134
4.5.2 Determination of fouling resistances .....	135
4.5.3 Normalized Flux Ratio (NFR) determination. ....	136
4.5.4 Determination of membrane fouling mechanism.....	137
4.5.5 Humic acid and BSA rejections.....	139
4.5.6 Membrane cleaning .....	140
4.5.7 Change in membrane properties between fouling and chemical cleaning. ....	142
4.6 Evaluation of prototype.....	149
4.7 Conclusion and recommendations .....	151
4.8 References .....	152
<b>CHAPTER 5.....</b>	<b>161</b>
<b>An analysis of the thermo-pneumatic properties of copper oxide-based nanofluids. ....</b>	<b>161</b>
5.1 Introduction.....	161
5.2 Experimental .....	162
5.2.1 Materials and methods.....	162
5.2.2 Synthesis and characterization of copper oxide nanoparticles. ....	162
5.2.3 Preparation and testing protocols of prepared nanofluids.....	163

5.2.4 Analysis of the heat transfer in the prepared nanofluids .....	164
5.2.5 Analysis of pressure generation by the nanofluids.....	168
5.3 Results and discussion.....	169
5.3.1 Synthesis and characterization of copper oxide nanoparticles. ....	169
5.3.2 Size and surface charge of copper oxide nanoparticles.....	174
5.3.3 Optical properties of copper oxide nanoparticles.....	179
5.4 Preparation and testing protocols of prepared nanofluids .....	180
5.4.2 Analysis of vapour pressure generation.....	190
5.5 Conclusion.....	193
5.6 References .....	194
<b>CHAPTER 6.....</b>	<b>199</b>
<b>EVALUATION OF THE PERFORMANCE OF THE SOLAR DRIVEN SYSTEM.</b>	
.....	<b>199</b>
6.1 Introduction.....	199
6.2 Experimental .....	200
6.2.1 Materials and methods.....	200
6.2.2 Analysis of the effects of temperature and working liquid volume on pressure generation. ....	200
6.2.3 Performance analysis of different working fluids in the generation of operational pressure. ....	202
6.3 Heat transfer analysis.....	205
6.4 Statistical analysis of the system's performance.....	206
6.3 Results and discussion.....	206
6.3.1 Operational pressure test.....	206
6.4 Heat transfer analysis in the system.....	213
6.4 Evaluation of the efficiency of solar driven membrane filtration pump .....	214
6.5 Statistical analysis of system performance.....	216
6.6 Conclusion.....	217
6.7 References .....	218
<b>CHAPTER 7 .....</b>	<b>219</b>
<b>CONCLUSIONS AND RECOMMENDATIONS.....</b>	<b>219</b>
7.1 Conclusions.....	220
7.2 Recommendations .....	223
<b>APPENDIX .....</b>	<b>225</b>

## LIST OF FIGURES

<b>Figure 2.1:</b> Diagram showing a general structure of a model humic acid (Rupiasih, 2016). .....	15
<b>Figure 2.2:</b> General description of some properties of humic substances (Rupiasih, 2016). .....	16
<b>Figure 2.3:</b> Schematic representation of a porous pot filter (Varkey, 2012). .....	22
<b>Figure 2.4:</b> Schematic representation of a biosand filter (Bitton, 2014). .....	23
<b>Figure 2.5:</b> Schematic representation of SODIS (WHO, 2011). .....	25
<b>Figure 2.6:</b> Schematic representation of a convectional water treatment plant (Argaw, 2003). .....	26
<b>Figure 2.7:</b> Diagram showing the general structure of a PES polymer (Knauer, 2016). .....	29
<b>Figure 2.8:</b> Structure of the semi-polyamide polymer in NF270 membranes (Mouhoumed <i>et al.</i> , 2014). .....	32
<b>Figure 2.9:</b> Schematic representation of concentration polarization at the surface of a membrane (Kimura, 1991). .....	34
<b>Figure 2.10:</b> Illustration of the four modes of fouling described by the Hermia model (Wang & Tarabara, 2008). .....	35
<b>Figure 2.11:</b> Diagram showing the different uses of energy in water treatment (Wakeel <i>et al.</i> , 2016). .....	37
<b>Figure 2.12:</b> Diagram showing the different renewable energy sources used in water treatment (Kashyout <i>et al.</i> , 2021). .....	38
<b>Figure 2.13:</b> Schematic representation of a solar power plant with an energy storage system. ....	41
<b>Figure 2.14:</b> Schematic representation of the stages of a vapour power cycle in a diaphragm pump. ....	49
<b>Figure 2.15:</b> T-s plane sketch for a diaphragm pump heat engine. ....	49
<b>Figure 2.16:</b> Schematic representation of the repulsion mechanisms in nanofluids (Yu & Xie, 2012). .....	56
<b>Figure 3.1:</b> Graphical representation of the preparation of the UF PES membranes using the phase inversion method. ....	82

<b>Figure 3.2:</b> Graphical representation of a plot used in the determination of the surface free energy using the OWRK model (Spooner, 2007). .....	85
<b>Figure 3.3:</b> Satellite (A and B) and horizontal (A1 and B1) images of the Florida Lake and Florida Stream sampling sites, respectively.....	92
<b>Figure 3.4:</b> Dimensions of the working liquid chamber of the solar-driven system. ....	100
<b>Figure 3.5:</b> Graphical representation of the chemical synthesis used in the preparation of copper (II) oxide nanoparticles. ....	102
<b>Figure 3.6:</b> Graphical representation of the hydrothermal synthesis of copper oxide nanorods.....	103
<b>Figure 4.1:</b> Stand-alone solar driven hydraulic pump membrane filtration system for surface water purification. ....	111
<b>Figure 4.2:</b> Satellite and horizontal images of the field prototype used in the study. ....	112
<b>Figure 4.3:</b> SEM images of the pristine UF membranes used in this study showing UF membrane's (a) top surface, (b) cross-section, and (c) Thin top layer of the UF membrane. ....	113
<b>Figure 4.4:</b> SEM images of the clean NF membranes used in this study showing (a) top surface and (b) cross-section of the membrane. ....	113
<b>Figure 4.5:</b> AFM images of surface of pristine UF membrane (a) 3D view of pristine membrane, and (b) 2D view of Pristine membrane.....	114
<b>Figure 4.6:</b> AFM images of surface of pristine NF membrane showing (a) 3D view and (b) 2D view. ....	115
<b>Figure 4.7:</b> Thermograms of the (a) UF and (b) NF membranes showing the thermal degradation of the polymeric membranes at different temperatures. ....	117
<b>Figure 4.8:</b> FTIR spectra of pristine UF and NF membranes showing peaks of functional groups at the surfaces of these membranes. ....	119
<b>Figure 4.9:</b> Identification of the main functional units in the different polymers..	120
<b>Figure 4.10:</b> Estimation of the MWCO values for UF and NF270 membranes. .	122
<b>Figure 4.11:</b> FEEM contour plots of (a) Florida stream and (b) Florida lake raw water showing different NOM fractions present in the water. ....	124
<b>Figure 4.12:</b> FEEM diagrams of Florida Stream (a) raw water and UF membrane permeates of the Florida stream water at (b) 2 and (c) 4 hours of filtration. ....	125

<b>Figure 4.13:</b> DOC values of UF membrane hourly filtrates from the filtration of the (a) the Florida Stream raw water, (b) Florida Lake raw water, NF membrane hourly permeates from the filtration of (c) the Florida Stream raw water, and (d) Florida Lake raw water. ....	126
<b>Figure 4.14:</b> UV-Vis spectra of the Florida Lake and Florida Stream raw water samples. ....	127
<b>Figure 4.15:</b> Uv-Vis absorbance spectra of Florida Lake raw water and hourly permeates from (a) UF and (b) NF membranes. ....	128
<b>Figure 4.16:</b> DOC removal with change in filtration time for Florida Stream and Florida Lake raw water using (a) UF membranes and (b) NF membranes.....	129
<b>Figure 4.17:</b> Relationship between %DOC removal and SUVA for membrane filtration using (a) UF and (b) NF membranes. ....	131
<b>Figure 4.18:</b> Metallic ion concentration of raw water and membrane1-hour filtrates for (a) Alkaline Earth Metals (Ca & Mg) and (b) selected Heavy Metals.....	132
<b>Figure 4.19:</b> Compaction of the membranes showing the changes in pure water fluxes of the (a) UF and (b) NF membrane.....	134
<b>Figure 4.20:</b> Determination of the pure water permeability coefficients (A) for the (a) UF and (b) NF membranes. ....	135
<b>Figure 4.21:</b> Membrane resistance values for (a) UF and (b) NF membranes from fouling studies using BSA as a model foulant.....	136
<b>Figure 4.22:</b> Normalized fluxes calculated after the filtration of Florida Lake real water by UF and NF270 membranes. ....	137
<b>Figure 4.23:</b> Modelling of fouling behaviour of UF membrane while filtering Florida Lake real water showing (a) Cake filtration, (b) Intermediate blockage, (c) Pore constriction, and (d) Complete blockage mechanisms. ....	138
<b>Figure 4.24:</b> Modelling of fouling behaviour of NF membrane while filtering Florida Lake real water showing (a) Cake filtration, (b) Intermediate blockage, (c) Pore constriction, and (d) Complete blockage mechanisms. ....	139
<b>Figure 4.25:</b> Alpha diagrams of the dissociation of NaOHCl in aqueous solution at different pH values (K. Li <i>et al.</i> , 2019). ....	140
<b>Figure 4.26:</b> Change in normalized flux with chemical cleaning for (a) UF and (b) NF270 membranes.....	141

<b>Figure 4.27:</b> SEM images of UF membrane coupons after fouling with humic acid synthetic water showing (a) fouled flat surface, (b) fouled cross section, (c) chemically cleaned flat surface, and (d) chemically cleaned cross-section of membrane coupons.....	142
<b>Figure 4.28:</b> SEM images of NF membrane coupons after fouling with Humic acid synthetic water showing (a) fouled flat surface, (b) fouled cross section, (c) chemically cleaned flat surface, and (d) chemically cleaned cross-section of membrane coupons.....	143
<b>Figure 4.29:</b> AFM images of surface of UF membrane after fouling with Humic Acid synthetic water showing (a) 3D mage and (b) Flat surface image of the fouled membrane. ....	144
<b>Figure 4.30:</b> AFM images of surface of UF membrane after fouling with Humic Acid synthetic water then cleaning with NaOCl solution showing (a) 3D mage and (b) Flat surface image of the cleaned membrane. ....	145
<b>Figure 4.31:</b> AFM images of surface of an NF membrane coupon that had been fouled by HA fouled showing (a) 3D mage of Fouled membrane, and (b) Flat surface image of fouled membrane. ....	146
<b>Figure 4.32:</b> AFM images of the chemically cleaned NF membrane that had been fouled with humic acid synthetic feed water solutions showing (a) 3D image and (b) Flat surface image of the fouled membrane.....	147
<b>Figure 4.33:</b> Contact angles of the (a) UF and NF270 (b) membranes before and after fouling (F) with 50ppm Humic acid (HA) feed solution and chemical cleaning (C). ....	148
<b>Figure 4.34:</b> Surface Free Energies (SFE) of pristine, fouled and chemically cleaned (a) UF and (b) membrane coupons.....	149
<b>Figure 4.35:</b> Correlation of time of day to flux over two months on field prototype with UF membrane. ....	150
<b>Figure 5.1:</b> Image showing the setup used in the heating experiment for the determination of the thermal transfer enhancement of copper oxide nanoparticles. ....	165
<b>Figure 5.2:</b> Image showing the experimental setup used in the measurement of temperature change with time of nanofluids cooling under ambient temperature. ....	166



<b>Figure 5.3:</b> Images showing how the measurement of heat transfer enhancement by copper oxide nanoparticles dispersed in the pure working liquid using a custom-made Transient Hot Wire Method apparatus.....	167
<b>Figure 5.4:</b> Images showing how the investigation of the relationship between temperature and pressure generated by the working liquid was carried out. ....	169
<b>Figure 5.5: Images of copper oxide nanoparticles showing (a) Black CuO nanoparticles and (b) Brown Cu<sub>2</sub>O nanoparticles.....</b>	<b>170</b>
<b>Figure 5.6:</b> SEM images of copper (II) oxide nanoparticles showing (i) CuO nanospheres, (ii) CuO nanorods, (iii) Cu <sub>2</sub> O nanospheres, and (iv) Cu <sub>2</sub> O nanorods. ....	<b>171</b>
<b>Figure 5.7:</b> EDS spectra of (a) CuO nanospheres, (b) CuO nanorods, (c) Cu <sub>2</sub> O nanospheres, and (d) Cu <sub>2</sub> O nanorods.....	<b>173</b>
<b>Figure 5.8:</b> ATR-FTIR spectra of Cu <sub>2</sub> O nanospheres, Cu <sub>2</sub> O nanorods, CuO nanorods, and CuO nanospheres. ....	<b>173</b>
<b>Figure 5.9:</b> Change in surface charge of the nanomaterials with change in pH for (a) CuO nanospheres, (b) CuO nanorods, (c) Cu <sub>2</sub> O nanospheres, and (d) Cu <sub>2</sub> O nanorods. ....	<b>177</b>
<b>Figure 5.10:</b> Change in particle size with pH of copper oxide nanoparticles showing (a) CuO nanospheres, (b) CuO nanorods, (c) Cu <sub>2</sub> O nanospheres, and (d) Cu <sub>2</sub> O nanorods.....	<b>178</b>
<b>Figure 5.11:</b> Optical properties of copper oxide nanoparticles showing the absorbance spectra of (i) CuO nanospheres, (ii) CuO nanorods, (iii) Cu <sub>2</sub> O nanospheres, and (iv) Cu <sub>2</sub> O nanorods. ....	<b>179</b>
<b>Figure 5.12:</b> Images of 0,10 %.w/w CuO nanospheres dispersed in water and prepared in the pH range 2 to 13 showing the samples (a) before and (b) after standing for 24 hours.....	<b>182</b>
<b>Figure 5.13:</b> Images of nanofluid samples with concentration of 0,10% w/w CuO in water and 0,10% w/w CuO in the pure working liquid (a) before and (b) after standing for 24 hours.....	<b>183</b>
<b>Figure 5.14:</b> Heating curves of copper oxide nanofluids from 26°C to 45°C at a constant temperature of 70°C.....	<b>185</b>

<b>Figure 5.15:</b> Cooling curves of copper oxide nanofluids within the temperature range of 68°C to 27°C at a constant air temperature of 27°C. ....	186
<b>Figure 5.16:</b> Cooling curves of copper oxide nanofluids from 68°C to 22,9°C at different concentrations under ambient air temperature of 22,9°C. ....	187
<b>Figure 5.17:</b> Temperature change with time after heat addition to the nanofluids of different weight fractions of CuO nanoparticles in 20 ml of the pure working liquid in an ice bath. ....	189
<b>Figure 5.18:</b> Variation of equilibrium pressure of working liquid with temperature change over the range of (a) 25° to 60° and (b) 25° to 40°. ....	191
<b>Figure 5.19:</b> Comparison of the time taken to develop a pressure of 40kPa between pure working liquid and a 0,1 %.w/w CuO/Working Liquid. ....	192
<b>Figure 6.1:</b> Images showing the measurement of the equilibrium vapour pressure with hanges in the volume of the working liquid and temperature of the water bath. ....	201
<b>Figure 6.2:</b> Images showing the procedure used in the determination of the relationship between the temperature of the pressurized working fluid and the temperature of the water bath. ....	202
<b>Figure 6.3:</b> Image showing how the permeate discharge of the filtration units with the pure working fluid and the nanofluid were monitored. ....	203
<b>Figure 6.4:</b> Images of satellite and horizontal illustrating the location of the prototypes and how they were tested under real-world conditions. ....	204
<b>Figure 6.5:</b> Changes in the gas pressure and temperature with change in the volume of the pure working liquid at a constant water bath temperature of 35 °C. ....	207
<b>Figure 6.6:</b> Comparison of flux generated by the pure working liquid and a 0,1% w/w CuO working liquid with changes in temperature while filtering DI water through (a) UF membranes and (b) NF membranes. ....	209
<b>Figure 6.7:</b> Evaluation of the effects of weather conditions: (i) Solar intensity, (ii) Air Temperature, and (iii) Wind speed, on flux production by the prototype using the pure working liquid. ....	211
<b>Figure 6.8:</b> permeate flux graphs showing the comparison of the performance of the prototypes using the pure working liquid and 0,1 % w/w CuO nanofluid filtering DI water through (a) UF membranes and (b) NF membranes in a real-world application. ....	213

**Figure 6.9:** Convective heat transfer coefficient of wind at different speeds  
(Shitzer, 2006)..... 234

## LIST OF TABLES

<b>Table 2.1:</b> Some physico-chemical drinking water quality parameters covered under SANS 241: 2015.....	14
<b>Table 2.2:</b> Some of the heavy metals found in water, their application, and effects on water quality and ecotoxicological effect (Mahurpawar, 2015). ....	17
<b>Table 2.3:</b> Relationship of zeta potential of nanoparticles to their stability in nanofluids (Choudhary <i>et al.</i> , 2017). ....	55
<b>Table 3.1:</b> ICP-MS instrument operational parameters used in metallic analysis of water. ....	93
<b>Table 3.2:</b> SANS 241: 2015 limits for some of the parameters analysed for drinking water. ....	94
<b>Table 3.3:</b> Fouling mechanisms dominant in membranes. Adopted from (Harivram <i>et al.</i> , 2019; Slimane <i>et al.</i> , 2019).....	98
<b>Table 3.4:</b> Classification of NOM using SUVA values (Moyo <i>et al.</i> , 2020). ....	99
<b>Table 4.1:</b> Assignment of the peaks in the FTIR spectra of the UF and NF270 membranes. ....	118
<b>Table 4.2:</b> Raw water composition for Florida Stream and Florida Lake samples against the SANS 241:2015 guidelines for acceptable drinking water quality. ...	122
<b>Table 4.3:</b> Classification of NOM using SUVA values.....	130
<b>Table 4.4:</b> Physico-chemical analysis of membrane permeate of Florida lake...	133
<b>Table 4.5:</b> Humic acid and BSA rejections by UF and NF270 membranes.....	140
<b>Table 5.1:</b> Peak assignment for copper oxide nanoparticles' ATR-FTIR spectra. ....	174
<b>Table 5.2:</b> Summary of the size and zeta potential values of the copper oxide nanoparticles at a pH of 7. ....	176
<b>Table 5.3:</b> Summary of copper oxide nanoparticles' optical properties (Gupta <i>et al.</i> , 2018). ....	180
<b>Table 6.1:</b> Parameters used in the evaluation of the efficiency of the solar-driven prototypes using different membranes and working liquids. ....	214
<b>Table 6.2:</b> Independent sample means t-test comparison between the flux produced by the pure working liquid and that of the nanofluid. ....	216

## LIST OF ABBREVIATIONS

---

MWCO	–	Molecular Weight Cut-Off
SUVA	–	Specific UltraViolet Absorbance
DOC	–	Dissolved Organic Carbon
TOC	–	Total Organic Carbon
TDS	–	Total Dissolved Solids
pH	–	Hydrogen ion potential
UF	-	Ultrafiltration
NF	–	Nanofiltration
MF	–	Microfiltration
RO	–	Reverse Osmosis
COD	-	Chemical Oxygen Demand
MBR	–	Membrane Bioreactor
PES	–	Polyether Sulfone
PA	–	Polyamide
PE	–	Polyester
EMPs	–	Emerging Micropollutants
POU	–	Point of Use
NOM	–	Natural Organic Matter
SODIS	–	Solar Disinfection
TOC	–	Total Organic Carbon
ICP-MS	-	Inductively Coupled Mass Spectrometry
FTIR	–	Fourier Transform Infrared
Uv- Vis	–	Ultraviolet Visible
FEEM	–	Fluorescence Excitation Emission Matrix
FRR	–	Flux Recovery Ratio
TMP	–	Transmembrane Pressure
BSA	-	Bovine Serum Albumin
RSI	–	Resistance in Series
NFR	-	normalized flux ratios
NS	–	Nanosphere
NR	–	Nanorod

FL	–	Florida Lake
FS	–	Florida Stream
DI	–	Deionized
BROCs	–	Bio-Recalcitrant Organic Compounds
DWS	–	Department of Water and Sanitation
RWH	–	Rainwater Harvesting
AMD	–	Acid Mine Drainage
NIBS	–	Non-Invasive Back Scatter
QSU	–	Quinine Sulfate Units
OWRK	–	Owens-Wendt-Rabel & Kaelble (OWRK)
DBPs	–	Disinfection By-products
SDHW	-	Solar Domestic Hot Water
FPC	–	Flat Plate Collector
PWL	-	Pure Working Liquid
WL	-	Working Liquid
SABS	-	South African Bureau of Standards
SANS	-	South African National Standards

## NOMENCLATURE

---

$R_T$	-	total membrane resistance ( $m^{-1}$ ).
$R_m$	–	intrinsic membrane resistance ( $m^{-1}$ )
$R_{rf}$	-	reversible fouling resistance ( $m^{-1}$ )
$R_{if}$	-	irreversible fouling resistance ( $m^{-1}$ ).
$\alpha$	–	alpha (statistical unit)
$E_b$	-	emissive power ( $W/m^2$ )
$\varepsilon$	-	emissivity
$q$	–	heat flux
$T$	–	temperature (K)
$W$	–	work (J)

$m$	–	mass (Kg)
$A_m$	–	membrane cross-sectional area ( $m^2$ )
$A$	–	membrane permeability ( $L/m^2.h.bar$ )
$\Delta P$	-	transmembrane pressure (Pa)
$t$	–	time (s)
$k$	–	thermal conductivity (W/m.K)
$\theta$	–	contact angle ( $^\circ$ )
$\delta$	–	surface free energy
$J_w$	–	Pure water flux ( $L/m^2.h$ )
$J_{w2}$	-	steady-state flux of the permeate after backwashing
$J_{BSA}$	–	steady-state flux of BSA feed solution
$n$	–	Hermas' model fouling mechanism constant
$K_{cf}$	–	Cake filtration constant
$K_{ib}$	–	Intermediate blocking constant
$K_{pc}$	–	Pore constriction constant
$K_{cb}$	–	Complete blocking constant
$R$	–	membrane rejection (%)
$C_p$	-	permeate concentration (ppm)
$C_f$	-	feed concentration. (ppm)
$V$	–	volume ( $m^3$ )
$w$	–	weight
$l$	–	length (m)
$\rho$	–	density
$Q$	–	permeate volumetric flow rate ( $m^3/s$ )
$\eta$	-	water viscosity (Pas)
$\eta_{exp}$	-	efficiency
$r_m$	–	pore radius of the membrane (nm)
$E_g^*$	-	band gap energy
$E_g^{bulk}$	-	bulk is the band gap energy
$\lambda_c$	-	absorbed wavelength
$h$	-	Planck's Constant ( $6.625 \times 10^{-34}$ J.s)

$m_e^*$	-	effective mass of band electron
$m_h^*$	-	effective mass of a hole
$e$	-	elementary charge
$\epsilon_0$	-	the permittivity of free space
$\epsilon$	-	relative permittivity
$\Delta H$	-	latent heat of vaporization
$R$	-	the ideal gas constant ( $8,314 \text{ Jmol}^{-1}.\text{K}^{-1}$ )
$H_0$	-	Null hypothesis
$H_A$	–	Alternative hypothesis



## CHAPTER 1

### INTRODUCTION

---

#### 1.1 Background

South Africa is categorized as a water-stressed country (Rodda *et al.*, 2016), receiving an annual average rainfall amount of 464 mm, nearly half of the Earth's average (Sershen, 2016) hence is grappled with water scarcity. It is also a widely industrious country with high urban population densities (Stats SA, 2006) that produce a lot of domestic, mining, agricultural and industrial waste; some of which is discharged into surface water sources thereby causing water pollution (Bartram & Ballance, 1996). Membrane technology is a viable option to solve these growing problems of water pollution (Bhattacharya, 2017). It also helps water treatment plants/companies meet the stringent water quality requirements. However, its reliance on applied pressure means that it is also energy intensive. This interconnectivity of water and energy means that the cost of water treatment is also tied to the cost of energy production and some areas without access to cheap energy sources usually suffer (Musingafi, 2014) from water scarcity. Despite their disadvantages, membrane techniques have several advantages over conventional water treatment technologies. Membrane technologies are compact (Stoller *et al.*, 2017) hence can be made as stand-alone plants, require less chemical usage, and produce consistent water quality (Pillay & Jacobs, 2004). This stand-alone capability makes these technologies highly suitable for remote locations with little infrastructure like rural areas. Sustainable water treatment can also be provided using renewable energy sources and solar energy is a viable option given its abundance in South Africa (Mulaudzi *et al.*, 2012). Against this background, this project aimed to develop/ optimize influential parameters of a novel solar-driven membrane technology system that was intended for surface water treatment in rural areas. A comparison between a custom-made ultrafiltration membrane and commercial nanofiltration membrane was made to determine the suitability of each membrane's utility in the solar-driven filtration system. The influence of solar irradiation on operational pressure was also studied and a nanofluid was developed to increase thermal energy transfer within the system.

## 1.2 Problem statement

A third of South Africa's 58,78 million people (Stats SA, 2019) live in rural areas with 77% of these individuals being classified as impoverished (Viljoen & Walt, 2019) hence cannot pay for services and products like electricity and potable water. These rural areas have low population densities across large areas hence difficult to provide with cost-effective utilities. This is coupled to a lack of infrastructural development, which means people in rural areas have limited access to basic services (Gopaul, 2006). The absence of electricity supply, water treatment and distribution facilities in these areas means that most people rely on surface water reservoirs, water tanks, boreholes, and rainwater harvesting. Most of these water sources are unprotected and the water is of unknown or poor quality which poses a great risk of water-related diseases for its users (Odiyo & Makungo, 2012). People in these areas also rely mostly on agricultural activity which leads to pollution of their water sources (Gopaul, 2006). Agricultural pesticides, mining chemicals, faecal matter and other contaminants from human-related activities in these areas, are either leached or washed into rivers and other water bodies through run-off from rainfall (Musingafi, 2014) thereby increasing water pollution. Humans and animals are also forced to share the same surface water sources which leads to a rise in the transmission of diseases between humans and livestock (Clifford *et al.*, 2008). There is also a rise in non-infectious diseases associated with the labour involved in fetching water from afar places in rural areas as water is not easily accessible. This mostly affects women and children who are involved in acquiring water in rural areas. As a result, there is an increase in early-onset of arthritic diseases, spine and hip damage in the affected women and children, as well as reduced milk quantity and quality in lactating women (Howard, 2003).

### 1.3 Justification

Several measures have been implemented to combat water scarcity around the globe. In South Africa, boreholes have been sunk, water tanks are being used to cart water in some areas, small water treatment plants have been built with connections to communal taps, and rainwater harvesting projects have been implemented, predominantly in rural areas (Odiyo & Makungo, 2012). Point of Use (POU) systems have also been promoted in some areas to mitigate the re-contamination that may occur between transportation of the water from the point of supply to that of use.

Rainwater harvesting (RWH) has been used as a temporary solution to reduce water demand in rural municipalities in South Africa by the Department of Water and Sanitation (DWS) and these have been found to be beneficial. However, RWH cannot be used alone (DWS, 2015) as it only rains a few months in a year hence the need to be used together with other water sources. It not suitable to use at a large scale as it leads to reduced runoff and recharge of other water sources thereby negatively affecting hydrological cycles (Maitre *et al.*, 2018).

Groundwater is also used by people in rural areas. This water is accessed through wells, springs, and boreholes and accounts for 13% of the water needs in South Africa (Zhuwakinyu, 2012). However, many areas in the country have dolomite rock formations which are prone to cracks and can leach pollutants into the groundwater. Mine pollution through acid mine drainage (Musingafi, 2014) and agricultural pollution through leaching of nutrients thereby lead to a high pollution of groundwater thus making it unsafe for human consumption. When compared with surface water sources, groundwater is generally less polluted but requires more energy to access which leads to higher costs and less desirability for people in rural areas.

Point of Use (POU) techniques have also been implemented in rural areas as these are easy to use (Mckenzie & Fleenor, 2011), convenient and suitable for small households. Solar disinfection (SODIS) is a one of the POU techniques used in South Africa. It is cheap as sunlight is free and abundant in South Africa, while also

plastic bottles used in this process can be reused many times. However, the water quality is not guaranteed as some inactivated micro-organisms can reactivate themselves once in the dark and cause diseases (Laurent, 2005). It also does not remove suspended particles hence is not suitable for turbid water, takes time to fully disinfect the water, the treated water is not immediately ready for drinking after treatment as it will be warm, and is not easily scalable. Other POU techniques like clay pots and bio-sand filters which utilize gravity filtration, also take time as the filtration is slow. On the other hand, chemical disinfection is easy and highly effective but also costly.

All these strategies have added to the water sources, but their drawbacks prevent them from being applicable in many areas. The lack of consistency in water quality produced by these methods is also a major drawback that can be addressed by membrane technology which has enabled its recent widespread adoption (Ezugbe & Rathilal, 2020). The compactness of membrane-based operations also makes it possible to develop small stand-alone water treatment plants suitable for small communities as well as being scalable. However, the main problem in the application of membrane technologies is that of fouling (Subhi *et al.*, 2013) and this affects the cost and ease of operation as there is a need for periodic membrane cleaning or replacement (Li *et al.*, 2019a). This hinders the implementation of membrane technologies particularly in rural areas given the scarcity of technical skills (Thoola, 2014) in these areas. This problem of fouling was solved through the implementation of chemical cleaning of the membrane.

However, energy is still needed for driving membrane filtration processes which is proportional to the pressure needed. Ultrafiltration requires relatively lower pressure (usually less than 20 bars) than other membrane techniques, e.g., nanofiltration and reverse osmosis (W. Guo *et al.*, 2012) and produces good quality drinking water thereby making it a viable option. The energy needed for filtration processes can be provided by solar energy. This is a viable source of energy in South Africa as the country has an abundant solar resource with daily solar radiation averaging between 4.5 and 7 KWh/m<sup>2</sup> which is one of the amongst the highest globally (Mulaudzi *et al.*,

2012). Given that the Sun shines everywhere within the country, solar energy can be used to power stand-alone, membrane-based water treatment technologies that can be installed anywhere in the country, especially in remote areas. To improve the efficiency of solar energy conversion into mechanical energy, nanofluids can be used in improving the rate of heat transfer in these solar-powered systems (Amalraj & Michael, 2019). However, solar energy is intermittent and has low energy density but is a renewable energy source (Chamsa-ard *et al.*, 2017) hence has no greenhouse gas emissions.

#### **1.4 Aim and objectives of the study**

- The aim of this work was to optimize a novel solar-driven membrane system developed for the production of clean drinking water for small, rural South African communities, from surface water sources without the use of electricity.

#### **1.5 Objectives**

This aim was achieved through the following:

- i. Evaluation and comparison of ultrafiltration and nanofiltration membranes' suitability for application in the solar-driven filtration system.
- ii. Determination of the physicochemical properties of real water samples collected from a lake and a stream.
- iii. Preparation and characterization of Copper oxide nanoparticles and nanofluid.
- iv. Investigation of the heat transfer properties and operational pressure generation capacity of copper oxide-based nanofluids.
- v. Evaluation of the performance of the solar-driven membrane filtration system under laboratory and real-world conditions.

## 1.6 Dissertation outline

A summary of each chapter discussed in this dissertation is as follows:

**Chapter 2** provides a comprehensive literature review on water scarcity, the water-energy nexus, membrane technology and key discussions on characterisation and analysis methods used in the study. Furthermore, alternative methods of water treatment are examined as well as the accepted water quality standards. The application of solar energy in water treatment is reviewed with a focus on the use of nanofluids to enhance heat transfer in solar-driven systems. The chapter is then concluded with an overview on factors affecting membrane performance.

**Chapter 3** focuses on the methodologies that were used in the study. Methods used in the preparation, characterization, filtration studies, fouling, and chemical cleaning done on the membranes are presented in detail. In addition to this, the synthesis and characterization methods used on the copper oxide nanoparticles are also outlined in chapter 3.

**Chapter 4** reports on results of the evaluation and comparison of the physico-chemical properties of ultrafiltration and nanofiltration membranes in surface water filtration. Physico-chemical analysis of the raw surface water from a lake and a stream as well as the membrane permeates are also investigated.

**Chapter 5** covers the results on the preparation and testing of copper oxide based nanofluids in the optimization of the thermo-pneumatic properties of the pure working liquid.

**Chapter 6** presents results on the evaluation and optimization of a solar-driven membrane filtration system for surface water purification. The system was evaluated in both laboratory and real-world settings.

**Chapter 7** outlines a comprehensive conclusion of the results produced in the study. The implications of the results are discussed and recommendations for future studies are put forward.

## 1.6 References

- Amalraj, S., & Michael, P. A. (2019). Synthesis and characterization of Al<sub>2</sub>O<sub>3</sub> and CuO nanoparticles into nano fluids for solar panel applications. *Results in Physics*, 15, 102797. <https://doi.org/10.1016/j.rinp.2019.102797>
- Bartram, J., & Ballance, R. (1996). Water quality monitoring. A practical guide to the design and implementation of freshwater quality studies and monitoring programmes. (1<sup>st</sup> ed.) *E&FN Spon*.  
<https://apps.who.int/iris/handle/10665/41851>
- Bhattacharya, S. S. A. (2017). Drinking water contamination and treatment techniques. *Applied Water Science*, 7(3), 1043–1067.  
<https://doi.org/10.1007/s13201-016-0455-7>
- Chamsa-ard, W., Brundavanam, S., Fung, C. C., & Fawcett, D. (2017). Nanofluid Types , Their Synthesis , Properties and Incorporation in Direct Solar Thermal Collectors : A Review. *Nanomaterials*, 7(131).  
<https://doi.org/10.3390/nano7060131>
- Clifford, D. L., Kazwala, R., Coppolillo, P., Ann, J., & Mazet, K. (2008). Evaluating and managing zoonotic disease risk in rural Tanzania. *Global Livestock CRSP Research Brief*. <https://doi.org/10.6084/M9.FIGSHARE.156276>
- DWS. (2015). South Africa Yearbook 2015/16: *Water and Sanitation*. South Africa Yearbook 2015/16 | *Government Communication and Information System*.  
<https://www.gcis.gov.za/content/resourcecentre/sa-info/yearbook2015-16>
- Ezugbe, E. O., & Rathilal, S. (2020). Membrane Technologies in Wastewater Treatment : *Membranes*, 10(89).  
<https://doi.org/doi:10.3390/membranes10050089>
- Gopaul, M. (2006). The significance of rural areas in South Africa for tourism. *University of South Africa*. <http://uir.unisa.ac.za -> dissertation.pdf>
- Guo, W., Ngo, H., & Li, J. (2012). A mini-review on membrane fouling. *Bioresource Technology*, 122, 27–34. <https://doi.org/10.1016/j.biortech.2012.04.089>

- Howard, G. (2003). Domestic Water Quantity, Service Level and Health. World Health Organization.  
[https://www.who.int/water\\_sanitation\\_health/diseases/WSH03.02.pdf](https://www.who.int/water_sanitation_health/diseases/WSH03.02.pdf)
- Laurent, P. (2005). Household Drinking Water Systems and Their Impact on People With Weakened Immunity. *East Africa Medical Journal*, 1–72.  
[http://www.who.int/household\\_water/research/HWTS\\_impacts\\_on\\_weakened\\_immunity.pdf](http://www.who.int/household_water/research/HWTS_impacts_on_weakened_immunity.pdf)
- Li, K., Li, S., Huang, T., Dong, C., Li, J., Zhao, B., & Zhang, S. (2019). Chemical cleaning of ultrafiltration membrane fouled by humic substances: Comparison between hydrogen peroxide and sodium hypochlorite. *International Journal of Environmental Research and Public Health*, 16(14).  
<https://doi.org/10.3390/ijerph16142568>
- Maitre, D. Le, Seyler, H., Holland, M., Smith-Adao, L., Maherry, A., Nel, J., & Witthuser, K. (2018). Identification, delineation and importance of the strategic water source areas of South Africa, Lesotho and Swaziland for surface water and groundwater. <https://water.cer.org.za/wp-content/uploads/2019/03/Identification-delineation-and-importance-of-the-strategic-water-source-areas-of-South-Africa-Lesotho-and-Swaziland-for-surface-water-and-groundwater.pdf>
- Mckenzie, E. R., & Fleenor, W. (2011). Point-Of-Use Drinking Water Treatment in the Developing World : Community Acceptance , Project Monitoring and Revision. *International Journal for Service Learning in Engineering*, 6, 14–32.  
<https://doi.org/10.24908/ijlsle.v6i1.3207>
- Mulaudzi, S. K., Muchie, M., & Makhado, R. (2012). Investigation of the Solar Energy Production and Contribution in South Africa. *African Journal of Science, Technology, Innovation and Development*, 4(January).  
<https://journals.co.za/doi/abs/10.10520/EJC134598>
- Musingafi, M. (2014). Fresh Water Sources Pollution : A Human Related Threat To Fresh Water Security in South Africa. *Journal of Public Policy and Governance*, 1(2), 72–81. <https://ideas.repec.org/a/rss/jnljpg/v1i2p3.html>
- Odiyo, J. O., & Makungo, R. (2012). Water quality problems and management in rural areas of Limpopo Province , South Africa. *WIT Transactions on Ecology and The Environment*, 164(July). <https://doi.org/10.2495/WP120121>



- Pillay, V. L., & Jacobs, E. P. (2004). The Development of Small-Scale Ultrafiltration Systems for Potable. In *Water Research Commission* (Issue 1070). <http://www.wrc.org.za/wp-content/uploads/mdocs/1070-1-041.pdf>
- Rodda, N., Schmidt, S., Dent, M., Bux, F., Hanke, N., & Fennemore, C. (2016). Water security in South Africa : perceptions on public expectations and municipal obligations , governance and water re-use. *Water SA*, 42(3), 456–465. <https://doi.org/http://dx.doi.org/10.4314/wsa.v42i3.11>
- Stats SA. (2006). Migration and urbanisation in South Africa. *Statistics South Africa*. <http://www.statssa.gov.za/publications/Report-03-04-02/Report-03-04-02.pdf>
- Stats SA. (2019). Mid-year population estimates. Statistics South Africa. <https://www.statssa.gov.za/publications/P0302/P03022019.pdf>
- Stoller, M., Miguel, J., Pulido, O., & Di, L. (2017). Study On Fouling Behaviour Of Ultrafiltration And Nanofiltration During Purification Of Different Organic Matter Polluted Wastewaters. *Chemical Engineering Transactions*, 60, 295–300. <https://doi.org/10.3303/CET1760050>
- Subhi, N., Leslie, G., Chen, V., Le-clech, P., Subhi, N., Leslie, G., Chen, V., Organic, P. L., Subhi, N., Leslie, G., Chen, V., & Le-clech, P. (2013). Organic Fouling of Ultrafiltration Membrane : Detailed Characterization by Liquid Chromatography with Organic Carbon Detector Organic Fouling of Ultrafiltration Membrane. *Separation Science and Technology*, 48(2), 199–207. <https://doi.org/10.1080/01496395.2012.686552>
- Thoola, M. I. (2014). Performance characteristics of Bio-ultrafiltration on local surface waters. *Durban University of Technology*. <https://openscholar.dut.ac.za/handle/10321/1385>
- Viljoen, G., & Walt, K. Van Der. (2019). South Africa ' s water crisis - An interdisciplinary approach. *SciELO South Africa*, 58 (3) <https://doi.org/10.17159/2224-7912/2018/v58n3a3>
- Zhuwakinyu, M. (2012). Water 2012. A review of South Africa's water sector. *Powertech*. <https://pmg.org.za/files/120904review.pdf> .

## CHAPTER 2

### LITERATURE REVIEW

---

#### 2.1 Introduction

This chapter covers water scarcity in South Africa, membrane preparation and characterization, synthesis, and characterization of nanoparticles, nanofluid preparation and evaluation, study of solar radiation transfer, and optimization of a solar-driven membrane filtration system.

#### 2.1 Drinking water challenges in low-income areas

Water scarcity is the most widely discussed topic globally and its significance is set to increase in the following years. It is defined as the shortage of adequate water resources to meet water usage demand for a given population resident in a geographic area. This shortage also includes, a lack of infrastructure to process (Musingafi, 2014), store, and access clean and portable water, (Klerk *et al.*, 2020) as well as low rainfall or drought leading to the reduction of water levels in reservoirs.

Water scarcity is worsened by both air and water pollution arising from industrial activities. With the rise in global industrial activities, there has been a rise in air pollution which has caused global warming (Stout, 1990). This warming of the Earth has led to higher rates of evaporation and changes to hydrological cycles resulting in global climate change. Climate change has resulted in higher occurrence of floods and droughts (Hoegh-Guldberg *et al.*, 2018) which have the worst impact in low-income areas by worsening water scarcity. On the other hand, mining, agricultural, industrial, and domestic activities by humans have resulted in water pollution (Bwapwa, 2018) as the waste from these activities are discharged or find their way into water bodies.

As previously mentioned in the previous chapter, water scarcity is widespread in South Africa thereby heightening the risk of water-related communicable diseases (Rother *et al.*, 2019). The demand for water in South Africa is also projected to

exceed supply in the coming years (around 2025 to 2030) if no changes are made (Zhuwakinyu, 2012) to address this water scarcity problem.

South Africa also faces a serious problem of poor water quality. Water quality is defined as a measure of the physicochemical and microbiological state of water (Bartram & Ballance, 1996), and is compromised due to the high levels of industrialization and urbanization in the country. Some industrial waste is discharged into water sources like rivers and dams without treatment while around 11% of all wastewater treatment plants in the country are not fully functional. The increasing population; 58,78 million as of 2019 statistics (Stats SA, 2019), has led to high rates of deforestation hence higher erosion and runoff into surface water sources as well as effluent disposal leading to increased surface water pollution and poor water quality.

The vast mining industry in the country produces acid mine drainage from the oxidation of pyrite in mine tailings as well as effluent with several heavy metals that is also discharged into surface water sources while some of this waste leaches into groundwater sources. On the other hand, agricultural chemical usage also results in water pollution from fertilizers and pesticides as well as from nutrients of plant and animal origin (Musingafi, 2014). With the rise in usage of pharmaceutical and personal care products as the standards of life of the people of South Africa improves, there also has been a rise of emerging micropollutants. These emerging micropollutants are unregulated or recently regulated substances, their metabolites and transformation products, that may adversely affect the health of plants, animals and human (Sanganyado & Kajau, 2021) even at very low concentrations.

With over 500 dams in the country, South Africa is heavily dependent on water storage to reduce water stress in different areas across the country as well as provide water for urban domestic usage, irrigation, and meet industrial requirements (Masindi & Duncker, 2016). It has also been reported that water levels in dams are dropping considerably, e.g., dams in Durban are 20% less than the capacity they had in 2010. This has prompted the set-up of a raft of strategies to secure water services including the implementation of Dams and water schemes (Colvin *et al.*,

2016), which seek to monitor water usage amongst the 500 government owned dams.

Municipal water authorities have put in place water restrictions at different levels to conserve water. Many water projects like the Mzimvubu water project in the Eastern cape (SA News, 2019), the Kalahari East water scheme in the Northern Cape (Frankson, 2016), and others have been proposed and these large scale projects will result in the building of dams, hydro-power stations, water reservoirs, water pipeline networks and upgrading of water pumps (DWS, 2015). These projects represent large scale reconciliation strategies to help curb the scourge of water scarcity but most of the projects are still under development. More actions need to be done to address the water crises in the country (Donnenfeld *et al.*, 2018).

Imposition of water restrictions by local authorities, e.g., the Cape Town municipality-imposed restrictions that effectively reduced the usage of water by 60% as of 2018 in comparison to the 1998 water usage (Parks & McLaren, 2019). Regulations have been put in place to improve sanitation services and raw water quality through the bucket eradication program and enhancing water research and development respectively (DWS, 2015). Rainwater harvesting and storage has also been implemented in the Eastern Cape with farmers being provided with water troughs to alleviate the effects of recurrent droughts that have caused severe water shortages (Ellis, 2019).

Currently, 60% of the country's wastewater is untreated (Donnenfeld *et al.*, 2018) which presents a major challenge of pollution. Several ways to improve water availability are focused on the need to implement more effective wastewater treatment technologies including the improvement on maintenance of the existing wastewater treatment facilities and stringent adherence to wastewater treatment regulations. There is also a need to incorporate new technologies in water treatment (Abdel-Raouf *et al.*, 2019) apart from the convectional techniques, e.g., desalination, ground-water extraction, and implementation of renewable energy in power generation to replace the water demand by processes such as thermal power generation. The new technologies developed should also be energy conservative

(Capodaglio & Olsson, 2020) and sustainable, especially given that South Africa is battling an energy crisis.

## **2.2 Potable water supply and quality challenges in rural areas.**

Surface water is water that is easily accessible from rivers, lakes and other water bodies found on the earth's surface (EPA, 2017). It is a common water source in rural areas but is usually of poor or unknown quality, which presents many challenges. In South Africa, two thirds of all the rivers in the country are considered to be polluted (Donnenfeld *et al.*, 2018) which worsens water scarcity in rural areas. The pollution occurs mainly from the discharge of untreated effluent from mining processes as well as agricultural chemicals (Rodda *et al.*, 2016) into the environment. In some areas, poor sanitation practices like open defecation or washing of clothes in rivers, worsen water quality as the faecal matter is transported into rivers and other surface water sources by runoff from rain. Humans, wild animals, and livestock, also share these surface water sources thereby contributing to cross infection and pollution of these water sources.

As such, surface water mostly contains natural organic matter (NOM), inorganics (minerals), humic substances, microbiological content, and many other foreign substances, e.g., emerging micropollutants. This contamination of surface waters leads to a great variation in surface water composition (Bartram & Ballance, 1996) which is also affected by seasonal changes (Chaukura *et al.*, 2018).

People in rural areas also access groundwater through wells, boreholes, and springs. The quality of groundwater is questionable, but it is generally considered to be less susceptible to pollution (Molekoa *et al.*, 2019). Several studies have reported that the main pollutants for groundwater in South Africa are total dissolved solids (TDS), chlorides, nitrates, fluorides, and microbiological content (Odiyo & Makungo, 2012). In rural areas, these pollutants are derived from agricultural waste, pit latrines, and mining waste that leaches through sand and underground rock formations thereby compromising the quality of groundwater in these areas.

Several efforts have been made to address water scarcity in rural areas. Decentralized water treatment has been implemented through the provision of disinfectants and education on boiling water as Point of Use (POU) systems for household water treatment. Municipalities, mines and other industries operating in these areas have also been instrumental in providing water services to their employees and the people dwelling in these areas (Swartz, 2009). These include the transport of water in water trucks, sinking of boreholes, piped water supply at communal tap-stands, implementation of rainwater harvesting schemes, etc. However, there are many issues associated with these methods, e.g., rusting of water tanks, poor hygiene, or drainage systems at the mouth of wells leading to recontamination of water.

According to (SABS Standards Division, 2015), acceptable limits for selected physico-chemical parameters of water quality are listed in **Table 2.1**.

**Table 2.1:** Some physico-chemical drinking water quality parameters covered under SANS 241: 2015.

<b>Water quality parameter</b>	<b>Risk</b>	<b>SANS 241: 2015 limits</b>
<b>pH value at 25°C</b>	Operational	<b>≥5 to ≤ 9.7</b>
<b>Total Dissolved Solids at 180°C</b>	Aesthetic	≤1200
<b>Dissolved Organic Carbon (mg/l)</b>		<10
<b>Electrical conductivity in mS/m at 25°C</b>	Aesthetic	≤170
<b>Turbidity in N.T.U</b>	Operational	≤1
	Aesthetic	≤5
<b>Iron as Fe (µg/l)</b>	Chronic health	≤ 2000
	Aesthetic	≤300
<b>Lead as Pb (µg/l)</b>	Chronic health	≤10
<b>Nickel as Ni (µg/l)</b>	Chronic health	≤70
<b>Manganese as Mn (µg/l)</b>	Chronic health	≤400
	Aesthetic	≤100

<b>Cadmium as Cd (<math>\mu\text{g}/\ell</math>)</b>	Chronic health	$\leq 3$
<b>Chromium as Cr (<math>\mu\text{g}/\ell</math>)</b>	Chronic health	$\leq 50$
<b>Cobalt as Co (<math>\mu\text{g}/\ell</math>)</b>	Chronic health	$\leq 500$
<b>Copper as Cu (<math>\mu\text{g}/\ell</math>)</b>	Chronic health	$\leq 2000$
<b>Vanadium as V (<math>\mu\text{g}/\ell</math>)</b>	Chronic health	$\leq 200$
<b>Cyanide (<math>\mu\text{g}/\ell</math>)</b>	Acute health chemical	$\leq 200$
<b>Calcium (<math>\mu\text{g}/\ell</math>)</b>	Aesthetic/Operational	$< 150000$
<b>Magnesium (<math>\mu\text{g}/\ell</math>)</b>	Aesthetic/ Health	$< 70000$

### 2.2.1 Natural Organic Matter (NOM)

Natural Organic Matter (NOM) is a generic term for a diverse mix of organic compounds (humic substances shown in figure 2.1, and non-humic substances) found in surface water bodies in nature (Jacangelo *et al.*, 1997). These substances come from the natural decomposition of animal and plant matter (W. Guo *et al.*, 2012) within and outside of aquatic systems as well as from anthropic sources, e.g., composting or oil spillages (Reyes & Crisosto, 2016). The structure of a model humic acid is shown in **Figure 2.1**.

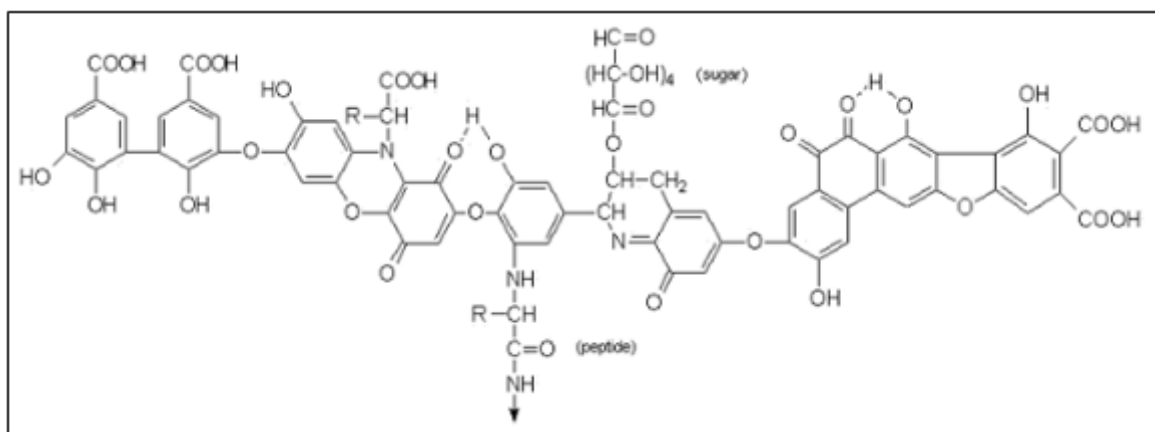


**Figure 2.1:** Diagram showing a general structure of a model humic acid (Rupiasih, 2016).

The presence of NOM in surface water is not desirable not only because these substances affect the colour (as shown in **Figure 2.2**), taste, and odour of water,

but they also affect water treatment. Humic acid, a component of NOM is a common membrane foulant (Lee *et al.*, 2004).

Humic substances (Pigmented Polymers)				
Fulvic acid		Humic acid		Humin
Light Yellow	Yellow Brown	Dark Brown	Grey Black	Black
<div> <div></div> <div>Increase in intensity of colour</div> <div></div> </div>				
<div> <div></div> <div>Increase in molecular weight</div> <div></div> </div>				
<div> <div></div> <div>Decrease in water solubility</div> <div></div> </div>				

**Figure 2.2:** General description of some properties of humic substances (Rupiasih, 2016).

### 2.2.2 Inorganic substances

Inorganic pollutants also impair surface waters. These pollutants come from several sources that include, industrial, mining, and agricultural effluent (Bartram & Ballance, 1996). Verlicchi & Grillini (2020) found that most South African surface waters are polluted with metallic elements (nickel, aluminium, iron, and chromium) that are mostly found at concentrations above those acceptable for drinking water according to drinking water regulations in the country. In South Africa, mining is the main source of inorganic pollutants through the release of acid mine drainage (AMD) from abandoned coal and metallic mines (Bwapwa, 2018) which has many heavy metals and causes metallic ions to be released from the soil by dissolving minerals or precipitating their salts.

Heavy metals (e.g., As, Fe, Co, Cr, Mn, Cu, Zn, Pb, etc.) are inorganic substances of concern and can be found in polluted water bodies especially ground water sources. These metals can be harmful to plants, animals, and humans, even in low concentrations. They are non-biodegradable and usually transformed into different forms of various toxicity, e.g., arsenic is a poisonous heavy metal that is used in the glass and steel manufacturing sectors as well as in pesticides used in agriculture



(Verlicchi & Grillini, 2019). Heavy metals can persist in the environment as they are cannot be degraded biologically or chemically but can be converted through biochemical processes into potentially more toxic compounds (Ebenebe *et al.*, 2017).

Edokpayi & Odiyo (2014) investigated the presence of selected heavy metals (Mn, Pb, Al, Cr, Cu, Fe, and Zn) in water samples taken from Dzindi river in the Limpopo province of South Africa. The researchers discovered that the water did not meet drinking water standards as all the investigated heavy metals except copper, were detected at levels above those acceptable for drinking water standards. The concentrations of the heavy metals were nonetheless below the limits for the water to be acceptable for use in irrigation.

Heavy metals of natural origin have also been detected in water sources but their concentrations are usually much lower than those from anthropogenic sources. Greenfield *et al.* (2012) analysed and detected selected heavy metals (Zn, Cu, Fe, Se, Cd, Pb, Al, As, Cr, and Mn) in the Nyl river in Limpopo and found that their concentrations were relatively high but fell below target water quality guidelines. Since the metal concentrations were relatively constant on a spatial scale, the researchers thus determined that these metals were of natural origin. Some heavy metals present in surface water are presented in **Table 2.2** together with their ecotoxicological effects.

**Table 2.2:** Some of the heavy metals found in water, their application, and effects on water quality and ecotoxicological effect (Mahurpawar, 2015).

Heavy metal	Application effluent	Ecotoxicological effect
Iron	Steel and appliances	Coronary heart disease.
Arsenic	Fertilizer, paints, and textiles.	Respiratory cancer.
Nickel	Electroplating	Cancer
Copper	Electricals	Liver and kidney damage.
Chromium	Metal plating and tanning.	Nasal septum perforation.

<b>Lead</b>	Batteries and fuel additive.	Central nervous disorders.
<b>Cadmium</b>	Pigments	Emphysema

A common method of removing these heavy metals in emergency situations, is the addition of alkaline substances (Meng *et al.*, 2019). Other methods used in the removal of heavy metals from water include, the use of ion-exchange resins, electrochemical separations (Raju, 2011), and membrane filtration.

### 2.2.3 Microbiological content

Surface waters also contain micro-organisms, some of which cause diseases. In urban areas, some of these pathogens (e.g., *Escherichia Coli*, *Shigella* and *Vibrio cholerae*), enter these water bodies from runoff or sewage directly spilled into water systems (Verlicchi & Grillini, 2020). One measure of microbiological content in water is the level of faecal pollution which is measured through the presence and amount of *Escherichia Coli* (Molelekwa *et al.*, 2014). Micro-organisms also thrive in water that has high levels of turbidity as often the turbidity is due to organic pollutants which the micro-organisms feed on.

In rural areas, there is open defecation on riverbeds, pit latrines close to wells, poor hygienic practices on the mouth of wells, and other improper sanitation practices that make the transfer of micro-organisms between humans and animals much easier. The run-off from rains washes these micro-organisms from faeces into surface water sources like rivers and dams, while some micro-organisms leach from pit latrines through soil and rock formations into wells. Wild animals also have access to surface water sources and can pollute these sources with pathogens hence making this water unsuitable for human consumption. Household sand filters can be used to reduce microbiological content in water to levels acceptable for drinking water quality and this improves water availability (Mwabi *et al.*, 2013).

Some micro-organisms may not be associated with water but their link with hygienic practices may also impact on water scarcity. Coronavirus is one such micro-

organism. While coronavirus is not a water-based virus, its mitigation strategies involve improving hygiene through frequent washing of hands with water and soap which uses water and very difficult in areas suffering from water scarcity (Boretti, 2020).

#### **2.2.4 Emerging Micropollutants (EMPs)**

Many researchers have reported the occurrence of emerging micro-pollutants (EMPs) in low concentrations in different surface waters (Stuart & Lapworth, 2013). Emerging micro-pollutants are defined as compounds that are not yet regulated (Li *et al.*, 2015) or recently discovered in the natural environment, whose toxicity implications after exposure to humans, animals, and plants are not yet fully understood (Lei *et al.*, 2015).

Some rural villages are located close to agricultural plantations, wood processing factories, mines, and textile factories. People in these areas may rely on surface water sources like rivers which may lie downstream to these industries and their water may contain pollutants from the industrial effluent (Wanda *et al.*, 2017). The raw sewage and other forms of industrial wastewaters spilled into surface waters have recently become a major source of emerging micro-pollutants (EMPs).

There are still a few studies on emerging micropollutants in South Africa. Wanda *et al.*, (2017) investigated the occurrence of selected emerging micropollutants (Bisphenol A, 4-Nonylphenol, caffeine, carbamazepine, galaxolide, and tonalide) in wastewater, surface, and groundwater samples taken from Mpumalanga, North-West, and Gauteng provinces in South Africa. The researchers discovered that their target analytes were present in all the samples but only the samples from the Mpumalanga province had concentrations of the EMPs that posed ecotoxicological danger.

### **2.3 Surface water treatment technology**

Generally, water treatment technologies can be classified as physical, chemical and energy intensive methods. Physical methods involve solid-liquid separations, chemical methods involve neutralization of the contaminant by reaction with added chemicals while energy intensive methods involve conditioning (thermal and electrochemical methods) and sterilization of the water (Cheremisinoff, 2002). The classes of water treatment techniques include simple household systems, point of use (POU) techniques, convectional treatment methods, and advanced water treatment techniques.

The selection of which treatment technique to use is governed by several factors which include, affordability, availability of resources (skilled labour, fuel, infrastructure, etc.), performance, and suitability of the technology to meet local conditions (Argaw, 2003). The differences between urban and rural areas in terms of demographics, geography, culture, etc., means different methods are suitable for each area.

### **2.3.1 Simple household water treatment techniques**

Simple household water treatment techniques include boiling, pasteurization, and disinfection. These are simple methods which are highly effective in killing pathogens in water. In pasteurization, water samples are heated by use of a fuel, e.g., solar radiation, to reach 60-70°C and kept at that temperature for a few minutes while for boiling, the water is boiled for one to three minutes. However, boiling and pasteurization all consume a lot of energy, and it takes time for the water to cool down hence the water cannot be consumed immediately after treatment. There are also some heat resistant pathogens that may survive and some pollutants will still be left in the water (Laurent, 2005), e.g., heavy metals. Disinfection of water can be achieved by Uv-radiation or chemical addition to the water. The effectiveness of disinfection by Uv-radiation is reduced in water with high levels of turbidity which limits its application. Disinfection may also lead to the formation of harmful disinfection by-products (DBPs), e.g., chlorine reacts with some NOM substances to produce trihalomethanes which may be carcinogenic (Zereffa *et al.*, 2017).

## 2.4 Filtration processes

Filtration is a physical process used to remove or reduce particulate matter from water (WHO, 2007). The particulate matter may include micro-organisms, suspended particles, and several, different dissolved substances (Machenbach, 2007). Filtration occurs by the entrapment of large particles outside the pores of the filtering media that blocks these particles from passing through the media which is a mechanism called mechanical straining. The suspended particles are also separated by adhesion onto the surfaces of the filtering media particles (National Drinking Water Clearing House, 1996).

Filtration occurs naturally when underground water moves through porous soil layers into surface water reservoirs. Other forms of water filtration include slow sand filtration in convectional water treatment plants, membrane filtration, cartridge filtration, etc. Each method has its benefits and limitations (National Drinking Water Clearing House, 1996) but in general, filtration processes are easy to carry out and involve lower costs than other techniques.

NOM can be removed from water by pre-filtration which can involve either physical sieving or chemical adsorption/ desorption followed by membrane or convectional water treatment techniques. Sieving and chemical adsorption methods target aquatic particles hence reduce solids loading onto membrane in the case of water treatment by membrane filtration. Lower solids loading reduces the risk of membrane fouling (Lienhard V *et al.*, 2016).

## 2.5 Point of Use (POU) water treatment techniques

Point of Use (POU) systems mostly use ion exchangers as well as absorptive media, filters (mostly ceramic pots) and disinfectants (e.g., bleach). These systems are simple to use hence are better suited for application in remote areas without centralized water treatment facilities and have low installation and maintenance cost as well as low energy requirements (Mecha & Pillay, 2014). However, in general, POU's are labour intensive, require frequent washing and only treat relatively small

amounts of water which is a significant draw-back in their application on a large scale. Pooi & Ng (2018) argued that there is a need for the use of a multiple barrier approach when using POU, to ensure their efficiency in pathogen removal is enhanced. This also adds on to the cost of implementing these systems and POU systems are also inefficient in the removal of dissolved solids.

### 2.5.1 Porous pot filter

Porous pot filters are usually made from mixing clay with sawdust or wheat flour then sintering the mould in a furnace. The sawdust and wheat flour additives are used as porogens to impart porosity on the filter pots (Meridian Institute, 2006). As these pots have been shown not to remove all pathogens, it has become common for the pots to be manufactured with the incorporation of additives with germicidal properties like silver or copper (Varkey, 2012). This type of filter has been shown to have up to 100% removal efficiency of *Escherichia coli* (Bitton, 2014) in trials performed in South Africa. After operating for some time, porous pot filters have been shown to have a tendency to experience pathogen breakthrough due to their depth filtration operation mode (Thoola, 2014). Porous pot filters are cheap and easy to use but require regular cleaning to maintain their performance. A general representation of porous pot filters is shown in **Figure 2.3**.

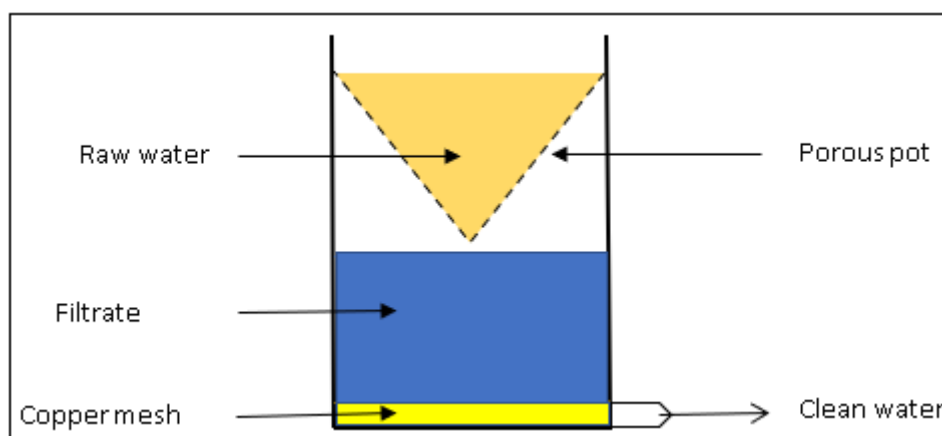


**Figure 2.3:** Schematic representation of a porous pot filter (Varkey, 2012).

### 2.5.2 Biosand filter

Biosand filters are a type of granular media filter made from packed sand beds (Bitton, 2014) which operate by gravity. They consist of a layer of coarse gravel on the bottom, with a fine gravel layer on top then a layer of clean sand above that. The filter has a biological layer that is first allowed to develop by treating the filter with water for 2 weeks before use, and this layer is responsible for the removal of micro-organisms while the sand traps organic matter. The filter is also efficient in removal of arsenic (76-91%) (Mahlangu & Mamba, 2012) and can reach 100% removal of protozoa (Zereffa *et al.*, 2017). Some solid contaminants are removed by mechanical entrapment between the sand particles, while the pathogens may die naturally in the filtration process due to lack of oxygen or food with some feeding on other pathogens and some getting adsorbed onto the filtration media (CAWST, 2009). The flow rate of the filter has also been shown to be dependent on the feed turbidity and size of the filter which usually make the filtration process to be slow. A schematic representation of the general configuration of a biosand filter is shown in **Figure 2.4**.

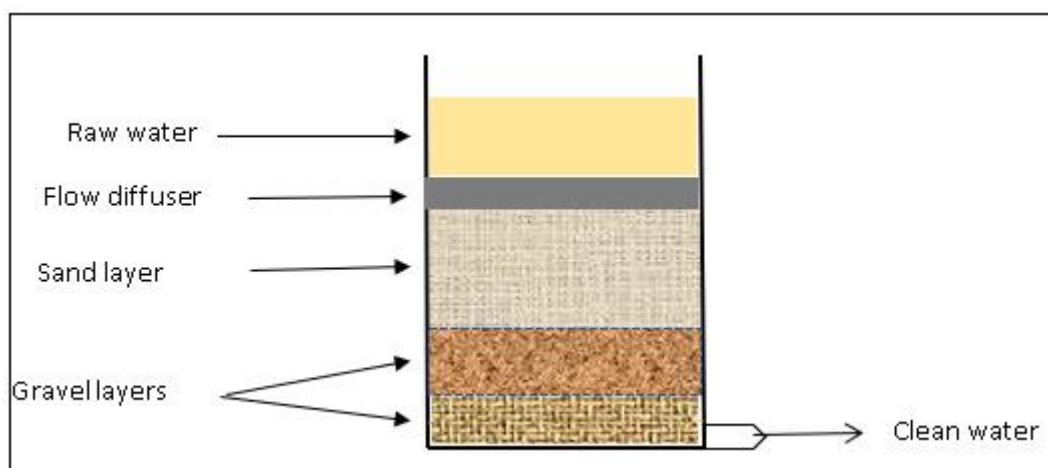


**Figure 2.4:** Schematic representation of a biosand filter (Bitton, 2014).

### 2.5.3 Activated carbon filter

These filters are made by packing granular activated carbon into layers. They are used to remove organic pollutants and some inorganic substances like sulphides,

heavy metals, and nitrogen from water through chemically reacting with these pollutants or physically adsorbing the pollutants onto the surface of the activated carbon. This removal of organic pollutants often leads to an improvement in the odour and taste of the water (Meridian Institute, 2006). The activated carbon has a large surface area and contaminants which can pass through its pores are more readily adsorbed onto its surface (Metcalf *et al.*, 2014).

#### **2.5.4 Fabric filters**

Fabric filters are made from a variety of cast, spun, compressed, or woven fibres through which water is passed. They are low cost filters which are fast and easy to use, but easily break thereby require frequent replacement (Thoola, 2014).

#### **2.5.5 Solar Disinfection (SODIS)**

In solar disinfection (SODIS), water is simply put into clear bottles and placed in the sun for some time. The ultraviolet (Uv) radiation in the sunlight will kill pathogens in the water while the heat from the radiative heating effect of the sun's radiation will also increase the temperature of the water (Pooi & Ng, 2018), hence denaturing the pathogens. It is a cheap method of water disinfection but is affected by weather conditions and takes a long time to treat small amounts of water (Garc *et al.*, 2021). A schematic representation of the SODIS process is shown in **Figure 2.5**.



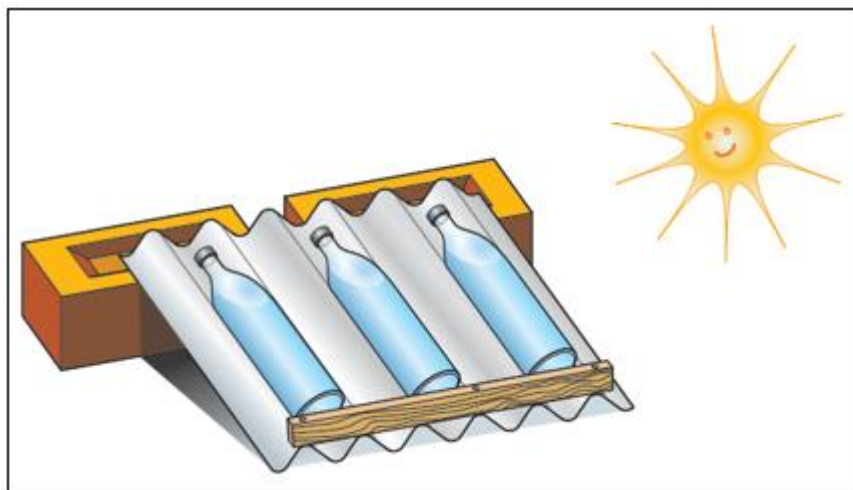


**Figure 2.5:** Schematic representation of SODIS (WHO, 2011).

## 2.6 Convectional Water Treatment

Conventional water-treatment plants are still in predominant usage in many areas of South Africa. These present challenges in that they are inefficient in removing micro-pollutants, have a large plant foot-print, and have high chemical consumption which also translates into high operational and maintenance costs (Challener, 2011). Convectional water treatment plants have five main treatment steps which are coagulation, flocculation, sedimentation, filtration, and disinfection. Coagulant aids like alum, ferric chloride, and synthetic polymers are added to the water to initiate the agglomeration of colloidal particles (Meridian Institute, 2006) left in the raw water after screening and pre-sedimentation steps. The water is then stirred to enhance the collision and adhesion of the colloids to form bigger particles (flocs) in the flocculation step. The flocs are left to stand in a sedimentation step within a clarification tank where they settle to the bottom of the tank by gravity. After clarification, the water is filtered to remove suspended solids then a disinfectant is added to kill all pathogens in the water (Argaw, 2003). These convectional water treatment steps are shown in **Figure 2.6**.

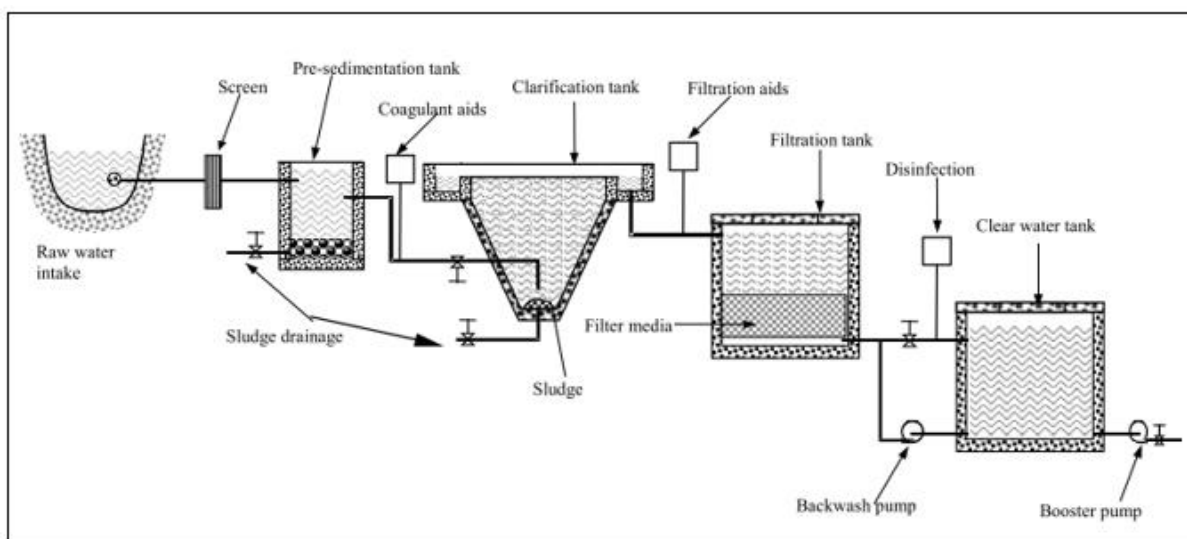


**Figure 2.6:** Schematic representation of a conventional water treatment plant (Argaw, 2003).

In the rural areas of South Africa, there have been efforts to use both centralized and decentralized water treatment and supply. The centralized system has been hampered due to the financial burden of providing piping networks to transport the water to the small communities which has resulted in the local municipalities resorting to use water trucks to ferry the water from the treatment plants (Swartz, 2009). Most households in urban areas in South Africa, i.e., around 89,8%, have access to piped water while in rural households it is only 6,8% (Lehohla, 2017).

### 2.7.3 Membrane filtration processes

A membrane is defined as a selective barrier that separates a feed into permeate and retentate streams (Ortega-Rivas, 2012) powered by transmembrane driving forces. Membrane processes are progressively being used in hybrid water treatment systems, to enhance the removal of pathogens, heavy metals, NOM, and other pollutants from water (Bhattacharya, 2017) due to their relatively constant permeate water quality. Membrane processes also offer lower cost when compared with conventional water treatment methods (Maddah *et al.*, 2017). However, membrane technology also has several disadvantages in that it relies heavily on hydraulic pressure, produces large concentrate volumes, and have operation that is adversely

affected by fouling (Motsa, 2015). The performance of membranes is also affected by several other factors which include, the quality of the feed, the operating conditions (temperature, pressure, pH, etc.,) and membrane orientation (dead-end or crossflow), etc.

Water-treatment through membrane processes uses different types of membranes which are differentiated according to the membrane's pore size. Membranes are categorized as microfiltration (MF), ultrafiltration (UF), nanofiltration (NF), and reverse osmosis (RO) membranes (Thoola, 2014) based on reducing pore sizes, respectively.

Microfiltration and ultrafiltration are classified as low-pressure membrane filtration processes (Guerra & Pellegrino, 2012) and can both be used for the pre-treatment and treatment of raw water, wastewater or other fluids in industrial processes. Microfiltration membranes have the largest pore size range (0.7–7  $\mu\text{m}$ ) when compared to other membrane processes and are only able to reject particles of sizes greater than 7  $\mu\text{m}$  which are mostly colloids and suspended particles (Plappally & Lienhard, 2013). The quality of the water produced is not suitable for drinking water purposes as MF cannot reject most pathogens and dissolved organic and inorganic content.

On the other hand, ultrafiltration membranes are able reject substances with small sizes than MF membranes can, and these include, suspended particles, some dissolved organic and inorganic macromolecules, as well as some pathogens (Mohamad *et al.*, 2013), e.g., viruses. Generally, the water produced from UF membrane filtration is of drinkable quality depending on the quality of the feed/raw water and it uses less energy while having higher permeabilities than both NF and RO (Pal *et al.*, 2018). This makes UF a viable alternative to several water treatment methods for the provision of clean drinking water.

Nanofiltration membranes, unlike microfiltration and ultrafiltration membranes, do not just rely on size exclusion to reject substances but also use electrostatic and dehydration effects (Wang *et al.*, 2021). These membranes are able to reject

suspended solids, dissolved organic compounds, microbiological content (Dach, 2009), as well as some dissolved inorganic content, i.e., multivalent ions and salts (Moitsheki, 2003). NF membranes produce potable drinking water of good quality but require pressure higher than that used in UF, and MF membranes hence have a high energy requirement.

On the other hand, RO membranes are non-porous membranes that separate solutes from the solvent using differences in their solubilities on the membrane (Shirazi *et al.*, 2010). These membranes are mainly used in desalination, drinking water and wastewater treatment but have the highest-pressure requirement of all the membrane techniques. RO membranes reject all the substances rejected by NF membranes as well as monovalent ions (*ibid*). As this filtration method strips the water of all ions, the water produced should be first treated before consumption, which further increases cost.

## 2.7 Ultrafiltration (UF) in water treatment

Ultrafiltration presents many advantages over conventional processes which include, no or little chemicals usage for membrane cleaning, reliable filtrate water quality with high pathogen removal, reduced energy requirement, and require a small plant size (Ezugbe & Rathilal, 2020). As such, when compared to conventional and advanced water treatment techniques, ultrafiltration has a lower cost (Li *et al.*, 2018).

Ultrafiltration membranes have pore sizes in the range of 1 to 100nm (Maddah *et al.*, 2017) and are generally able to filter out both organic and inorganic polymeric substances with high molecular weights ( $10^3$  to  $10^6$  Da) but leave behind low molecular-weight organics, including micropollutants (Liao *et al.*, 2020) as well as metallic ions. These membranes operate on low pressure (1 - 10 bars) (Maddah *et al.*, 2017) with negligible osmotic pressure differential thereby offer high performance but only filter out high-molecular weight substances

Ultrafiltration is a growing technology used in water treatment. This is evidenced by its local adoption; an example being the water treatment plant for Eskom's Tutuka power plant in Mpumalanga which uses ultrafiltration as a pre-treatment step before reverse osmosis of the raw water at the power plant (Ras & von Blottnitz, 2012). As a low-pressure membrane, the system can be run under low pressures which is a significant advantage as low energy is consumed hence low operational cost (Chao *et al.*, 2018).

Ultrafiltration membranes can be prepared from ceramics, metals, and polymers. PES is one of the common polymers used in making ultrafiltration membranes due to its good thermomechanical and separation properties as well as chemical resistance (Mahdi *et al.*, 2019). However, PES is hydrophobic in nature thus tends to foul more easily during use. The structure of the polymer is shown in **Figure 2.7**. The amorphous polymer has a high degree of toughness due to the connecting oxygen units and its phenyl units make it rigid (Knauer, 2016).

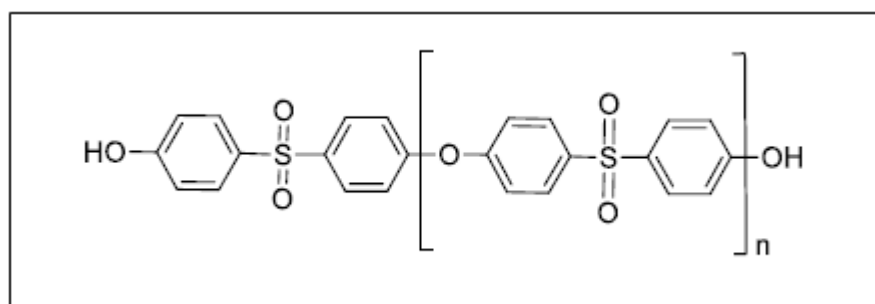


**Figure 2.7:** Diagram showing the general structure of a PES polymer (Knauer, 2016).

Bernat *et al.* (2007) investigated the rejection of some heavy metals (iron, copper, and chromium) using a 5kDa MWCO ceramic, ultrafiltration membrane. The researcher found that the presence of soluble charged hydroxide species of the heavy metals improved rejection rates of these metals as these hydroxides formed stable active layers on the surface of the membrane. The rejection of iron species was found to be related to the iron (III)/iron (II) ratio as iron (III) while copper ions were not rejected. On the other hand, the rejection of chromium species increased

proportionally with an increase in pH, given that chromium hydroxide species increase at high pH.

## **2.8 Application of membrane filtration/technology in SA**

Previous research in ultrafiltration has extensively covered its use in water treatment for small communities in rural areas. Pillay & Jacobs (2004) produced a report on studies which involved the use of capillary ultrafiltration membranes. The membranes were developed at the University of Stellenbosch in the early 90s and have been tested in field trials predominantly carried out in KwaZulu Natal province. Of significance is the A3 Wiggins plant constructed in 1997 by the Umgeni water-process evaluation facility at their waterworks in Durban, which served as a training unit and field-trial modification facility. Later studies include, the A5 Crammond facility installed in the Natal midlands with an installed capacity of 4.8 kl/day. These studies have re-enforced the idea that the locally made capillary ultrafiltration units could endure years in use with cleaning procedures able to retain the flux over extended periods of time. As such, these studies have also proven that ultrafiltration is a robust water treatment technique. However, implementation of ultrafiltration on a large scale in South Africa has not yet been done despite this promising research (ibid).

Ultrafiltration membranes were also used on a pilot scale in treating Membrane Bio-Reactor (MBR) effluent of a wastewater treatment plant in Cape Town where these membranes showed rejection rates of over 40% for nitrates, phosphates, ammonium salts and chemical oxygen demand (COD) (Aziz, 2021). The water produced by the UF membranes met standards for reuse in cooling water applications but not for irrigation. This is beneficial as water reuse is one method to reduce water scarcity.

In Tshaanda rural village, ultrafiltration membranes were used to treat groundwater to provide drinking water for the rural community in that area (Molelekwa *et al.*, 2014). The groundwater did not need any pre-treatment for suspended solids as its turbidity was constantly under 5 NTU with an average electrical conductivity value

of 300  $\mu\text{S}/\text{cm}$  at 25°C, which were within drinking water standards. Pathogens like *Escherichia Coli* and *enterococci* were detected in the water during the rainy season and UF treatment was able to remove this microbiological content to values within acceptable drinking water limits. The overall quality of the water after UF treatment also fell within drinking water standards.

Nanocomposite ultrafiltration membranes have also been synthesized and applied in water treatment. (Mathumba et al., 2020) prepared photo-catalytically active PES membranes and used these membranes to filter and degrade methyl orange dye. The membranes had improved dye rejection than the pristine membranes without nanoparticles and the titanium dioxide nanoparticles used were able to degrade the methyl orange dye under Uv radiation.

Outside of South Africa, there are numerous ultrafiltration studies that have been carried out. These studies have proven that ultrafiltration is effective in reduction of Total Organic Carbon (Kenway, 2001), removal of some heavy metals (Bernat et al., 2007), (e.g. manganese, aluminium and iron) and pathogens (Pirnie, 2001) e.g. bacteria.

Xia et al. (2004) who studied the use of ultrafiltration membranes in treatment of raw water in China, discovered that permeate flux in coagulation-ultrafiltration processes was higher than in coagulation-sand-filtration-ultrafiltration hybrid processes for medium turbidity raw water. Arhin et al. (2019), also investigated hybrid ultrafiltration systems and found that a hybrid Polyaluminium Chloride (PACl) coagulation-UF system showed a 21% increase in flux rate compared with convectional UF systems and had reduced fouling. This presents cost reduction opportunities water treatment systems given that coagulation has been proven to increase flux and extend membrane life.

With such improvements in ultrafiltration, there is a growing global adoption of ultrafiltration systems in water treatment plants on a large scale, e.g., UF water treatment plants have recently been built in countries like Malaysia (Ming et al.,

2015) and USA (Pressdee & Hill, 2006). This shows that ultrafiltration has great potential in the future of water purification.

## 2.9 Application of Nanofiltration membranes/ technology in South Africa

Most commercial nanofiltration membranes are manufactured from polyamide (PA) or cellulose acetate polymers (Maddah *et al.*, 2017) as the top selective layers that are polymerized onto a polysulfone support. NF270 membranes have a polyamide (structure shown in **Figure 2.8**) selective top-layer on a polyether sulfone support layer. These membranes are negatively charged thereby causing the size separation of substances to be aided by electrostatic interactions between the membrane and the contaminants. This is seen in the enhanced rejection of multivalent cations which are adsorbed onto the membrane surface thereby increasing the membrane's surface charge (Agboola *et al.*, 2014). As such nanofiltration membranes have a pronounced Donnan exclusion than either ultrafiltration or microfiltration membranes. Most nanofiltration membranes also have molecular weight cut-off in the range 300 – 500 Da (Timmer, 2001) and pore diameters of less than 1 nm (Maddah *et al.*, 2017). Nanofiltration membranes are also operated in a transmembrane pressure range of 5 – 20 bars (Moitsheki, 2003) hence have a higher energy requirement than ultrafiltration membranes which is a disadvantage in its usage.

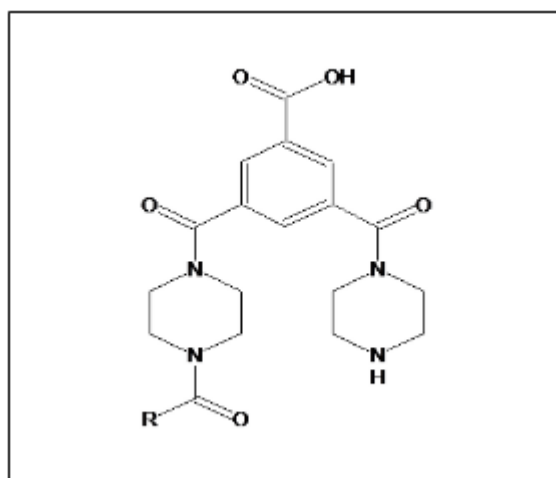


**Figure 2.8:** Structure of the semi-polyamide polymer in NF270 membranes (Mouhoumed *et al.*, 2014).



Nanofiltration membranes have been used extensively in wastewater treatment studies in South Africa due to their ability to produce high quality permeate. Aziz (2021) investigated the ability of NF membranes to treat wastewater for reuse in irrigation and cooling water applications. The wastewater was taken from a wastewater treatment plant in Cape Town and the NF membrane showed excellent rejection of selected inorganics, i.e., over 90% for phosphates, nitrates, ammonium salts, and chemical oxygen demand (COD). The permeate was suitable for both irrigation and cooling water use thereby providing an alternative to reduce water scarcity through water reuse. However, the NF membranes were shown to have a higher specific energy consumption requirement of 1,42 when compared to UF membranes in the same application. Nanofiltration membranes were also proven to be effective in the treatment of effluent that contains dyes from textile processes in South Africa and the permeate was found to be of suitable quality that allowed for reuse (Chollom, 2015).

Nanocomposite NF membranes have also been fabricated to improve the membranes' performance. Lakhotia *et al.* (2018) prepared thin film nanocomposite NF membranes with cerium oxide nanoparticles and used these membranes in the desalination of seawater. The researchers found that the nanocomposite NF membranes had improved salt rejections greater than 90%, had a high resistance to attack by *Escherichia coli*, and had reduced fouling as compared to the polyamide membranes without the nanoparticles.

## 2.10 Membrane fouling

The high costs of operation (pressure generation) and plant installation costs (automation) are slowly being replaced as technology progresses and renewable energy is being incorporated in the water treatment plants. However, the inherent problem of using membrane technology that remains problematic in all membrane separation processes is fouling (Mancinelli & Hallé, 2015).

Fouling can result from either concentration polarization or the accumulation of material on the surface of the membrane. These processes both have the effect of reducing the flow of solvent across the membrane as well as altering the selectivity of the membrane (W. Chen *et al.*, 2018).

Concentration polarization occurs because of the sieving effect of membranes where some solutes accumulate on the membrane's surface in the mass transfer boundary layer. This solute accumulation causes the solvent activity to reduce and promotes back diffusion of solutes into the bulk layer (W. Guo *et al.*, 2012) thereby decreasing the transmembrane pressure and flux. The process of concentration polarization is depicted in **Figure 2.13** showing the changes in solute concentration at the surface of a membrane.

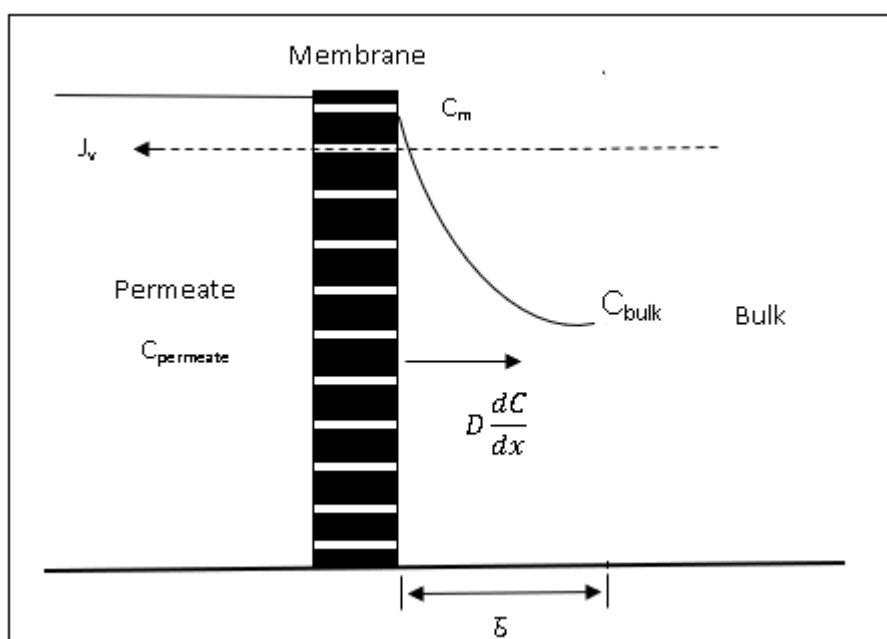


**Figure 2.9:** Schematic representation of concentration polarization at the surface of a membrane (Kimura, 1991).

Fouling occurs by different mechanisms of deposition of foulants on the surface of the membrane as well as inside its pores. This can occur through pore constriction in which the pore diameter is reduced, pore blockage where the pore entry point is completely covered by foulants, cake formation where the foulants cover the membrane's surface, intermediate blockage where some pores are partially

blocked, together with concentration polarization on the membrane's surface, (Guo *et al.*, 2012) as shown in **Figure 2.10**. In ultrafiltration membranes, pore blocking has been observed to be the main contributor to fouling (Wang & Tarabara, 2008).

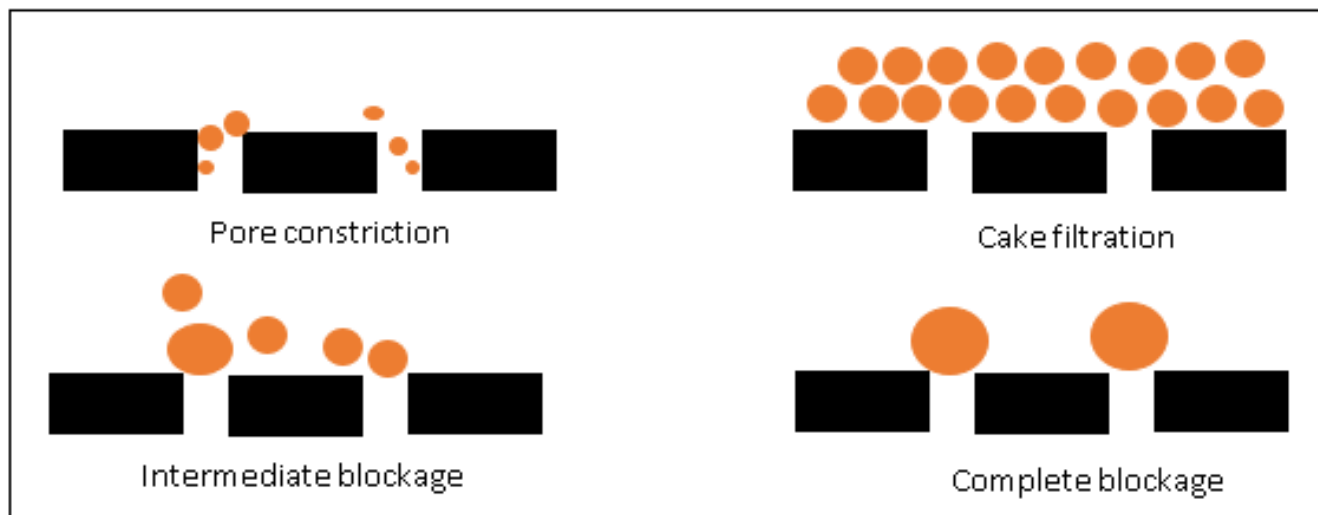


**Figure 2.10:** Illustration of the four modes of fouling described by the Hermia model (Wang & Tarabara, 2008).

Low pressure membrane fouling can be modelled by applying the mechanical sieving principle which explains that macromolecules with high molecular weight (MW) will clog the membrane's pores on surface, while micro molecules with low MW will enter pores. The polarity and MW of the NOM is of major importance as the membrane's surface charge facilitates the attachment of foulant to the membrane's surface via mainly electrostatic interactions (Mohamad *et al.*, 2013). NOM in aqueous solutions also tends to form colloids by binding together and these colloids move to the surface of the membrane through hydrodynamic forces and attach to the surface due to physicochemical interactions, e.g. Lifshitz – van der Waals forces, electrostatic forces and acid-base interactions (Gao *et al.*, 2019).

Li *et al.* quoted by Gao *et al.* (2019) empirically showed that MW of fractions of NOM <3kDa MW caused the greatest decline in flux and explained that this was due to molecular interaction, other than physical sieving. Other studies also showed that MW fractions >30kDa caused significant decline in flux. Jacquim *et al.* quoted by Gao *et al.* (2019), showed that high MW hydrophilic organics cause reversible fouling while low MW hydrophobic organics cause irreversible fouling.

Lee *et al.* (2004) reported that there is a high membrane fouling tendency when there are divalent ions or substances with high charge ratios and molecular weights in the feed solution. Inorganic fouling or scaling results in scale formation on the surface of a membrane when the solubilities of the inorganic salts in the water are exceeded. This is greatest in NF and RO membranes (Shirazi *et al.*, 2010).

Biological material may also adhere to the membrane's surface and survive by feeding on nutrients from the foulants attached on the surface of the membrane. As the microorganisms grow they block the pores of the membrane thereby causing biofouling (Ezugbe & Rathilal, 2020). Biofouling can be reduced by increasing membrane hydrophilicity (Barghi, 2014).

Methods implemented to reduce fouling include chemical treatment, back-wash, pre-treatment, and pre-filtration of the feed. Air/Water backwash also known as sparging, has been shown to be more effective than normal backwash in ultrafiltration due to the help of the air in dislodging the cake (Cordier *et al.*, 2020). Membranes can also be modified to resist fouling and these membranes have higher fluxes and longer operational lives.

### **2.10.1 Energy Sources for membrane filtration**

A lot of energy sources have been used for membrane filtration. These energy sources can be broadly categorised either as fossil fuels or renewable energy sources. Fossil fuels (coal, oil, natural gas, nuclear energy) have been dominant in the provision of energy not only for water treatment but for almost all industrial, agricultural, and mining processes. In South Africa, coal accounts for over 70% (Jain & Jain, 2018) of the total electrical energy production in the country but there has been a rise in the use of renewable sources with the rise in the uptake of green technology. The fossil fuels are burnt to generate energy and this combustion generates greenhouse gases (Khan & Arsalan, 2016) which not only pollute the environment but also lead to global warming and climate change (Stout, 1990). Fossil fuels are also of finite supply hence not sustainable in the long run.

The production of energy from convectional sources like coal and natural gas, uses large amounts of water in cooling water and other applications hence there is an energy-water nexus as energy produced from these sources is also used in water treatment (Macknick *et al.*, 2012). Energy from the fossil fuels and renewable sources is used for various uses in water and wastewater treatment technologies as shown in **Figure 2.11**.

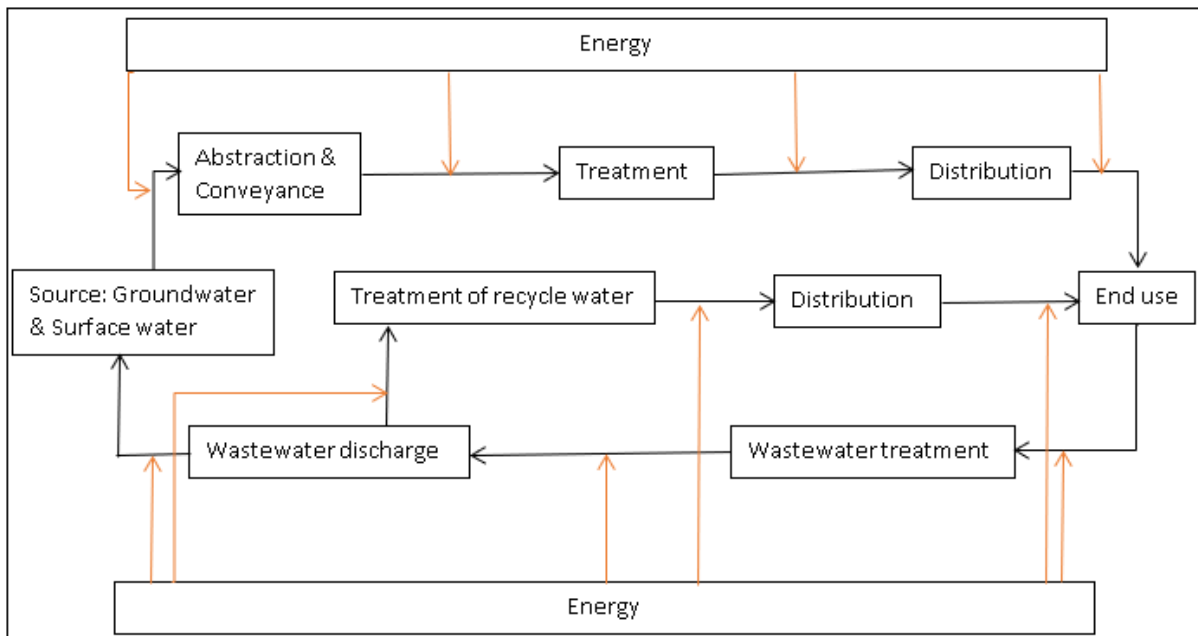


**Figure 2.11:** Diagram showing the different uses of energy in water treatment (Wakeel *et al.*, 2016).

The drawbacks of using fossil fuels have heightened interest in renewable energy sources to improve sustainability and lower operational costs in water treatment. Renewable energy sources that have been used for membrane filtration processes in water treatment include, geothermal, wind, solar, and tidal/wave energy (Ali *et al.*, 2018). The different applications of these energy sources in different water treatment applications are shown in **Figure 2.12**.

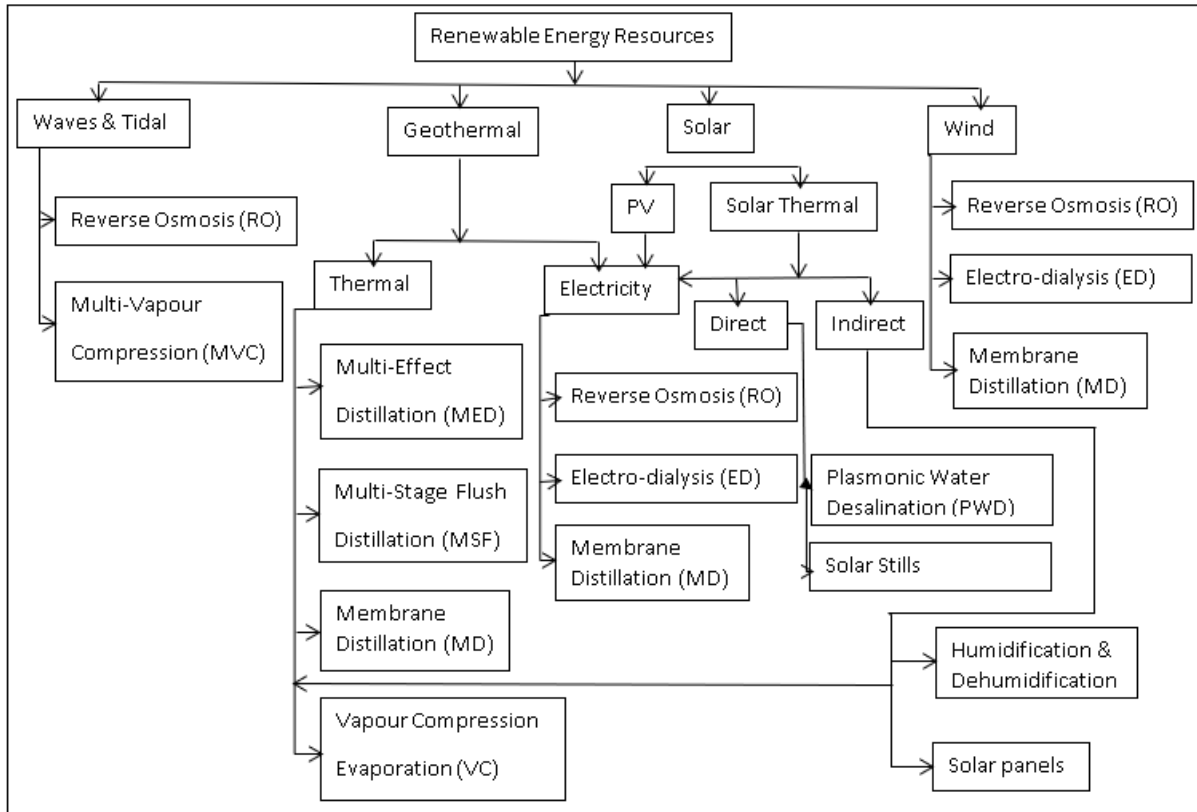


**Figure 2.12:** Diagram showing the different renewable energy sources used in water treatment (Kashyout *et al.*, 2021).

Globally, solar energy has the potential to produce the largest amount of energy when compared to other energy sources (Ali *et al.*, 2018) as solar energy is the most abundant energy resource on the planet (Khan & Arsalan, 2016). It is also abundant in many areas across the globe and can be easily converted to useful energy, thus making it accessible even in remote or underdeveloped areas where it can be harnessed at the point of use. This removes the need for infrastructure like the electrical grid and makes it possible to construct stand-alone water treatment plants (Zhang *et al.*, 2018) at low cost for small communities, e.g., people in rural areas.

Solar energy can be utilized in water treatment either as thermal or electrical energy. The sun's radiation can be converted to produce electrical energy by photovoltaic (PV) solar cells (Lienhard *et al.*, 2012). This energy can then be used to power pumps and other systems in water treatment. In solar thermal systems, the direct radiation from the sun is captured and used to distil water (Ahmed & Ibrahim, 2016) in solar stills (desalination), heat the feed fluid in membrane systems, e.g.,

membrane distillation (Zhang *et al.*, 2018), and generate electrical energy used to drive water treatment systems, through the production of vapour pressure in heat engines (Kurhe *et al.*, 2017).

### **2.11 Application of Solar energy in water treatment**

Water purification is a process that uses a lot of energy, and the use of renewable energy in this area is growing due to its high energy demand. The presence of high solar flux around the year in South Africa presents an opportunity to harness the power of the sun. Students at the University of Venda, in the Limpopo province engaged nearby communities and applied solar disinfection to treat water for drinking water purposes in that area (Harshfield, 2015). Solar disinfection was chosen as it is a simple and cheap way of disinfecting water through exposing the water to direct sunlight for several hours. It is an effective method that kills most pathogens in the water but takes time, is suitable for production of small amounts of water at a time, is less efficient on turbid water (Borde *et al.*, 2016), and does not remove other pollutants like heavy metals.

Solar energy has been used in many studies and water treatment projects and has shown great promise. Use of solar energy can be traced to the emergence of solar stills used for solar distillation of saline water and the first one was constructed in Chile in 1872, then the subsequent development of solar collectors which were used in water treatment in the USA (Ugwisishwu *et al.*, 2016).

Solar energy usage in water treatment has improved over the years with new technologies being studied and implemented. Aluminium based mirrors have been shown to have a high reflectance of around 93% and this has made the mirrors good candidates for use in solar concentration for photocatalysis. In photocatalysis, biorecalcitrant organic compounds (BROCs) are converted into highly reactive transient compounds e.g., superoxide radicals which are biodegradable using solar energy (UV light in particular) (Fendrich *et al.*, 2019).

Solar pasteurizers which work by heating water to a high enough temperature to deactivate pathogens have also been developed (Hall & Hall, 2016). This is a form of solar disinfection. Recent advances have also seen the development of solar thermal desalination using membranes coated with light absorbing nanoparticles. Saline feed is evaporated across the membrane and the distillate is condensed on the permeate side. Solar energy is used to heat the membrane to drive the permeation process (Dongare *et al.*, 2019).

#### **2.11.1 Solar-thermal energy conversion**

Solar irradiation can be converted to electrical energy or thermal energy. Many studies have been carried-out in which solar energy was used in water treatment, and this has resulted in many novel water treatment technologies, e.g., sea water desalination. To enhance solar energy, there is a need to use solar concentrators, e.g., parabolic solar concentrators which use a parabolic-shaped surface, coated with a reflective material to direct sunlight onto a receiver (Rao *et al.*, 2020) as shown in **Figure 2.13**.



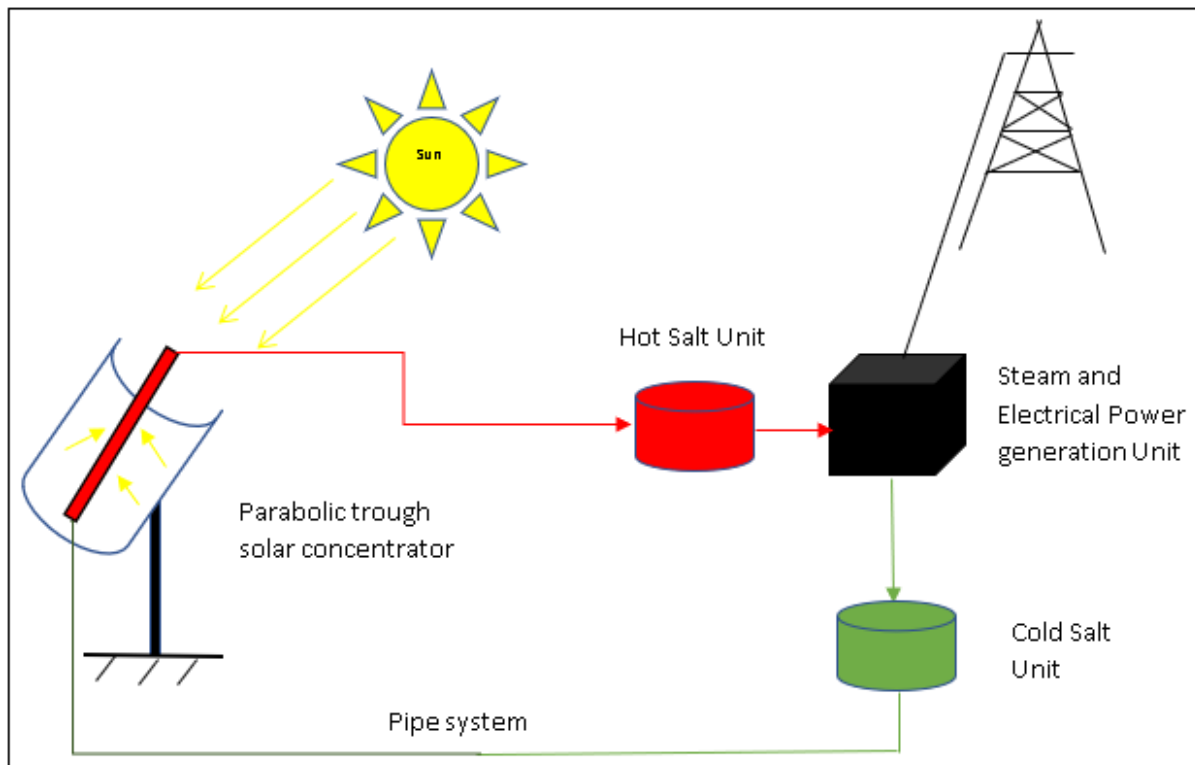


**Figure 2.13:** Schematic representation of a solar power plant with an energy storage system.

Concentrating the radiation flux at a receiver has the advantage of reaching high temperatures in the working fluid, up to  $1300^{\circ}\text{C}$  (Codd *et al.*, 2020) hence achieving a higher thermodynamic efficiency. Sunlight is concentrated by the parabolic solar concentrator onto the receiver which then converts the radiation to heat energy which is then transferred to the heat transfer fluid.

The efficiency of solar energy transfer and conversion dynamics is dependent on many factors. These dynamics directly lead to changes in temperature of the working liquid in the receiver. The efficiency of CSP plants is mostly affected by the heat engine component which controls the temperatures of the solar storage, receiver, and concentrator (Stein & Buck, 2017). On the other hand, the parabolic dish reaches the highest operating temperature of  $1500^{\circ}\text{C}$  at a concentration ratio of 3000. However, the average annual efficiency of the parabolic dish is 30 % which is lower than the central receiver which attains the highest efficiency at 35 % (Chen *et al.*, 2020).

Solar concentrator efficiency is affected by parameters like the presence of solar tracking, reflectance, and the size of the reflective area. The thermal conductivity of the receiver's surface and working liquid, affects the absorbance of the thermal energy and subsequent conversion into useful energy.

After concentration of the solar radiation, it is used to heat a working fluid. The working fluid is heated to its boiling point and the vapour created is then used to develop pressure that is used to perform mechanical work (Narayan & Gupta, 2015) in the form of either driving turbines or generating fluid pressure. The turbines will drive generators which produce electricity that is then transmitted to operate electrical equipment which can be used in water treatment while the fluid pressure produced may be used to drive membrane filtration processes. In desalination and membrane distillation process, the concentrated heat can be used to directly heat the feed.

In vapour power cycle engines, water or volatile organic liquids can be used as the working liquid. The choice of the working liquid is critical and will depend on the energy source, i.e., low grade heat, solar energy, geothermal energy, fossil fuels, as well as the working liquid's boiling point (Wang *et al.*, 2017). The efficiency and performance of these heat engines can thus be improved in several ways that include, improving heat transfer, working fluid properties, and piping design (Nouman, 2012), etc. Heat transfer within liquids can be improved by the incorporation of nanoparticles with higher thermal conductivities than the base fluid (Awais *et al.*, 2021). The nanofluid produced will have a higher thermal conductivity hence a lower enthalpy of vaporization thereby increasing the efficiency of the heat engine.

### **2.11.2 Solar energy storage**

Solar energy storage has improved the usefulness of the solar technology as this now means that solar energy can be used throughout the night when the sun is not there. Thermal energy storage also allows compensating for insolation variations, due to changes in ambient conditions e.g., the passage of clouds blocking the Sun's

rays. Chaichan & Kazem (2015) demonstrated solar energy storage by using paraffin wax which changed phase into a liquid when heated then solidified on cooling as it gave out stored the heat energy. This is principally how phase change materials (PCM) work in storing energy. Most solar thermal applications use salts as their energy storage substances due to their high heat capacities (Hentschke, 2016).

## 2.12 Heat transfer in systems

Heat is defined as a form of energy that is transferred using a temperature difference between reservoirs (Shepherd, 2013). It is transferred through three main mechanisms which are conduction, convection, and radiation (Dewitt *et al.*, 2007). These mechanisms will be explained in greater detail in the **Sections 2.12.1 to 2.12.3.**

### 2.12.1 Conduction

Conduction is defined as the heat transfer that occurs when there exists a temperature gradient between two points within a given medium, e.g., a solid or a stationary liquid. Atoms are constantly moving and colliding (e.g., diffusion of gas molecules) with those around them hence transporting thermal energy, (Raju, 2011) and the rate of collisions is proportional to the temperature of the particles. More energetic atoms are thus at higher temperatures and as they collide with less energetic ones, they transfer some of their energy to them which results in heat transfer. This heat transfer can be calculated using the Fourier's law shown in **Equation 2.1** (Dewitt *et al.*, 2007).

$$q'_x = -K \frac{dT}{dx} \quad \text{Equation 2.1}$$

Where  $q'_x$  is heat flux ( $\text{W}/\text{m}^2$ ),  $K$  is the thermal conductivity of the medium ( $\text{W}/\text{m.K}$ ),  $dT$  is the temperature gradient and  $dx$  is distance between the points of energy

transfer (m). The minus sign indicates that heat is transferred from a point of higher temperature to that of lower temperature.

### 2.12.2 Convection

Convection is defined as the heat transfer resulting from both random molecular motion (diffusion) and macroscopic fluid motion (advection). When a temperature gradient exists within the fluid, different regions of the fluid will move due to having different densities (a phenomena known as buoyancy) (Raju, 2011) and the bulk transport of the fluid molecules as well as their random interactions will result in heat transfer to other regions of the fluid, or from and to other surfaces or media. The energy transferred is referred to as sensible heat or internal thermal energy and the bulk transport of the fluid can be forced (e.g., using fan) or natural (buoyancy). However, when there is a phase change (e.g., boiling and condensation) as a result of the heat transfer, there will also be latent heat exchange (Dewitt *et al.*, 2007). The heat transfer by convection can be calculated by using the Newton's law of cooling which is shown in the **Equation 2.2**.

$$q'' = h(T_s - T_\infty) \quad \text{Equation 2.2}$$

Where:  $q''$  is the convective heat flux ( $\text{W}/\text{m}^2$ ),  $h$  is convective heat transfer coefficient ( $\text{W}/\text{m}^2\cdot\text{K}$ ),  $T_s$  is the temperature (K) of the surface and  $T_\infty$  is the temperature (K) of the fluid. Note that the heat flux is positive when  $T_s > T_\infty$  and heat is transferred from the surface to the fluid.

### 2.12.3 Radiation

Radiation is defined as the transfer of energy through emission of electromagnetic waves due to electronic transitions within atoms and molecules of matter that is above absolute zero temperature. Unlike conduction and convection, radiation does not require a medium to occur (Dewitt *et al.*, 2007). Radiation of a black body (ideal

radiator) can be calculated using the Stefan-Boltzmann's law shown in **Equation 2.3**.

$$E_b = \sigma T_s^4 \quad \text{Equation 2.3}$$

Where  $E_b$  is the emissive power ( $\text{W/m}^2$ ) of a black body,  $\sigma$  is the Stefan-Boltzmann constant ( $5,67 \times 10^{-8} \text{ W/m}^2 \cdot \text{K}^4$ ) and  $T_s$  is the surface temperature.

However, real surfaces do not radiate as well as black bodies hence their emissivity ( $\epsilon$ ) falls within the range:  $0 < \epsilon < 1$  and the heat flux for a real surface is thus calculated as shown in **Equation 2.4**.

$$E = \epsilon \sigma T_s^4 \quad \text{Equation 2.4}$$

The radiated energy is absorbed by the surroundings when there is a temperature gradient and the net heat flux ( $q'''$ ) transferred per unit area ( $A$ ) can be calculated using **Equation 2.5**.

$$q''' = h_r A (T_s - T_{\text{surr}}) \quad \text{Equation 2.5}$$

Where:  $h_r$  is the radiative heat transfer coefficient,  $T_s$  and  $T_{\text{surr}}$  are the temperatures of the radiating surface and surroundings, respectively.

For a horizontal body exposed to the Sun, the radiative heat transfer (Tiwari *et al.*, 2016) can be calculated using **Equation 2.6**.

$$Q = A \epsilon \sigma (T_1^4 - T_{\text{sky}}^4) \quad \text{Equation 2.6}$$

Where,  $T_1$  is the temperature of the horizontal body,  $T_{\text{sky}}$  is the temperature of the Sun,  $\epsilon$  is the emittance of the horizontal body,  $\sigma$  is the Stefan Boltzmann's constant, and  $A$  is the area of the horizontal body.

The sky temperature can be estimated from the ambient air temperature, using **Equation 2.7**.

$$T_{\text{sky}} = 0,0552T_a^{1,5} \quad \text{Equation 2.7}$$

Where:  $T_a$  is the ambient air temperature in Kelvins.

### 2.13 Thermal conductivity

This is a property of the material that is thermally conductive and varies with temperature. Heat flows through solid materials either through thermally activated electrons (predominant for conductors) and lattice waves generated by atomic activity. Thermal conductivity of conductors generally decreases as the temperature increases, as the higher flow of electrons is restricted by resistance while in insulators, the thermal conductivity generally increases with an increase in temperature as the atomic activity generates more lattice waves (Kothandaraman, 2006).

### 2.14 Thermodynamics of heat driven systems.

Thermodynamic processes are defined as changes to systems between two states that are in equilibrium (Massoud, 2005). A reversible process is defined as one in which the process can infinitesimally go either forward or backwards without leaving any net changes to either the system or the surroundings (Shepherd, 2013). The converse is true for an irreversible process. Most processes are irreversible due to several factors including friction, hysteresis effects, etc.

Practically, heat transfer is an irreversible process as to be reversible, the heat transfer should occur across reservoirs with infinitesimal temperature differences, infinite areas and over an infinite amount of time. Heat transfer can occur under a range of conditions which include, isothermal, adiabatic, and isobaric conditions.

Isothermal processes occur at constant temperature, while isobaric processes occur at constant pressure (Shepherd, 2013).

### 2.14.1 Laws of thermodynamics

When there is heat transfer within the system, it is important to understand how thermal equilibrium is achieved in the system using thermodynamics. The first law of thermodynamics states that the total energy of a system is conserved and is mathematically depicted as shown in **Equation 2.8** (Dewitt *et al.*, 2007).

$$\Delta E_{st}^{tot} = Q - W \quad \text{Equation 2.8}$$

Where  $\Delta E_{st}^{tot}$  is the change in the total energy of the system,  $Q$  is the net heat transferred and  $W$  is the net work done by the system.

The Second law of thermodynamics states that the total entropy of the system will either remain constant for reversible processes or increase for irreversible processes (Goff *et al.*, 1988). These laws can be used to explain the heat transfer processes that occur in heat engines.

### 2.15 Heat engines

Heat engines are defined as systems in which heat is converted to work usually with the aid of a cyclic working fluid that absorbs heat ( $Q_H$ ) from a reservoir at a higher temperature ( $T_H$ ), performs some mechanical work ( $W$ ) and then releases some heat ( $Q_C$ ) to a reservoir at a lower temperature ( $T_C$ ) (Goff *et al.*, 1988).

Heat engines utilize different working fluids and thermodynamic cycles. Organic Rankine Cycle (ORC) heat engines are a type of vapour power cycle engine, and these utilize volatile liquids (mainly hydrocarbons) as their working fluids. Another class of heat engines are diaphragm pumps which also utilize volatile working fluids

to generate pressure that causes a positive displacement which performs useful work. Due to the low boiling point of the working liquids used, these engines can be powered by solar energy.

All heat engines operate through cyclic processes and there is conservation of energy which means that heat input into the system will result in heat released and work done according to the first law of thermodynamics as shown in **Equation 2.8**. Also, no heat engine can operate at 100% due to the second law of thermodynamics and the efficiency of all heat engines can thus be calculated using **Equation 2.9**.

$$e = 1 + \frac{Q_C}{Q_H} \quad \dots \quad \text{Equation 2.9}$$

### 2.15.1 Diaphragm pump operation.

A diaphragm pump operates by absorbing heat from its surroundings and vaporizing a volatile liquid that generates pressure which moves a diaphragm thereby performing work. As shown in **Figure 2.14** addition of heat to the liquid causes it to become a saturated liquid (2) when its boiling point is reached. A saturated liquid will only remain fully in liquid form without any addition of heat, so when just a small amount of heat is added, the volatile liquid starts to vaporize isothermally as shown at stage 3 and 4. The vapour produced then causes the diaphragm/piston to rise due to an increase in the pressure of the gas. When the outside pressure is constant the expansion is said to be isobaric. In pressure driven systems e.g., membrane filtration, isobaric expansion of the volatile liquid providing the pressure, occurs when the system pressure  $\leq$  bubble pressure of the membrane. At higher temperatures above the boiling point of the volatile liquid, all the liquid will be converted into gas and the gas continues to expand with addition of more heat until the piston is fully extended. Lowering the temperature will result in the process being reversed from stage 5 to 1.



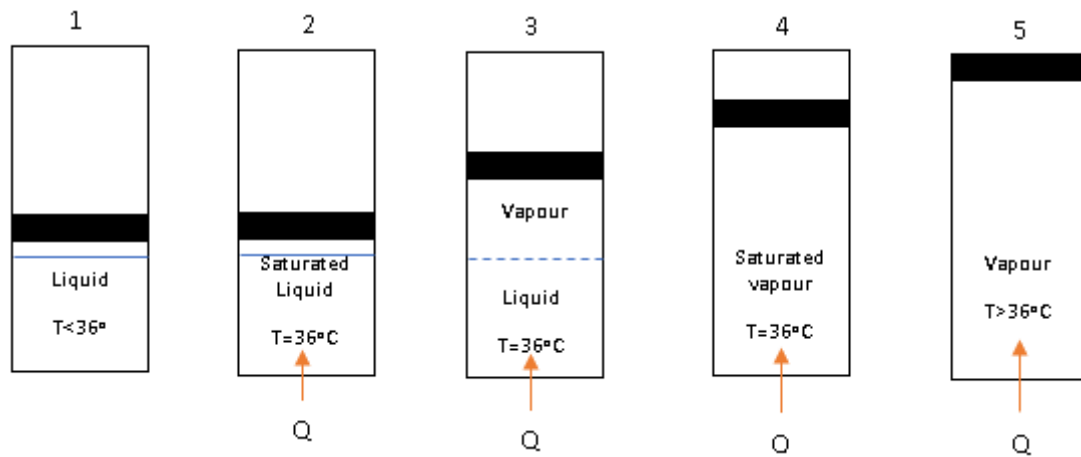


**Figure 2.14:** Schematic representation of the stages of a vapour power cycle in a diaphragm pump.

A temperature against entropy ( $T$ - $s$ ) plane sketch shown in **Figure 2.15** shows the different stages of work and energy transfers in a complete vapour power cycle. In stages 2 to 3, heat is added to the system and the volatile liquid turns from liquid to gas. This gas then performs useful work in stages 3 to 4. The gas then loses its heat energy in stages 4 to 1 then some work is added to the system in stages 1 to 2.

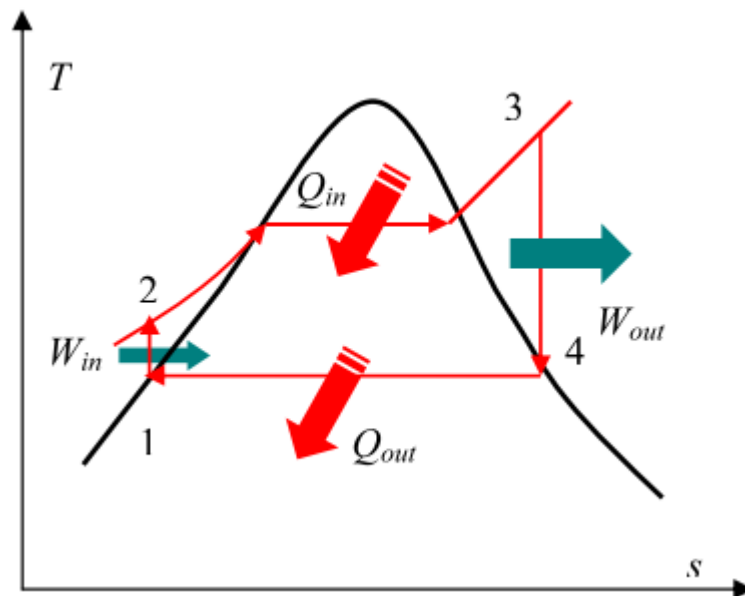


**Figure 2.15:**  $T$ - $s$  plane sketch for a diaphragm pump heat engine.

## 2.16 Nanofluids

Nanofluids were first developed by Choi & Eastman (1995) who defined them as fluids containing nano-sized suspended particles, e.g., metals. Metals are generally used in formulating nanofluids as they have high thermal conductivities than non-metals hence metallic liquids will have much higher thermal conductivities than those liquids without metals. As such, metal-fluid suspensions have significantly higher thermal conductivities than pure fluids, e.g., engine oil and water (Deshmukh *et al.*, 2019) when the suspended metals are nanoparticles.

Nanoparticles are particles with diameters  $<100$  nm and these exhibit different properties from those of conventional solids and have much larger surface areas (Lu *et al.*, 2016) hence are suitable candidates for suspensions in liquids to improve heat transfer. Heat transfer is known to occur on particle surfaces hence nanoparticles exhibit enhanced thermal conductivity due to their large surface areas (Chamsa-ard *et al.*, 2017). It is important to note that nanofluids exhibit enhanced heat transfer properties due to the nanoparticles but there is still little research on their effects in pressure generation by volatile working fluids.

### 2.16.1 Heat transfer mechanisms in nanofluids.

The transfer of heat in nanofluids is attributed to several heat transfer mechanisms. The main factor leading to heat transfer is the random collisions of the nanoparticles and the base-fluid caused by Brownian motion. There are three types of collisions, i.e., collision of the base fluid molecules, collision between the base fluid molecules and nanoparticles, and collision between the nanoparticles (Okonkwo *et al.*, 2020). The interfacial layer formed by the region of first contact between the surface of the nanoparticles and the first fluid layer of the base fluid forms a structure known as a nanolayer (Ozerinc *et al.*, 2010). This solid-liquid nano-structured layer was shown to enhance heat transfer.

Strong Van der Waals' forces lead to the aggregation of nanoparticles into clusters. These clusters were shown to enhance thermal conductivity (Mirmohammadi, 2012). The growth of clusters through a higher particle loading will lead to

sedimentation which reduces thermal conductivity. Thermal gradients within the nanofluid results in the transfer of nanoparticles at a higher temperature to a region of lower temperature through a process called thermophoresis.

## 2.17 Parameters influencing heat transfer in nanofluids.

Heat transfer in nanofluids is affected by several parameters linked to the different properties of the base fluid and those of the dispersed nanoparticles. The size, shape, thermal conductivity, concentration, and charge of the nanoparticles as well as the pH and temperature of the base fluid are some of these influential properties. These will be discussed in further detail in the following sections.

### 2.17.1 Thermal conductivity of nanofluids

The transfer of heat is dependent upon the thermal conductivity of the substances involved in the transfer. Improving heat transfer is important in all heat engines as this leads to lower operating costs or reduction in the sizes of these systems. The enhancement of the thermal conductivity of the base fluid by dispersion of CuO and Al<sub>2</sub>O<sub>3</sub> nanoparticles in different base-fluids (water, ethylene glycol, and EG; a mixture of ethylene glycol with water at a 60:40 ratio) was studied by (Asthana *et al.*, 2013). The researchers found that the CuO had a higher thermal conductivity enhancement than Al<sub>2</sub>O<sub>3</sub> under the same conditions, and that it produced an enhancement of approximately 23%, 18%, and 30% for water, ethylene glycol, and EG, respectively.

The thermal conductivity of nanofluids can be measured using the Transient Hot Wire Method and applying Fourier's equation (Jiang *et al.*, 2015) shown in **Equation 2.12**.

$$k = \frac{q/4\pi}{d\Delta T/d\ln t} \quad \text{Equation 2.12}$$

Where:  $k$  is the measured thermal conductivity of the nanofluid,  $q$  is the power input per unit length of hot wire, and  $T$  is the wire temperature at time  $t$ .

### 2.17.2 Effect of temperature

The thermal conductivity of nanofluids is affected by changes in temperature. Changes in temperature affect the Brownian motion of the suspended nanoparticles and their clustering (Ozerinc *et al.*, 2010). Several researchers have reported an increase in thermal conductivity with an increase in temperature. This increase was attributed to a higher particle diffusivity in the nanofluid due to an increase in Brownian motion with an increase in temperature (Mukherjee *et al.*, 2016). However, (Jiang *et al.*, 2015) made a contradictory finding. They dispersed 20 nm Cu nanoparticles in n-tetradecane to form the nanofluids that they tested for changes in thermal conductivity in the temperature range of 306.22 – 452.66 K. They determined that the thermal conductivity of the nanofluid decreased with an increase in temperature. Sridhara & Satapathy (2011) stated that the characteristics of the base fluid was a major determinant in the relationship of the thermal conductivity of nanofluids to changes in temperature.

### 2.17.3 Specific heat capacity of nanofluids

There is a lack of data on the thermal properties, e.g., specific heat capacity, of nanofluids. The addition of nanoparticles in solids and liquids has been shown to increase the specific heat capacity of the nanocomposites and nanofluids formed, respectively, through the formation of nanolayers around the nanoparticles which have a much larger heat capacity than the bulk fluid. The nanoparticles have a long range ( $\geq 100\text{nm}$ ) effect thereby allowing for large changes in specific heat capacity for small additions of the nanoparticles (Hentschke, 2016). Chieruzzi *et al.* (2013) investigated the enhancements in heat capacity of a  $\text{NaNO}_3\text{-KNO}_3$  binary salt mixture after addition of selected nanoparticles (alumina, silica, and titania) at different weight concentrations. The researchers found that the specific heat

capacity of the solid salt was increased by 15 to 57% while that of the molten salt was increased by 1 to 22% for 1 wt.% concentrations of the nanoparticles.

The heat capacity of a nanofluid can be estimated from a theoretical model shown in **Equation 2.13**.

$$C_{p,nf} = \frac{\rho_{np}\phi_{np}C_{p,np} + \rho_f\phi_fC_{p,f}}{\rho_{np}\phi_{np} + \rho_f\phi_f} \quad \text{Equation 2.13}$$

Where  $C_p$  is specific heat,  $\phi$  is the volume fraction,  $\rho$  is the density, and the subscripts np, nf, and f refer to nanoparticle, nanofluid, and base fluid, respectively.

#### 2.17.4 Effect of the size and shape of nanoparticles

The size of nanoparticles in nanofluids is dependent on several parameters like sonication time, volume concentration, etc. However, it is very difficult to have the same size distribution in nanofluids used in repeat experiments hence difficult to directly compare the effect of nanoparticles in nanofluids prepared in different studies (Marcelino *et al.*, 2016). The effect of the size of silver nanoparticles (20 nm, 30 nm, 50 nm, and 80 nm) dispersed in ethyl-glycol at 0,3 wt.% on the thermal conductivity of the nanofluids produced was investigated by (Warrier & Teja, 2011). The researchers discovered that the thermal conductivity of the nanofluids decreased with a decrease in the size of the nanoparticles.

The shape of nanoparticles has been shown to also significantly affect the thermal conductivity of nanofluids. Zhu *et al.* (2018) prepared CuO nanospheres and CuO nanowires which they then used to prepare nanofluids. The researchers determined that nanofluids prepared using CuO nanowires had a higher thermal conductivity than those prepared with CuO nanospheres. In another study, (Jeong *et al.*, 2013) determined that rectangular and spherical ZnO nanoparticles had thermal conductivity enhancements of 12% and 18%, respectively, at a 5.0 vol.% concentration in water. It is thus evident that the shape of nanoparticles affects their enhancement in thermal conductivity of the base fluid.

### 2.17.5 Effect of volume fraction of nanoparticles

The increase in the volume fraction of CuO nanoparticles in the nanofluid was shown to lead to a gradual decrease in the specific heat capacity of the nanofluid (Sandhu & Dasaroju, 2010) and an increase in thermal conductivity between the range of 0,05 and 1% for MWCNT-TiO<sub>2</sub>/ethylene glycol nanofluid (Okonkwo *et al.*, 2020). Generally, at low volume fractions, there are minor differences in the specific heat and densities of nanofluids and their base-fluids (Wu *et al.*, 2009).

The concentration of nanoparticles within the nanofluid influences the rate of heat transfer within the fluid as well as its viscosity. As such, an increase in the volume fraction of dispersed nanoparticles in a nanofluid leads to an increase in the thermal conductivity of the fluid. This was proven by (Murshed *et al.*, 2005) who prepared TiO<sub>2</sub>-water nanofluids with volume fractions in the range 0,005 -0,05 and found that the thermal conductivities of the nanofluids increased considerably with an increase in volume fraction achieving a maximum thermal conductivity of 36% for a 5 % vol nanofluid. However, an increase in the concentration of nanoparticles also increase the possibility of agglomeration and sedimentation of the nanoparticles hence there is a need to find an optimum volume fraction for each type of nanoparticle-base fluid combination (Bozorgan & Shafahi, 2015).

### 2.17.6 Effect of charge and pH of the nanoparticles

Nanoparticles have a very large ratio of surface-to-volume atoms and an increase in their surface free energies is seen with a decrease in the size of the nanoparticles (Jia *et al.*, 2008). The charge of nanoparticles is controlled by the pH of the base fluid, with acidic pH causing the nanoparticles to accumulate charge on its surface while the charge is reduced in alkaline pH (Gowda *et al.*, 2010). When the pH of nanofluids is changed beyond that of the isoelectric (point of zero charge) point(s) of the nanoparticles, there is an increase in charged species around the particles leading to a lower possibility of agglomeration or clustering of the nanoparticles. This

improves the stability of the nanofluid (Bozorgan & Shafahi, 2015) as well as the thermal conductivity of the nanofluid (Asthana *et al.*, 2013).

Gowda *et al.* (2010) investigated the effect of surface energy (zeta potential) on the stability and thermal conductivity of nanofluids prepared by dispersing alumina and copper oxide in deionized water and ethylene glycol. They varied the pH of the solution to alter the surface energy of the particles and found that the high surface energy (low pH) nanoparticles had better dispersion in the nanofluid hence produced nanofluids with higher thermal conductivity at comparable volume fraction loadings. The relationship between surface charge of nanoparticles to their stability when dispersed in base fluids is shown in **Table 2.3**.

**Table 2.3:** Relationship of zeta potential of nanoparticles to their stability in nanofluids (Choudhary *et al.*, 2017).

Zeta potential (Absolute value (mV))	Stability
0	Little or no stability
15	Some stability but settling lightly
30	Moderate stability
45	Good stability, possible settling
60	Very good stability, little settling likely

#### 2.17.7 Stability of nanoparticles

The dispersed nanoparticles can aggregate in the base fluid with time and thereby reduce the thermal absorptivity efficiency. This aggregation is a result of collision and adhesion of the nanoparticles in the base fluid and can be modelled by the Derjaguin, Verway, Landau, and Overbeek (DVLO) theory. The DLVO theory states that the colloidal stability of particles is a function of the sum of the van der Waals attractive forces and electrical double layer repulsive forces that exist between particles (Tran & Nguyen, 2014) as they approach and collide with each other due

to Brownian motion. Thus, stable suspensions are those in which the repulsive forces are greater than the attractive forces hence preventing the adhesion of particles to form aggregates (Yu & Xie, 2012). As such, stable nanofluids have dominant repulsive forces.

Stability in nanofluids can be promoted by two distinct mechanisms: either electrostatic repulsion or steric repulsion, shown in **Figure 2.16**. Polymers can be added to the colloidal suspension and these will adsorb onto the surface of the nanoparticles, forming a protective coating that inhibits further growth of the particles and repels other particles away by steric repulsion (Yu & Xie, 2012).

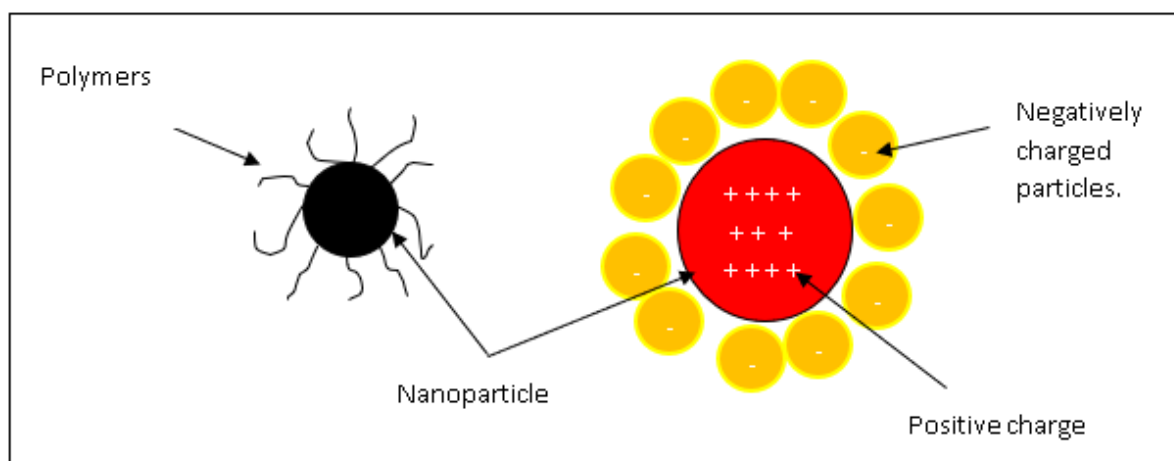


**Figure 2.16:** Schematic representation of the repulsion mechanisms in nanofluids (Yu & Xie, 2012).

In electrostatic repulsion, there is the formation of surface charge on the nanoparticles due to preferential adsorption of ions, isomorphic substitution of ions, build-up, or loss of electrons on the surface of the dissociation of surface charged ions, or physical adsorption of charged particles. This results in the particles having a net surface charge which allows these particles to repel each other (Yu & Xie, 2012).

The stability of nanofluids over time is adversely affected by the tendency of nanoparticle aggregates to crystallize in suspension when their densities exceed that of the base fluid. Other factors affect the stability of nanofluids include pH,



presence of stabilizers, method of preparation (i.e., single step chemical or physical and two-step method) and the time of agitation. Asthana *et al.* (2013) determined that 0,01 %w/v. CuO dispersed in water had good stability at acidic pH (5-6) and basic pH (8-9). However, stability measurements are difficult to compare due to the absence of a standard method of measuring the stability of the nanofluids with several approaches being used by different researchers (Okonkwo *et al.*, 2020).

## **2.18 Integration of membrane processes with pre-treatment steps and surface water treatment**

Pre-treatment of membrane feed is essential to reduce membrane fouling and can be achieved by many methods including sand-filtration, disinfection, passing the feed through biological reactors, chemical treatment, adsorption (Pellegrin *et al.*, 2011), aeration, or using another membrane process. The pre-treatment is designed to reduce the microbiological, inorganic, or organic content in the feed thereby reducing the particles that reach the surface of the membrane (Alsawaftah *et al.*, 2021).

Wend & Camper (2003) pre-treated feed solutions of RO membranes to reduce biofouling by removing micro-organisms from the feed through passing it first through bioreactors and this improved the productivity of the membranes. Adsorption of organic matter on activated carbon is also a recommended pre-treatment method to reduce organic fouling, while inorganic fouling may be reduced by precipitating metallic salts through addition of coagulants and aeration of the feed (Lainé *et al.*, 2003). In a study in China, raw water from Binxian reservoir was pre-treated to reduce turbidity using sand filtration and flocculation, before passing the feed through ultrafiltration membranes (Bokhary *et al.*, 2018; Xia *et al.*, 2004) reported that MF membranes are usually used as a pre-treatment method for waste derived in the forestry industry before ultrafiltration.

The integration of different water treatment methods together with membrane techniques shows that membranes are part of a bigger water treatment system hence cannot work on their own. Membrane technology has improved water and

wastewater treatment, and is also applicable to surface water treatment (X. Li *et al.*, 2018). Pre-treatment of the feed solution improves the membrane's performance as well as the permeate quality (Biłyk & Molczan, 2006).

## 2.19 Factors influencing membrane performance

Several factors affect the membrane's performance and these can be generally classified as feed water quality, membrane properties (e.g., concentration polarization, structural parameter (S), solute rejection, permeability), and operating conditions (e.g., temperature, initial flux, recovery) (Motsa, 2015). Mass transfer across the membrane is also affected by the process temperature as temperature affects solute solubility and concentration polarization. Other factors that impact on the mass transfer across the membrane which are used to formulate the structural parameter of membranes are the membrane thickness, tortuosity, and porosity. The thickness of the membrane determines the total resistance of the membrane thereby the thicker the membrane, the slower the rate of mass transfer across the membrane (Wenten, n.d.) The transmembrane pressure (Ariono *et al.*, 2018) as well as the pore size, and porosity of the membrane influence (Chan & Ng, 2016) how fast solutes and solvents pass through the membrane. It is also important to consider the mode of operation as energy recovery maximization and concentration polarization minimization, can be achieved through the operation of membrane processes in batch mode rather than crossflow mode (Davies, 2011). Fouling also reduces the flux of a membrane over time hence negatively impacts on the membrane's performance (Bokhary *et al.*, 2018).

## 2.20 References

- Abdel-Raouf, M. E., Maysour, N., Farag, R. K., & Abdul-Raheim, M. (2019). Wastewater Treatment Methodologies , Review Article International Journal of Environment & Agricultural Science Wastewater Treatment Methodologies , Review Article. *International Journal of Environment & Agricultural Science*, 3(1), 1–25.

- Agboola, O., Maree, J., & Mbaya, R. (2014). Characterization and performance of nanofiltration membranes. *Environ Chem Lett*, 12, 241–255.  
<https://doi.org/10.1007/s10311-014-0457-3>
- Ahmed, H. M., & Ibrahim, G. (2016). Performance Evaluation of a Conventional Solar Still with Different Types and layouts of Wick Materials Performance Evaluation of a Conventional Solar Still with Different Types and layouts of Wick Materials. *Journal of Energy Technologies and Policy*, 6(September).  
[https://www.researchgate.net/publication/309463087\\_Performance\\_Evaluation\\_of\\_a\\_Conventional\\_Solar\\_Still\\_with\\_Different\\_Types\\_and\\_layouts\\_of\\_Wick\\_Materials](https://www.researchgate.net/publication/309463087_Performance_Evaluation_of_a_Conventional_Solar_Still_with_Different_Types_and_layouts_of_Wick_Materials)
- Ali, A., Tufa, R. A., Macedonio, F., Curcio, E., & Drioli, E. (2018). Membrane technology in renewable-energy-driven desalination Membrane technology in renewable-energy-driven desalination. *Renewable and Sustainable Energy Reviews*, 81(February), 1–21. <https://doi.org/10.1016/j.rser.2017.07.047>
- Alsawaftah, N., Abuwatfa, W., Darwish, N., & Hussein, G. (2021). A Comprehensive Review on Membrane Fouling : Mathematical. *Water*, 13(1327). <https://doi.org/https://doi.org/10.3390/w13091327>
- Argaw, N. (2003). Renewable Energy in Water and Wastewater Treatment. NREL/SR-500-30383. *National Renewable Energy Laboratory*.  
<https://www.nrel.gov/docs/fy03osti/30383.pdf>
- Arhin, S. G., Banadda, N., Komakech, A. J., Pronk, W., & Marks, S. J. (2019). Application of hybrid coagulation-ultrafiltration for decentralized drinking water treatment: impact on flux, water quality and costs. *Water Supply*, 1–9.  
<https://doi.org/10.2166/ws.2019.097>
- Ariono, D., Wardani, A. K., Jenderal, U., Yani, A., & Hakim, A. N. (2018). Determination of fouling mechanism of electroplating. *Journal Teknologi, May*. <https://doi.org/10.11113/jt.v80.12739>
- Asthana, S., Petroleum, B., & Rattan, S. (2013). Comparative Studies of Copper Oxide with Aluminium Oxide Nanoparticles in Conventional Thermal Fluids for Its Enhanced Efficiency as Coolant Proceedings of the National Academy of Sciences , Physical Sciences Comparative studies of Copper oxide with

- Alumi. *Proceedings of the National Academy of Sciences.*, June.  
<https://doi.org/10.1007/s40010-012-0057-1>
- Awais, M., Ullah, N., Ahmad, J., Sikandar, F., Ehsan, M. M., Salehin, S., & Bhuiyan, A. A. (2021). International Journal of Thermo fluids Heat transfer and pressure drop performance of Nano fluid : A state-of- the-art review. *International Journal of Thermofluids*, 9, 100065.  
<https://doi.org/10.1016/j.ijft.2021.100065>
- Aziz, M. (2021). The Removal of Selected Inorganics from Municipal Membrane Bioreactor Wastewater Using UF / NF / RO Membranes for Water Reuse Application : A Pilot-Scale Study. *Membranes*, 11(117).  
<https://doi.org/https://dx.doi.org/10.3390/membranes11020117>
- Barghi, H. (2014). Functionalization of Synthetic Polymers for Membrane Bioreactors Hamidreza Barghi Functionalization of Synthetic Polymers for Membrane Bioreactors. *Chalmers University of Technology*.
- Bartram, J., & Ballance, R. (1996). Water quality monitoring. A practical guide to the design and implementation of freshwater quality studies and monitoring programmes. (1<sup>st</sup> ed.) *E&FN Spon*.  
<https://apps.who.int/iris/handle/10665/41851>
- Bernat, X., Sánchez, I., Stüber, F., Bengoa, C., Fortuny, a, Fabregat, a, & Font, J. (2007). Removal of heavy metals by ultrafiltration. *European Congress of Chemical Engineering, September*, 16–20.  
[https://folk.ntnu.no/skoge/prost/proceedings/ecce6\\_sep07/upload/454.pdf](https://folk.ntnu.no/skoge/prost/proceedings/ecce6_sep07/upload/454.pdf)
- Bhattacharya, S. S. A. (2017). Drinking water contamination and treatment techniques. *Applied Water Science*, 7(3), 1043–1067.  
<https://doi.org/10.1007/s13201-016-0455-7>
- Biłyk, A., & Mołczan, M. (2006). The Effect of Feed Water Pretreatment on Ultrafiltration Membrane Performance. *Polish J. of Environ. Stud.*, 15(5), 719–725. <http://www.pjoes.com/pdf-87924-21783?filename=21783.pdf>
- Bitton, G. (2014). Water treatment technologies for developing countries 8.1. In *Microbiology of Drinking Water Production and Distribution*, (1<sup>st</sup> ed.). (pp. 173–194). <https://onlinelibrary.wiley.com/doi/pdf/10.1002/9781118743942.ch8>

- Bokhary, A., Tikka, A., Leitch, M., & Liao, B. (2018). Membrane Fouling Prevention and Control Strategies in Pulp and Paper Industry Applications : A Review Membrane Fouling Prevention and Control Strategies in Pulp and Paper Industry Applications : A Review Graphical abstract Keywords. *Journal of Membrane Science and Research*, May, 180–197.  
<https://doi.org/10.22079/JMSR.2018.83337.1185>
- Borde, P., Elmusharaf, K., Mcguigan, K. G., & Keogh, M. B. (2016). Community challenges when using large plastic bottles for Solar Energy Disinfection of Water ( SODIS ). *BMC Public Health*, 1–8. <https://doi.org/10.1186/s12889-016-3535-6>
- Boretti, A. (2020). Covid19 pandemic as a further driver of water scarcity in Africa. *GeoJournal*, 7(Boulding). <https://doi.org/10.1007/s10708-020-10280-7>
- Bozorgan, N., & Shafahi, M. (2015). Performance evaluation of nanofluids in solar energy : a review of the recent literature. *Micro and Nano Systems Letters*, 1–15. <https://doi.org/10.1186/s40486-015-0014-2>
- Bwapwa, J. K. (2018). Review on Main Issues Causing Deterioration of Water Quality and Water Scarcity : Case Study of South Africa. *Environmental Management and Sustainable Development*, 7(3), 14–34.  
<https://doi.org/10.5296/emsd.v7i3.13156>
- Capodaglio, A. G., & Olsson, G. (2020). Energy Issues in Sustainable Urban Wastewater Management : Use , Demand Reduction and Recovery in the Urban Water Cycle. *Sustainability*, 12(266).  
<https://doi.org/doi:10.3390/su12010266>
- CAWST. (2009). Biosand filter manual design, construction, installation, operation and maintenance. (Issue September). *Centre for Affordable Water and Sanitation Technology*.  
[https://sswm.info/sites/default/files/reference\\_attachments/CAWST%202009%20Biosand%20Filter%20Manual.pdf](https://sswm.info/sites/default/files/reference_attachments/CAWST%202009%20Biosand%20Filter%20Manual.pdf)
- Chaichan, M. T., & Kazem, H. A. (2015). Water solar distiller productivity enhancement using concentrating solar water heater and phase change material (PCM). *Case Studies in Thermal Engineering*, April.

<https://doi.org/10.1016/j.csite.2015.03.009>

- Challener, C. (2011). Handbook for the operation of Water treatment works. In *Chemistry & Industry* (Vol. 3).  
<http://content.ebscohost.com/ContentServer.asp?T=P&P=AN&K=57995235&S=R&D=bth&EbscoContent=dGJyMNxb4kSepY4yOvsOLCmr06eqK9SsKi4SK+WxWXS&ContentCustomer=dGJyMPGut1C0rLNRuePfgeyx44Dt6fIA>
- Chamsa-ard, W., Brundavanam, S., Fung, C. C., & Fawcett, D. (2017). Nanofluid Types , Their Synthesis , Properties and Incorporation in Direct Solar Thermal Collectors : A Review. *Nanomaterials*, 7(131).  
<https://doi.org/10.3390/nano7060131>
- Chan, M., & Ng, S. (2016). Effect of membrane properties on contact angle Effect of Membrane Properties on Contact Angle. *AIP Conference Proceedings*, 020035 (September). <https://aip.scitation.org/doi/10.1063/1.5055437>
- Chao, G., Shuili, Y., Yufei, S., Zhengyang, G., & Wangzhen, Y. (2018). A Review of Ultrafiltration and Forward Osmosis : application and modification. *Earth and Environmental Science*, 128. <https://doi.org/10.1088/1755-1315/128/1/012150>
- Chaukura, N., Ndlangamandla, N. G., Moyo, W., Msagati, T. A. M., Mamba, B. B., & Nkambule, T. T. I. (2018). Natural organic matter in aquatic systems – a South African perspective. *SciELO SA*. 44(4), 624–635.  
[http://www.scielo.org.za/scielo.php?script=sci\\_arttext&pid=S1816-79502018000400024](http://www.scielo.org.za/scielo.php?script=sci_arttext&pid=S1816-79502018000400024)
- Chen, Q., Wang, Y., Zhang, J., & Wang, Z. (2020). The Knowledge Mapping of Concentrating Solar Power Development Based on Literature Analysis Technology. *Energies*, 13. <https://doi.org/doi:10.3390/en13081988>
- Chen, W., Qian, C., Zhou, K., & Yu, H. (2018). Molecular Spectroscopic Characterization of Membrane Fouling : A Critical Review. *Chem*, 4(7), 1492–1509. <https://doi.org/10.1016/j.chempr.2018.03.011>
- Cheremisinoff, N. (2002). Handbook of Water and Wastewater Treatment Technologies. *Butterworth-Heinemann*. <https://doi.org/10.1016/B978-075067498-0/50000-0>

- Chieruzzi, M., Cerritelli, G. F., Miliozzi, A., & Kenny, J. M. (2013). Effect of nanoparticles on heat capacity of nanofluids based on molten salts as PCM for thermal energy storage. *Nano Express*, 8(448), 1–9.  
<https://doi.org/10.1186/1556-276X-8-448>
- Choi, S., & Eastman, J. A. (1995). Enhancing thermal conductivity of fluids with nanoparticles. *ASME International Mechanical Engineering Congress & Exposition*. [https://ecotert.com/pdf/196525\\_From\\_unt-edu.pdf](https://ecotert.com/pdf/196525_From_unt-edu.pdf)
- Chollom, M. (2015). The applicability of nanofiltration for the treatment and reuse of textile reactive dye effluent. *Water SA*, 41(3).  
<https://doi.org/10.4314/wsa.v41i3.12>
- Choudhary, R., Khurana, D., Kumar, A., & Subudhi, S. (2017). Stability analysis of Al<sub>2</sub>O<sub>3</sub> / water nanofluids. *Journal of Experimental Nanoscience*, 12(1), 140–151. <https://doi.org/10.1080/17458080.2017.1285445>
- Codd, D. S., Gil, A., Manzoor, M. T., & Tetreault-friend, M. (2020). Concentrating Solar Power ( CSP ) — Thermal Energy Storage ( TES ) Advanced Concept Development and Demonstrations. *Sustainable and Renewable Energy*, 7, 17–27. <https://doi.org/https://doi.org/10.1007/s40518-020-00146-4>
- Colvin, C., Muruven, D., Lindley, D., Gordon, H., & Schachtschneider, K. (2016). Water : Facts and Futures Rethinking South Africa’s Water Future. *WWF-SA*. [http://awsassets.wwf.org.za/downloads/wwf009\\_waterfactsandfutures\\_report\\_web\\_\\_lowres\\_.pdf](http://awsassets.wwf.org.za/downloads/wwf009_waterfactsandfutures_report_web__lowres_.pdf)
- Cordier, C., Eljaddi, T., Ibourohim, N., Stavrakakis, C., Sauvade, P., Coelho, F., & Moulin, P. (2020). Optimization of Air Backwash Frequency during the Ultrafiltration of Seawater. *Membranes*, 10(78), 1–10.  
<https://doi.org/10.3390/membranes10040078>
- Dach, H. (2009). Comparison of nanofiltration and reverse osmosis processes for a selective desalination of brackish water feeds. tel-0043351. *Engineering Sciences*. <https://tel.archives-ouvertes.fr/tel-00433513>
- Davies, P. A. (2011). A solar-powered reverse osmosis system for high recovery of freshwater from saline groundwater. *DES*, 271(1–3), 72–79.  
<https://doi.org/10.1016/j.desal.2010.12.010>

- Deshmukh, G., Jose, N., Shidhav, R., Suryawanshi, A., Datir, R., & Ravindra, M. R. (2019). Nanofluids : An Introduction to New Generation Heat Transfer Fluids. *ACTA Scientific Agriculture*, 3(2), 41–48.  
<https://actascientific.com/ASAG/pdf/ASAG-03-0327.pdf>
- Dewitt, D., Bergman, T., & Lavine, A. (2007). Fundamentals of Heat and Mass Transfer (Sixth). *John Wiley & Sons, Inc.*  
[https://www.researchgate.net/publication/260081006\\_Fundamentals\\_of\\_Heat\\_and\\_Mass\\_Transfer](https://www.researchgate.net/publication/260081006_Fundamentals_of_Heat_and_Mass_Transfer)
- Dongare, P. D., Neumann, O., & Halas, N. J. (2019). Solar thermal desalination as a nonlinear optical process. *PNAS*, July.  
<https://doi.org/10.1073/pnas.1905311116>
- Donnenfeld, Z., Crookes, C., & Hedden, S. (2018). A delicate balance Water scarcity in South Africa (March). <https://issafrica.org/research/southern-africa-report/a-delicate-balance-water-scarcity-in-south-africa>
- DWS. (2015). South Africa Yearbook 2015/16: Water and Sanitation. South Africa Yearbook 2015/16 | *Government Communication and Information System*.  
<https://www.gcis.gov.za/content/resourcecentre/sa-info/yearbook2015-16>
- Ebenebe, P. C., Shale, K., Sedibe, M., Tikilili, P., & Achilonu, M. C. (2017). South African Mine Effluents : Heavy Metal Pollution and Impact on the Ecosystem. *International Journal of Chemical Sciences*, 15(4), 1–12.
- Edokpayi, J. N., & Odiyo, J. O. (2014). Assessment of heavy metal contamination of Dzindi River , in Limpopo Province, South Africa. *International Journal of Natural Sciences Research*, 2(10), 185–194.  
<https://www.tsijournals.com/articles/south-african-mine-effluents-heavy-metal-pollution-and-impact-on-the-ecosystem.pdf>
- Ellis, E. (2019). *Eastern Cape government finally declares province a disaster area*. Daily Maverick. <https://www.dailymaverick.co.za/article/2019-10-16-eastern-cape-government-finally-declares-province-a-disaster-area/>
- EPA. (2017). *Fresh Surface Water | EPA's Report on the Environment (ROE) | US EPA*. <https://www.epa.gov/report-environment/fresh-surface-water>
- Ezugbe, E. O., & Rathilal, S. (2020). Membrane Technologies in Wastewater



- Treatment : *Membranes*, 10(89).  
<https://doi.org/doi:10.3390/membranes10050089>
- Fendrich, M. A., Quaranta, A., Orlandi, M., Bettonte, M., & Miotello, A. (2019). Applied sciences Solar Concentration for Wastewaters Remediation : A Review of Materials and Technologies. *Applied Sciences*, 9.  
<https://doi.org/10.3390/app9010118>
- Frankson. (2016). Kalahari East Water Scheme receives R630 million | Infrastructure. *Infrastructure News*.  
<https://infrastructurenews.co.za/2016/02/29/kalahari-east-water-scheme-receives-r630m/>
- Gao, K., Li, T., Liu, J., Dong, B., & Chu, H. (2019). Ultrafiltration membrane fouling performance by mixtures with micromolecular and macromolecular organics. *Environmental Science Water Research and Technology*5, 5, 277–286.  
<https://doi.org/10.1039/c8ew00642c>
- Garc, Á., Garc, R. A., & Mcguigan, K. G. (2021). Solar Water Disinfection to Produce Safe Drinking Water : A Review of Parameters , Enhancements , and Modelling. *Molecules*, 26(3431).  
<https://doi.org/https://doi.org/10.3390/molecules26113431>
- Goff, H., Main, G. L., & Warrington, R. O. (1988). Heat Engines. *Mechanical Engineering*, 110(6), 44–49.  
[https://doi.org/10.1243/pime\\_proc\\_1949\\_160\\_012\\_02](https://doi.org/10.1243/pime_proc_1949_160_012_02)
- Gowda, R., Sun, H., Wang, P., Charmchi, M., Gao, F., Gu, Z., & Budhlall, B. (2010). Effects of Particle Surface Charge , Species , Concentration , and Dispersion Method on the Thermal Conductivity of Nanofluids. *Advances in Mechanical Engineering*. <https://doi.org/10.1155/2010/807610>
- Greenfield, R., Vuren, J. H. J. Van, & Wepener, V. (2012). Heavy metal concentrations in the water of the Nyl River system , South Africa. *South Africa Journal of Aquatic Science*, 37(219–224).  
<https://doi.org/10.2989/16085914.2011.653005>
- Guerra, K., & Pellegrino, J. (2012). Investigation of Low-Pressure Membrane Performance , Cleaning , and Economics Using a Techno-Economic Modeling

- Approach (174).  
[https://www.usbr.gov/research/projects/download\\_product.cfm?id=606](https://www.usbr.gov/research/projects/download_product.cfm?id=606)
- Guo, W., Ngo, H., & Li, J. (2012). A mini-review on membrane fouling. *Bioresource Technology*, 122, 27–34. <https://doi.org/10.1016/j.biortech.2012.04.089>
- Hall, M. S., & Hall, M. S. (2016). Solar-Powered Water Purification System with Energy Storage. Summer.  
[https://opensiuc.lib.siu.edu/cgi/viewcontent.cgi?article=1001&context=esh\\_2016](https://opensiuc.lib.siu.edu/cgi/viewcontent.cgi?article=1001&context=esh_2016)
- Harshfield, E. (2015). Water Purification in Rural South Africa : Ethical Analysis and Reflections on Collaborative Community Engagement Projects in *Engineering*. May. <https://doi.org/10.24908/ijlsle.v4i1.2223>
- Hentschke, R. (2016). On the specific heat capacity enhancement in nanofluids. *Nanoscale Research Letters*, 11(88). <https://doi.org/10.1186/s11671-015-1188-5>
- Hoegh-Guldberg, O., D., Jacob, M. Taylor, M. Bindi, S. Brown, I. Camilloni, A. Diedhiou, R. Djalante, K.L. Ebi, F. Engelbrecht, J. Guiot, Y. Hijioka, S. Mehrotra, A. Payne, S.I. Seneviratne, A. Thomas, R. Warren, and G. Zhou, 2018: Impacts of 1.5°C Global Warming on Natural and Human Systems. In: Global Warming of 1.5°C. An IPCC Special Report on the impacts of global warming of 1.5°C above pre-industrial levels and related global greenhouse gas emission pathways, in the context of strengthening the global response to the threat of climate change, sustainable development, and efforts to eradicate poverty. In *Press*.
- Jacangelo, J. G., Trussell, R. R., & Watson, M. (1997). Role of membrane technology in drinking water treatment in the United States. *Desalination*, 113(2–3), 119–127. [https://doi.org/10.1016/S0011-9164\(97\)00120-3](https://doi.org/10.1016/S0011-9164(97)00120-3)
- Jain, S., & Jain, P. K. (2018). The rise of Renewable Energy implementation in South Africa ScienceDirect ScienceDirect ScienceDirect The rise The of Renewable Energy implementation South using the heat demand-outdoor a long-term district heat demand forecast. *Energy Procedia*, 143(March), 721–726. <https://doi.org/10.1016/j.egypro.2017.12.752>

- Jeong, J., Li, C., Kwon, Y., Lee, J., Hyung, S., & Yun, R. (2013). Particle shape effect on the viscosity and thermal conductivity of ZnO nanofluids Effet de forme de particules sur la viscosite ` nes ZnO thermique de nanofrigorige. *International Journal of Refrigeration*, 36(8), 2233–2241. <https://doi.org/10.1016/j.ijrefrig.2013.07.024>
- Jia, M., Lai, Y., Tian, Z., & Liu, Y. (2008). Calculation of the surface free energy of fcc copper nanoparticles Calculation of the surface free energy of fcc copper nanoparticles. *Modelling and Simulation in Materials Science and Engineering*, 17. <https://doi.org/10.1088/0965-0393/17/1/015006>
- Jiang, H., Xu, Q., Huang, C., & Shi, L. (2015). Effect of temperature on the effective thermal conductivity of n-tetradecane-based nanofluids containing copper nanoparticles. *Particuology*, 22, 95–99. <https://doi.org/10.1016/j.partic.2014.10.010>
- Kashyout, A. E. B., Hassan, A., Hassan, G., & El-banna, H. (2021). Hybrid renewable energy / hybrid desalination potentials for remote areas : selected cases studied. *RSC Advances*, 11, 13201–13219. <https://doi.org/10.1039/d1ra00989c>
- Kenway, S. E. (2001). The efficiency of ultrafiltration membrane at removing TOC and THMFP in a British Columbia surface water. *University of British Columbia*. <https://open.library.ubc.ca/media/download/pdf/831/1.0063725/3>
- Khan, J., & Arsalan, M. H. (2016). Solar power technologies for sustainable electricity generation – A review. *Renewable and Sustainable Energy Reviews*, 55, 414–425. <https://doi.org/10.1016/j.rser.2015.10.135>
- Kimura, S. (1991). Characterization of Ultrafiltration Membranes. *Polymer Journal*, 23(5), 389–397. <https://doi.org/10.1295/polymj.23.389>
- Klerk, E., Kersley, R., & Isaac, O. (2020). Water scarcity: Addressing the key challenges. In *Davos edition 2020*. <https://www.creditsuisse.com/media/assets/corporate/docs/about-us/research/publications/water-scarcity-en.pdf>
- Knauer, K. M. (2016). Surface and Interfacial Design and Control of High Performing Thermoplastics : Polysulfones and Beyond by. *University of*

- Southern Mississippi*. <https://core.ac.uk/download/pdf/301298597.pdf>
- Kothandaraman, C. (2006). Fundamentals of Heat and Mass Transfer (Revised Th). *New Age International Publishers*.
- Kurhe, N., Funde, A., Gokhale, P., Jadkar, S., Ghaisas, S., & Date, A. (2017). Development of Low Temperature Heat Engine for Water Pumping Application. *Energy Procedia*, 110(December), 292–297. <https://doi.org/10.1016/j.egypro.2017.03.142>
- Laîné, J., Campos, C., Baudin, I., & Janex, M. (2003). Understanding membrane fouling : a review of over a decade of research. *Water Science and Technology: Water Supply*, 3(5–6), 155–164. [https://www.oieau.org/eaudoc/system/files/documents/39/196335/196335\\_doc.pdf](https://www.oieau.org/eaudoc/system/files/documents/39/196335/196335_doc.pdf)
- Lakhotia, S. R., Mukhop, M., & Kumari, P. (2018). Cerium oxide nanoparticles embedded thin-film nanocomposite nanofiltration membrane for water treatment. *Scientific Reports*, 8(April), 1–10. <https://doi.org/10.1038/s41598-018-23188-7>
- Laurent, P. (2005). Household Drinking Water Systems and Their Impact on People With Weakened Immunity. *East Africa Medical Journal*, 1(February), 1–72. [http://www.who.int/household\\_water/research/HWTS\\_impacts\\_on\\_weakened\\_immunity.pdf](http://www.who.int/household_water/research/HWTS_impacts_on_weakened_immunity.pdf)
- Lee, N., Buisson, H., Amy, G., & Croue, J. (2004). Identification and understanding of fouling in low-pressure membrane ( MF / UF ) filtration by natural organic. *Water Research*, 38, 4511–4523. <https://doi.org/10.1016/j.watres.2004.08.013>
- Lehohla, P. (2017). The state of basic service delivery in South Africa : In-depth analysis of the Community Survey 2016 data. *Statistics South Africa*. (Issue 03). <http://www.statssa.gov.za/publications/Report%2003-01-22/Report%2003-01-222016.pdf>
- Lei, M., Zhang, L., Lei, J., Zong, L., Li, J., Wu, Z., & Wang, Z. (2015). Overview of Emerging Contaminants and Associated Human Health Effects. *BioMed Research International*. <https://doi.org/10.1155/2015/404796>

- Li, H., Dong, Z., Weng, Q., Chang, C., & Liu, B. (2015). Emerging Pollutants – Part I: Occurrence , Fate and Transport. *Water Environment Research*, 87(10), 1849–1872. <https://doi.org/10.2175/106143015X14338845156425>
- Li, X., Jiang, L., & Li, H. (2018). Application of Ultrafiltration Technology in Water Treatment Application of Ultrafiltration Technology in Water Treatment. *Earth and Environmental Science*. <https://doi:10.1088/1755-1315/186/3/012009>
- Liao, Z., Nhat, M., Wan, G., Xie, J., Ni, L., Qi, J., Li, J., & Iris, A. (2020). Low pressure operated ultra fi ltration membrane with integration of hollow mesoporous carbon nanospheres for e ff ective removal of micropollutants. *Journal of Hazardous Materials*, 397(December), 122779. <https://doi.org/10.1016/j.jhazmat.2020.122779>
- Lienhard, J. H., Antar, M. A., Bilton, A., Blanco, J., & Zaragoza, G. (2012). *Solar Desalination*. (pp. 277–347). Begell House. 10.1615/AnnualRevHeatTransfer.2012004659.
- Lienhard V, J., Thiel, G. P., Lienhard, John H.; Thiel, Gregory P.; Warsinger, David M.; and Banchik, Leonardo D,(2016). Low Carbon Desalination: Status and Research, Development, and Demonstration Needs, Report of a workshop conducted at the Massachusetts Institute of Technology in association with the Global Clean Water Desalination Alliance. *World Water and Food Security Lab*, Cambridge, Massachusetts, November 2016.
- Lu, H., Wang, J., Stoller, M., Wang, T., Bao, Y., & Hao, H. (2016). An Overview of Nanomaterials for Water and Wastewater Treatment. *Advances in Materials Science and Engineering*, 2016. <https://doi.org/http://dx.doi.org/10.1155/2016/4964828>
- Machenbach, I. (2007). Drinking Water Production by Coagulation and Membrane Filtration (Issue September). *Norwegian University of Science and Technology*. [https://ntnuopen.ntnu.no/ntnu-xmlui/bitstream/handle/11250/242076/124226\\_FULLTEXT01.pdf?sequence=2&isAllowed=y](https://ntnuopen.ntnu.no/ntnu-xmlui/bitstream/handle/11250/242076/124226_FULLTEXT01.pdf?sequence=2&isAllowed=y)
- Macknick, J., Sattler, S., Meldrum, J., Heath, G., Clemmer, S., & Rogers, J.

- (2012). Operational water consumption and withdrawal factors for electricity generating technologies : a review of existing literature.  
<https://doi.org/10.1088/1748-9326/7/4/045802>
- Maddah, H. A., Alzhrani, A. S., Almalki, A. M., Bassyouni, M., Abdel-Aziz, M. H., Zoromba, M., & Shihon, M. A. (2017). Determination of the treatment efficiency of different commercial membrane modules for the treatment of groundwater. *Journal of Materials and Environmental Science*, 8(6).
- Mahdi, N., Kumar, P., Goswami, A., Perdicakis, B., Shankar, K., & Sadrzadeh, M. (2019). Robust polymer nanocomposite membranes incorporating discrete Tio2 nanotubes for water treatment. *Nanomaterials*, 9(9), 1–18.  
<https://doi.org/10.3390/nano9091186>
- Mahlangu, T. O., & Mamba, B. B. (2012). A comparative assessment of chemical contaminant removal by three household water treatment filters. *Water SA*, 38(1), 39–48.
- Mahurpawar, M. (2015). Effects of heavy metals on human health. *International Journal of Research*, 0530.  
<https://doi.org/10.29121/granthaalayah.v3.i9SE.2015.3282>
- Mancinelli, D., & Hallé, C. (2015). Membrane Science & Technology Nano-Filtration and Ultra-Filtration Ceramic Membranes for Food Processing : A Mini Review. *Journal of Membrane Science & Technology*, 5(2).  
<https://doi.org/10.4172/2155-9589.1000140>
- Marcelino, E. W., Silva, D. D. O., & Riehl, R. R. (2016). A review on the influence of nanoparticle size in thermal enhancement of CuO-Water nanofluids and their characteristics. *Heat Powered Cycles Conference*.
- Masindi, V., & Duncker, L. (2016). State of Water and Sanitation in South Africa (Issue March). <https://doi.org/10.13140/RG.2.2.11466.77761>
- Massoud, M. (2005). Engineering Thermofluids: Thermodynamics, Fluid Mechanics, and Heat Transfer. *Springer*.
- Mathumba, P., Maziya, K., Kuvarega, A. T., Dlamini, L. N., & Malinga, S. P. (2020). Photocatalytic degradation of a basic dye in water by nanostructured

- HPEI / TiO<sub>2</sub> containing membranes. *Water SA*, 46(3), 500–505.  
<https://doi.org/https://doi.org/10.17159/wsa/2020.v46.i3.8660> Research
- Mecha, C. A., & Pillay, V. L. (2014). Development and evaluation of woven fabric micro filtration membranes impregnated with silver nanoparticles for potable water treatment. *Journal of Membrane Science*, 458, 149–156.  
<https://doi.org/10.1016/j.memsci.2014.02.001>
- Meng, Q., Nan, J., Wang, Z., Ji, X., Wu, F., Liu, B., & Xiao, Q. (2019). Study on the efficiency of ultrafiltration technology in dealing with sudden cadmium pollution in surface water and ultrafiltration membrane fouling. *Environmental Science and Pollution Research*, 26, 16641–16651.  
<https://doi.org/https://doi.org/10.1007/s11356-019-04691-4>
- Meridian Institute. (2006). Overview and Comparison of Conventional and Nano-Based Water Treatment Technologies. *Meridian Institute*.  
<http://www.merid.org/nano/watertechpaper>
- Metcalf, G., Pillay, L., Murutu, C., Chiburi, S., Gumede, N., & Gaydon, P. (2014). Wastewater reclamation for potable reuse. *Water Research Commission*.  
<https://www.green-cape.co.za/assets/Sector-files/water/Reclamation-and-reuse/WRC-Wastewater-reclamation-for-potable-reuse-volume-2-integration-of-MBR-technology-with-advanced-treatment-processes-2014.pdf>
- Ming, C., Aroua, M. K., Hussain, M. A., & Ismail, W. M. Z. W. (2015). Practical performance analysis of an industrial-scale ultrafiltration membrane water treatment plant. *Journal of the Taiwan Institute of Chemical Engineers*, 46, 132–139. <https://doi.org/10.1016/j.jtice.2014.09.013>
- Mirmohammadi, S. A. (2012). Investigation on Thermal Conductivity , Viscosity and Stability of Nanofluids. *Royal Institute of Technology*. <https://www.diva-portal.org/smash/get/diva2:561791/FULLTEXT02.pdf>
- Mohamad, S. H., Idris, M. I., Abdullah, H. Z., & Ismail, A. F. (2013). Short Review of Ultrafiltration of Polymer Membrane As a Self-Cleaning and Antifouling in the Wastewater System. *Advanced Materials Research*, 795(2013), 318–323.  
<https://doi.org/10.4028/www.scientific.net/AMR.795.318>
- Moitsheki, L. J. (2003). Nanofiltration: Fouling and chemical cleaning.

- Potchefstroom University for Christian Higher Education.*  
[http://repository.nwu.ac.za/bitstream/handle/10394/391/moitsheki\\_lj.pdf](http://repository.nwu.ac.za/bitstream/handle/10394/391/moitsheki_lj.pdf)
- Molekoa, M. D., Avtar, R., Kumar, P., Minh, H. V., & Kurniawan, T. A. (2019). Hydrogeochemical Assessment of Groundwater Using Statistical Approach. *Water*. <https://doi.org/10.3390/w11091891>
- Molelekwa, G. F., Mukhola, M. S., Bruggen, B. Van Der, & Luis, P. (2014). Preliminary Studies on Membrane Filtration for the Production of Potable Water : A Case of Tshaanda Rural Village in South Africa. *PLoS ONE*, 9(8), 1–10. <https://doi.org/10.1371/journal.pone.0105057>
- Motsa, M. M. (2015). Fundamental mechanisms of fouling and cleaning of forward osmosis membranes mimicking seawater desalination and waste water reclamation. *Ghent University*.  
<https://ujcontent.uj.ac.za/vital/access/services/Download/uj:16492/SOURCE1>
- Mouhoumed, E. I., Szymczyk, A., Schäfer, A., Paugam, L., Mouhoumed, E. I., Szymczyk, A., Schäfer, A., Paugam, L., & Physico-, Y. La. (2014). Physico-chemical characterization of polyamide NF / RO membranes : Insight from streaming current measurements. <https://hal.archives-ouvertes.fr/hal-0098753>
- Mukherjee, S., Mishra, P. C., Parashar, S. K. S., & Chaudhuri, P. (2016). Role of temperature on thermal conductivity of nanofluids: a brief literature review. *Heat and Mass Transfer*. <https://doi.org/10.1007/s00231-016-1753-1>
- Murshed, S. M. S., Leong, K. C., & Yang, C. (2005). Enhanced thermal conductivity of TiO<sub>2</sub> - Water based nanofluids. *International Journal of Thermal Sciences*, 44(4), 367–373.  
<https://doi.org/10.1016/j.ijthermalsci.2004.12.005>
- Musingafi, M. (2014). Fresh Water Sources Pollution : A Human Related Threat To Fresh Water Security in South Africa. *Journal of Public Policy and Governance*, 1(2), 72–81.
- Mwabi, J. K., Mamba, B. B., & Momba, M. N. B. (2013). Removal of waterborne bacteria from surface water and groundwater by cost-effective household water treatment systems (HWTS): A sustainable solution for improving water quality in rural communities of Africa. *Water SA*, 39(4), 445–456.



<https://doi.org/http://dx.doi.org/10.4314/wsa.v39i4.2>

Narayan, S., & Gupta, V. (2015). Overview of working of stirling engines. *Journal of Engineering Studies and Research*, 21(4), 45–53.

<https://doi.org/10.29081/jesr.v21i4.132>

National Drinking Water Clearing House. (1996). *Filtration*. National Drinking Water Clearing House Tech Brief.

<https://files.knowyourh2o.com/Waterlibrary/privatewell/filtration.pdf>

Nouman, J. (2012). *Comparative studies and analyses of working fluids for Organic Rankine Cycles - ORC*. KTH School of Industrial Engineering and Management. <https://www.diva-portal.org/smash/get/diva2:555314/FULLTEXT01.pdf>

Odiyo, J. O., & Makungo, R. (2012). Water quality problems and management in rural areas of Limpopo Province , South Africa. *WIT Transactions on Ecology and The Environment*, 164(July). <https://doi.org/10.2495/WP120121>

Okonkwo, E. C., Wole, I., Ismail, O., Yasser, W. A., Tareq, M. A., Ansari, A., & Deionized, D. I. (2020). An updated review of nanofluids in various heat transfer devices. In *Journal of Thermal Analysis and Calorimetry* (Issue March). Springer International Publishing. <https://doi.org/10.1007/s10973-020-09760-2>

Ortega-Rivas, E. (2012). Membrane Separations. In *Food Engineering Series* (pp. 199–214). [https://doi.org/10.1007/978-1-4614-2038-5\\_8](https://doi.org/10.1007/978-1-4614-2038-5_8)

Ozerinc, S., Gu, V., Sadık, K., & Almila, Y. (2010). Enhanced thermal conductivity of nanofluids : a state-of-the-art review. *Microfluid Nanofluid*, 8, 145–170. <https://doi.org/10.1007/s10404-009-0524-4>

Pal, M., Ayele, Y., Hadush, M., Panigrahi, S., & Jadhav, V. (2018). Air & Water Borne Diseases Public Health Hazards Due to Unsafe Drinking Water. *Air Water Borne Dis*, 7(June). <https://doi.org/10.4172/2167-7719.1000138>

Parks, R., & McLaren, M. (2019). Experiences and lessons in managing water. *Imperial College London*. 29. <https://www.imperial.ac.uk/media/imperial-college/grantham-institute/public/publications/briefing-papers/Experiences->

and-lessons-in-managing-water.pdf

- Pellegrin, M., Greiner, A. D., Diamond, J., Aguinaldo, J., Arabi, S., Min, K., Burbano, M. S., & Mccandless, R. (2011). *Membrane Processes* (Vol. 83, Issue 10). <https://doi.org/10.2175/106143011X13075599869290>
- Pillay, V. L., & Jacobs, E. P. (2004). The Development of Small-Scale Ultrafiltration Systems for Potable. In *Water Research Commission* (Issue 1070).
- Pirnie, M. (2001). Low-pressure membrane filtration for pathogen removal: application, implementation, and regulatory issues.  
<https://nepis.epa.gov/Exe/ZyPURL.cgi?Dockey=P10056FL.TXT>
- Plappally, A. K., & Lienhard V, J. H. (2013). Costs for water supply, treatment, end-use and reclamation. *Desalination and Water Treatment*, 51(1–3), 200–232. <https://doi.org/10.1080/19443994.2012.708996>
- Pooi, C. K., & Ng, H. Y. (2018). Review of low-cost point-of-use water treatment systems for developing communities. *Clean Water*, 11(August ), 4,6.  
<https://doi.org/10.1038/s41545-018-0011-0>
- Pressdee, J., & Hill, C. (2006). Minneapolis Water Works Ultrafiltration Plant makes a big splash in the membrane world. *American Membrane Technology Association*.
- Raju, K. (2011). Fluid Mechanics, Heat Transfer, and Mass Transfer. *John Wiley & Sons, Inc.*
- Rao, D. K., Reddy, K. S., & Rao, V. V. S. (2020). Enhancement Of Energy Efficiency With Modeled Design Of Concentrated Solar Power Technology Using Parabolic Dish And Trough. *International Journal of Scientific & Technology Research*. 9(04), 736–744.
- Ras, C., & von Blottnitz, H. (2012). A comparative life cycle assessment of process water treatment technologies at the Secunda industrial complex, South Africa. *Water SA*, 38(4), 549–554. <https://doi.org/10.4314/wsa.v38i4.10>
- Reyes, T. G., & Crisosto, J. M. (2016). Characterization of Dissolved Organic Matter in River Water by Conventional Methods and Direct Sample Analysis-

- Time of Flight-Mass Spectrometry. *Journal of Chemistry*, 2016.  
<https://doi.org/10.1155/2016/1537370>
- Rodda, N., Schmidt, S., Dent, M., Bux, F., Hanke, N., & Fennemore, C. (2016). Water security in South Africa : perceptions on public expectations and municipal obligations , governance and water re-use. *Water SA*, 42(3), 456–465. <https://doi.org/http://dx.doi.org/10.4314/wsa.v42i3.11>
- Rother, H. A., Wijesekerab, S., & Wardb, F. (2019). The impact of the environment on South Africa’s child and adolescent health: An overlooked health risk. *South African Child Gauge*, October.
- Rupiasih, N. N. (2016). A Review : Compositions , Structures , Properties and Applications of Humic Substances. *Journal of Advances in Science and Technology*, 8(June 2005), 16–25.
- SA News. (2019). Mzimvubu project to improve water supply, create jobs / SA News. <https://www.sanews.gov.za/south-africa/mzimvubu-project-improve-water-supply-create-jobs>
- SABS Standards Division. (2015). SANS 241-1 : 2015 South African National Standard. SABS.  
<https://store.sabs.co.za/catalog/product/view/id/2135761/s/sans-241-1-2015-ed-2-00/>
- Sandhu, H. K., & Dasaroju, G. (2010). Preparation and characterization of nanofluids and some investigation in biological applications. *Thapar University*. <https://doi.org/10.13140/RG.2.1.3485.7442/1>
- Sanganyado, E., & Kajau, T. A. (2021). The fate of emerging pollutants in aquatic systems: An overview. In *Emerging Freshwater Pollutants*.  
<https://doi.org/https://doi.org/10.1016/B978-0-12-822850-0.00002-8> 3
- Shepherd, P. J. (2013). Fundamentals of Thermodynamics. In *A Course in Theoretical Physics*. Wiley. <https://doi.org/10.1002/9781118516911.ch5>
- Shirazi, S., Lin, C., & Chen, D. (2010). Inorganic Fouling of Pressure-Driven Membrane Processes - A Critical Review. *Desalination*, 250(2010), 236–248.  
<https://doi.org/doi:10.1016/j.desal.2009.02.056>

- Sridhara, V., & Satapathy, L. N. (2011). Al<sub>2</sub>O<sub>3</sub>-based nanofluids : a review. *Nanoscale Research Letters*, 6(1), 456. <https://doi.org/10.1186/1556-276X-6-456>
- Stats SA. (2019). Mid-year population estimates. *Statistics South Africa*. <https://www.statssa.gov.za/publications/P0302/P03022019.pdf>
- Stein, W. H., & Buck, R. (2017). Advanced power cycles for concentrated solar power. *Solar Energy*, 152, 91–105. <https://doi.org/10.1016/j.solener.2017.04.054>
- Stout, G. E. (1990). Climate and water. In *Eos, Transactions American Geophysical Union* (Vol. 71, Issue 12). <https://doi.org/10.1029/90EO00112>
- Stuart, M., & Lapworth, D. (2013). Emerging Organic Contaminants in Groundwater. In *Smart Sensors for Real-Time Water Quality Monitoring* (pp.259-284) [https://doi.org/10.1007/978-3-642-37006-9\\_12](https://doi.org/10.1007/978-3-642-37006-9_12)
- Swartz, C. D. (2009). A Planning Framework to Position Rural Water Treatment in South Africa for the Future. *Water Research Commission*.
- Thoola, M. I. (2014). Performance characteristics of Bio-ultrafiltration on local surface waters. *Durban University of Technology*. <https://openscholar.dut.ac.za/handle/10321/1385>
- Timmer, J. M. (2001). Properties of nanofiltration membranes : model development and industrial application. *Eindhoven University of Technology*. <https://doi.org/10.6100/IR545659>
- Tiwari, G. N., Tiwari, A., & Shyam. (2016). Solar Water-Heating Systems Á Natural circulation Á Forced circulation Á Heat (Issue i). <http://link.springer.com/10.1007/978-981-10-0807-8>
- Tran, T. H., & Nguyen, V. T. (2014). Copper Oxide Nanomaterials Prepared by Solution Methods , Some Properties, and Potential Applications : A Brief Review. *International Scholarly Research Notices*. <https://doi.org/http://dx.doi.org/10.1155/2014/856592>
- Ugwuishi, B. O., Owoh, I. P., & Udom, I. J. (2016). Solar energy applicationn in waste treatment - A review. *Nigerian Journal of Technology*, 35(2), 432–440.

<http://dx.doi.org/10.4314/njt.v35i2.27>

Varkey, A. J. (2012). Point-of-use water purification using clay pot water filters and copper mesh. *Water SA*, 38(5), 721–726.

<https://doi.org/http://dx.doi.org/10.4314/wsa.v38i5.10>

Verlicchi, P., & Grillini, V. (2019). Surface and Groundwater Quality in South African Area—Analysis of the Most Critical Pollutants for Drinking Purposes. *Proceedings*, 48(1), 3. <https://doi.org/10.3390/ecws-4-06430>

Verlicchi, P., & Grillini, V. (2020). Surface Water and Groundwater Quality in South Africa and Mozambique — Analysis of the Most Critical Pollutants for Drinking Purposes and Challenges in Water Treatment Selection. *Water*, 12(305). <https://doi.org/10.3390/w12010305>

Wakeel, M., Chen, B., Hayat, T., Alsaedi, A., & Ahmad, B. (2016). Energy consumption for water use cycles in different countries : A review. *Applied Energy*, 178(19), 868–885. <https://doi.org/10.1016/j.apenergy.2016.06.114>

Wanda, E., Nyoni, H., Mamba, B., & Msagati, T. (2017). Occurrence of Emerging Micropollutants in Water Systems in Gauteng, Mpumalanga , and North West Provinces, South Africa. *International Journal of Environmental Research and Public Health*, 14(79). <https://doi.org/10.3390/ijerph14010079>

Wang, F., & Tarabara, V. V. (2008). Pore blocking mechanisms during early stages of membrane fouling by colloids. *Journal of Colloid and Interface Science*, 328(2), 464–469. <https://doi.org/10.1016/j.jcis.2008.09.028>

Wang, H., Li, H., Wang, L., & Bu, X. (2017). Thermodynamic Analysis of Organic Rankine Cycle with Hydrofluoroethers as Working Fluids. *Energy Procedia*, 105, 1889–1894. <https://doi.org/10.1016/j.egypro.2017.03.554>

Wang, S., Wang, Z., Xia, J., & Wang, X. (2021). Polyethylene-supported nanofiltration membrane with in situ formed surface patterns of millimeter size in resisting fouling. *Journal of Membrane Science*, 620, 118830. <https://doi.org/10.1016/j.memsci.2020.118830>

Warrier, P., & Teja, A. (2011). Effect of particle size on the thermal conductivity of nanofluids containing metallic nanoparticles. *Nanoscale Re*, 6(247), 1–6.

<http://dx.doi.org/10.1186/1556-276X-6-247>

- Wend, C. F., & Camper, A. K. (2003). Pre-treatment for membrane water treatment systems a laboratory study. *Water Research* 37, 3367–3378.  
<http://citeseerx.ist.psu.edu/viewdoc/download?doi=10.1.1.598.222&rep=rep1&type=pdf>
- Wenten, I. G. (n.d.). Membrane in water and wastewater treatment. *Institut Teknologi Bandung*.
- WHO. (2007). Physical removal processes: sedimentation and filtration. *World Health Organisation*.  
[https://www.who.int/water\\_sanitation\\_health/dwq/WSH02.07\\_5.pdf](https://www.who.int/water_sanitation_health/dwq/WSH02.07_5.pdf)
- WHO. (2011). Emergency treatment of drinking-water at the point of use. *World Health Organisation*.  
[https://www.who.int/water\\_sanitation\\_health/publications/2011/WHO\\_TN\\_05\\_Emergency\\_treatment\\_of\\_drinking\\_water\\_at\\_the\\_point\\_of\\_use.pdf?ua=1](https://www.who.int/water_sanitation_health/publications/2011/WHO_TN_05_Emergency_treatment_of_drinking_water_at_the_point_of_use.pdf?ua=1)
- Wu, D., Zhu, H., Wang, L., & Liu, L. (2009). Critical issues in nanofluids preparation, characterization, and thermal conductivity. *Current Nanoscience*, 5, 103–112. <http://dx.doi.org/10.2174/157341309787314548>
- Xia, S., Nan, J., & Liu, R. (2004). Study of drinking water treatment by ultrafiltration of surface water and its application to China. *Desalination*, 170, 41–47.  
<https://doi.org/10.1016/j.desal.2004.03.014>
- Yu, W., & Xie, H. (2012). A Review on Nanofluids : Preparation , Stability Mechanisms , and Applications. *Journal of Nanomaterials*.  
<https://doi.org/10.1155/2012/435873>
- Zereffa, E. A., Bekalo, T. B., Program, C., Science, A., & Science, C. (2017). Clay Ceramic Filter for Water Treatment. *Materials Science and Applied Chemistry*, 34(May), 69–74. <https://doi.org/10.1515/msac-2017-0011>
- Zhang, Y., Sivakumar, M., Yang, S., Enever, K., & Ramezaniapour, M. (2018). *Application of solar energy in water treatment processes : A review* [University of Wollongong]. <https://ro.uow.edu.au/eispapers1/841>
- Zhu, D., Wang, L., Yu, W., & Xie, H. (2018). Intriguingly high thermal conductivity

increment for CuO nanowires contained nanofluids with low viscosity.

*Scientific Reports*, 1–12. <https://doi.org/10.1038/s41598-018-23174-z>

Zhuwakinyu, M. (2012). *Water 2012*. A review of South Africa's water sector.

*Powertech*. <https://pmg.org.za/files/120904review.pdf>

## CHAPTER 3

### EXPERIMENTAL METHODOLOGY

---

#### 3.1 Introduction

In this chapter all the materials, general methods, and characterization techniques used in this study are detailed. It is divided into several sections which include, membrane preparation, characterization, and evaluation of the membranes, as well as the preparation and characterization of nanoparticles.

#### 3.1 Reagents and materials

All chemicals used in this study were of analytical grade and no further purification was done on any of the reagents. Commercial NF270 membrane coupons were used in this study together with UF membrane coupons that were prepared through the phase inversion method using a custom method developed in a previous study. Polyether sulfone (PES) (Solvay Specialty Polymers, USA) was used as the polymer, poly(ethylene glycol) (PEG) (Bio Ultra 400 Sigma-Aldrich, Germany) as the pore former and membrane modifier to increase hydrophilicity, Hirose non-woven support, 1-methyl-2-pyrrolidone (NMP) anhydrous 99,5% (Sigma-Aldrich, Germany) as the solvent, and deionized water (H<sub>2</sub>O) from a Milli- Q Elix Integral 10 Water purification system (Merck Millipore, United States) as the non-solvent in the UF membrane phase inversion method. PEG (400Da; 1,5kDa; 6kDa and 10kDa) (Sigma-Aldrich, Germany), and Sodium Iodide (Promark Chemicals, South Africa) were used in the determination of Molecular Weight Cut-Off (MWCO) of the membranes. Humic acid (Aldrich Chemistry, Switzerland) and Bovine Serum Albumin (Sigma-Aldrich, USA) were used in separation, rejection, and fouling tests on the membrane coupons. NaOCl Bleach (Reckitt Benckiser, South Africa) was used for the chemical cleaning of the membranes. Preparation of the nanoparticles was done using copper (II) chloride (97% Aldrich Chemistry, United Kingdom) and cuprous chloride (Associated Chemical Enterprises, Johannesburg, South Africa) as copper oxide precursors, sodium hydroxide (Promark Chemicals, Robertsham, South Africa) as a precipitating agent, and hydrochloric acid (37%, Sigma-Aldrich)



to regulate pH. The nanofluids were prepared using copper oxide nanoparticles, sodium Dodecyl Sulfate ( $\geq 98.5\%$  GC, Sigma-Aldrich, Japan) and tri-sodium citrate (Saarchem PTY LTD, Krugersdorp, RSA) as surfactants, as well as the pure working liquid (95% UL, Ultrafine Limited, London, United Kingdom) and deionized water from a Milli- Q Elix Integral 10 Water purification system (Merck Millipore, United States) used as base fluids.

### 3.2 Membrane preparation

The ultrafiltration membrane used in this study was previously prepared in another study and was chosen for this study because of its promising performance in terms of water flux ( $568,66 \text{ L} \cdot \text{m}^{-2} \cdot \text{h}^{-1}$ ) and rejections of BSA, HA, and Acid blue dye of 88,06%, 68,89%, and 22,47%, respectively (Unpublished work). The PES polymer was used due to its good thermal and chemical properties (Wen *et al.*, 2022). The membranes were prepared using a phase inversion method that is represented graphically in **Figure 3.1**. An excess amount of PES was dried in the oven at  $120^\circ\text{C}$  for 12 h to remove moisture. The dry polymer was then allowed to cool down in a desiccator and the membrane dope solution was prepared with the following composition: 20 wt.% PES, 44wt.% NMP and 36 wt.% PEG. The mixture was then continuously stirred using an overhead stirrer at approximately  $60^\circ\text{C}$  for at least 14 hours at 350 rpm to ensure complete dissolution of the polymer. The dope solution was then allowed to cool to room temperature in a tightly closed container that was kept standing overnight to completely degas. A casting knife and a glass plate were then used to cast the solution before immersion of the plate into a coagulation bath containing 15 vol.% NMP and 85 vol.% water. The prepared membranes were then kept in ultra-pure water at  $4^\circ\text{C}$  before characterization and filtration studies. A commercial nanofiltration membrane (NF270) was also used in the study for comparison on performance against the UF membrane on the solar-driven filtration system. This membrane has reported values for permeability of  $11.3 \pm 1.0 \text{ L/hm}^2 \text{ bar}$  (May *et al.*, 2021) and MWCO of 200 g/mol (Cabrera-González *et al.*, 2022).



**Figure 3.1:** Graphical representation of the preparation of the UF PES membranes using the phase inversion method.

### 3.2.1 Membrane characterization

The membranes were characterized using Scanning Electron Microscopy, Atomic Force Microscopy, Drop Shape Analysis, Thermogravimetric analysis, and Fourier Transform Infrared Spectroscopy. The characterization techniques are discussed in further detail in the following sections.

### 3.2.2 Scanning Electron Microscopy

The morphology of the flat sheet membranes (clean and fouled) was studied using scanning electron microscopy (Jeol IT300 Tokyo, Japan). Small pieces of dry PES membrane coupons were fractured in liquid nitrogen and affixed onto the sample stubs. The membrane coupons were freeze fractured in liquid nitrogen (Xie *et al.*, 2020) to preserve the structure of the cross-section from deformation thus allowing it to be observed on the SEM micrograph in its unaltered state. A Quorum Q150R ES (United Kingdom) coating machine was used to coat the samples using gold. An Energy Dispersive Spectroscopy (EDS) accessory with a Silicone detector was also used to determine the elemental composition of the samples.

### 3.2.3 Atomic Force Microscopy

The topology and roughness measurements of the membranes were analysed using an Alpha 300 atomic force microscope, (WiTec Innovations, Germany). Small pieces of dry PES and NF270 membranes were cut and affixed to a glass substrate. Membrane scan areas of 25  $\mu\text{m}$  x 25  $\mu\text{m}$  were analysed on the instrument using non-contact imaging mode which provides a higher atomic resolution through the minimization of surface alteration (Figoli *et al.*, 2017). Similar scan areas were taken for all membranes to allow for comparability as the roughness measurements change with changing scan sizes due to changes in spatial wavelength and fractal structure formation on the membrane's surface (Dach, 2009).

### 3.2.4 Wettability measurements.

Wettability is defined as the tendency of two materials (one solid and one liquid) to remain in contact with each other (Yu & Xie, 2012b) through a balance of intermolecular forces at the solid-liquid interface. Contact angle measurements were used to determine the degree of the membrane's surface wettability. PES and NF270 membrane coupons were dried overnight in an oven set to 40°C before affixing small pieces of these membranes on glass slides using double sided adhesive tape. The sessile drop method was then used on a Kruiss Drop Shape Analyzer (DSA30, Hamburg, Germany), to determine the contact angles and surface free energies of the membranes. In each water contact angle analysis, 2  $\mu\text{l}$  droplets of ultrapure water were dropped onto the flat membrane surfaces and angle measurements were immediately taken. Determination of surface free energies of the membranes were done using the contact angles of ultrapure water, diiodomethane and glycerol. The Owens-Wendt-Rabel & Kaelble (OWRK) model was then used to calculate the surface free energy values for each membrane analysed. To reduce experimental error, at least 10 measurements were taken for each liquid, and the average value was reported as the contact angle.

### 3.2.4.1 Owens-Wendt-Rabel & Kaelble (OWRK) Model

The OWRK model requires the use of at least two solutions that account for dispersive and polar properties needed in the calculation. Polar liquids like water and glycerol, and dispersive liquids like diiodomethane and  $\alpha$ -bromonaphthalene are often utilized in contact angle measurements for surface free energy determinations using this model (Biolin Scientific, 2014). **Equation 3.1** shows the OWRK model in the linearized form of  $y=mx + c$ .

$$\frac{\sigma_l(\cos\theta+1)}{2\sqrt{\sigma_l^D}} = \left(\sqrt{\sigma_s^D}\right) \frac{\sqrt{\sigma_l^P}}{\sqrt{\sigma_l^D}} + \sqrt{\sigma_s^D} \quad \text{Equation 3.1}$$

Where:  $\sigma_l$  is the surface energy of the liquid,  $\sigma_l^D$  is the dispersive component of the liquid,  $\sigma_s^D$  is the dispersive component of the solid,  $\sigma_s^P$  is the polar component of the solid,  $\sigma_l^P$  is the polar component of the liquid, and  $\theta$  is the contact angle of the liquid on the solid.

The contact angle values of the different liquids are then used to develop a graph shown in **Figure 3.2**. The graph has a slope equal to  $\sqrt{\sigma_s^P}$  and y intercept equal to  $\sqrt{\sigma_s^D}$ .

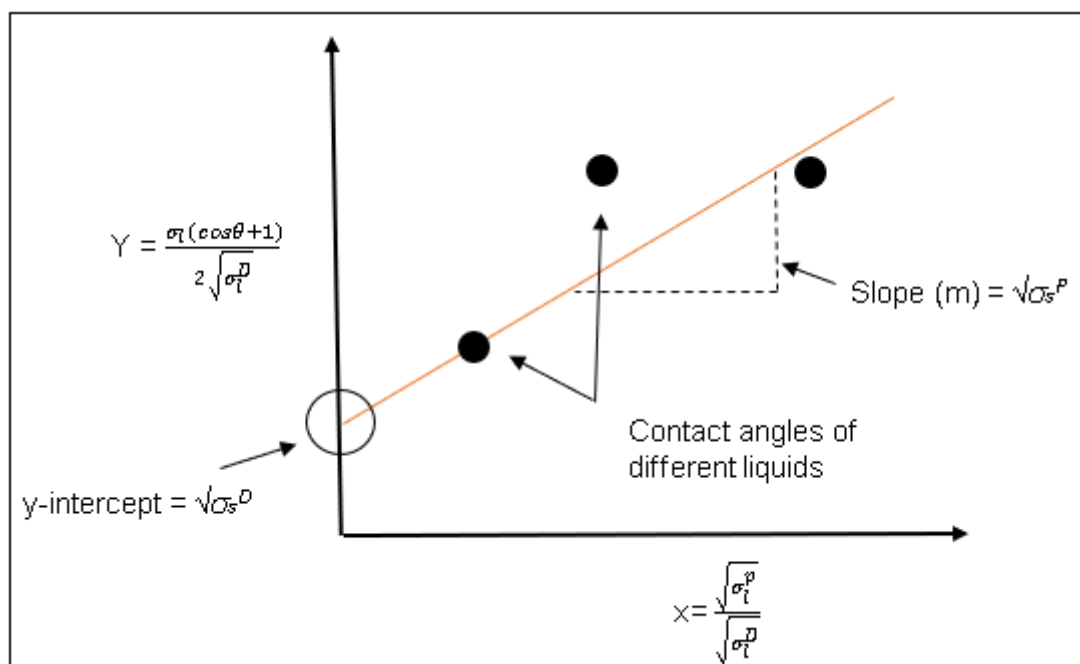


**Figure 3.2:** Graphical representation of a plot used in the determination of the surface free energy using the OWRK model (Spooner, 2007).

To calculate the surface free energy (SFE) of the solid surface, **Equation 3.2** is then used, taking the values from **Figure 3.2**.

$$\sigma_s = \sigma_s^D + \sigma_s^P \quad \text{Equation 3.2}$$

Where  $\sigma_s^D$  and  $\sigma_s^P$  are the dispersive and polar components of the surface energy of the solid, respectively.

### 3.2.5 Thermal stability of the membranes

Thermal degradation of the prepared membrane was studied using thermogravimetric analysis (TA Discovery TGA 5500, New Castle, USA.) A small piece (~10 mg) of the PES membrane was air-dried, and its thermal degradation properties were analysed on a TGA instrument without any sample preparation. The sample was heated from 30°C to 800°C at a heating rate of 10°C/min in air. The

analysis was done in a reaction atmosphere with air to allow for the analysis of the oxidation of the polymeric membranes.

### 3.2.6 Membrane surface functionality

Membrane surface functionality was determined using a Fourier transform infrared spectrometer (Perkin Elmer, USA) in the mid-IR ( $400\text{cm}^{-1}$  -  $4000\text{cm}^{-1}$ ) spectrum range. Surface properties affect fouling and cleaning efficiency as foulants may interact with various functional groups on the surface of the membrane thereby altering the degree of fouling or fouling reversibility (Servos *et al.*, 2014). A small piece of the membrane was dried in an oven at  $40^{\circ}\text{C}$  for 24 hours, placed on the instrument and a background scan was run first, followed by a scan from 650 to  $4000\text{cm}^{-1}$  wavenumbers at a resolution of  $4\text{cm}^{-1}$  with 4 scans.

### 3.3 Membrane filtration studies

All filtration studies were done using a dead-end filtration unit (Sterlich Corporation P/N HP4750, U.S) shown in **Figure 3.3** with an effective membrane coupon permeation area of  $1,453 \times 10^{-3} \text{ m}^2$  and a capacity of 300ml. The filtration studies were done to determine the permeation properties of the membrane.

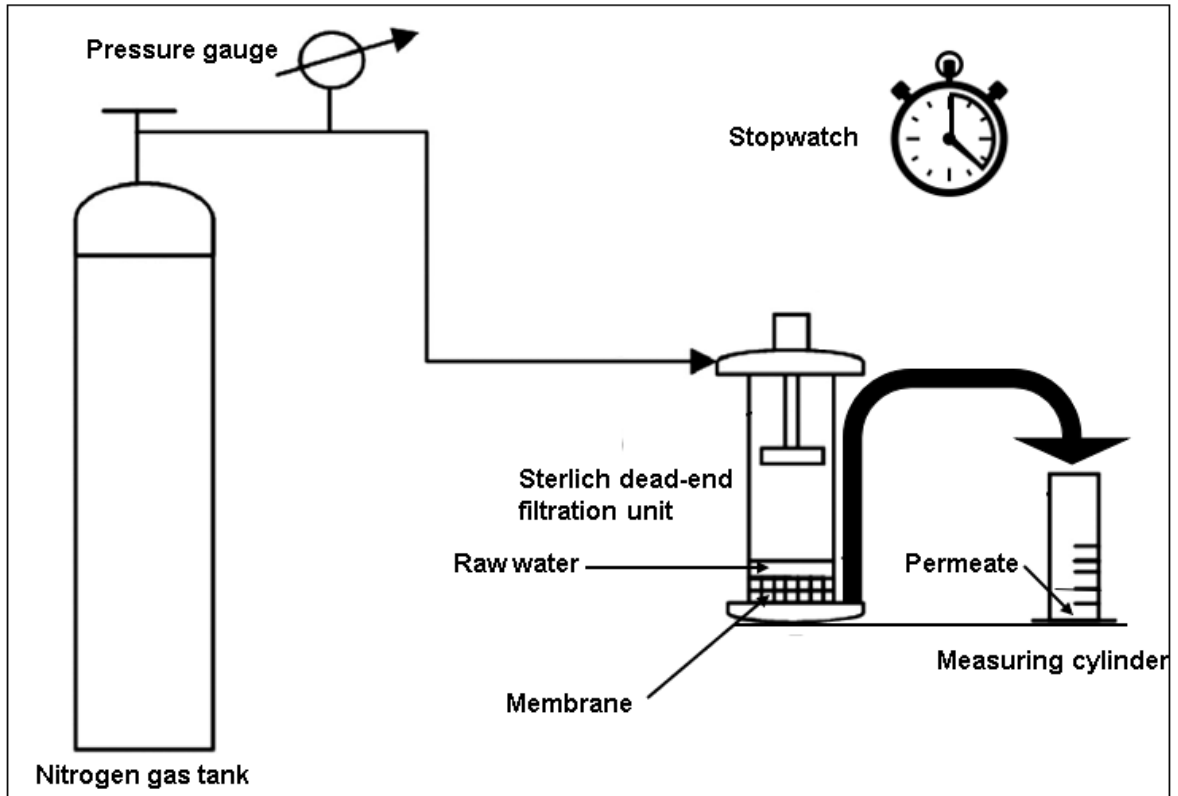


**Figure 3.3:** Schematic representation of the filtration apparatus used in the performance tests of the membranes.

Membrane coupons were pre-compacted at 6 bars of transmembrane pressure using deionized water and the flux measurements were taken 10-minute intervals until a constant flux reading was reached. A higher pre-compaction pressure (6 bars) was used than the operating pressure (2 bars) to reduce the impact of compaction during filtration on transmembrane pressure drop (Saha & Das, 2015) and membrane pore structure alteration that leads to flux decline (Dang *et al.*, 2006). The membrane flux at the pre-compaction pressure was calculated using **Equation 3.3**.

$$J_w = \frac{V}{A_m \Delta t} \quad \text{Equation 3.3}$$

Where:  $J_w$  is the pure water flux,  $V$  is the permeate volume,  $\Delta t$  is the permeation time, and  $A_m$  is the surface area of the membrane.

The pre-compaction studies were repeated three times with three different membrane coupons for each membrane type, i.e., UF and NF, and the minimum time for attainment of constant flux for each membrane was noted. All membrane coupons were then pre-compacted for the minimum time before use in the following studies.

Measurements of the pure water permeability coefficients of the membranes were then done by varying the transmembrane pressure between 1 to 6 bars in one-hour intervals using compressed nitrogen for the driving pressure and deionized water as the feed in dead-end filtration setup. The steady state membrane fluxes at each transmembrane pressure were calculated using **Equation 3.3**. The pure water permeability coefficients of the membranes were then determined from a graph of transmembrane pressure against flux, with a mathematical description shown in **Equation 3.4**.

$$A = \frac{J_w}{(\Delta P - \Delta \pi)}$$

**Equation 3.4**

Where  $\Delta P$  is the change in the transmembrane pressure,  $\Delta \pi$  is the osmotic pressure, and  $A$  is the pure water permeability coefficient.

The water uptake values of the membranes were determined by a gravimetric method. Membrane coupons were first dried in an oven at 40°C for 24 hours then three dry membrane coupons with an area of 3 cm x 3 cm each, were cut and weighed on an analytical mass balance for each membrane type (UF and NF). The membrane coupons were then put in deionized water overnight then patted in-between paper towels to remove excess water and re-weighed. The membrane's water uptake was then calculated using **Equation 3.5** and the average of each set of results was taken as the membrane's % water uptake value to minimize experimental errors.

$$\text{Water uptake (\%)} = \frac{W_w - W_d}{W_w} \times 100 \quad \text{Equation 3.5}$$



Where:  $W_w$  is the weight of the wet membrane and  $W_d$  is the weight of the dry membrane.

The overall porosities of the membranes were determined through gravimetry and the results for the wet and dry measurements from the membrane water uptake results were used in this measurement. The thickness ( $l$ ) of the dry membranes was measured using an external digital micrometer (0-25 mm/0-1, RS PR, UK) and the average of six measurements was taken as the thickness of each membrane coupon. The overall porosity of each membrane was then calculated using **Equation 3.6**.

$$\varepsilon = \frac{w_1 - w_2}{Al\rho_w} \quad \text{Equation 3.6}$$

Where  $\varepsilon$  is the overall porosity,  $w_1$  is the weight of the wet membrane;  $w_2$  is the weight of the dry membrane;  $A$  is the membrane effective area (m),  $\rho_w$  is the water density (998kg/m<sup>3</sup>at 25°C) and  $l$  is the thickness (m).

The average pore sizes of the membranes were then calculated through filtration tests and incorporated the calculated overall porosities. Membrane coupons of the UF and NF membranes were cut and placed in the dead-end filtration apparatus and deionized water was used as the feed solution in the filtration test operated at a transmembrane pressure of 2 bars. The permeate volumetric flow rate ( $Q$ ) was then calculated using **Equation 3.7**.

$$Q = \frac{V}{t} \quad \text{Equation 3.7}$$

Where:  $Q$  is the permeate volumetric flow rate (m<sup>3</sup>/s),  $V$  is the volume of permeate (m<sup>3</sup>) collected and  $t$  is the filtration time in seconds.

The Guerout-Elford-Ferry equation shown in **Equation 3.8** was then used to calculate the average pore size ( $r_m$ ) of the membranes (Mahdi et al., 2019) using the previously determined values of overall porosity, membrane thickness and permeate volumetric flow rate.

$$r_m = \sqrt{\frac{(2,9-1,75\varepsilon).8\eta lQ}{\varepsilon A \Delta P}} \quad \text{Equation 3.8}$$

Where:  $\eta$  is the water viscosity ( $8.9 \times 10^{-4}$  Pas at 25 °C), and  $\Delta P$  is the transmembrane pressure (Pa) which was 200kPa (2bars) in the analysis.

The determination of the MWCO of the membranes was then done using a colorimetric method (Izzati *et al.*, 2017). Polyethylene glycol solutions of different molecular weights (400kDa; 1,5kDa; 6kDa; 10kDa) at a concentration of 100ppm, were prepared and filtered through membrane coupons. A 100ppm solution of sodium iodide (NaI) was then prepared and 8ml of this solution was pipetted into 2ml aliquots of the membrane permeate collected at recoveries from 10% to 90% of the feed solution. The solutions were then shaken and left to stand for 30 minutes before reading on a Uv-Vis spectrometer (Lambda 650 S, Perkin Elmer, United States of America) at a wavelength of 203 nm. Prior to analysis, the spectrometer was calibrated using standards prepared from the NaI stock solution (100ppm) in the concentration range of 25ppm to 100ppm with deionized water being used as the blank solution. The solute rejections for each PEG solution used, were calculated using the **Equation 3.9** after performing back calculations to determine the concentrations of the PEG in the permeate aliquots taken at different recoveries.

$$\%R = \left(1 - \frac{C_p}{C_f}\right) \quad \text{Equation 3.9}$$

Where R is the solute rejection,  $C_p$  is the permeate concentration and  $C_f$  is the feed concentration.

The MWCO was then taken to be the smallest molecular weight of the substance that had at least a 90% rejection for each membrane.

### 3.4 Surface water studies

#### 3.4.1 Sampling sites and sample collection

Real water samples were collected from two surface water bodies, i.e., Florida Lake ( $26^{\circ}10'38.6''\text{S}$   $27^{\circ}54'14.6''\text{E}$ ) and Florida Stream ( $26^{\circ}09'34.4''\text{S}$   $27^{\circ}54'22.8''\text{E}$ ) in Florida, Johannesburg. The satellite and horizontal images of these sampling sites are shown in **Figure 3.4**. Sampling was achieved by simple immersion and overflowing the sampling bottles, then immediately, tightly closing the cap. The sample glass bottles were placed in a light-proof and thermally insulated container with ice to allow for rapid cooling. Samples were kept at temperatures below  $10^{\circ}\text{C}$  while transporting to the laboratory and at  $4^{\circ}\text{C}$  in storage at the UNISA CSET laboratory in Florida, Johannesburg.



**Figure 3.4:** Satellite (A and B) and horizontal (A1 and B1) images of the Florida Lake and Florida Stream sampling sites, respectively.

### 3.4.2 Sample analyses

The real water samples were immediately analysed for their physico-chemical properties (pH, TDS, Turbidity and Electroconductivity) after sample collection. Other parameters such as organic and inorganic elemental analyses were determined within a period not exceeding 24 hours after sample collection.

The temperature of all water samples was first equilibrated to room temperature then the chemical composition of the samples were determined using the following instruments: ICP Mass Spectrometer NexION 350D (Perkin Elmer, United States of America) for inorganic elemental composition, TOC Teledyne Tekmar Fusion UV/Persulfate Analyser (United States of America) for Dissolved Organic Carbon (DOC), Uv-Vis Lambda 650 S (Perkin Elmer, United States of America) for organic analysis, and FEEM (Aqualog Horiba with UV-800, Jobin Yvon Technology, USA) for the determination of the nature of the organics within the water samples. All raw water samples and humic acid samples were first filtered through a 0,45 µm glass fibre filter before analysis for DOC as the DOC of a sample is represented by the Total Organic Carbon (TOC) which is not filtered out by a 0,45 µm filter (Carifio, 2016).

The Uv-Vis spectrometer was run using method settings that included, a wide scan (600 – 200 nm), slit width of 2nm, data interval of 1nm, and scan speed of 266,75 nm/min. The sample was analysed in a 1cm quartz cuvette. Fluorescence EEMs were taken in the 200 nm to 600 nm excitation wavelength range with a 2nm increment, and 248.58 to 830.59 nm emission wavelength with a 3,28 nm increment interval. The FEEM intensities were calibrated using Raman water standard at a wavelength of 350 nm in the emission wavelength interval set for the instrument before sample analysis. The FEEM data treatment included normalization to Quinine Sulfate Units (QSU), applying inner-filter effects, and Rayleigh 1<sup>st</sup> and 2<sup>nd</sup> order settings at an order of 14 nm.

Metal species in the water samples were identified using an inductive coupled plasma – mass spectrometry instrument (NexION 350D (Perkin Elmer, United States of America)). The operational parameters set on the ICP-MS instrument are listed in **Table 3.1**. Calibration standards for the instrument were made using serial dilutions from a 100-ppm commercial standard to make 5 working standards in the range 0 to 1 ppm. The calibration standards were then acidified using nitric acid to 10 %w/w nitric acid before adding the dilution volumes of deionized water to bring the volume to 10ml for each standard using micropipettes. The acidification with nitric acid was done to keep the metallic ions in dissolved in solution during analysis. These standards were used to calibrate the instrument and the samples were analysed for the following elements: Fe, Pb, Cr, Co, Ca, Ni, Cu, Ti, Mn, Mg, V, and Cd.

**Table 3.1:** ICP-MS instrument operational parameters used in metallic analysis of water.

Parameter	ICP-MS
RF power, W	1500
Plasma gas flow rate, Lmin <sup>-1</sup>	17
Auxiliary gas flow rate, Lmin <sup>-1</sup>	1.2
Carrier gas flow rate, Lmin <sup>-1</sup>	0.92
Scan/ reading	50
Replicates	3
Detector	Dual
Cones sampler/ skimmer	Pt

Both raw water and membrane permeate samples were prepared by acidifying with nitric acid to form a sample concentration of 10 wt.% before analysis. to metallic ions

in solution. The concentrations of the analytes were then compared to the SANS 241: 2015 limits shown in **Table 3.2**.

**Table 3.2:** SANS 241: 2015 limits for some of the parameters analysed for drinking water.

Water quality parameter	SANS 241: 2015 limits
DOC (ppm)	-
UVA2254 (a.u)	-
SUVA (L/mg.m)	-
pH value at 25°C	≥5 to ≤ 9.7
Total Dissolved Solids at 180°C	≤1200
Electrical conductivity in mS/m at 25°C	≤170
Turbidity in N.T.U	≤1 (Operational) ≤5 (Aesthetic)
Iron as Fe (µg/ℓ)	≤ 2000 (Chronic Health) ≤300 (Aesthetic)
Lead as Pb (µg/ℓ)	≤10
Nickel as Ni (µg/ℓ)	≤70
Manganese as Mn (µg/ℓ)	≤400 (Chronic Health) ≤100 (Aesthetic)
Cadmium as Cd (µg/ℓ)	≤3
Chromium as Cr (µg/ℓ)	≤50
Cobalt as Co (µg/ℓ)	≤500
Copper as Cu (µg/ℓ)	≤2000
Vanadium as V(µg/ℓ)	≤200
Calcium (µg/l)	<150000 Aesthetic/Operational
Magnesium (µg/l)	<70000 Aesthetic/ Health

### 3.5 Membrane testing protocols.

#### 3.5.1 Membrane filtration with real and synthetic water samples

Real water samples from the Florida Lake were filtered through the membranes and the fluxes were determined over the filtration periods at a constant transmembrane pressure of 2 bars. Humic acid and BSA solutions with concentrations of 50ppm were also prepared and filtered through the membranes (UF and NF). The concentrations of the feed and filtrate solutions were measured by scanning the solutions at a wavelength of 254 nm and 280 nm for humic acid and BSA, respectively, on a Uv-Vis spectrometer (Lambda 650 S, Perkin Elmer, United States of America). The rejections of the BSA and humic acid solution at 50ppm concentrations were then calculated using **Equation 3.9**.

### 3.5.2 Membrane fouling and cleaning

The efficiency of backwashing and chemical cleaning in retaining flux was investigated by filtering real water samples through the membranes and periodically backwashing or chemically cleaning the membrane coupons when the normalized flux had reached 50%. Backwashing was performed by reversing the orientation of the membrane then continuing filtration in dead-end mode using deionized water for 30 minutes before returning the membrane to its normal configuration within the dead-end filtration apparatus. Chemical cleaning was done by taking out the fouled membrane from the dead-end filtration apparatus and soaking the membrane coupon for 30 minutes in a 0,35 vol% NaOCl solution prepared by using a commercial branded bleach solution. The membrane coupon was then rinsed with deionized water then placed back into the filtration apparatus and filtration tests were continued. The fluxes at the start of filtration and periodic intervals were noted down and the normalized fluxes were calculated. The cleaning efficiency of each chemical cleaning step was determined using Flux Recovery Ratio (FRR) that was calculated using **Equation 3.10**.

$$\text{FRR (\%)} = \frac{J_2}{J_1} \times 100 \quad \text{Equation 3.10}$$

Where:  $J_1$  is the initial pure water flux and  $J_2$  is the water flux after each chemical cleaning stage.

Fouling studies of the membrane were done through the Resistance in Series (RIS) model using Bovine Serum Albumin (BSA) as a model foulant. A 100 ppm BSA feed solution (pH = 8.49) was filtered through the membrane coupons at a transmembrane pressure of 4 bars for 2 hours. The transmembrane pressure was set to 4 bars to increase the flux to a measurable rate in the filtration time used for both membranes. The fluxes at different times were then determined, i.e., the pure water flux at 4 bars ( $J_w$ ), the steady-state flux of the BSA solution ( $J_{BSA}$ ), the pure water flux after 2 hours of fouling the membrane ( $J_{w2}$ ), and the flux of deionized water after fouling and backwashing the membrane ( $J_{w1}$ ) were noted down (Gebru & Das, 2017). The fouling resistances caused by the gel or cake layer formation on the membrane's surface (Nora *et al.*, 2017) and the pore constriction due to the adsorption of BSA on the membrane were then calculated using the Resistance In Series (RIS) model. The RIS model is used to estimate membrane resistances from changes in the flux at different membrane fouling stages (Shirazi *et al.*, 2010). The internal membrane resistance ( $R_m$ ) was calculated using Darcy's law shown in **Equation 3.11**.

$$R_m = \frac{TMP}{\mu \times J_w} \quad \text{Equation 3.11}$$

Where  $J_w$  is the initial pure water flux of the membrane before fouling tests,  $\mu$  is the viscosity of water at a given temperature ( $8.90 \times 10^{-4}$  Pa.s at 25°C), TMP is the Transmembrane pressure and  $R_m$  is the intrinsic membrane resistance ( $m^{-1}$ ).

The total resistance ( $R_T$ ) (Wirko *et al.*, 2019) was calculated using **Equation 3.12**.

$$J_{w2} = \frac{TMP}{\mu \cdot R_T} \quad \text{Equation 3.12}$$



Where:  $J_{w2}$  is the steady-state flux of the permeate through the membrane ( $\text{m}^3/(\text{m}^2.\text{s})$ ), and  $R_T$  is the total resistance ( $\text{m}^{-1}$ ).

The pure water flux after fouling ( $J_w$ ) and the intrinsic membrane resistances were used to calculate the resistance due to irreversible fouling using **Equation 3.13**.

$$R_{if} = \frac{\text{TMP}}{\mu J_{w1}} - R_M \quad \text{Equation 3.13}$$

Where  $R_{if}$  is the irreversible fouling resistance ( $\text{m}^{-1}$ ).

The total resistance can be calculated as the sum of all the membrane and fouling resistances as shown in **Equation 3.14**. As such, the reversible fouling ( $R_{rf}$ ) was then calculated by difference.

$$R_T = R_m + R_{rf} + R_{if} \quad \text{Equation 3.14}$$

Where:  $R_{rf}$  is the reversible fouling resistance ( $\text{m}^{-1}$ ).

The comparison of the fouling capacities of the different membranes was done using normalized flux ratios (NFR) which was calculated using **Equation 3.15**.

$$\text{NFR}(\%) = \left( \frac{J_{w2}}{J_{BSA}} \right) \times 100 \quad \text{Equation 3.15}$$

The predominant fouling mechanisms in the membranes were determined through fouling studies using 50 ppm humic acid synthetic water samples. Humic acid was used as a model foulant in the fouling mechanism determination. The humic acid samples were filtered through both the UF and NF membranes at a transmembrane pressure of 4 bars with the flux measurements being taken at 15-minute intervals until the normalized flux went below 50%. The fouling mechanism for each membrane (UF and NF) were then determined using the Hermas' fouling model (Wirko et al., 2019) that is based on the differential **Equation 3.16**.

$$\frac{d^2t}{dV^2} = k \left( \frac{dt}{dV} \right)^n$$

**Equation 3.16**

Where:  $V$  is the permeate volume per membrane surface area ( $m^3$ ),  $t$  is the filtration time (s),  $k$  is a phenomenological coefficient, and  $n$  is a general index corresponding to a specific fouling mechanism.

Depending on the value of  $n$ , four different fouling mechanisms can be identified by using the Hermas' fouling model. **Table 3.3** shows the different fouling mechanisms together with the linearized forms of each fouling mechanism.

**Table 3.3:** Fouling mechanisms dominant in membranes. Adopted from (Harivram *et al.*, 2019; Slimane *et al.*, 2019).

Fouling Mechanism	N	K (Hermia model constant)	Flux expression	Linearized form	Fouling concept
<b>Cake filtration</b>	0	$K_{cf}$	$J = \frac{J_o}{(2K_{cf}J_o^2t + 1)^{\frac{1}{2}}}$	$\frac{1}{J^2} = \frac{1}{J_o^2} + K_{cf}t$	Deposit formed on membrane surface
<b>Intermediate blocking</b>	1	$K_{ib}$	$J = \frac{J_o}{K_{ib}J_o t + 1}$	$\frac{1}{J} = \frac{1}{J_o} + K_{ib}t$	Pore blockage and deposit on surface
<b>Pore constriction</b>	1,5	$K_{pc}$	$J = \frac{4J_o}{\left(K_{pc}J_o^{\frac{1}{2}} + 2\right)^2}$	$\frac{1}{\sqrt{J}} = \frac{1}{\sqrt{J_o}} + K_{pc}t$	Pore constriction
<b>Complete blocking</b>	2	$K_{cb}$	$J = J_o \exp(-K_{cb}t)$	$\ln J = \ln J_o - K_{cb}t$	Pore blocking

### 3.5.3 Specific UltraViolet Absorbance (SUVA) and % Dissolved Organic Carbon (DOC) removal

Specific Ultraviolet Absorbance (SUVA) was used to evaluate the presence of both humic and non-humic substances (S. S. Marais et al., 2018) as well as to differentiate the nature of the Natural Organic Matter (NOM) within the water samples (Moyo *et al.*, 2020). SUVA values were calculated using **Equation 3.17**.

$$\text{SUVA} = \frac{\text{UV}_{254} (\text{cm}^{-1}) \times 100 \frac{\text{cm}}{\text{m}}}{\text{DOC} \left( \frac{\text{mg}}{\text{l}} \right)} \quad \text{Equation 3.17}$$

Where:  $\text{UV}_{254}$  is the absorbance of the sample at 254  $\text{cm}^{-1}$  wavelength and DOC is the Dissolved Organic Carbon of the sample.

SUVA can be used to differentiate the nature of NOM in water samples into three categories as shown in **Table 3.4**. (Moyo *et al.*, 2020). and this information was used to classify the NOM in the raw water and membrane permeate samples.

**Table 3.4:** Classification of NOM using SUVA values (Moyo *et al.*, 2020).

SUVA value range ( $\text{L} \cdot \text{mg}^{-1} \cdot \text{m}^{-1}$ )	Type of NOM
>4	Hydrophobic
2 – 4	Transphilic
<2	Hydrophilic

The % Dissolved Organic Carbon (DOC) removal was calculated using **Equation 3.18** and the DOC values of the raw water and membrane permeate samples.

$$\% \text{DOC removal} = \frac{\text{DOC}_f - \text{DOC}_p}{\text{DOC}_f} \times 100 \quad \text{Equation 3.18}$$

Where:  $\text{DOC}_f$  is the Dissolved Organic Carbon in the feed solution and  $\text{DOC}_p$  is the Dissolved Organic Carbon in the permeate.

### 3.6 Determination of the working volume of the prototype.

The minimum volume of the working fluid needed for the operation of the solar-driven pump was calculated using the volume of the working liquid chamber (0,440L) calculated from dimensions of the prototype shown in **Figure 3.5** and the expansion factor of the working liquid (208,23 L<sub>gas</sub>/L<sub>liquid</sub>) using **Equation 3.19**.

u

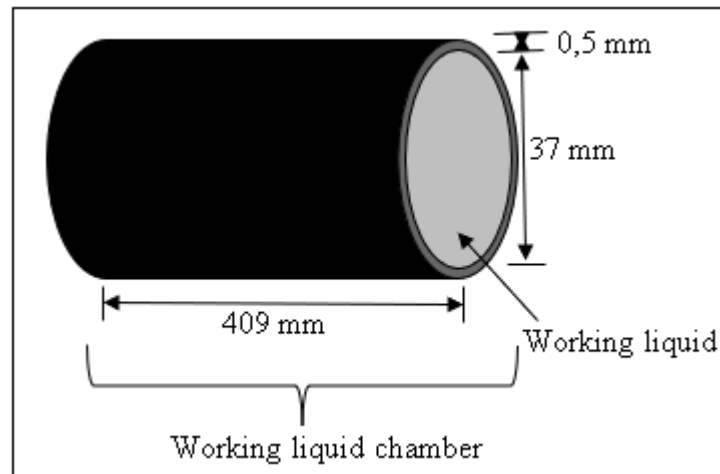


**Figure 3.5:** Dimensions of the working liquid chamber of the solar-driven system.

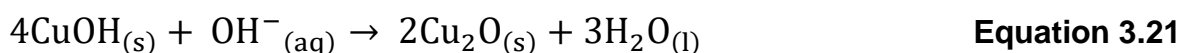
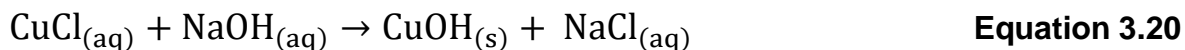
$$V_{\min, \text{wl}} = \frac{V_{\text{wc}}}{\text{Exp}_f} \quad \text{Equation 3.19}$$

Where:  $V_{\min, \text{wl}}$  is the minimum volume of working liquid,  $V_{\text{wc}}$  is the volume of the working liquid chamber, and  $\text{Exp}_f$  is the expansion factor of the pure working liquid.

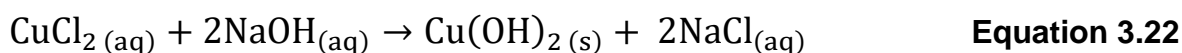
### 3.7 Synthesis of copper oxide nanoparticles.

Copper oxide nanospheres and nanorods were prepared through chemical precipitation and hydrothermal methods, respectively, using both Copper (I) chloride and Copper (II) chloride as copper precursors. During the chemical precipitation synthesis, drops of a 0.1 molar solution of sodium hydroxide were added to a 0,1-molar solution of the copper precursor solution with continuous stirring until the solution reached a pH of 11. The reaction of the greenish copper (I) chloride with

sodium hydroxide produced a yellowish intermediate solution of copper (I) hydroxide precipitate which is highly unstable and was oxidized at room temperature to form the brownish copper (I) oxide as shown in **Equations 3.20 and 3.21**.



The copper (I) oxide and  $\text{Cu}(\text{OH})_2$  precipitates were then washed with deionized water under vacuum filtration until the filtrate reached a neutral pH. The copper (I) oxide nanoparticles were then dried in an oven at 80°C for 12 hours before storing them in airtight containers. Before storage, the solid compound was reduced into a fine powder by grinding it using a pestle and mortar. On the other hand, the reaction of the blue copper (II) chloride with sodium hydroxide produced a black copper (II) hydroxide precipitate as shown in **Equation 3.22**.



The copper (II) hydroxide black precipitate was washed with deionized water under vacuum filtration then dried in an oven at 80°C for 12 hours. After this it was then calcined in a muffle furnace at 500 °C for 3 hours to produce copper (II) oxide nanoparticles as shown in **Equation 3.23** (Phiwdang *et al.*, 2013). The copper (II) oxide nanoparticles were then cooled, ground using a pestle and mortar then stored in air-tight containers.



The graphical representation of the chemical precipitation synthesis method that was used in the preparation of the copper (II) oxide nanoparticles is shown in **Figure 3.6**.

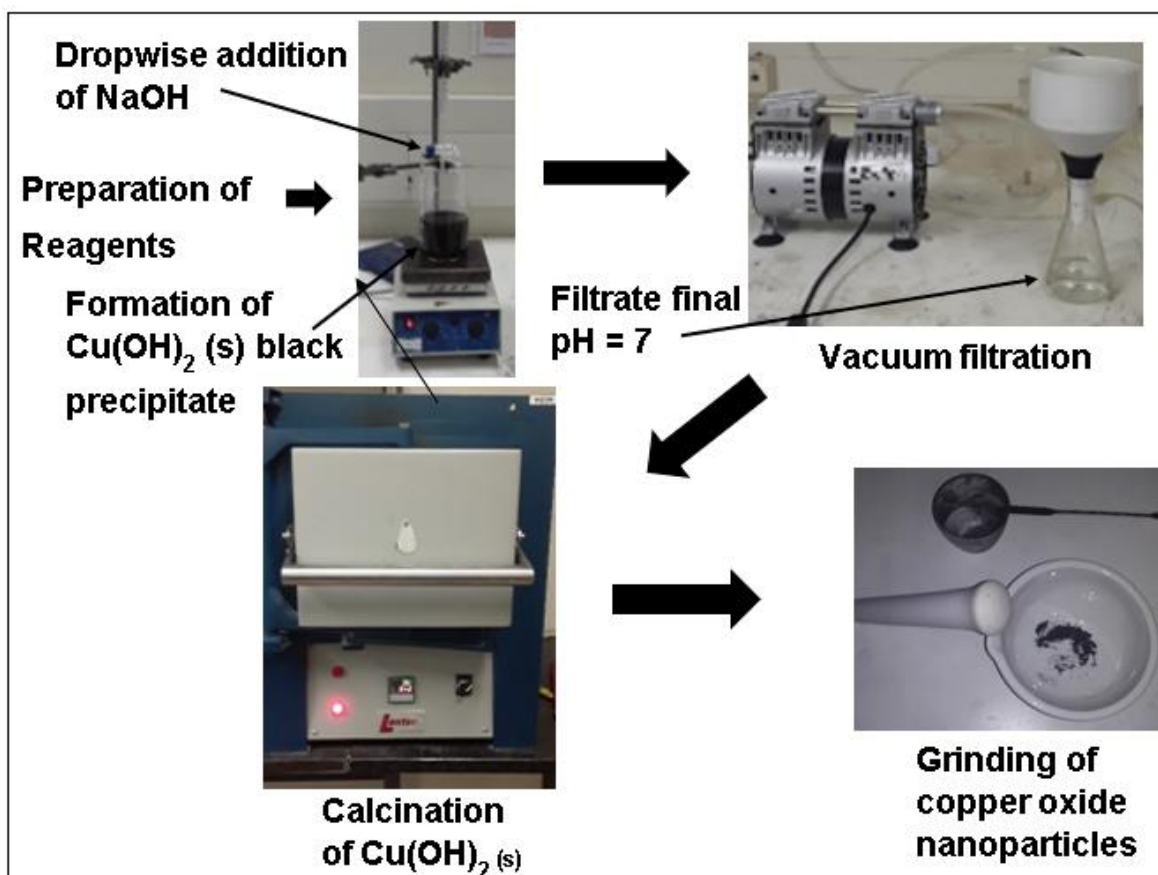


**Figure 3.6:** Graphical representation of the chemical synthesis used in the preparation of copper (II) oxide nanoparticles.

In the hydrothermal synthesis of the copper oxide nanoparticles, 0,45 g of trisodium citrate, was mixed separately with 0,50 g of each copper precursor. A 40ml aliquot of deionized water was then added to each of the mixtures then the mixture was stirred for 15 mins after which 0,24 g of sodium hydroxide was also added and stirring of the mixtures was continued for an hour. The solutions were then transferred into separate Teflon-lined autoclaves and heated in an oven at 140 °C for 24 hours (Shrestha *et al.*, 2010). The high temperature and pressure conditions in the autoclave led to the dissociation of water shown in **Equation 3.24** which then formed ions that hydrolysed the copper ions in solution (**Equation 3.25 and 3.26**). The copper hydroxide and copper di-hydroxide formed were then dehydrated to form copper (I) and copper (II) oxide nanoparticles, respectively, depending on the precursor used, as shown in **Equation 3.27** for the copper (II) chloride precursor and **Equation 3.28** for the copper (I) chloride precursor.



The copper oxide solutions were then repeatedly centrifuged and washed with deionized water until the supernatant reached neutral pH. The nanoparticles were then dried in an oven at 80°C for three hours, cooled, and ground in a pestle and mortar, then stored in separate airtight containers to avoid oxidation or absorption of atmospheric moisture. The graphical representation of the hydrothermal method used in the preparation of copper oxide nanoparticles is shown in **Figure 3.7**.

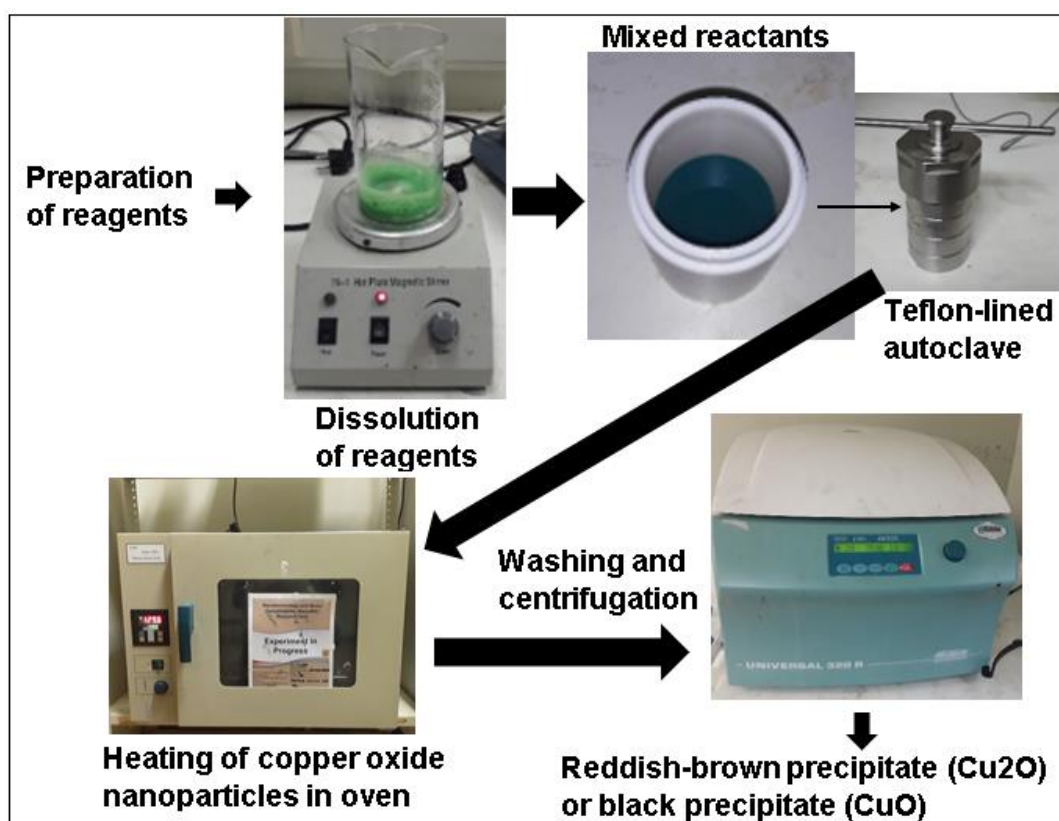


**Figure 3.7:** Graphical representation of the hydrothermal synthesis of copper oxide nanorods.

The yield of the nanoparticles produced in both methods was determined using **Equation 3.29**.

$$\% \text{Yield} = \frac{\text{Actual Yield}}{\text{Theoretical Yield}} \times 100 \quad \text{Equation 3.29}$$

### 3.7.1 Characterization of nanoparticles.

The morphology of the nanoparticles was investigated as detailed in **Section 3.2.2**. The samples were prepared by spotting glass slides with 0,1% w/w copper oxide nanofluid samples and drying in an oven. The surface functionality of the nanoparticles was determined as described in **Section 3.2.6**. The sample preparation involved mixing a small amount of the copper oxide nanoparticles with a small amount of potassium bromide (KBr) then grinding this mixture into a fine powder. The powder was then dried overnight in an oven at 110°C before making compressing it into a pellet. A background scan was first completed before scanning the pellet on the instrument in the range of 450 cm<sup>-1</sup> to 4000 cm<sup>-1</sup>.

The size and surface charge (zeta potential) of the nanomaterials were analysed using a Zeta sizer (Malvern Zeta sizer nano range, United Kingdom). Samples of the nanoparticles were dispersed in water to form nanofluids with 0,1% w/w copper oxide concentrations. These samples were transferred into DTS0012 disposable cuvettes to measure the sizes of the CuO nanoparticles using the dynamic light scattering method with a 173° Backscatter angle using the Non-Invasive Backscatter (NIBS) default setting. The average value of three repeated measurements was reported as the mean diameter of the nanoparticles in each sample that was analysed. For surface charge, a dip cell (DTS1070, Malvern instruments) was used, and this was filled with the nanofluid making sure that there were no air gaps in the cell. The Smoluchowski model was used to evaluate the zeta potentials of the suspended copper oxide nanoparticles in each nanofluid at 25°C. Both size and surface zeta potential were measured using automatic measurement duration and an equilibration time of 120 seconds.



The isoelectric points of the copper oxide based nanofluids were determined using a Malvern Multi-Purpose Titrator (MPT) Zeta sizer nanorange (Malvern, United Kingdom). A 0,1% w/w copper oxide nanofluid sample was titrated using the MPT over a pH range of 2 to 12 with 1-unit increments. The pH of the nanofluids were adjusted using 0,1 molar solutions of hydrochloric acid and sodium hydroxide, respectively, in the titration.

The optical properties of the nanoparticles were investigated as detailed in **Section 3.4.2**. The Uv-Vis absorbance spectra of the 0,1 % w/w copper oxide nanofluids with water as the base fluid were used to determine the band-gap energies of the nanoparticles. The cut-off wavelength of the spectra was determined by making a tangent to peak in the wavelength spectrum and taking the wavelength at the x-intercept. This wavelength was used to determine the band gap energy of the CuO nanoparticles using **Equation 3.30**.

$$E_g^* = \frac{hc}{\lambda_c} \quad \text{Equation 3.30}$$

Where:  $E_g^*$  is the band gap energy,  $\lambda_c$  is the absorbed wavelength by the sample,  $c$  is the speed of light, and  $h$  is Planck's constant.

After the calculation of the band gap energies of the copper oxide nanoparticles, **Equation 3.31** was then used to calculate the approximate size of the CuO nanoparticles (Ramani *et al.*, 2016).

$$E_g^* = E_g^{\text{bulk}} + \frac{h^2\pi^2}{2r^2} \left( \frac{1}{m_e^*} + \frac{1}{m_h^*} \right) - \frac{1.8e^2}{4\pi\epsilon\epsilon_0 r} - \frac{0,124e^4}{h^2(4\pi\epsilon\epsilon_0)^2} \left( \frac{1}{m_e^*} + \frac{1}{m_h^*} \right)^{-1} \quad \text{Equation 3.31}$$

Where:  $E_g^*$  is the band gap energy of the nanoparticles, which is determined from the UV-Visible absorbance spectrum,  $E_g^{\text{bulk}}$  is the band gap energy of the bulk Cu at room temperature, which has the value of  $3.88 \times 10^{-19}$  J,  $h$  is Planck's Constant

$(6.625 \times 10^{-34} \text{ J.s})$ ,  $r$  is the particle radius,  $m_e^*$  is the effective mass of band electron in CuO,  $m_h^*$  is effective mass of a hole in CuO,  $e$  is the elementary charge,  $\epsilon_0$  is the permittivity of free space,  $\epsilon$  is the relative permittivity of CuO.

To simplify the calculation of the size of the nanoparticles, **Equation 3.31** was reduced into a quadratic equation by making  $r^2$  the subject of the equation (Makori *et al.*, 2017) and applying the quadratic formula as shown in **Equations 3.32 to 3.35**.

$$r = \frac{-b \pm \sqrt{b^2 - 4ac}}{2a} \quad \text{Equation 3.32}$$

The values of the coefficients were thus be defined as shown in **Equations 3.33 to 3.35**.

$$A = \left[ E_g^* - E_g^{\text{bulk}} + \frac{0,124e^4}{h^2(4\pi\epsilon\epsilon_0)^2} \left( \frac{1}{m_e^*} + \frac{1}{m_h^*} \right)^{-1} \right] \quad \text{Equation 3.33}$$

$$b = \left[ \frac{1.8e^2}{4\pi\epsilon\epsilon_0} \right] \quad \text{Equation 3.34}$$

$$c = -\frac{h^2\pi^2}{2} \left( \frac{1}{m_e^*} + \frac{1}{m_h^*} \right) \quad \text{Equation 3.35}$$

### 3.8 References

- Biolin Scientific. (2014). Estimating Clonality. In *Lecture on Contact Angles* (Vol. 3, Issue 1). <http://arxiv.org/abs/1408.1149>
- Cabrera-González, M., Ahmed, A., Maamo, K., Salem, M., Jordan, C., & Harasek, M. (2022). Evaluation of Nanofiltration Membranes for Pure Lactic Acid Permeability. *Membranes*, 12(3).  
<https://doi.org/10.3390/membranes12030302>
- Carifio, B. A. (2016). Extending the Service Life of Activated Carbon Filters  
Extending the Service Life of Activated Carbon Filters. *Journal of the New England Water Works Association*, 225–233.
- Dach, H. (2009). Comparison of nanofiltration and reverse osmosis processes for a selective desalination of brackish water feeds. *Engineering Sciences*.
- Dang, H. T., Narbaitz, R. M., Matsuura, T., & Khulbe, K. C. (2006). A Comparison of Commercial and Experimental Ultrafiltration Membranes via Surface Property Analysis and Fouling Tests A Comparison of Commercial and Experimental Ultrafiltration Membranes via Surface Property Analysis and Fouling Tests. *Water Quality Research Journal of Canada*, 41(1), 84–93.  
<https://doi.org/10.2166/wqrj.2006.009>
- Figoli, A., Hoinkis, J., Alsoy, S. A., & Bundschuh, J. (2000). *Application of Nanotechnology in Membranes*.
- Gebru, K. A., & Das, C. (2017). Preparation and Characterization of CA – PEG – TiO<sub>2</sub> Membranes : Effect of PEG and TiO<sub>2</sub> on Morphology , Flux and Fouling Performance. *Journal of Membrane Science and Research*, 3, 90–101. <https://doi.org/10.22079/jmsr.2016.22820>
- Harivram, A. S. K., Aryanti, N., & Wardhani, D. H. (2019). Flux Decline and Blocking Mechanism in Ultrafiltration of Glycerin-Rich Solution. *Journal of Physics: Conference Series*, 1295(1). <https://doi.org/10.1088/1742-6596/1295/1/012028>

## CHAPTER 4

---

### EVALUATION OF CUSTOM-MADE UF AND COMMERCIAL NF270 MEMBRANES IN A SOLAR-INDUCED PRESSURE-DRIVEN SYSTEM

#### 4.1 Introduction

This chapter is divided into two parts: Part one was aimed at discussing the performances of a nanoparticle free, custom-made ultrafiltration and a commercial nanofiltration membrane as potential membrane options for the solar-driven filtration prototype. Here, the layout/configuration, operations and potential of the solar driven membrane filtration system were demonstrated. As stated in previous sections, potable water in rural areas is sourced directly from rivers, wells and boreholes and directly used without treatment. Usually, the quality is good, and the installation of an ultrafiltration membrane is to ensure the removal of microbes, dissolved organic macromolecules, and some heavy metals. However, with the evolution of feed streams due to direct and indirect pollutions, the impact of a more selective membrane on the permeate quality was investigated. The performance of the membranes in terms of permeate flux and quality was also ascertained. The aim of testing these two classes of membranes was to determine their suitability for the system not direct comparison. The ultrafiltration membrane was prepared using a phase-inversion method and the physicochemical properties and performance of the membranes were then evaluated. Before enhancing the system, the prototype was tested using deionized water as a proof of concept. Once the behaviour of the system was established, several attempts were made to improve its efficiency, and these are discussed partly in part two of this chapter and the subsequent chapters.

#### 4.2 Experimental

##### 4.2.1 Materials and methods

This chapter used the same polymers and solvents listed in **Chapter 3 Subsection 3.1**. The composition of the UF membrane was 20wt.% PES, 44wt.% NMP, and 36wt.% PEG, and was previously prepared in a study conducted by Mamba et al,

2021. The aim was to engineer/tune the morphology of the membrane such that it contained both spongy and macro-void features.

#### **4.2.2 Membrane preparation and characterization**

The UF membrane was prepared as detailed in **Section 3.2**. The UF and NF270 membranes were then subsequently characterized as detailed in sections 3.2.2 to 3.3.3. The aim of this characterization was to determine the physico-chemical properties of the membrane. The morphology of the flat sheet membranes (pristine, chemically cleaned, and fouled) was studied using scanning electron microscopy (Jeol IT300 Tokyo, Japan) while Energy Dispersive Spectroscopy (EDS) was used to determine elemental composition, as outlined in section **3.2.2**. The membrane topology and roughness were analysed using an Alpha 300 atomic force microscope, WiTec Innovations (Germany) as detailed in **Section 3.2.3**. Membrane surface wettability measurements and Surface Free Energy (SFE) calculations were determined and computed as described in **Section 3.2.4 & 3.2.4.1** using a Kruss goniometer. The thermal properties of the membranes were also investigated as detailed in section **3.2.5**. After membrane characterization, the separation properties of the membranes were then investigated. The membranes' pure water fluxes, permeability coefficients, water uptake values, overall porosities, pore sizes, and MWCO values were determined as described in **Section 3.3.3**

#### **4.2.3 Water analysis**

Real water samples were collected from two surface water sources as described in **Section 3.4.1** and subsequently analysed as detailed in **Section 3.4.2** to ascertain their composition. The analysis was also extended to the permeate to determine the filtration efficiency.

#### **4.2.4 Membrane fouling and testing protocols**

The performance, fouling properties, and cleaning protocols of the membranes were investigated as outlined in **sections 3.5.1 and 3.5.2**.

#### **4.2.5 Prototype schematic and description**

The prototype used in this study was constructed as shown in **Figure 4.1**. The prototype uses a positive displacement diaphragm pump that has two main parts, i.e., the working liquid chamber and the water chamber, that then connected to a membrane filtration unit. A small volume of the volatile liquid was placed in the working liquid chamber while DI water was put in the water chamber and either an ultrafiltration or a nanofiltration membrane was then placed in the membrane unit. The water chamber and the working liquid chamber was separated by a flexible diaphragm which was chemically inert to attack by the volatile liquid and mechanically strong to resist breaking during operation. The system was operated by exposing the working liquid chamber to a heat source and this caused the volatile liquid to evaporate and increase the pressure inside the working chamber. The high pressure inside the working chamber then developed a positive pressure difference between the two compartments thereby forcing water out of the hydraulic pump system and into the membrane unit where the water was filtered. The laboratory prototype was constructed in the same way as the field prototype with the major difference being size. Both were designed as single stroke hydraulic pumps that required refilling once all the water had been expelled from the water chamber.

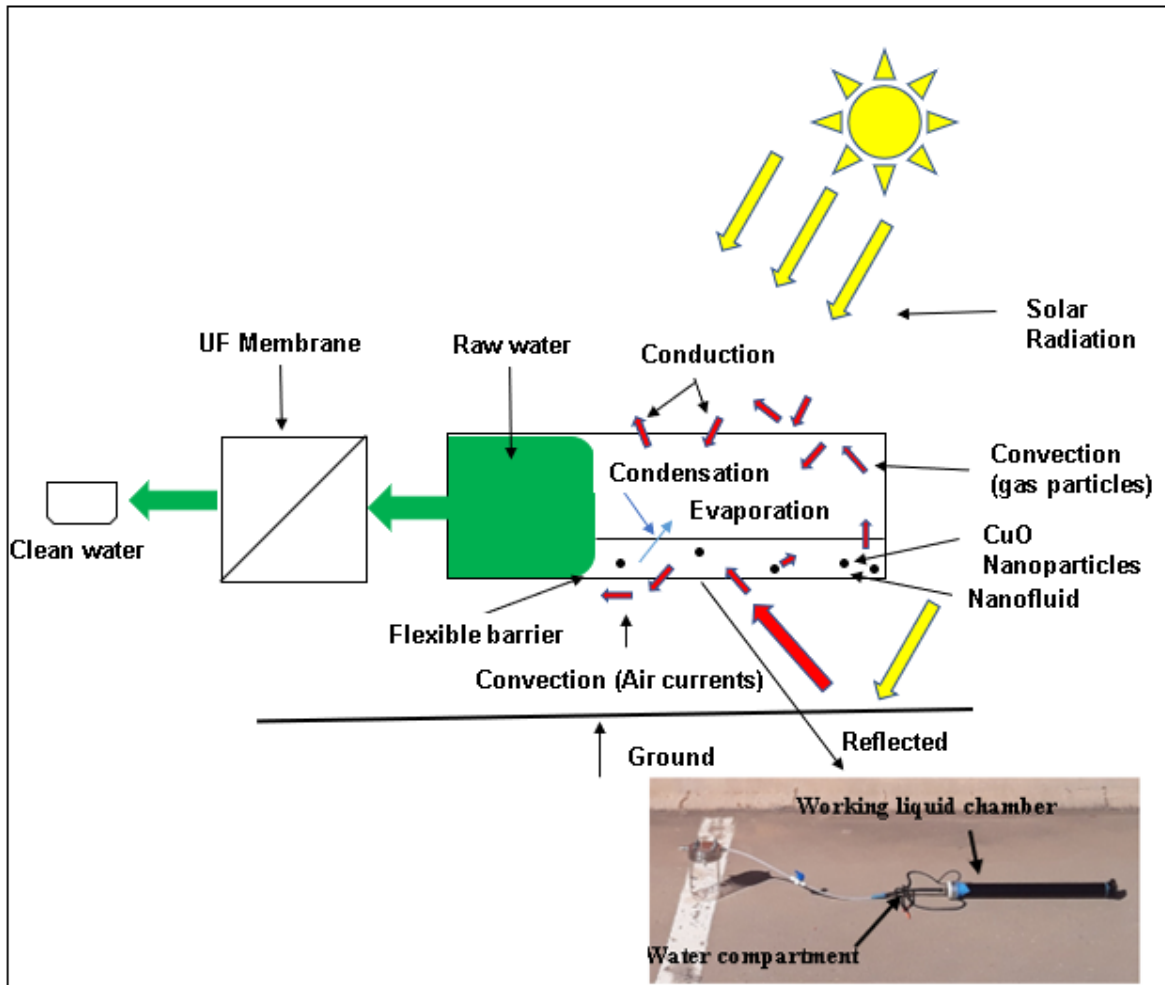


**Figure 4.1:** Stand-alone solar driven hydraulic pump membrane filtration system for surface water purification.

The field prototype was set-up as shown in **Figure 4.2** at the UNISA CSET Florida Campus' Horticultural section (26°09'27.8"S 27°54'15.6"E). Weather conditions at the location of the system set-up were monitored through a Watchdog 2900 professional weather station that had a pyranometer for measuring the solar radiation in  $\text{Watt/m}^2$ , a weathervane for determining the wind speed in km/h, and a thermocouple that measured the ambient air temperature. The prototype had an 89-litre working liquid chamber and the water capacity of its water chamber was 105 litres. The minimum volume of pure working liquid was determined using **Equation 3.29**.



**Figure 4.2:** Satellite and horizontal images of the field prototype used in the study. The system was run with an ultrafiltration membrane over a two-month period and the average daily fluxes for each month were determined.

## 4.3 Results and Discussion

### 4.3.1 Membrane preparation and characterization.

The morphology of the UF membrane's top surface was neat, typical of polymeric surfaces, while the cross-section showed an asymmetric structure with a selective, thin top-layer responsible for the separation processes (Kajitvichyanukul *et al.*, 2011) and a porous, support layer that had finger like macro-voids and sponge like cavities as shown in **Figure 4.3**. The macro-voids in the sublayer lead to higher permeability of the membrane which favours the application of moderate pressure in ultrafiltration applications (Nora *et al.*, 2017). It also means that the membrane has more interstitial volume for water uptake. The observed structure is a function or typical of membranes containing large amounts of PEG.



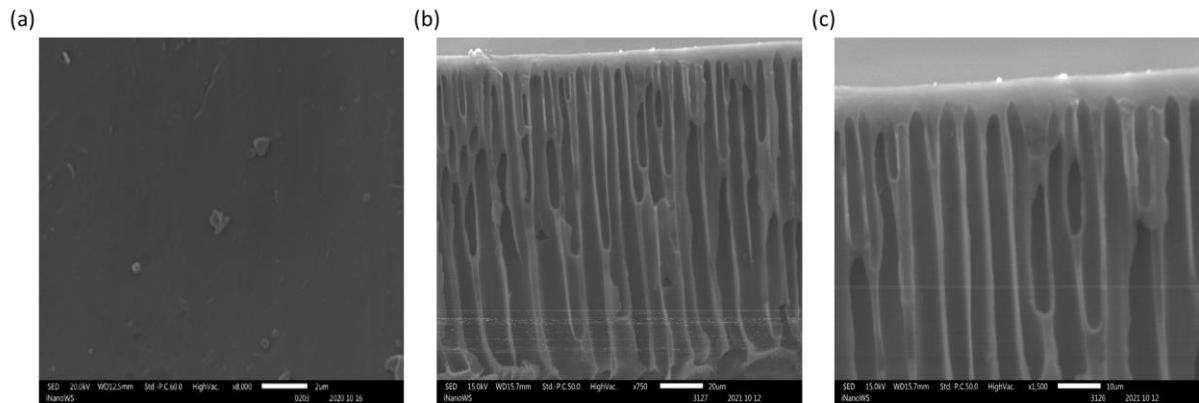


**Figure 4.3:** SEM images of the pristine UF membranes used in this study showing UF membrane's (a) top surface, (b) cross-section, and (c) Thin top layer of the UF membrane.

The SEM images of the pristine NF270 membrane shown in **Figure 4.4**, shows a smooth top surface with no visible defects while the cross-section showed three layers, i.e., a thin and compact top-layer (Polyamide), a porous mid-layer (Polyether sulfone), and a fibrous support layer (Polyester).

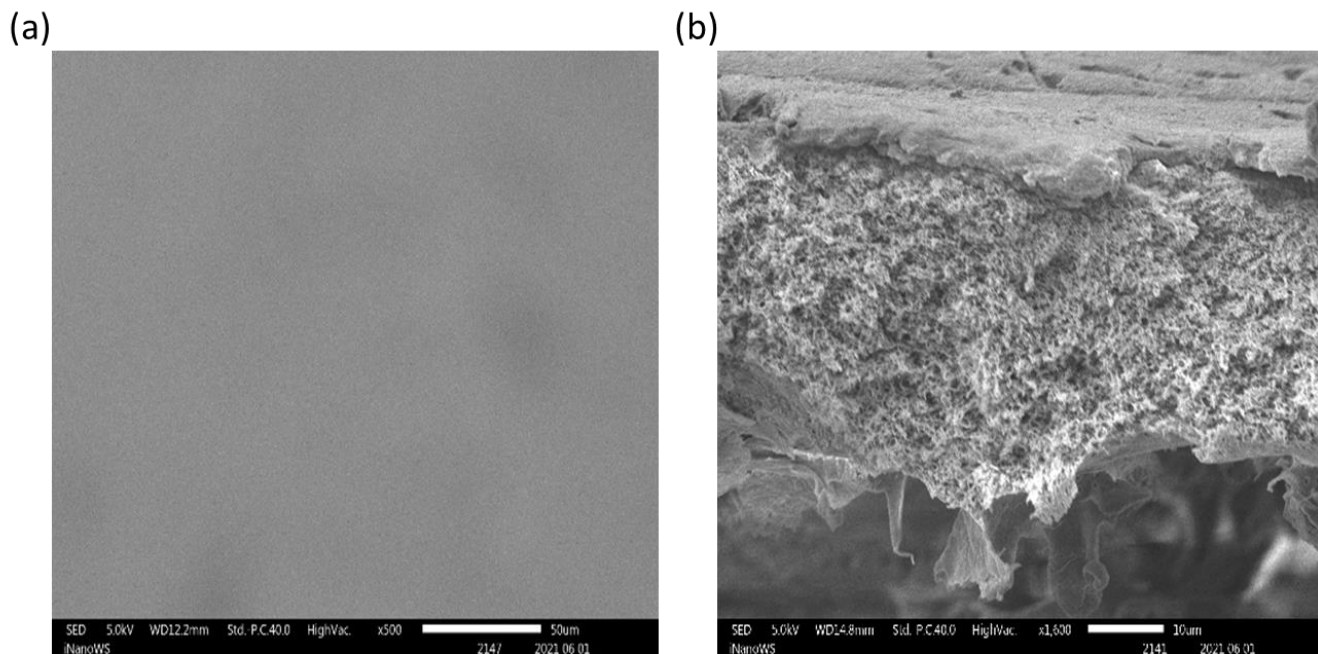


**Figure 4.4:** SEM images of the clean NF membranes used in this study showing (a) top surface and (b) cross-section of the membrane.

The topology of the membranes was analysed to investigate the fouling tendency of the membranes as rough surfaces experience a higher degree of fouling than smooth ones (Servos *et al.*, 2014). The susceptibility of membranes to fouling increases with an increase in the membrane's surface roughness (Du *et al.*, 2020) through the increase in clogging of foulants in surface depressions hence affecting the membrane's performance and washing (Vatanpour *et al.*, 2020). Apart from increasing the exposed surface of the membrane, an increase in roughness also negatively affects the hydrodynamics of water molecules near the membrane surface (Cuperus & Smolders, 1991). The hydrophilicity (Mahdi *et al.*, 2019) and flux (Agboola *et al.*, 2014) of membranes has been shown to increase with an increase in the surface roughness of membranes as roughness is also related to surface porosity (Keurentjes *et al.*, 1989). **Figure 4.5** shows the AFM images of the pristine UF membrane. The roughness measurements of the UF membrane were found to be SA (Arithmetic mean height) = 57.3354 nm and SQ (Root Mean Square Height) = 85.8205 nm. (Mahdi *et al.*, 2019) determined a pristine PES membrane to have a roughness of 57,1 nm which compares well to that determined experimentally in this study.

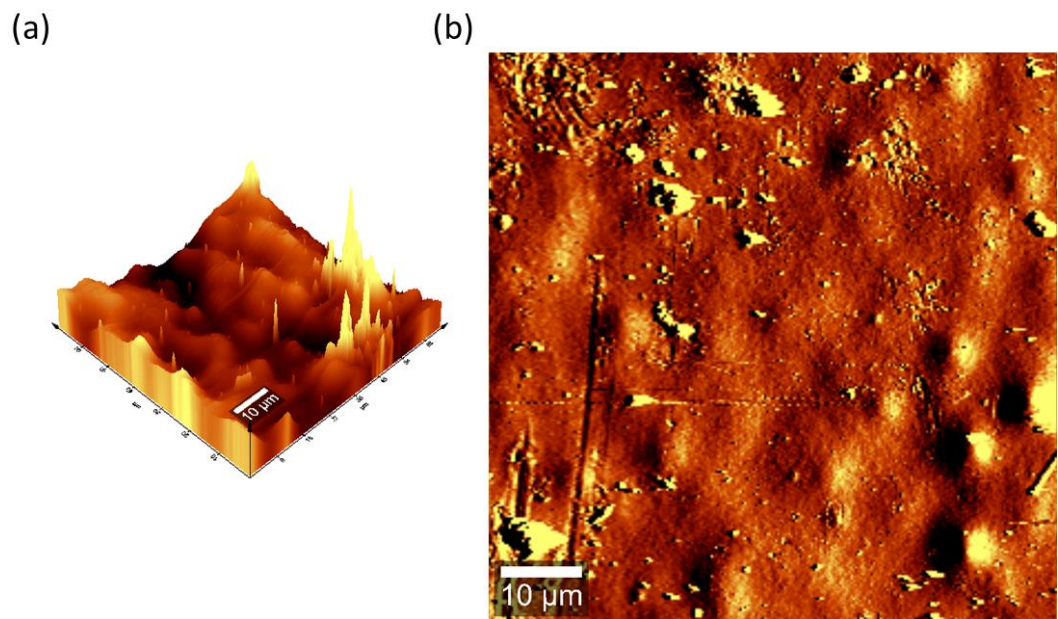


**Figure 4.5:** AFM images of surface of pristine UF membrane (a) 3D view of pristine membrane, and (b) 2D view of Pristine membrane.

On the other hand, the roughness measurements for the pristine NF membrane were determined to be SA -166.928 nm and SQ - 219.406 nm and their AFM micrographs are shown in **Figure 4.6**. This result greatly deviated from that reported by (Wang *et al.*, 2021) who reported an RMS roughness value for an NF270 membrane of  $6.1 \pm 1.8$  nm (scan area was not reported). This may be explained by the scan size used as demonstrated by (Dach, 2009) who showed that the scan area impacts roughness measurement values and reported NF270 roughness values of  $45 \pm 5$  nm and  $13 \pm 5$  nm for scan sizes of  $50 \mu\text{m} \times 50 \mu\text{m}$  and  $1 \mu\text{m} \times 1 \mu\text{m}$ , respectively. As such AFM results are only comparable when the same method and scan area are used (Agboola *et al.*, 2014).

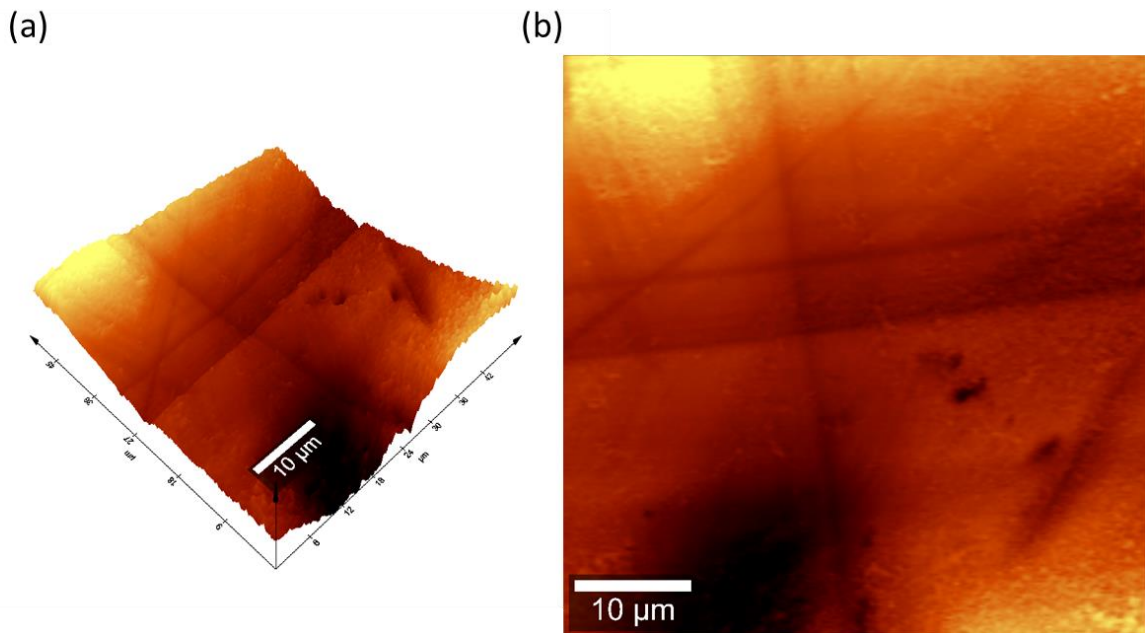


**Figure 4.6:** AFM images of surface of pristine NF membrane showing (a) 3D view and (b) 2D view.

Contact angle measurements were used to determine membrane surface wettability. Higher surface hydrophilicity of membranes is related to a higher adsorption of water molecules on the surface of the membrane. This leads to less fouling and a higher membrane performance (Khan *et al.*, 2020) as most organic foulants (usually proteins) are hydrophobic in nature (Vatanpour *et al.*, 2020) hence they adsorb easily on hydrophobic surfaces (Mohamad *et al.*, 2013). Hydrophilic surfaces are also able to facilitate the formation of thin layers of water on surface

through hydrogen bonding of the surface functional groups with water hence lowering the chances of hydrophobic units (foulants) to attach on the surface (Mahdi *et al.*, 2019). The contact angle of the material is also affected by the surface roughness (Keurentjes *et al.*, 1989) and porosity (Ghiggi *et al.*, 2017). The water contact angle of the pristine UF membrane was determined to be  $67,82 \pm 2,86^\circ$  while that of the NF270 membrane was found to be  $51,58 \pm 4,01^\circ$ . In literature, the reported values of contact angles for PES and NF270 membranes are  $65,1 \pm 2^\circ$  (Mahdi *et al.*, 2019) and  $32,6^\circ$  (Metcalf *et al.*, 2014), respectively, and these values compare well to the experimentally determined values in this study. Both UF and NF270 membranes had contact angles lower than  $90^\circ$  which shows that they are both hydrophilic with the NF270 membrane being more hydrophilic than the UF membrane. The UF membrane was made from just PES which has low hydrophilic nature (Muhamad *et al.*, 2015) which was mixed with PEG to improve its hydrophilicity, (Li *et al.*, 2015) whilst the NF had a polyamide layer which has a high affinity for water. The surface free energy (SFE) of the membranes was calculated to understand the potential interactions between foulants and the membrane's surface (Schuster *et al.*, 2015). SFE is a measure of the energy required for substances to be adsorbed onto the surface of another substance thereby forming a new surface. High values of SFE indicate a high degree of surface inhomogeneity which leads to a higher tendency of adsorbing organic substances (Kozbial *et al.*, 2014). The SFE of the UF membrane was found to be  $45,17 \pm 10,46$  mN/m which was lower than that of the NF270 membrane that was found to be  $47.89 \pm 2,16$  mN/m.

The thermal stabilities of the membranes were studied to investigate the degradation of the membranes at high temperature hence their thermal stability under operation. The thermogram of PES shown in **Figure 4.7(a)**, shows an initial 0,5 % weight loss between 0 °C and 110 °C due to evaporation of moisture and an additional 3,2% weight loss between 110 °C and 290 °C due to loss of residual solvents, i.e., 1-methyl-2-pyrrolidone (NMP) (boiling point – 202 °C) and PEG 400 (boiling point – 290 °C) from the membrane. Thermal degradation of the polymer then started at  $458 \pm 2^\circ\text{C}$  with a peak of thermal degradation rate at  $555 \pm 2^\circ\text{C}$  (Ghiggi *et al.*, 2017). The NF270 thermogram shown in **Figure 4.7 (b)** shows no

initial decrease in the weight of the polymer from 0°C to close to 380°C indicating that the membrane was completely dry. Thermal degradation starts to occur at  $381 \pm 2^\circ\text{C}$  peaking at  $462 \pm 2^\circ\text{C}$ . This shows that the UF membrane with PES polymer is more thermally stable than the NF270 membrane with the polyamide polymer indicating the presence of stronger chemical bonds in the UF membrane (Muhamad *et al.*, 2015).

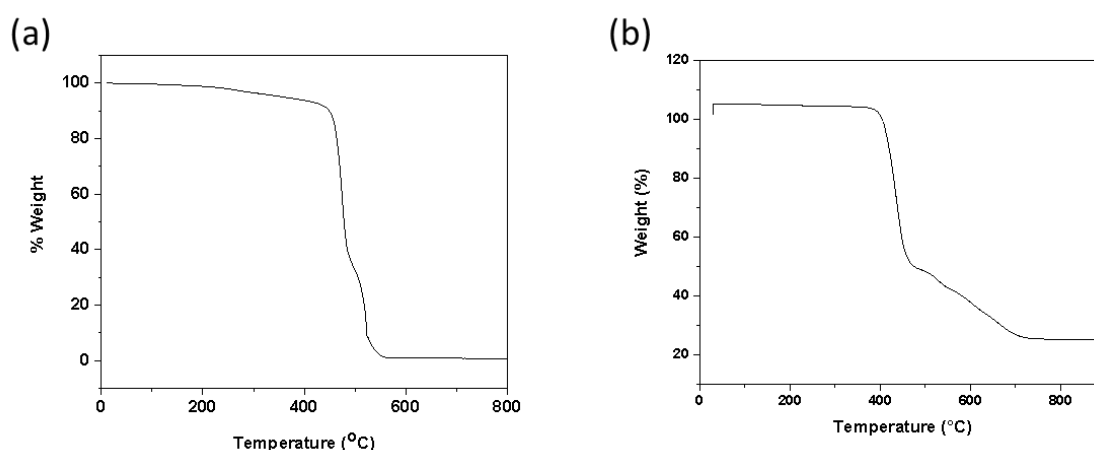


**Figure 4.7:** Thermograms of the (a) UF and (b) NF membranes showing the thermal degradation of the polymeric membranes at different temperatures.

The surface functionalities of the membranes were analysed to identify the functional groups at the surface of the membranes. The FTIR spectra for the UF and NF membranes are shown in **Figure 4.8** with peaks assigned to different functional units as shown in **Table 4.1**. The peak at  $3608\text{ cm}^{-1}$  is due to the O-H stretching in PEG molecules within the PES membrane while the  $567\text{ cm}^{-1}$  peak is due to C-C deformation (Charles *et al.*, 2009) in the PA polymer of the NF270 membrane. Some of the peaks registered in the spectra of the NF270 membrane were due to the polyether sulfone (PES) mid-layer and poly-ester (PE) support layer as the FTIR technique has a high depth of penetration (Mouhoumed *et al.*, 2014).

**Table 4.1:** Assignment of the peaks in the FTIR spectra of the UF and NF270 membranes.

Peak(s) (cm <sup>-1</sup> )	Peak Range (cm <sup>-1</sup> )	Functional unit(s)	Source
<b>3608</b>	3500 - 3700	O-H stretching	PEG
<b>3441</b>	3510 -3460 cm <sup>-1</sup> & 3415 – 3380 cm <sup>-1</sup>	aromatic primary amines (N-H) stretching	PA
<b>2881</b>	2900 - 2880	methyne (=CH-) stretching	PA
<b>1711</b>	1725 – 1705	Ketone group (C=O) amide I of poly(piperazine- amide) (-C=O) (S. Wang et al., 2021)	PA
<b>1406</b>	1420 – 1370	Organic sulfonates	PES
<b>1410</b>			PA
<b>1310</b>	1340 - 1250	aromatic amino C-N bond stretch	PA
<b>1239</b>	1270 - 1230	aromatic ether (C-O-C)	PES
<b>1243</b>		stretch	PA
<b>1151, 1010</b>	1225 – 950	aromatic C-H in-plane	PES
<b>1090, 1017</b>	(Coates, 2000)	bending	PA
<b>873, 834</b> <b>871</b>	900 – 860	1,3-Disubstitution meta on the aromatic ring	
<b>873, 834, 716</b> <b>871, 719</b>	900 - 670	aromatic C-H out of plane bending	PES PA PE

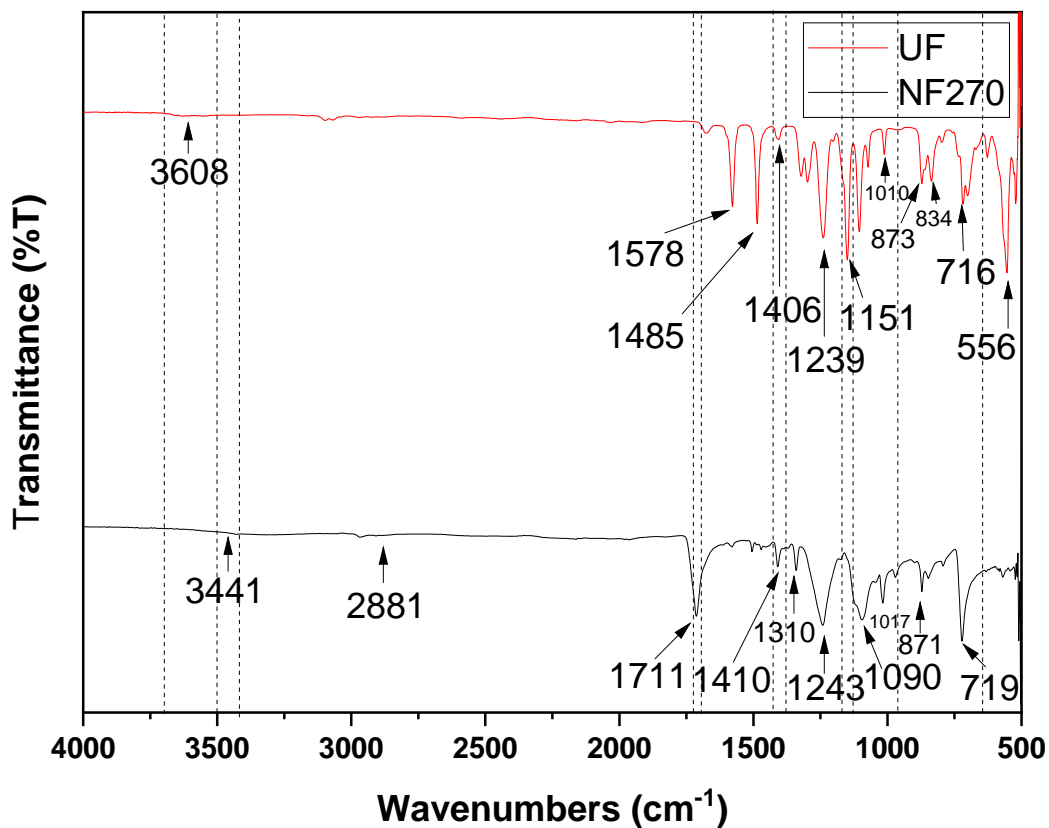


**Figure 4.8:** FTIR spectra of pristine UF and NF membranes showing peaks of functional groups at the surfaces of these membranes.

The peaks in the FTIR spectra of the UF and NF270 membranes were assigned to different functional units in the polymers of the membranes and some of these functional units are shown on the different polymers in **Figure 4.9**.

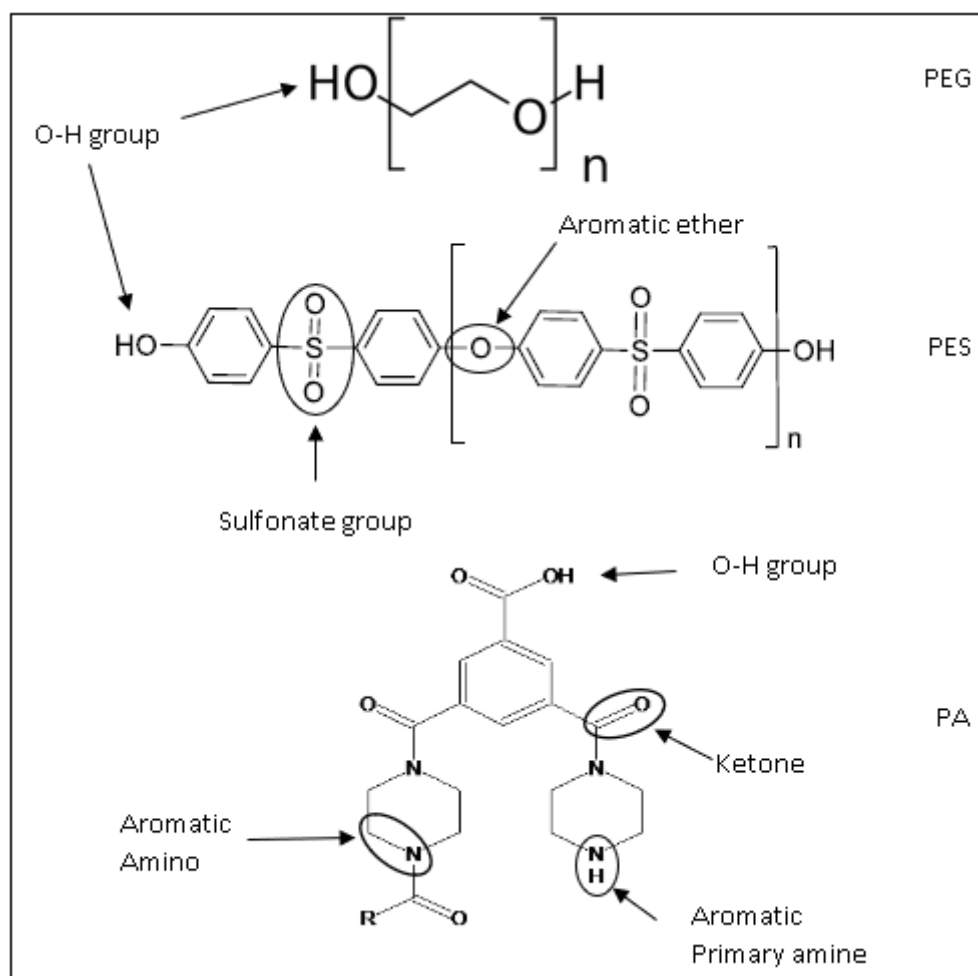


**Figure 4.9:** Identification of the main functional units in the different polymers.

The water uptake of membranes was measured to determine the total volume of all the membrane pores (Barghi, 2014). It gives an indication of the water-swelling capacity which is a useful indirect measure of the membrane's hydrophilicity and flux performance (Pandey *et al.*, 2015). The UF and NF270 membrane water uptake values were determined to be 70,7 % and 21,3%, respectively. The UF membrane had a higher water uptake than that of the NF270 membrane which is supported by the larger macro-voids in the UF membrane seen in the SEM images. The implication of this higher water uptake is that the UF membrane has a high flux performance than the NF270 membrane. The overall porosity values of the membranes also supported the water uptake values as the values were determined to be 61,6% and 28,2% for UF and NF membranes, respectively. Membrane thickness is also a factor in the flux performance of the membrane, as generally, a decrease in the membrane thickness leads to an increase in flux (Wenten, n.d).



Thicker membranes have higher mechanical strength but offer high resistance to flow (Moitsheki, 2003) due to an increase in tortuosity as the path travelled by the water molecules (or solution) is elongated with an increase in membrane thickness. The average thickness of the UF membrane was found to be  $0,101 \pm 0,007$  mm while that of the NF membrane was  $0,126 \pm 0,002$  mm. The pore size range of the membranes determines their classification and rejection capabilities and is useful in determining fouling susceptibility. Membranes with smaller pores are less susceptible to fouling than those with larger pores as they suffer mostly from adsorption than the larger pores which get clogged by foulants (Bokhary *et al.*, 2018). The pore sizes of the UF and NF270 membranes were determined to be 81,3 nm and 0,514 nm, respectively. The size of membrane pores restricts the passage of solutes through the membrane as those solutes which have sizes larger than the pore size are rejected. The size of the solute is related to its molecular weight and the smallest molecular weight of solute that is rejected by the membrane at 90% rejection is known as the Molecular Weight Cut-Off (MWCO) of that membrane. **Figure 4.10** shows the approximate MWCO ranges of the UF and NF270 membranes. The MWCO of the UF membrane was estimated to be around 4000 Da which is within 1000 – 500000 range reported in literature (Kimura, 1991; Ranville & Muzny, 2006). A range of MWCO values have been reported by different researchers for PES membranes and these include, 5 kDa (Carbonell-Alcaina *et al.*, 2016), 150 kDa (Li *et al.*, 2019), and 300 kDa (Muhamad *et al.*, 2015). The UF membrane used in this study was thus classified as a tight ultrafiltration membrane as it lies on the lower end (1000 – 10000 Da) of the MWCO range of UF membranes and can reject soluble organic matter from feed water (Bick *et al.*, 2012) as well as bacteria, viruses, colloidal silica particles, and albumin proteins (Ranville & Muzny, 2006). On the other hand, the MWCO of the NF270 membrane was estimated to be <400 Da which is within the range of 300 – 500 Da for most NF membranes (Hernando, 2016) and agrees with the MWCO for the NF270 membrane of 300 Da (Dach, 2009) reported in literature.

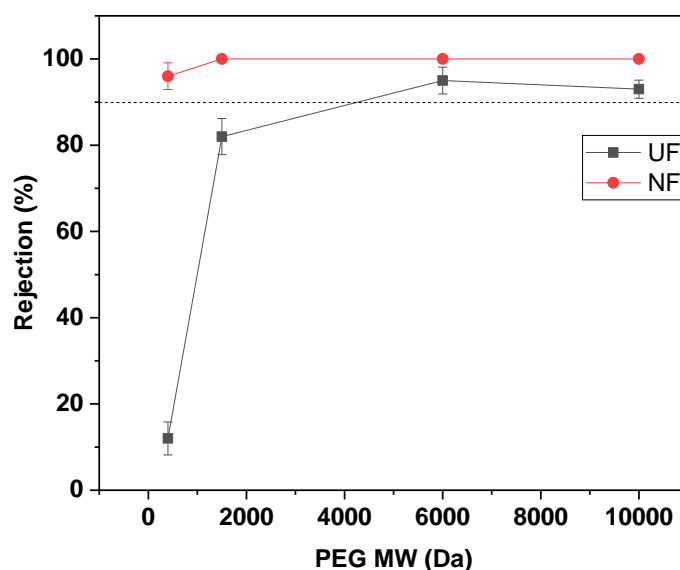


**Figure 4.10:** Estimation of the MWCO values for UF and NF270 membranes.

#### 4.3.2 Real water sample analysis

A summary of the real water samples' composition is given in **Table 4.2**. The physico-chemical properties of the raw water samples from both the Florida Stream and the Florida lake fell within the SANS241:2015 limits except for turbidity and cadmium concentration for the Florida lake sample that was on the maximum allowable value. Prolonged exposure or consumption of cadmium leads to ovarian and breast cancer (Qu *et al.*, 2018) and as such is cadmium is considered a priority toxin when considering public health (Tchounwou *et al.*, 2012). As such, the Florida Lake raw water was determined to be more polluted than the Florida Stream raw water and both where not suitable for direct human consumption given that no microbiological content data were analysed as well as the bad colour and smell of the water.

**Table 4.2:** Raw water composition for Florida Stream and Florida Lake samples against the SANS 241:2015 guidelines for acceptable drinking water quality.

Water parameter	quality	SANS 241: 2015 limits	Florida Stream	Florida Lake
-----------------	---------	-----------------------	----------------	--------------

<b>DOC (mg/l)</b>	10	3,05	9,323
<b>UVA2254 (a.u)</b>	-	0,0317	0,1124
<b>SUVA (L/mg.m)</b>	-	1,04	1,21
<b>pH value at 25°C</b>	≥5 to ≤ 9.7	7,12	7,11
<b>Total Dissolved Solids at 180°C</b>	≤1200	77,1	103
<b>Electrical conductivity in mS/m at 25°C</b>	≤170	141.2	206
<b>Turbidity in N.T.U</b>	≤1 (Operational) ≤5 (Aesthetic)	1,74	8,94
<b>Iron as Fe (µg/ℓ)</b>	≤ 2000 (Chronic Health) ≤300 (Aesthetic)	307	26
<b>Lead as Pb (µg/ℓ)</b>	≤10	0	2
<b>Nickel as Ni (µg/ℓ)</b>	≤70	0	0
<b>Manganese as Mn (µg/ℓ)</b>	≤400 (Chronic Health) ≤100 (Aesthetic)	43	8
<b>Cadmium as Cd (µg/ℓ)</b>	≤3	0	3
<b>Chromium as Cr (µg/ℓ)</b>	≤50	0	0
<b>Cobalt as Co (µg/ℓ)</b>	≤500	0	2
<b>Copper as Cu (µg/ℓ)</b>	≤2000	0	0
<b>Vanadium as V(µg/ℓ)</b>	≤200	0	2
<b>Calcium (µg/l)</b>	<150000 Aesthetic/Operational	697	7034
<b>Magnesium (µg/l)</b>	<70000 Aesthetic/ Health	369	4348

FEEM works through the analysis of emission wavelengths produced from exciting a sample at a certain wavelength. This information is used to characterize natural organic matter into separate fractions (S. S. Marais et al., 2018). As shown in **Figure**

**4.11**, the Florida lake water has higher concentrations of Humic/ Fulvic acids (x350/m420-480), Humic (x260/m380-460) and Tryptophan (x275/m340) than the Florida stream water. The Florida lake also has Tyrosine (x275/m310) which appears to be absent in the Florida stream water.

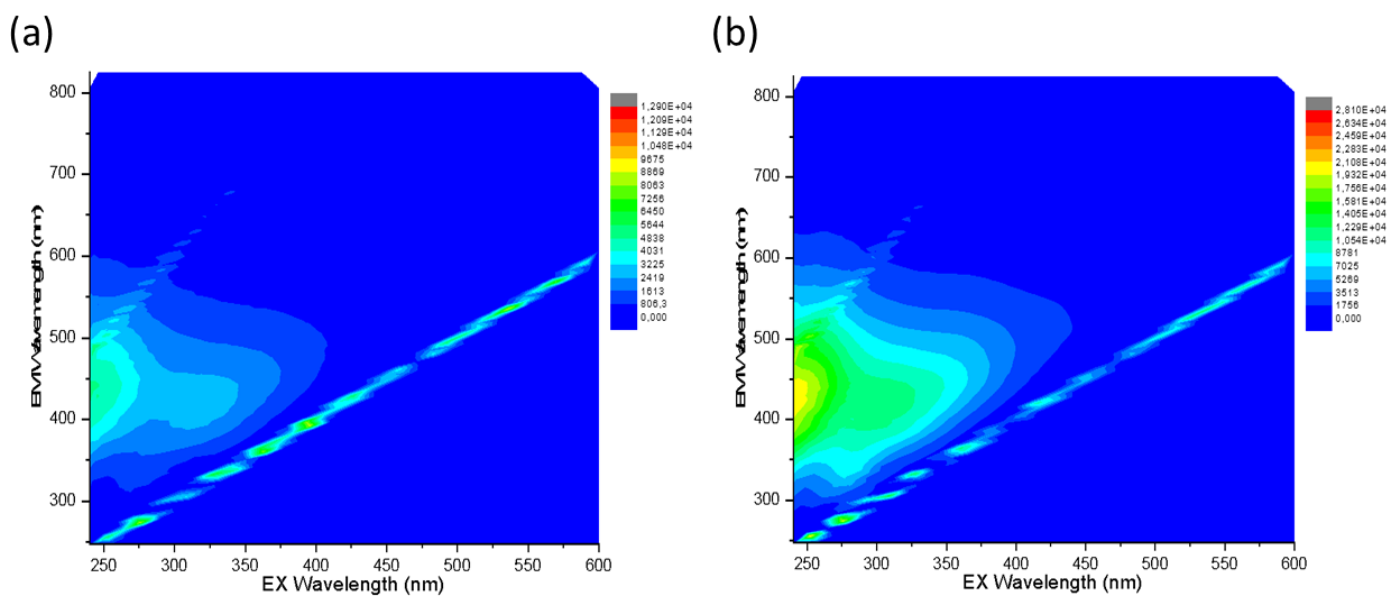


**Figure 4.11:** FEEM contour plots of (a) Florida stream and (b) Florida lake raw water showing different NOM fractions present in the water.

The filtration of the Florida stream raw water showed that the UF membrane rejected most of the natural organic matter after 4 hours as shown in **Figure 4.12**. Initially the membrane removed most Humic/ Fulvic acids (x350/m420-480), and Humic (x260/m380-460) leaving Tryptophan (x275/m340) and Tyrosine (x275/m310) sections. These fractions were removed after 4 hours of filtration leaving only trace amounts of natural organic matter. There was a general increase in the rejection of NOM with increase in filtration time. This was attributed to a higher level of fouling of the membrane which increased rejection. The main foulants of the membrane were thus determined to be humic and fulvic acids. This assertion is supported by the experimental work done by (Guo *et al.*, 2021) who determined that fluorescent organic matter fractions of humic acids and proteins were the main foulants in ultrafiltration of surface water.

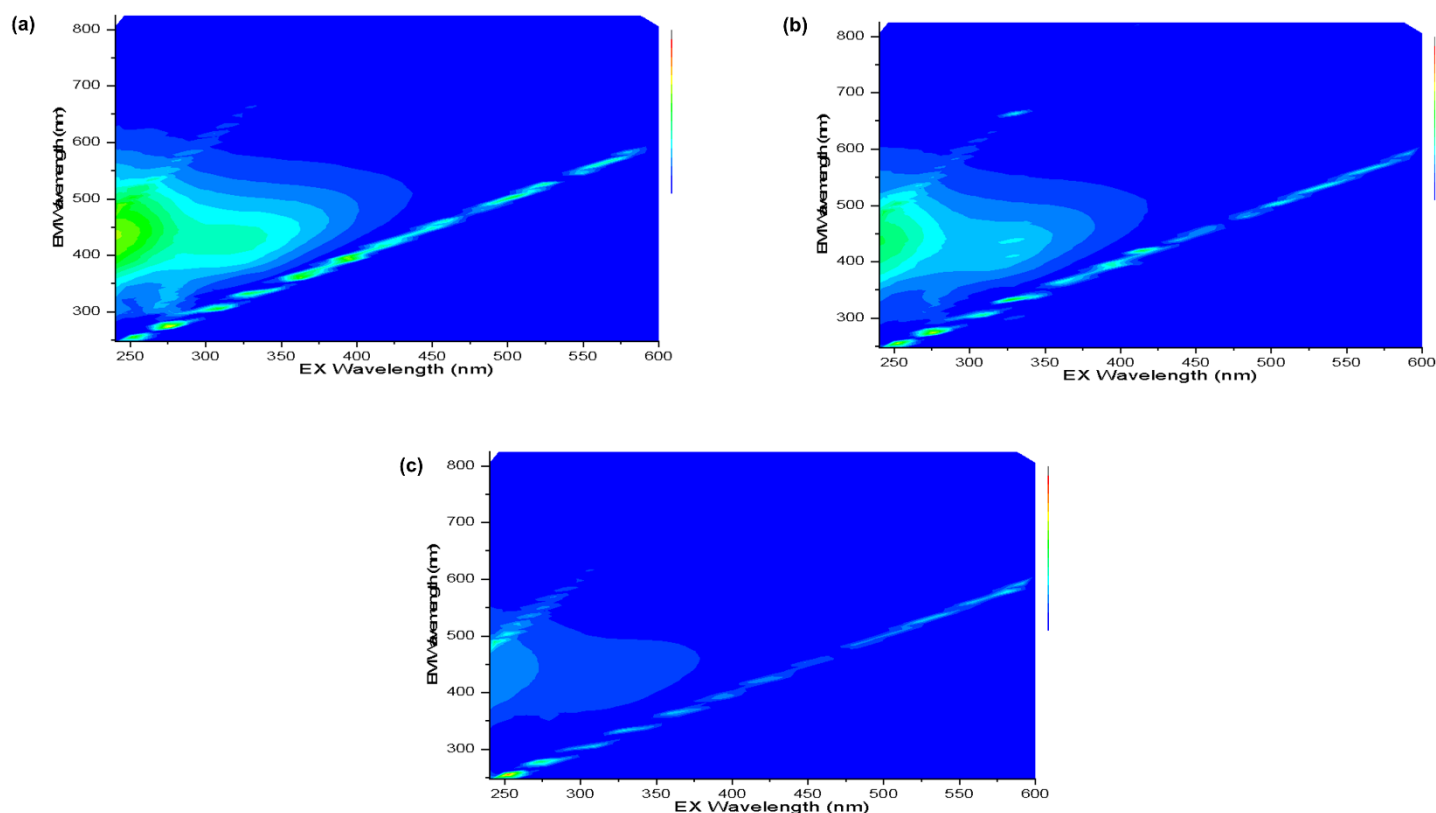


**Figure 4.12:** FEEM diagrams of Florida Stream (a) raw water and UF membrane permeates of the Florida stream water at (b) 2 and (c) 4 hours of filtration.

The DOC of the water was analysed to determine the amount of dissolved organic matter (Haarhoff *et al.*, 2010) in each filtration stage as there is a direct proportion relationship between NOM and DOC (Ming *et al.*, 2015). The results for the DOC values for the filtrate produced from filtering Florida Stream and Florida Lake raw water are displayed in **Figure 4.13**, respectively.

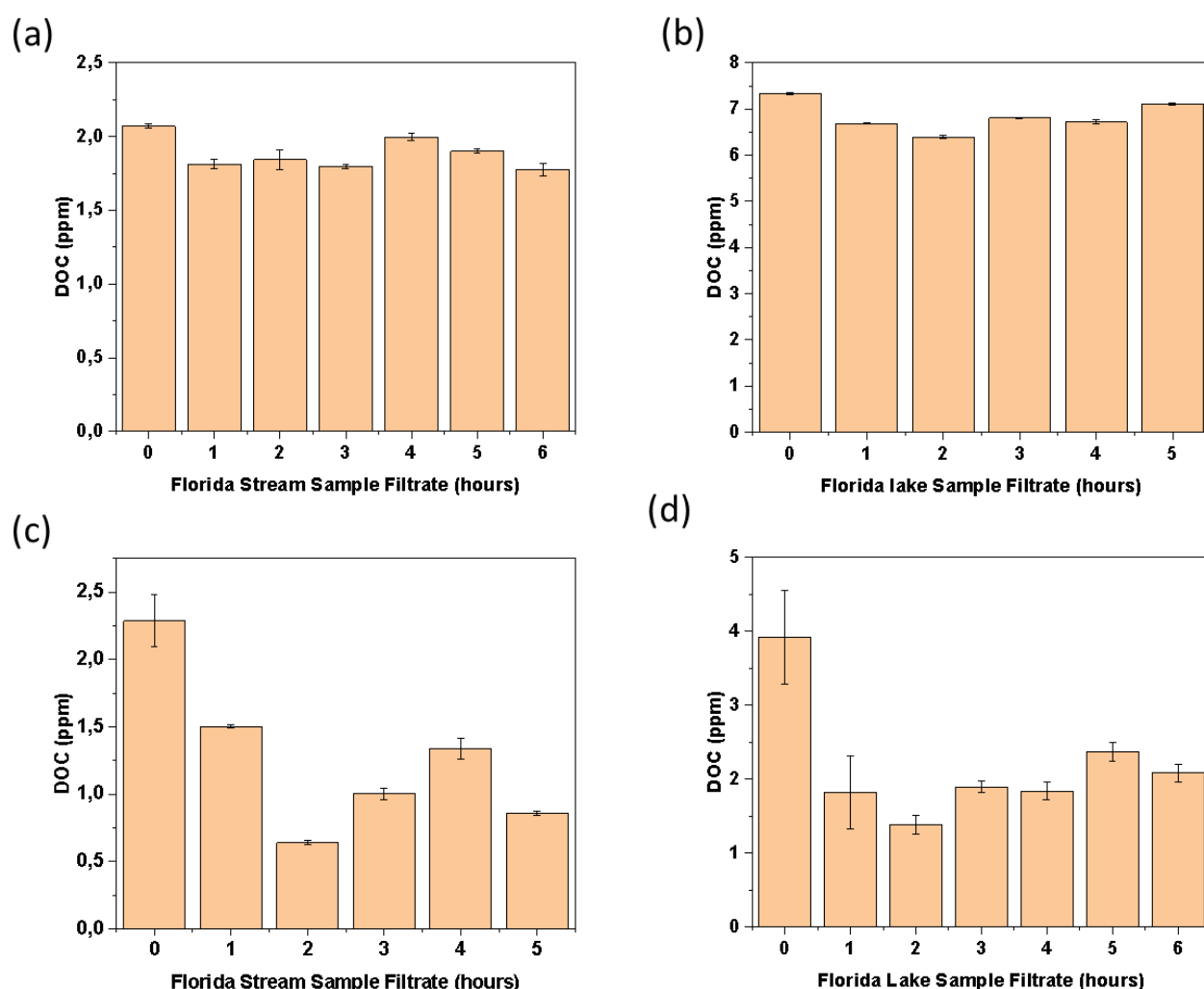


**Figure 4.13:** DOC values of UF membrane hourly filtrates from the filtration of the (a) the Florida Stream raw water, (b) Florida Lake raw water, NF membrane hourly permeates from the filtration of (c) the Florida Stream raw water, and (d) Florida Lake raw water.

Uv absorbances in the range 220 – 280 nm are common bulk water parameters that serve as indicators for the presence of different fractions of NOM which include, aromatic and carboxylic compounds at 220 nm, nitrites at 214 nm, and trihalomethanes at 272 nm (S. S. Marais et al., 2018). The Florida lake raw water samples had a higher absorbance than that of the Florida stream raw water in the range 220 – 280 nm as shown in **Figure 4.14**. As such, the Florida Lake raw water had a higher NOM concentration than the Florida Stream raw water.

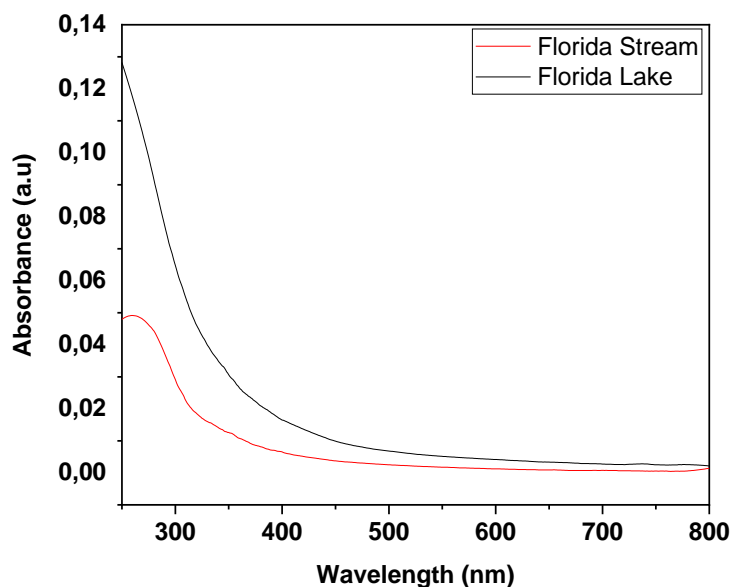


**Figure 4.14:** UV-Vis spectra of the Florida Lake and Florida Stream raw water samples.

The absorbances of both UF and NF membrane filtrates shown in **Figure 4.15 (a)** show that the membranes progressively removed absorbing species with an increase in filtration time. This was due to increases in membrane rejections due to an increase in fouling which constricts membrane pores. However, the UF membrane only reduced the absorbing species by small amounts as opposed to the NF270 membrane shown in **Figure 4.15 (b)** which showed large increases in absorbance reductions. Absorbances at 254 nm ( $UV_{254}$ ) can be used to determine the presence of aromatic compounds (Moyo *et al.*, 2020) as well as humic (Carifio, 2016) and fulvic acids (Zularisam *et al.*, 2006) in the water. There was a 20% decline in absorbance at  $UV_{254}$  for the UF membrane permeates which compares well with the 25%  $UV_{254}$  removal reported by (Malczewska & Żak, 2019) for the ultrafiltration of raw water from the Oder River (Poland) using PES membranes. However, the removal at  $UV_{220}$  was very small at 2% for the UF membrane. The NF270 membrane permeates showed a measurable decline in this absorbance for each progressive hourly permeate with an average removal of 28% for  $UV_{254}$  and 34% for  $UV_{220}$ . The NF270 membrane's polyamide top-layer has ionizable carboxylic and amine groups that form electrostatic interactions with foulants in the feed water and cause

substances to be rejected through dielectric exclusion (Hernando, 2016). The ionization of the surface groups of the NF membrane is affected by the pH of the solution (Mahlangu *et al.*, 2014) with carboxylic acids ionizing at alkaline pH and amine groups ionizing at acidic pH (Mahlangu & Mamba, 2021). The pH of the feed water was determined to be slightly alkaline (7,11 – 7,12) hence the NF membrane was slightly negatively charged due to the ionization of the carboxylic groups on the surface of the membrane. At this pH, the NF membrane was thus able to reject negatively charged aromatic and carboxylic compounds evidenced by the high removals of Uv<sub>254</sub> and Uv<sub>220</sub> while the UF membrane only managed to reject large aromatic compounds through size exclusion.

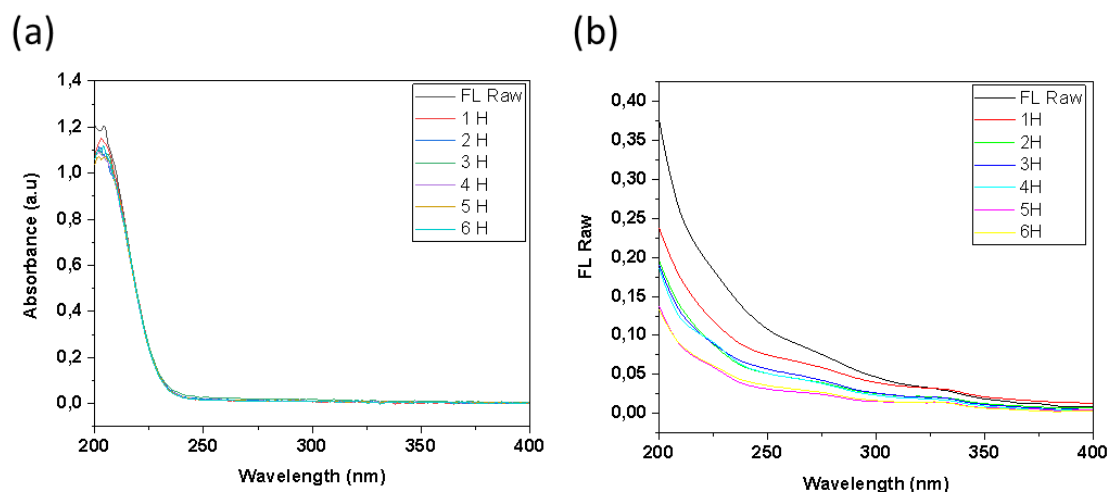


**Figure 4.15:**Uv-Vis absorbance spectra of Florida Lake raw water and hourly permeates from (a) UF and (b) NF membranes.

#### **4.3.3 Correlation between %DOC removal and filtration time**

The changes in %DOC removal with filtration time for the filtration of the Florida Stream and Florida Lake raw water by the UF and NF membranes are shown in **Figure 4.14**. The change in DOC values for the UF membrane for both water sources showed that there is an average of less than 25% reduction in DOC between the raw water and the permeates. This is in agreement with a 35% DOC removal efficiency that was determined for the ultrafiltration of raw water at the



Kagithane Drinking Water Treatment Plant by (Mutlu *et al.*, 2017). As such, ultrafiltration techniques must be coupled with other water treatment techniques to effectively remove NOM. The change in the DOC of both the Florida Stream and Florida Lake water samples changed by an average of 50% from the raw water to the permeates of the NF membrane as shown in **Figure 4.16**. This compares well with the value of 77% DOC removal that was determined by (García-Pacheco *et al.*, 2020) when they filtered synthetic river water using nanofiltration membranes. The low variability in the DOC values in the filtrate water samples for both the NF and UF membranes is indicative of similar NOM characteristics (Haarhoff *et al.*, 2010) as the feed water samples were taken from similar sources in the same season. NOM content in surface water sources changes with change in seasons.

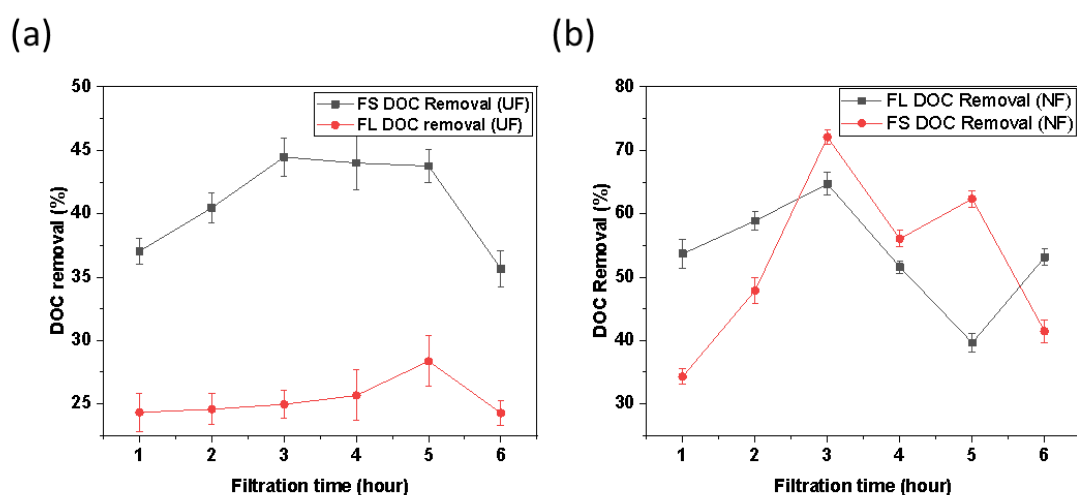


**Figure 4.16:** DOC removal with change in filtration time for Florida Stream and Florida Lake raw water using (a) UF membranes and (b) NF membranes.

#### 4.3.4: Comparison between %DOC removal and SUVA for the UF and NF membranes

The feed raw water samples were classified according to their SUVA values as shown in **Table 4.3**. SUVA is a basic water parameter that is used to determine the amount of humic acids within a water sample and also provides a measure of the

reactivity of NOM (Świetlik & Sikorska, 2006). The fouling potential of NOM substances was determined by Fan *et al* (2001) as follows: hydrophilic neutrals>hydrophobic acids> transphilic acids. A high SUVA value is indicative of high aromaticity in the organic content within the water sample (Zularisam *et al.*, 2006) as well as high alkalinity and hardness of the NOM contained within the water sample (Archer & Singer, 2006).

**Table 4.3:** Classification of NOM using SUVA values.

Raw water sample	SUVA (L.mg <sup>-1</sup> .m <sup>-1</sup> )	Classification
Florida Lake	2,57	Transphilic
Florida Stream	1,04	Hydrophilic
Humic acid (50ppm)	16,0	Hydrophobic

The SUVA values of the feed and permeate water from both UF and NF membrane filtration were compared with the respective %DOC removals in each filtration process as shown in **Figure 4.17**. As shown in Figure 4.17 there is a general increase in %DOC removal with an increase in the SUVA values of the feed water in membrane filtration (Hernando, 2016) given that positive correlation of the data with  $R^2 > 50\%$ . This correlation is greater for the nanofiltration ( $R^2 = 0,93$ ) than for ultrafiltration ( $R^2 = 0,77$ ). This shows that the characteristics of NOM affect DOC removal efficiency.

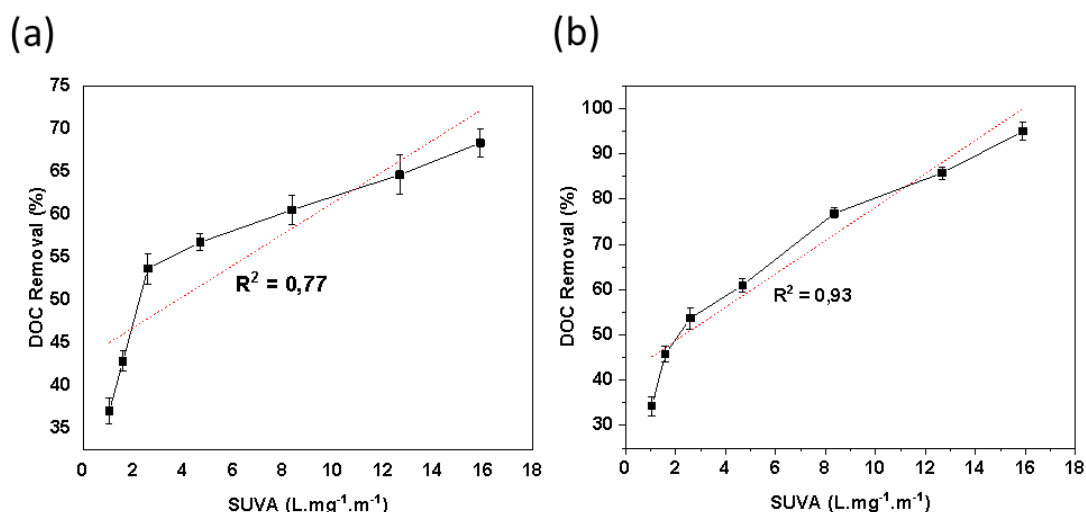


**Figure 4.17:** Relationship between %DOC removal and SUVA for membrane filtration using (a) UF and (b) NF membranes.

#### 4.3.4 Removal of metallic ions by UF and NF270 membranes.

The removal of calcium, magnesium, and some heavy metal ions by the UF and NF membranes are shown in **Figure 4.18**. The concentration of calcium and magnesium ions in water is a measure of its hardness. Hardness affects the lathering properties of soap as well as scale formation inside pipes carrying water thereby either clogging the pipes or protecting it from corrosion hence is an important water quality parameter (Challener, 2011). Magnesium and calcium also form divalent cations in solution which react with NOM substances disrupting the hydrocarbon chain repulsion and bridging the chains onto membrane surfaces thus increasing fouling rate (Zularisam *et al.*, 2006). Both calcium and magnesium ions were at high concentrations in the feed water and the UF membrane only rejected both ions at less than 12% while the NF membrane rejected the same ions at over 85%. This can be explained by the fact that NF membranes rely on the Donnan effect and steric hindrance for the rejection of salts (Liu *et al.*, 2018) and ions while UF membranes only rely on steric hindrance (size exclusion). Heavy metals are usually large positively charged ions (Merwe, 1998) in solution and these are toxic to both plants and animals hence are of public health concern. Due to their size, some of these heavy metals are rejected by ultrafiltration membranes. Of the selected heavy metals analysed in the ultrafiltration process, Co, Cd, V, and Pb were

rejected at >99,99%, with Fe at 78% and Mn at almost 0% at a pH range of 7.11 to 7.12. This is in agreement with studies done by (Bernat *et al.*, 2007) in an attempt to reject iron, chromium, and copper metal ions from synthetic solutions using a 5-kDa ultrafiltration membrane. The researchers found that only iron (III) species were rejected from the solutions and explained that the metal-ion speciation played an important role in the separation as the iron in aquatic solutions formed charged, soluble hydroxide ions that were adsorbed on the membrane active layer. Only iron (III) formed charged, soluble hydroxide ions in solution and these had the largest theoretical rejection of 68,7% at a pH of 2. The NF membrane was able to reject cobalt, lead, and manganese at >99,99%, as well as molybdenum ions at >90%. This is supported by the fact that most heavy metals are found in the divalent state or higher (Le & Nunes, 2016) in solution hence the electrostatic repulsions enhance the size exclusion thus making it a lot easier for nanofiltration membranes to reject them.

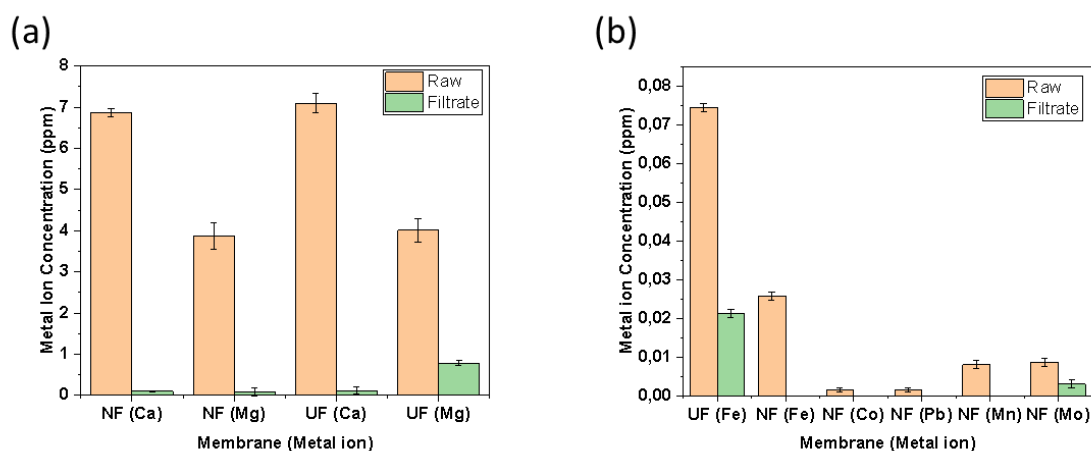


**Figure 4.18:** Metallic ion concentration of raw water and membrane 1-hour filtrates for (a) Alkaline Earth Metals (Ca & Mg) and (b) selected Heavy Metals.

#### 4.3.5 Physico-chemical properties of the membrane permeate.

Raw water from the Florida lake was chosen for filtration tests as it was more polluted than Florida stream raw water. The analyses result of the raw and one hour permeate samples from the UF and NF membranes are summarized in **Table 4.4**.

All the permeates of both UF and NF270 membranes were within drinking water limits except only for the electrical conductivity of the UF permeate. As such, both membrane filtration methods are suitable for application in surface water treatment for drinking water purposes.

**Table 4.4:** Physico-chemical analysis of membrane permeate of Florida lake.

<b>Water quality parameter</b>	<b>SANS limits</b>	<b>241: 2015 Florida Lake</b>	<b>UF</b>	<b>NF270</b>
<b>pH value at 25°C</b>	≥5 to ≤ 9.7	7,11	7,20	7,05
<b>Total Dissolved Solids at 180°C</b>	≤1200	103	102	51,7
<b>Electrical conductivity in mS/m at 25°C</b>	≤170	206	204	117,7
<b>Turbidity in N.T.U</b>	≤1 (Operational) ≤5 (Aesthetic)	8,94	0,79	0,00
<b>Iron as Fe (µg/ℓ)</b>	≤ 2000 (Chronic Health) ≤300 (Aesthetic)	26	15	0,00
<b>Lead as Pb (µg/ℓ)</b>	≤10	2	0,00	0,00
<b>Nickel as Ni (µg/ℓ)</b>	≤70	0	0,00	0,00
<b>Manganese as Mn (µg/ℓ)</b>	≤400 (Chronic Health) ≤100 (Aesthetic)	8	8	0,00
<b>Cadmium as Cd (µg/ℓ)</b>	≤3	3	0,00	0,00
<b>Chromium as Cr (µg/ℓ)</b>	≤50	0	0,00	0,00
<b>Cobalt as Co (µg/ℓ)</b>	≤500	2	0,00	0,00
<b>Copper as Cu (µg/ℓ)</b>	≤2000	0	0,00	0,00
<b>Vanadium as V(µg/ℓ)</b>	≤200	2	0,00	0,00
<b>Calcium (µg/l)</b>	<150000 Aesthetic/Operational	6800	6306	1271
<b>Magnesium (µg/l)</b>	<70000 Aesthetic/ Health	3884	3534	1422

## 4.5 Membrane testing protocols

### 4.5.1 Membrane pure water flux and permeability coefficient

Compaction tests were carried out on both the UF and NF270 membranes to determine the compaction behaviour of these membranes (Omalanga, 2015) as well as the minimum filtration time to acquire stable fluxes thus improving the reproducibility of membrane tests. Steady state flux was obtained after 130 minutes for the UF membrane and the NF270 membrane showed a steady state flux over the compaction time with three outliers as shown in **Figure 4.19**. The causes of the outliers could not be established. It was established that the commercial NF270 membrane was already compacted, and all other UF membrane tests were subsequently carried out on UF membrane coupons that had been compacted at 6 bars for 130 minutes.

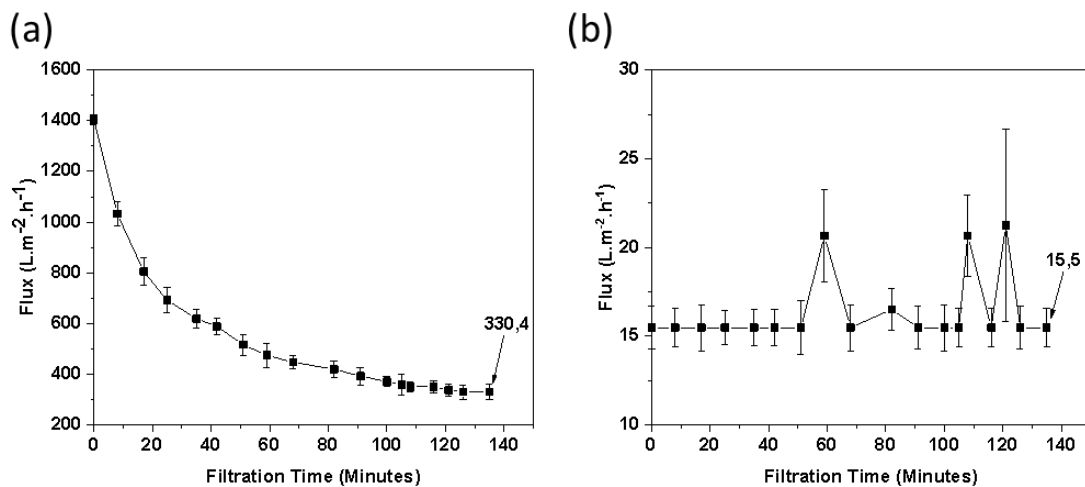


**Figure 4.19:** Compaction of the membranes showing the changes in pure water fluxes of the (a) UF and (b) NF membrane.

The permeability coefficients (A-values) of the membranes were determined from the graph of transmembrane pressure against pure water flux shown in **Figure 4.20**. The pure water permeability coefficient was used to evaluate the operational performance of the membranes (Malczewska & Žak, 2019). The A-value for the UF membrane was determined to be  $57,0 \pm 0,4 \text{ L.m}^{-2}.\text{h}^{-1}.\text{bar}^{-1}$  while that of the NF270 membrane was  $2,17 \pm 0,3 \text{ L.m}^{-2}.\text{h}^{-1}.\text{bar}^{-1}$ . (Mahdi *et al.*, 2019) reported a

permeability of  $36,284 \text{ L.m}^{-2}.\text{h}^{-1}$  for a PES membrane while (May *et al.*, 2021) and (Jung *et al.*, 2019) reported pure water permeability coefficient values of  $11.3 \pm 1.0 \text{ L/h.m}^2 \text{ bar}^{-1}$  and  $11.1 \text{ L.m}^{-2}.\text{h}^{-1}.\text{bar}^{-1}$ , respectively, for the commercial NF270 membrane. The reported values for the NF270 permeability were much higher than the one determined in this study and this may be attributed to the change in properties of the membrane that occurs when membranes are dried (Mecha & Pillay, 2014).

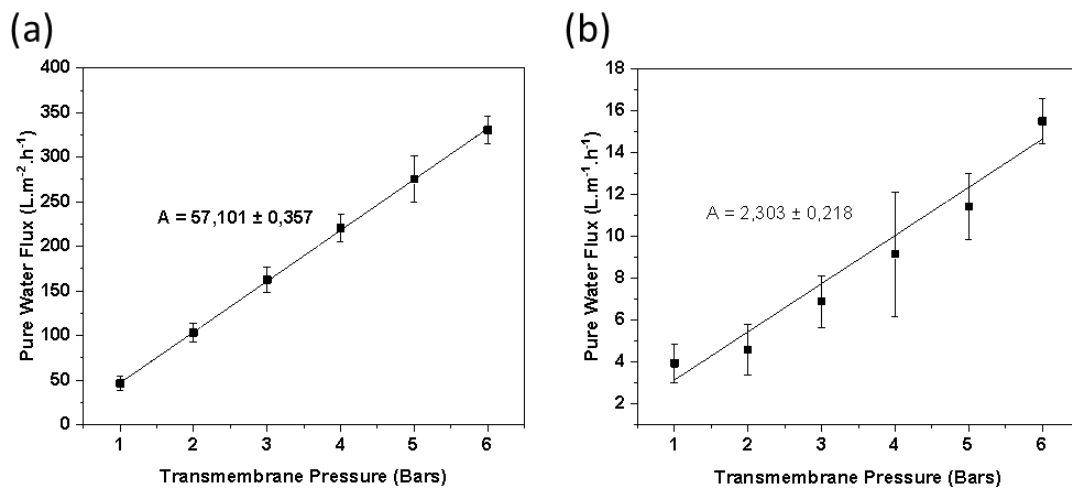


**Figure 4.20:** Determination of the pure water permeability coefficients (A) for the (a) UF and (b) NF membranes.

#### 4.5.2 Determination of fouling resistances

Fouling is a major factor in the operational efficiency (Sorlini & Torretta, 2017) of membranes. **Figure 4.21** shows the experimentally determined resistances of the UF and NF270 membranes. It was seen that the NF membrane had much larger intrinsic membrane and reversible fouling resistances than the UF membrane. The larger intrinsic membrane resistance of the NF membrane is due to the membrane having much smaller pores than those of the UF membrane. The reversible fouling resistance of the NF membrane is high due to the membrane's small effective membrane surface area as well as its high antifouling properties that are due to the

surface properties of the PA layer (May *et al.*, 2021). The high individual resistances of the NF membrane led to it having a high total membrane resistance that is much higher than the UF membrane and explains its lower permeability. A high ratio of  $R_r$  in  $R_t$  is indicative of a membrane with high antifouling properties as the fouling it experiences is mostly reversible (Vatanpour *et al.*, 2020). The NF membrane had a high ratio of  $R_r$  in  $R_t$  of 0,64 when compared to that of the UF membrane of 0,36, which supports that the NF270 membrane has good antifouling properties.

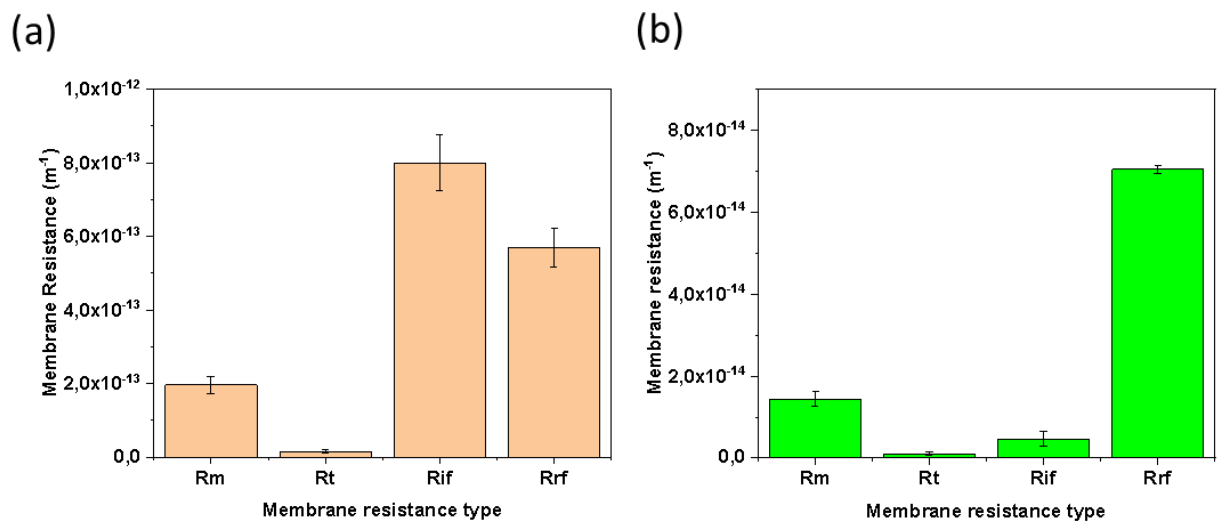


**Figure 4.21:** Membrane resistance values for (a) UF and (b) NF membranes from fouling studies using BSA as a model foulant.

#### 4.5.3 Normalized Flux Ratio (NFR) determination.

The Normalized Flux Ratio is an important parameter that helps in evaluating the performance of membranes. Membranes with greater NFR values or those close to one, have better anti-fouling capacities (Gebru & Das, 2017) hence offer better performance. The NFR value of the NF270 membrane was determined to be 0,694 while that of the UF membrane was found to be 0,652 which indicates that the NF membrane has a lower tendency of fouling than the UF membrane and supports the inference from the reversible fouling resistances of the membranes discussed in **Section 4.5.2**.



#### 4.5.4 Determination of membrane fouling mechanism

Normalized fluxes are important when comparing flux decline between different membranes as the initial flux of the membrane is factored in the flux change. **Figure 4.22** shows the normalized fluxes of the UF, and NF 270 membranes calculated from the filtration of real water samples from the Florida Lake. The flux decline profiles shows that the ultrafiltration membrane has a higher rate of flux decline than the nanofiltration membrane which is also consistent with flux experiments done on NF90 and UF membranes by (Wang & Tarabara, 2008).

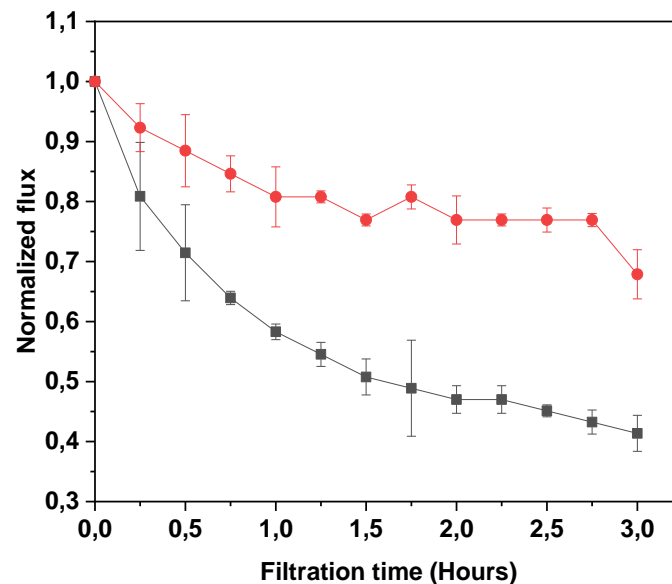


**Figure 4.22:** Normalized fluxes calculated after the filtration of Florida Lake real water by UF and NF270 membranes.

The tendency of different pore blocking mechanisms to be dominant in membrane filtration processes for different feed solutions can be evaluated by fitting linear regression analysis on flux decline data (Wang & Tarabara, 2008). The correlation values can then be used to determine the order of pore blockage mechanism hence understand more on how fouling occurs. The fluxes of the membranes while filtering humic acid synthetic water samples were fitted to Hermia's fouling model's linearized equations to produce **Figure 4.23** for the UF membrane and **Figure 4.24** for the NF membrane. The correlation values ( $R^2$ ) of the different fouling models

were determined and the model with the largest  $R^2$  value was taken as the model that best fitted the dominant fouling model for each membrane. Cake filtration was shown to be the dominant fouling model for the UF membrane while pore constriction was found to be dominant for the NF membrane as shown in **Figure 4.23 (a) and Figure 4.24 (c)**, respectively. UF membranes are reported in literature to adsorb foulants on their surfaces and form cake layers (Wang & Tarabara, 2008) whilst some foulants are also able to enter and clog their pores (Alsawafah *et al.*, 2021). (Wang & Tarabara, 2008) reported that pore blockage was the dominant fouling mechanism for UF membranes and intermediate blocking for NF membranes in their membrane fouling experiments.

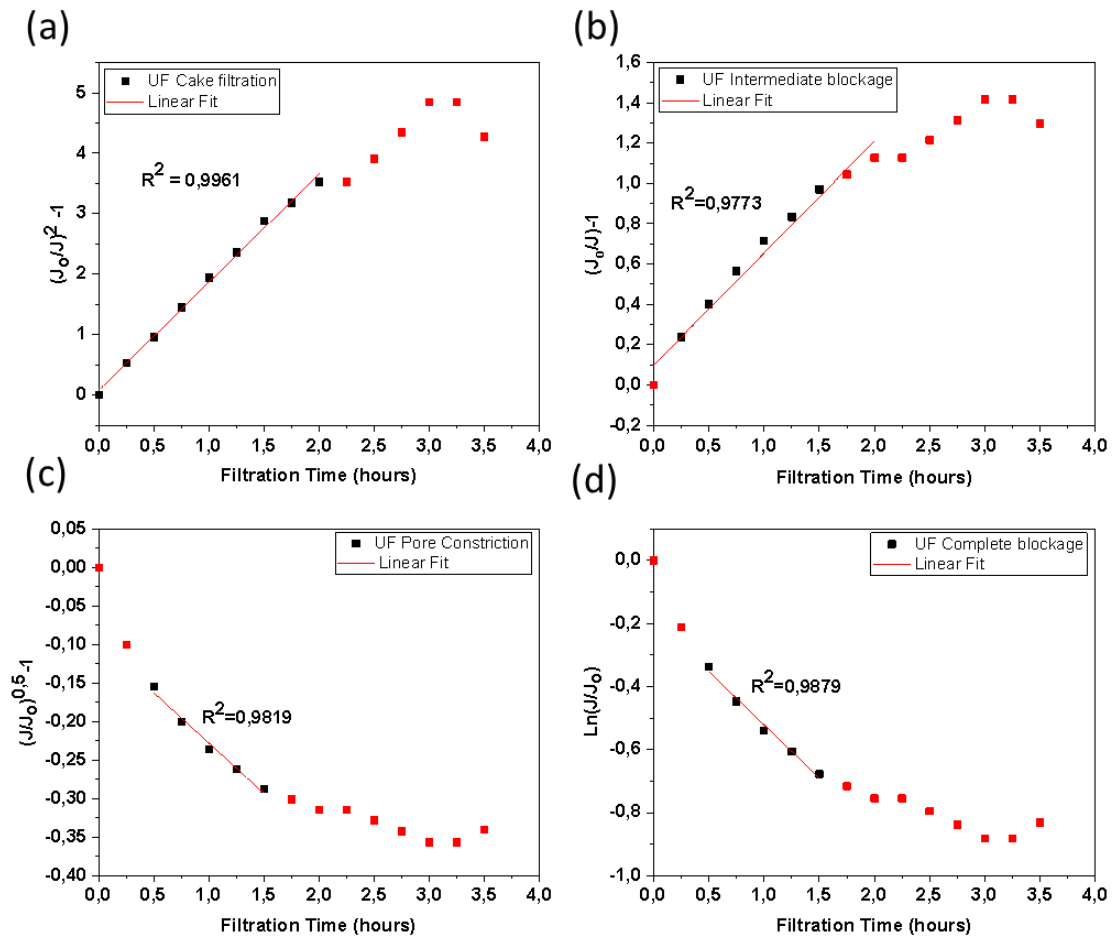


**Figure 4.23:** Modelling of fouling behaviour of UF membrane while filtering Florida Lake real water showing (a) Cake filtration, (b) Intermediate blockage, (c) Pore constriction, and (d) Complete blockage mechanisms.

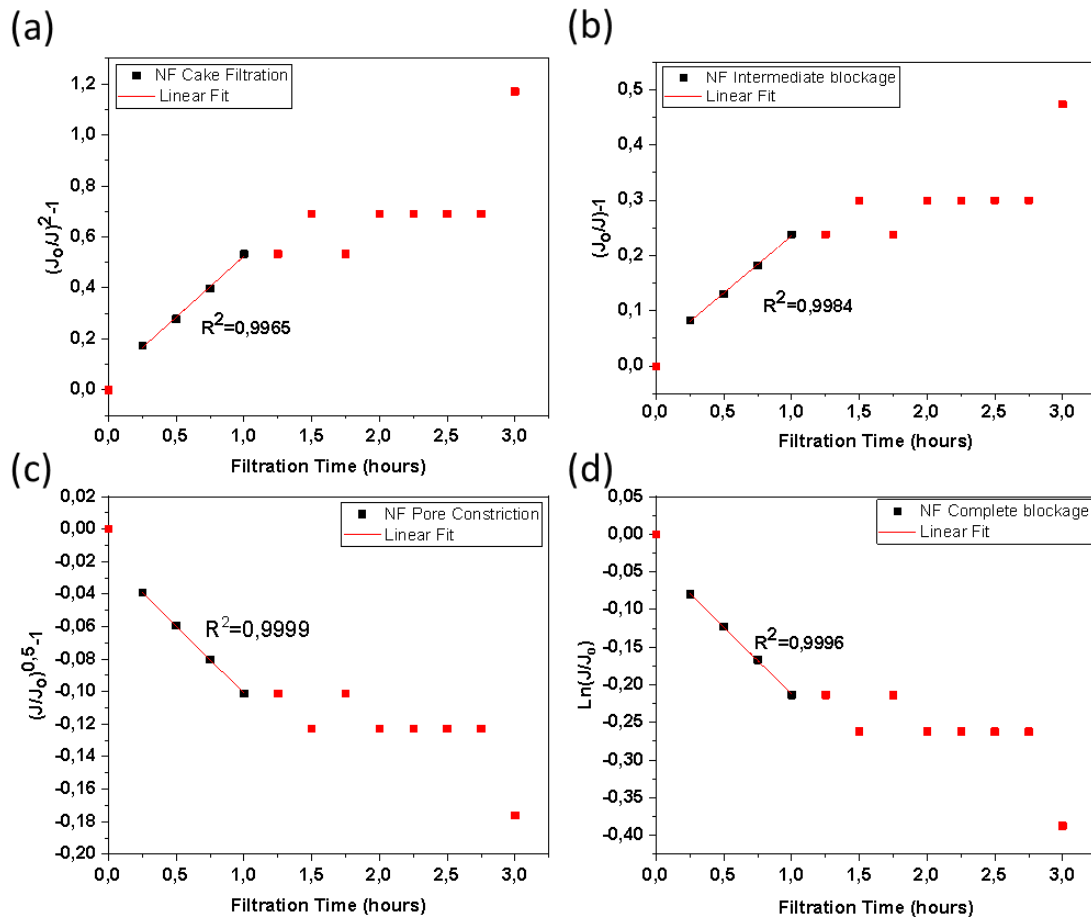


**Figure 4.24:** Modelling of fouling behaviour of NF membrane while filtering Florida Lake real water showing (a) Cake filtration, (b) Intermediate blockage, (c) Pore constriction, and (d) Complete blockage mechanisms.

#### 4.5.5 Humic acid and BSA rejections

Over 70% of Natural Organic Matter (NOM) is composed of humic acid compounds (Mamba *et al.*, 2009) which makes humic acid to be a suitable model humic matter foulant while BSA can be used to a model protein foulant (Padmanaban *et al.*, 2020) as it is a serum albumin which are the most common proteins (Salgin *et al.*, 2017). The rejection of these model foulants are presented in **Table 4.5** and shows that the NF membrane had higher rejections for both humic acid and BSA foulants than the UF membrane. The molecular weight of humic acids is in the range of 500 – 100000 Da (Machenbach, 2007) while for BSA it is 67 kDa (Salgin *et al.*, 2017). This means

that BSA is larger than most humic acids hence its higher rejections by both membranes.

**Table 4.5:** Humic acid and BSA rejections by UF and NF270 membranes.

At 4 bars		UF	NF
Humic acid rejection		66,08%	96,19%
BSA rejection		90,12	91,05

#### 4.5.6 Membrane cleaning

Membrane cleaning is important in reversing fouling effects through removal of the foulant material from the membrane surface and enhance the membrane's performance (García-Fayos *et al.*, 2013). In chemical cleaning, the foulant reacts with a chemical cleaning agent and the chemical speciation is affected by the pH of the solution (Olutona *et al.*, 2012). The pH of the cleaning solution was measured to be 11,06. At a pH above 10, the distribution of species in the solution is shown in **Figure 4.24** which shows that the dominant species are  $\text{HOCl}^{-1}$  and  $\text{ClO}^{-1}$ .

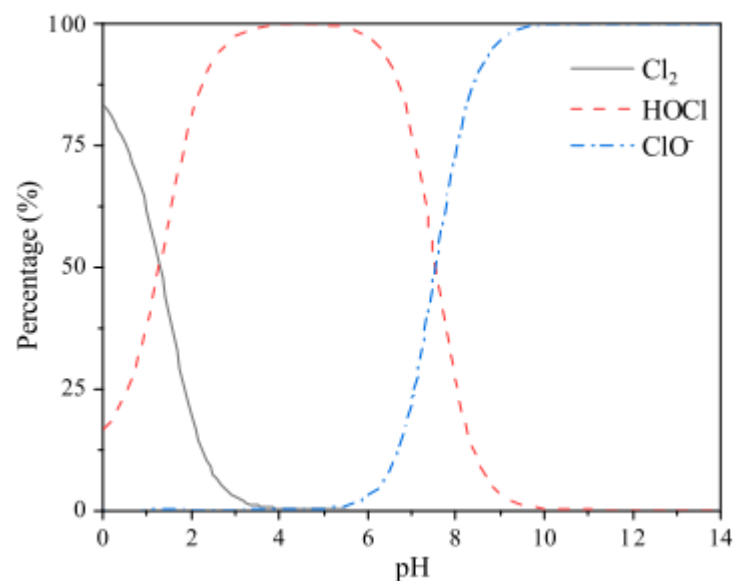
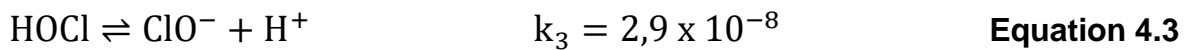
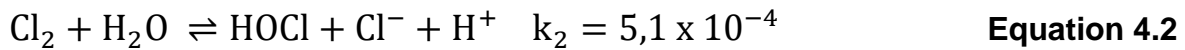
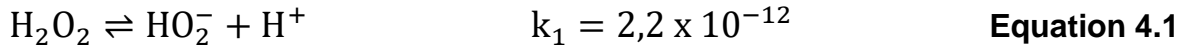


**Figure 4.25:** Alpha diagrams of the dissociation of NaOCl in aqueous solution at different pH values (K. Li *et al.*, 2019b).

The dissociation constants at 25°C for a NaOCl solution shown in **Equations 4.1 to 4.3** (Li *et al.*, 2019) show that the alkaline pH ranges for NaOCl had the highest cleaning efficiency in membrane cleaning.



The efficiency of the chemical cleaning process can be evaluated using the Flux Recovery Ratio (FRR). The normalized flux changes at each cleaning stage for both the NF and UF membranes are shown in **Figure 4.26**. The flux change after cleaning the UF membrane is almost the same at each successive stage. The increase in normalized flux after a successive chemical clean for the NF membrane indicates that the cleaning process was able to remove foulants from the membrane's surface. Both UF (93,5%) and NF (97,9%) membranes showed flux recovery ratios of above 90% indicating a high efficiency of the chemical cleaning. A higher FRR can also be used to indicate a higher antifouling tendency of the membrane (Mahdi *et al.*, 2019) hence the NF membrane had a higher antifouling tendency than the UF membrane.

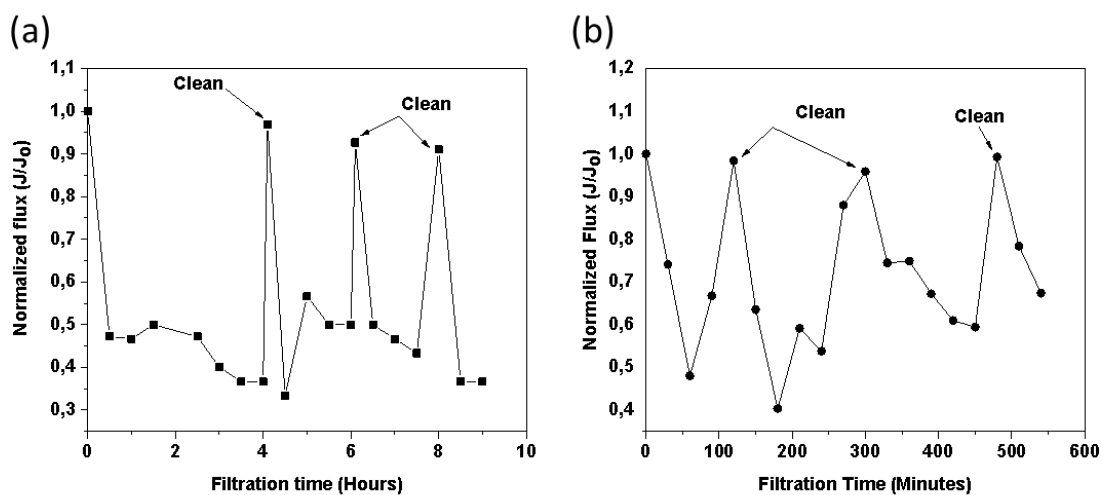


**Figure 4.26:** Change in normalized flux with chemical cleaning for (a) UF and (b) NF270 membranes.

#### **4.5.7 Change in membrane properties between fouling and chemical cleaning.**

The morphology of the membranes changed with the adhesion of the foulants onto the membrane's surface when real and synthetic water samples were filtered. SEM images of the fouled and cleaned, UF membrane coupons that were fouled using humic acid synthetic water samples are shown in **Figure 4.27**. Chemical cleaning visibly reduced the amount of foulants on the membranes' surfaces. The fouled membrane coupons had cake layers from the foulants which were observed on the surfaces of both membranes, while some sediments were observed to be constricting the macro-voids of the UF membranes.

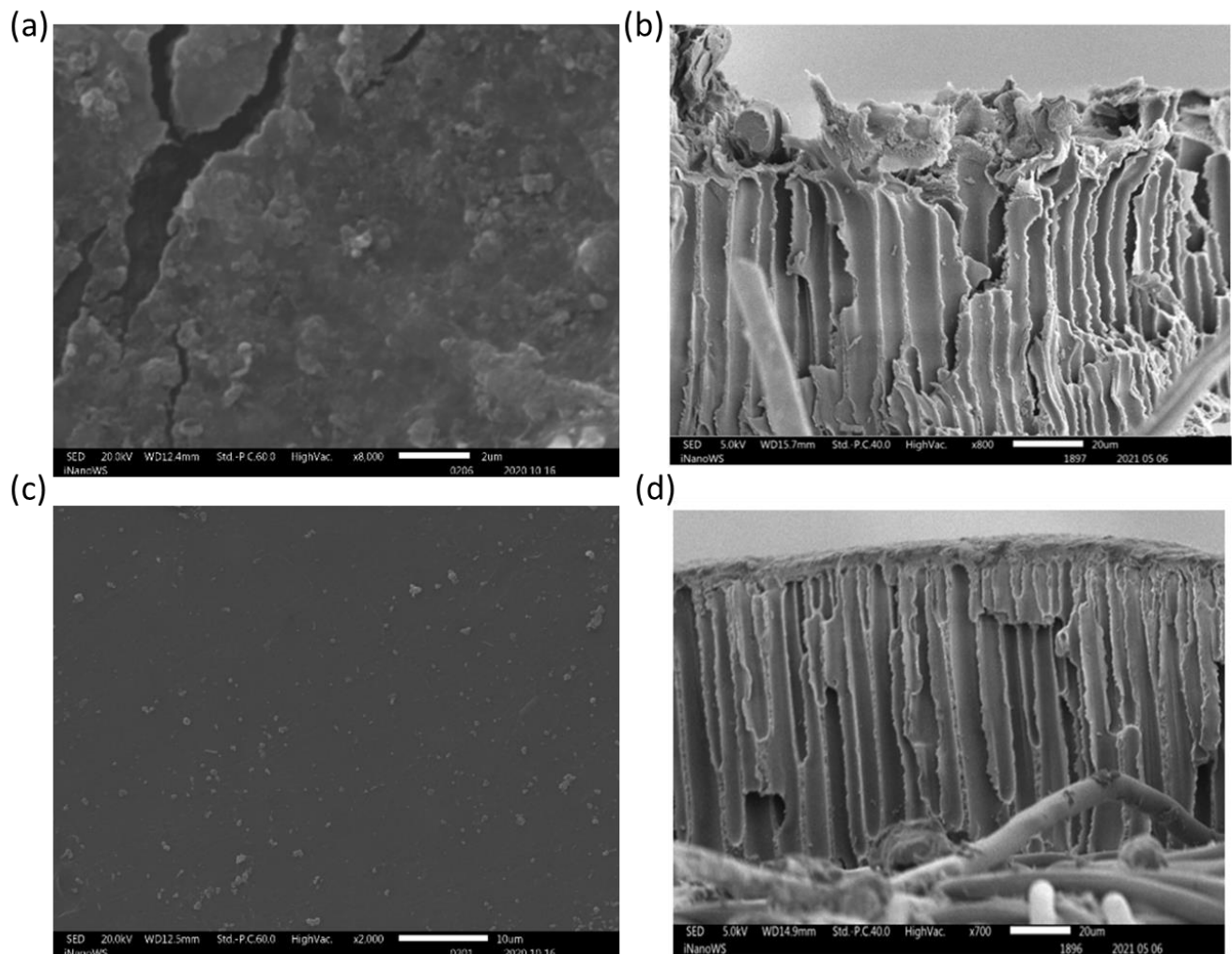


**Figure 4.27:** SEM images of UF membrane coupons after fouling with humic acid synthetic water showing (a) fouled flat surface, (b) fouled cross section, (c)

chemically cleaned flat surface, and (d) chemically cleaned cross-section of membrane coupons.

The SEM images of the fouled and chemically cleaned NF membrane coupons are shown in **Figure 4.28**. The flat surface and cross-sectional SEM images of the NF membrane shows a compact layer of humic acid that attached to the surface after fouling with humic acid. This layer was reduced after chemical cleaning as evidenced by the smoother appearance of the flat surface image and reduced cake layer thickness in the cross-sectional SEM image.

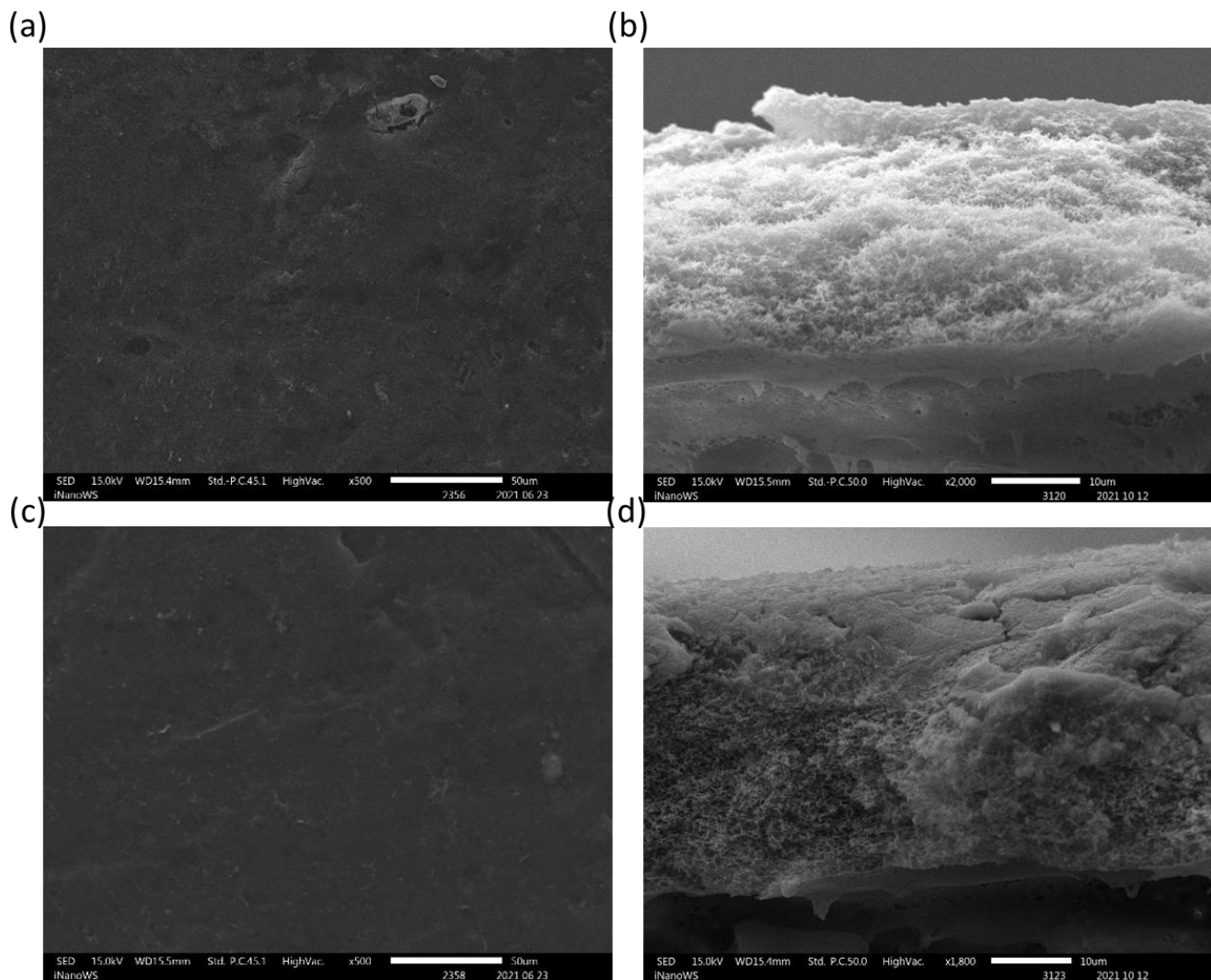


**Figure 4.28:** SEM images of NF membrane coupons after fouling with Humic acid synthetic water showing (a) fouled flat surface, (b) fouled cross section, (c)

chemically cleaned flat surface, and (d) chemically cleaned cross-section of membrane coupons.

Surface roughness is a more important factor in controlling membrane fouling when compared with the membrane's contact angle as it affects how foulants interact with the surface of the membrane. This leads to foulants filling up depressions and pores on the surface of the membranes which can be detected on AFM images (N. Lee et al., 2004). **Figure 4.29** shows the AFM images of UF membrane coupons that had been fouled with humic acid. The UF membrane had a SA roughness value of 495.917 nm and SQ of 683.19 nm after fouling. There was a marked increase in roughness due to the foulants attached to the membrane's surface that produced a more pronounced ridge and valley surface morphology as shown in the 3D micrograph of the UF membrane in **Figure 4.29 (a)**. The increase in roughness of the fouled membrane when compared with the clean membrane is supported by research done by (Huang *et al.*, 2021) who measured the roughness of different types of ultrafiltration membrane before and after fouling with different foulants and found that the roughness increased in most of the analysed samples.

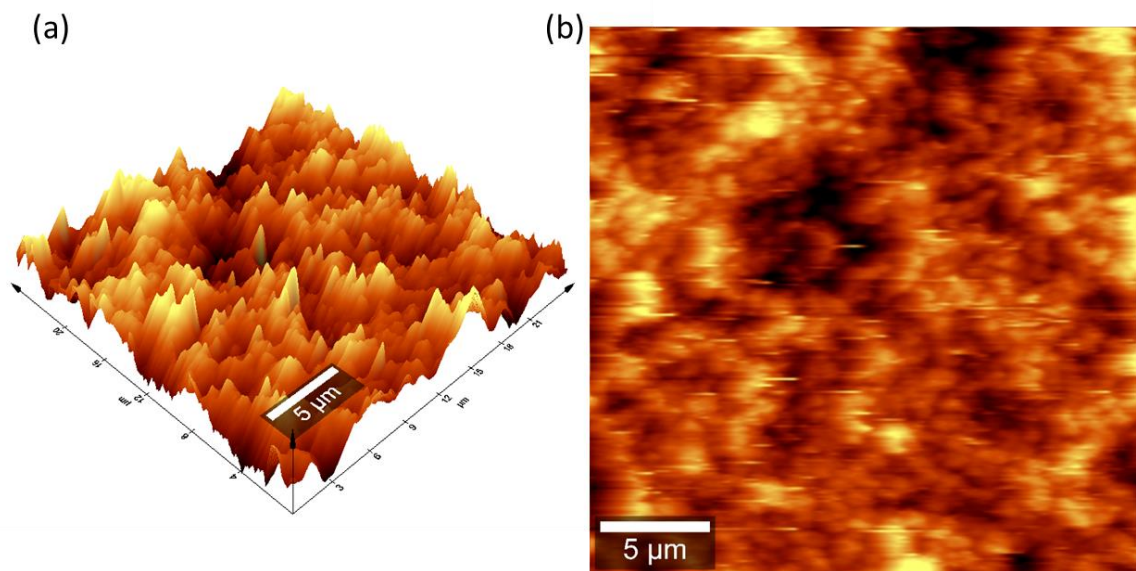


**Figure 4.29:** AFM images of surface of UF membrane after fouling with Humic Acid synthetic water showing (a) 3D mage and (b) Flat surface image of the fouled membrane.



The cleaned UF membrane had an SA roughness of 196.109 nm and SQ roughness of 258.661nm which were both smaller than their respective roughness values for the fouled membrane. The AFM micrographs are shown in **Figure 4.30** and the 3D AFM micrograph shows a marked decrease in the number and heights of surface ridges which shows a decrease in the amount of foulants attached to the membrane's surface.

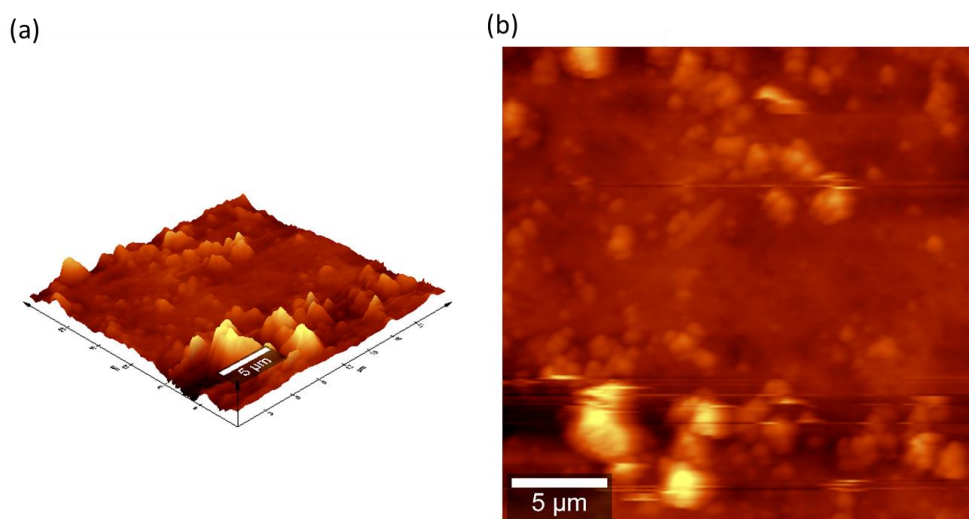


**Figure 4.30:** AFM images of surface of UF membrane after fouling with Humic Acid synthetic water then cleaning with NaOCl solution showing (a) 3D mage and (b) Flat surface image of the cleaned membrane.

Nanofiltration membrane coupons were fouled using humic acid feed solutions and their AFM images are shown in **Figure 4.31**. The membrane had a roughness SA of 141.907 nm and SQ of 185.407 nm. The roughness measurements of the fouled membrane were determined to be smaller than those of the pristine membrane.

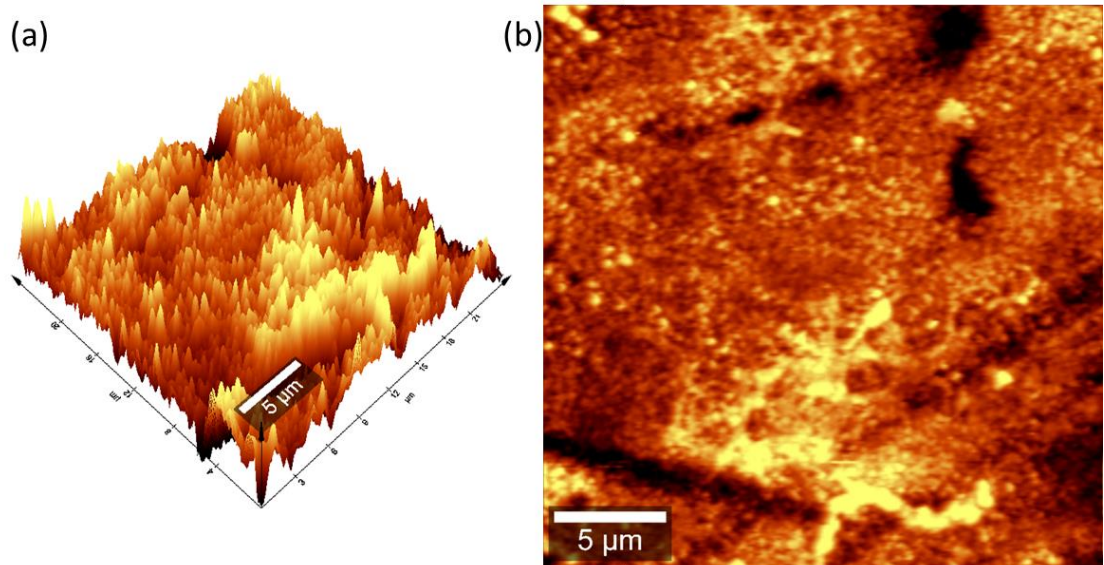


**Figure 4.31:** AFM images of surface of an NF membrane coupon that had been fouled by HA fouled showing (a) 3D mage of Fouled membrane, and (b) Flat surface image of fouled membrane.

The AFM images of the chemically cleaned NF membrane coupons after they had been fouled using humic acid synthetic feed water are shown in **Figure 4.32**. The roughness measurements of the cleaned NF membrane were determined to be  $SA = 83.8371 \text{ nm}$  and  $SQ = 106.751 \text{ nm}$ . These roughness measurements were much lower than for the fouled membrane and shows that some of the attached foulants were removed by the chemical cleaning.

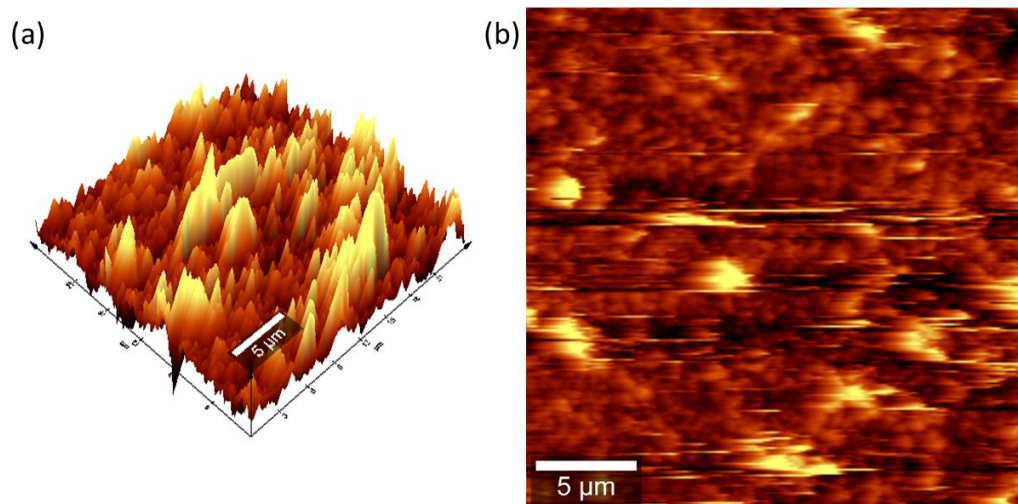


**Figure 4.32:** AFM images of the chemically cleaned NF membrane that had been fouled with humic acid synthetic feed water solutions showing (a) 3D image and (b) Flat surface image of the fouled membrane.

The attachment of foulants onto the membrane's surface alters its wettability and these changes can be investigated by measuring the water contact angles of the membrane after fouling and cleaning processes. **Figure 4.33** shows the changes in contact angles of the UF and NF270 membranes before and after fouling with 50ppm of Humic Acid (HA) feed solution and chemically cleaning with a NaOCl solution. Fouled UF and NF270 membranes had lower contact angles than those of the pristine membranes implying a higher hydrophilicity. This was attributed to polar organic groups in NOM that had adsorbed on the membrane surface. The lowering of contact angles of the membranes after fouling is supported by work done by (Li *et al.*, 2015) who measured contact angles of PES ultrafiltration membranes before and after fouling with model foulants and found that the contact angle of the fouled membranes were much lower than those of the pristine membranes. The removal of these foulants by chemical cleaning led to an increase in the contact angles of the cleaned membranes. Chemical cleaning did not remove all foulants as the

contact angles after the cleaning process were still lower than that of the pristine membrane. The difference in contact angles of the pristine and chemically cleaned membranes was smallest for the NF membrane which supports the idea that the NF270 membrane had higher antifouling properties than the UF membrane.

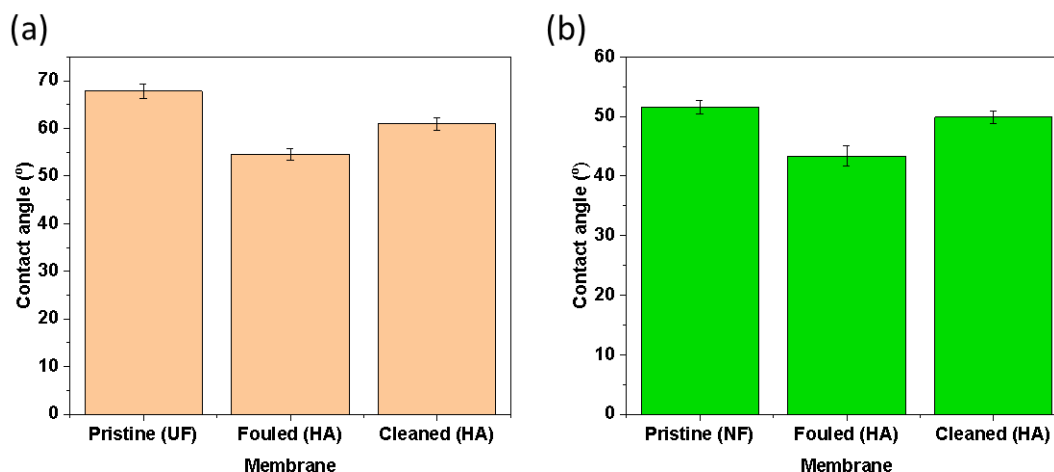


**Figure 4.33:** Contact angles of the (a) UF and NF270 (b) membranes before and after fouling (F) with 50ppm Humic acid (HA) feed solution and chemical cleaning (C).

The changes in hydrophilicity of the membrane were supported by changes in surface free energy of the membranes using humic acid as a model foulant. **Figure 4.34** shows the changes in the surface free energy of the pristine UF and NF membranes, after fouling, and chemical cleaning, respectively. There was a general decrease in the SFE from that of the pristine UF membrane after fouling. Chemical cleaning of the membrane led to an increase in the SFE, but this increase led to a SFE value of the cleaned membrane that was above that of the pristine membrane. This may indicate a degradation of the UF membrane surface after chemical cleaning. For the NF membrane, there was a general increase in the SFE from that of the pristine to that of the fouled membrane. Chemical cleaning led to a decrease in the SFE of the membrane, but this was still above that of the SFE. This may be explained by the presence of foulants on the membrane surface after chemical cleaning. The SFE value of the pristine NF membrane was shown to be higher than that of the UF membrane, which indicates a higher antifouling tendency as the

foulants must overcome a higher energy value to attach to the surface of the NF membrane as opposed to that of the UF membrane.

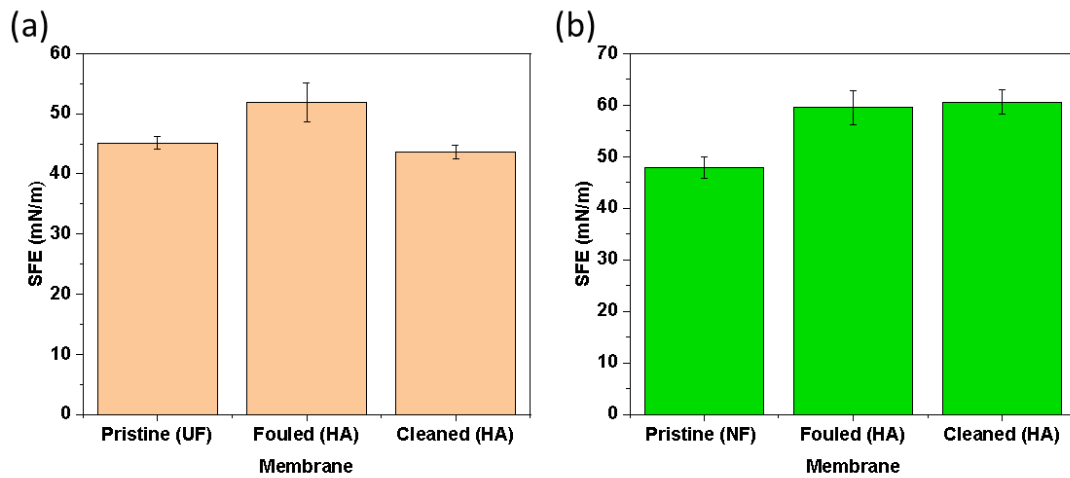


**Figure 4.34:** Surface Free Energies (SFE) of pristine, fouled and chemically cleaned (a) UF and (b) membrane coupons.

#### 4.6 Evaluation of prototype using deionized water

The ability of the system to generate enough transmembrane pressure to power the ultrafiltration process was proven by the production of permeate by the system under real world conditions. This test proved the feasibility of the system and the effect of the amount of solar radiation on flux was investigated. These tests were conducted in the November – December period which is amongst the warmest times in the country. The test also served as a proof of concept . **Figure 4.35** shows the average performances of the system in two selected segments of each month. It was observed that the pressure generation and permeate flux production were directly dependent on the prevailing atmospheric temperature and solar irradiation. The maximum flux was recorded in the midday period (1100 – 1400 hours) which marked the hottest time of the day. At this time of the day, the atmospheric air temperature and solar irradiation were at their peaks as shown in **Table 4.6**.

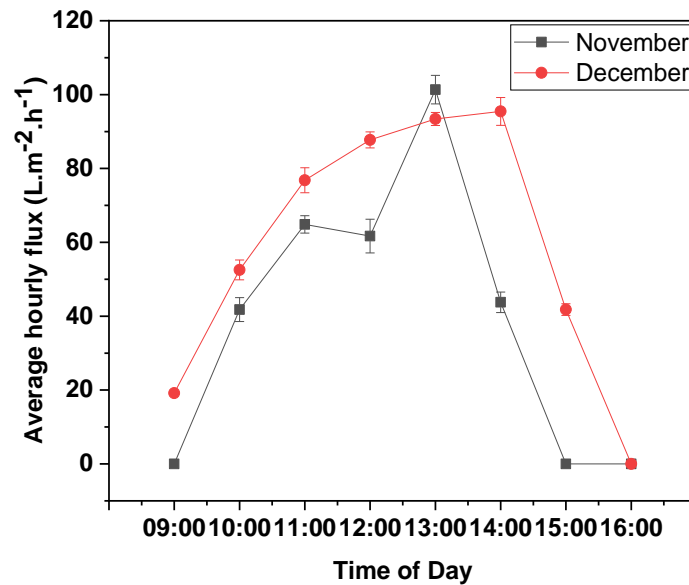


**Figure 4.35:** Correlation of time of day to flux over two months on field prototype with UF membrane.

**Table 4.6:** Average hourly weather conditions recorded for specific periods in November and December

Time of Day	November hourly averages			December hourly averages		
	Solar intensity (W/m <sup>2</sup> )	Air temperature (°C)	Wind speed (KPH)	Solar intensity (W/m <sup>2</sup> )	Air temperature (°C)	Wind speed (km/h)
0900	661	20	4	656	24	1
1000	734	28	3	753	24	0
1100	934	31	11	925	29	1
1200	981	31	8	1075	32	4
1300	911	32	3	751	31	0
1400	887	31	8	715	30	7
1500	651	26	1	607	27	3
1600	592	24	4	472	26	8

As shown in **Table 4.6**, the air temperature and solar irradiation gradually increased during the morning hours, peaked during the afternoon hours, then declined to a minimum in the evening hours. This decline in temperature and solar irradiation is necessary in the operation of the system as it allows for the condensation of the working liquid thereby completing the cycle of expansion and compression of the system. There was no observable correlation between wind speed and time of day. The system was also observed to have a few challenges as there was some heat

transfer into the feed water during operation which led to the production of warm water that cannot be directly consumed. Rural homestead settings also have high water demands during the morning and evening hours which will be difficult to meet using this system as maximum water production was reached by the system during the afternoon hours as shown **Figure 4.35**. As such, the next sections of this study sought to improve the heat transfer and pressure generation capacity of the working liquid, as well as the flux production of the system.

## **4.7 Conclusions**

The stand-alone solar driven system was successfully field-tested using ultrafiltration membranes and proved the feasibility of the application of these membranes on the system. It was also shown that the flux produced was also directly proportional to the solar radiation received as well as the air temperature. Surface water samples were successfully collected from a lake and a stream and analysed using different analytical techniques. The raw water from these surface water sources were found to be not severely impaired, but not safe for direct consumption. As such, the objective of determining the physicochemical properties of raw surface water samples was successfully achieved. Ultrafiltration (UF) and nanofiltration (NF) membranes used in the filtration processes were characterized successfully using different techniques. The UF membrane was found to have lower rejections and anti-fouling properties than the NF membrane. The dominant fouling mechanism affecting the UF membrane was identified to be cake filtration while that for the NF membrane was pore constriction. Chemical cleaning using NaOCl successfully retained the flux of both membranes to above 90% which meant that this is a good cleaning method. The filtrates from both ultrafiltration and nanofiltration of the raw water samples had water qualities that fell within the tested drinking water quality guidelines. Overall, the UF membrane was found to be more suitable for application on the prototype as it produced a much higher flux than the NF membrane. This is ideal for the prototype as weather conditions are variable and there is not always a high solar insolation to sustain the high pressures required for high flux production using an NF membrane. The objective of evaluating and

comparing the suitability of ultrafiltration and nanofiltration membranes for application in the solar-driven filtration system was thus met.

## **4.8 References**

- Agboola, O., Maree, J., & Mbaya, R. (2014). Characterization and performance of nanofiltration membranes. *Environ Chem Lett*, 12, 241–255.  
<https://doi.org/10.1007/s10311-014-0457-3>
- Alsawaftah, N., Abuwatfa, W., Darwish, N., & Hussein, G. (2021). A Comprehensive Review on Membrane Fouling : Mathematical. *Water*, 13(1327). <https://doi.org/10.3390/w13091327>
- Archer, A. D., & Singer, P. C. (2006). An evaluation of the relationship between SUVA and NOM coagulation using the ICR database. *American Water Works Association*, 98(7), 110–123. <http://www.jstor.org/stable/41313741>.
- Barghi, H. (2014). Functionalization of Synthetic Polymers for Membrane Bioreactors Hamidreza Barghi Functionalization of Synthetic Polymers for Membrane Bioreactors. *Chalmers University of Technology*.
- Bernat, X., Sánchez, I., Stüber, F., Bengoa, C., Fortuny, a, Fabregat, a, & Font, J. (2007). Removal of heavy metals by ultrafiltration. *European Congress of Chemical Engineering, September*, 16–20.  
[https://folk.ntnu.no/skoge/prost/proceedings/ecce6\\_sep07/upload/454.pdf](https://folk.ntnu.no/skoge/prost/proceedings/ecce6_sep07/upload/454.pdf)
- Bick, A., Gillerman, L., Manor, Y., & Oron, G. (2012). Economic Assessment of an Integrated Membrane System for Secondary Effluent Polishing for Unrestricted Reuse. *Water*, 219–236. <https://doi.org/10.3390/w4010219>
- Bokhary, A., Tikka, A., Leitch, M., & Liao, B. (2018). Membrane Fouling Prevention and Control Strategies in Pulp and Paper Industry Applications. *Journal of Membrane Science and Research*, May, 180–197.  
<https://doi.org/10.22079/JMSR.2018.83337.1185>
- Carbonell-Alcaina, C., Corbatón-Báguena, M.-J., Álvarez-Blanco, S., Bes-Piá, A., Mendoza-Roca, J. A., & Pastor-Alcañiz, L. (2016). Determination of fouling mechanisms in polymeric ultrafiltration membranes using residual brines from table olive storage wastewaters as feed. *Journal of Food Engineering*, 187,



- 14–23. <https://doi.org/10.1016/j.jfoodeng.2016.04.016>
- Carifio, B. A. (2016). Extending the Service Life of Activated Carbon Filters  
Extending the Service Life of Activated Carbon Filters. *Journal of the New England Water Works Association*, 225–233.
- Challener, C. (2011). Handbook for the operation of Water treatment works. In  
*Chemistry & Industry* (Vol. 3).  
<http://content.ebscohost.com/ContentServer.asp?T=P&P=AN&K=57995235&S=R&D=bth&EbscoContent=dGJyMNxb4kSepY4yOvsOLCmr06eqK9SsKi4SK+WxWXS&ContentCustomer=dGJyMPGut1C0rLNRuePfgeyx44Dt6fIA>
- Charles, J., Ramkumaar, G. R., Azhagiri, S., & Gunasekaran, S. (2009). FTIR and Thermal Studies on Nylon-66 and 30 % Glass Fibre Reinforced Nylon-66.  
*Journal of Chemistry*, 6(1), 23–33. <https://doi.org/10.1155/2009/909017>
- Coates, J. (2000). Interpretation of Infrared Spectra , A Practical Approach.  
*Encyclopedia of Analytical Chemistry*, 1–23.  
<https://doi.org/10.1002/9780470027318.a5606>
- Cuperus, F. P., & Smolders, C. A. (1991). Characterization of UF Membranes  
Membrane Characteristics and Characterization Techniques. *Advances in Colloid and Interface Science*, 34, 135–173. [https://doi.org/10.1016/0001-8686\(91\)80049-P](https://doi.org/10.1016/0001-8686(91)80049-P)
- Dach, H. (2009). Comparison of nanofiltration and reverse osmosis processes for a selective desalination of brackish water feeds. tel-0043351. *Engineering Sciences*. <https://tel.archives-ouvertes.fr/tel-00433513>
- Du, X., Shi, Y., & Jegatheesan, V. (2020). A Review on the Mechanism , Impacts and Control Methods of Membrane Fouling in MBR System. *Membranes*, 10(24), 1–33. <https://doi.org/doi:10.3390/membranes10020024>
- García-Fayos, B., Arnal, J. M., & Sancho, M. (2013). Cleaning of ultrafiltration membranes after the treatment of surface water: Static-dynamic test.  
*Desalination and Water Treatment*, 51(1–3), 609–616.  
<https://doi.org/10.1080/19443994.2012.704687>
- García-Pacheco, R., Li, Q., Comas, J., Taylor, R. A., & Le-Clech, P. (2020). Novel housing designs for nanofiltration and ultrafiltration gravity-driven recycled membrane-based systems. *Science of the Total Environment*, 144181.  
<https://doi.org/10.1016/j.scitotenv.2020.144181>

- Gebru, K. A., & Das, C. (2017). Preparation and Characterization of CA – PEG – TiO<sub>2</sub> Membranes : Effect of PEG and TiO<sub>2</sub> on Morphology , Flux and Fouling Performance. *Journal of Membrane Science and Research*, 3, 90–101.  
<https://doi.org/10.22079/jmsr.2016.22820>
- Ghiggi, F. F., Pollo, L. D., Cardozo, N. S. M., & Tessaro, I. C. (2017). Preparation and characterization of polyethersulfone / N-phthaloyl- chitosan ultra fi ltration membrane with antifouling property. *European Polymer Journal*, 92(April), 61–70. <https://doi.org/10.1016/j.eurpolymj.2017.04.030>
- Guo, Y., Liang, H., Li, G., Xu, D., Yan, Z., Chen, R., Zhao, J., & Tang, X. (2021). A solar photo-thermochemical hybrid system using peroxydisulfate for organic matters removal and improving ultrafiltration membrane performance in surface water treatment. *Water Research*, 188, 116482.  
<https://doi.org/10.1016/j.watres.2020.116482>
- Haarhoff, J., Kubare, M., Mamba, B., Krause, R., Nkambule, T., Matsebula, B., & Menge, J. (2010). NOM characterization and removal at six Southern African water treatment plants. *Drinking Water Engineering and Science*, 3, 53–61.  
<http://dx.doi.org/10.5194/dwes-3-53-2010>
- Hernando, N. P. (2016). Nanofiltration and Hybrid Sorption – Ultrafiltration Processes for Improving Water Quality. *Universitat Politècnica de Catalunya*.  
<https://www.tdx.cat/bitstream/handle/10803/403852/TNPH1de1.pdf?sequence=2.xml>
- Huang, W., Zhu, Y., Dong, B., Lv, W., Yuan, Q., Zhou, W., & Lv, W. (2021). Investigation of membrane fouling mechanism of intracellular organic matter during ultrafiltration. *Scientific Reports*, 11(1), 1–16.  
<https://doi.org/10.1038/s41598-020-79272-4>
- Jung, O., Saravia, F., Wagner, M., Heißler, S., & Horn, H. (2019). Quantifying concentration polarization-Raman Microspectroscopy for In-Situ Measurement in a flat Sheet cross-flow Nanofiltration Membrane Unit. *Scientific Reports*, 9(15885). <https://doi.org/10.1038/s41598-019-52369-1>
- Kajitvichyanukul, P., Shammas, N. K., Hung, Y.-T., Wang, L. K., & Ananpattarachai, J. (2011). Membrane and Desalination Technologies. In L. Wang, J. Chen, Y. Hung, & N. Shammas (Eds.), *Handbook of Environmental Engineering 13: Membrane and Desalination Technologies* (Volume 13, Vol.

- 13). Humana Press. <http://www.springerlink.com/index/10.1007/978-1-59745-278-6>
- Keurentjes, J. T. F., Harbrecht, J. G., Brinkman, D., Hanemaaijer, J. H., Cohen Stuart, M. A., & Riet, van 't, K. (1989). Hydrophobicity measurements of microfiltration and ultrafiltration membranes. *Journal of Membrane Science*, 47(3), 333–344. [https://doi.org/10.1016/S0376-7388\(00\)83084-7](https://doi.org/10.1016/S0376-7388(00)83084-7)
- Khan, B., Haider, S., Khurram, R., Wang, Z., & Wang, X. (2020). Preparation of an Ultrafiltration ( UF ) Membrane with Narrow and Uniform Pore Size Distribution via Etching of SiO<sub>2</sub> Nano-Particles in a Membrane Matrix. *Membranes*. <https://doi.org/10.3390/membranes10070150>
- Kimura, S. (1991). Characterization of Ultrafiltration Membranes. *Polymer Journal*, 23(5), 389–397. <https://doi.org/10.1295/polymj.23.389>
- Kozbial, A., Li, Z., Conaway, C., McGinley, R., Dhingra, S., Vahdat, V., Zhou, F., Urso, B. D., Liu, H., & Li, L. (2014). Study on the Surface Energy of Graphene by Contact Angle Measurements. *Langmuir*, 30, 8598–8606. <https://doi.org/dx.doi.org/10.1021/la5018328>
- Le, N. L., & Nunes, S. P. (2016). Materials and membrane technologies for water and energy sustainability. *Sustainable Materials and Technologies*. <https://doi.org/10.1016/j.susmat.2016.02.001>
- Lee, N., Buisson, H., Amy, G., & Croue, J. (2004). Identification and understanding of fouling in low-pressure membrane ( MF / UF ) filtration by natural organic. *Water Research*, 38, 4511–4523. <https://doi.org/10.1016/j.watres.2004.08.013>
- Li, F., Deng, C., Du, C., Yang, B., & Tian, Q. (2015). Fouling mechanism and cleanability of ultrafiltration membranes modified with polydopamine-graft-PEG. *Water SA*, 41(4), 448–456. <https://doi.org/10.4314/wsa.v41i4.03>
- Li, K., Li, S., Huang, T., Dong, C., Li, J., Zhao, B., & Zhang, S. (2019). Chemical Cleaning of Ultrafiltration Membrane Fouled by Humic Substances: Comparison between Hydrogen Peroxide and Sodium Hypochlorite. *International Journal of Environmental Research and Public Health*, 16(14). <https://doi.org/10.3390/ijerph16142568>
- Liu, Y., Lin, B., Liu, W., Li, J., Gao, C., & Pan, Q. (2018). Preparation and characterization of a novel nano filtration membrane with chlorine-tolerant property and good separation performance. 36430–36440.

- <https://doi.org/10.1039/c8ra06755d>
- Machenbach, I. (2007). Drinking Water Production by Coagulation and Membrane Filtration. *Norwegian University of Science and Technology* (Issue September).
- Mahdi, N., Kumar, P., Goswami, A., Perdicakis, B., Shankar, K., & Sadrzadeh, M. (2019). Robust polymer nanocomposite membranes incorporating discrete TiO<sub>2</sub> nanotubes for water treatment. *Nanomaterials*, 9(9), 1–18. <https://doi.org/10.3390/nano9091186>
- Mahlangu, O. T. & Mamba B. B., (2021). Interdependence of Contributing Factors Governing Dead-End Fouling of Nanofiltration Membranes. *Membranes*. <https://doi.org/10.3390/membranes11010047>
- Mahlangu, T. O., Msagati, T. A. M., Hoek, E. M. V., Verliefde, A. R. D., & Mamba, B. B. (2014). Rejection of pharmaceuticals by nanofiltration ( NF ) membranes : Effect of fouling on rejection behaviour. *Physics and Chemistry of the Earth*, 76–78, 28–34. <https://doi.org/10.1016/j.pce.2014.11.008>
- Malczewska, B., & Žak, A. (2019). Structural Changes and Operational Deterioration of the Uf Polyethersulfone (Pes) Membrane Due to Chemical Cleaning. *Scientific Reports*, 9(1), 1–15. <https://doi.org/10.1038/s41598-018-36697-2>
- Mamba, B., Krause, R., Malefetse, T., Sithole, S., & Nkambule, T. (2009). Humic acid as a model for natural organic matter ( NOM ) in the removal of odorants from water by cyclodextrin polyurethanes. *Water SA*, 35(1), 117–120. <http://dx.doi.org/10.4314/wsa.v35i1.76648>
- Marais, S. S., Ndlangamandla, N. G., Bopape, D. A., Strydom, W. F., Moyo, W., Chaukura, N., Kuvarega, A. T., Kock, L. De, Mamba, B. B., Msagati, T. A. M., & Nkambule, T. I. (2018). *Natural organic matter (NOM) in South African waters: Vol. I* (Issue 2468). [http://www.wrc.org.za/wp-content/uploads/mdocs/2468\\_FinalReporVoll.pdf](http://www.wrc.org.za/wp-content/uploads/mdocs/2468_FinalReporVoll.pdf)
- May, P., Laghmari, S., & Ulbricht, M. (2021). Concentration Polarization Enabled Reactive Coating of Nanofiltration Membranes with Zwitterionic Hydrogel. *Membranes*, 11(187), 1–24. <https://doi.org/https://doi.org/10.3390/membranes11030187>
- Mecha, C. A., & Pillay, V. L. (2014). Development and evaluation of woven fabric

- micro filtration membranes impregnated with silver nanoparticles for potable water treatment. *Journal of Membrane Science*, 458, 149–156.  
<https://doi.org/10.1016/j.memsci.2014.02.001>
- Merwe, I. W. Van Der. (1998). Application of nanofiltration in metal recovery. *The Journal of The South African Institute of Mining and Metallurgy*.
- Metcalf, G., Pillay, L., Murutu, C., Chiburi, S., Gumede, N., & Gaydon, P. (2014). *Wastewater reclamation for potable reuse (2). Water Research Commission*.  
<https://www.green-cape.co.za/assets/Sector-files/water/Reclamation-and-reuse/WRC-Wastewater-reclamation-for-potable-reuse-volume-1-evaluation-of-membrane-bioreactor-technology-for-pretreatment-2014.pdf>
- Ming, C., Aroua, M. K., Hussain, M. A., & Ismail, W. M. Z. W. (2015). Practical performance analysis of an industrial-scale ultrafiltration membrane water treatment plant. *Journal of the Taiwan Institute of Chemical Engineers*, 46, 132–139. <https://doi.org/10.1016/j.jtice.2014.09.013>
- Mohamad, S. H., Idris, M. I., Abdullah, H. Z., & Ismail, A. F. (2013). Short Review of Ultrafiltration Polymer Membrane As a Self-Cleaning and Antifouling in the Wastewater System. *Advanced Materials Research*, 795, 318–323.  
<https://doi.org/10.4028/www.scientific.net/AMR.795.318>
- Moitsheki, L. J. (2003). Nanofiltration: Fouling and chemical cleaning. *Potchefstroom University for Christian Higher Education*.  
[http://repository.nwu.ac.za/bitstream/handle/10394/391/moitsheki\\_lj.pdf](http://repository.nwu.ac.za/bitstream/handle/10394/391/moitsheki_lj.pdf)
- Mouhoumed, E. I., Szymczyk, A., Schäfer, A., Paugam, L., Mouhoumed, E. I., Szymczyk, A., Schäfer, A., Paugam, L., & Physico-, Y. La. (2014). Physico-chemical characterization of polyamide NF / RO membranes : Insight from streaming current measurements. <https://hal.archives-ouvertes.fr/hal-0098753>
- Moyo, W., Chaukura, N., Motsa, M. M., Msagati, T. A. M., & Mamba, B. B. (2020). Monitoring the characteristics and removal of natural organic matter fractions in selected South African water treatment plants. *Water Practice & Technology*, 15(4), 932–946. <https://doi.org/10.2166/wpt.2020.075>
- Muhamad, M. S., Salim, M. R., & Lau, W. (2015). Preparation and characterization of PES / SiO<sub>2</sub> composite ultrafiltration membrane for advanced water treatment. *Korean J. Chem. Eng.*, 32(11), 2319–2329.  
<https://doi.org/10.1007/s11814-015-0065-3>

- Mutlu, O., Demirkol, G. T., & Çetin, E. (2017). Removal of natural organic matter from drinking water by hybrid coagulation/adsorption - membrane filtration. *Fresenius Environmental Bulletin*, 26(113), 499–509.
- Nora, A., Hamzah, S., & Ali, A. (2017). Preparation and Characterization of Asymmetric Ultrafiltration Membrane for Lysozyme Separation : Effect of Polymer Concentration *Journal of Applied Membrane Science & Technology*. 11. <https://doi.org/10.11113/amst.v11i1.76>
- Olutona, G. O., Aribisala, O. G., & Akintunde, E. A. (2012). A study of chemical speciation of metals in aquatic bottom sediment of Aiba reservoir , Iwo , Nigeria. *Journal of Environmental Science and Technology*, 6(8), 312–321. <https://doi.org/10.5897/AJEST11.227>
- Omalanga, S. L. (2015). Effect of functionalized multi-walled carbon nanotubes on a polysulfone ultrafiltration membrane. *Universtiy of the Witwatersrand*.
- Padmanaban, V. C., Samal, A. K., & Hawari, A. H. (2020). Organic Fouling in Forward Osmosis : A Comprehensive Review. *Water*, 12(1505). <https://doi.org/doi:10.3390/w12051505>
- Pandey, T. P., Lavina, S., Vezzu, K., Yang, Y., Poynton, S. D., Varcoe, J. R., Seifert, S., Liberatore, M. W., Noto, V. Di, & Herring, A. M. (2015). Interplay between water uptake, ion interactions, and conductivity in an e-beam grafted poly(ethylene-co-tetrafluoroethylene) anion exchange membrane. *Phys. Chem...*, 15, 4367–4378. <https://doi.org/10.1039/c4cp05755d>
- Qu, L., Huang, H., Xia, F., Liu, Y., Dahlgren, R. A., Zhang, M., & Mei, K. (2018). Risk analysis of heavy metal concentration in surface waters across the rural-urban interface of the Wen-Rui Tang River, China. *Environmental Pollution*, 237, 639–649. <https://doi.org/10.1016/j.envpol.2018.02.020>
- Ranville, J., & Muzny, C. (2006). Predicting Membrane Flux Decline Using Parameters Derived from Field-Flow Fractionation Measurements U.S. *Department of the Interior Bureau of Reclamation* (Issue 102).
- Salgin, S., Takac, S., & Ozdamar, T. (2017). Adsorption of bovine serum albumin on polyether sulfone ultrafiltration membranes : Determination of interfacial interaction energy and effective diffusion coefficient Adsorption of bovine serum albumin on polyether sulfone ultrafiltration membranes. *Journal of Membrane Science*, 278, 251–260.

- <https://doi.org/10.1016/j.memsci.2005.11.008>
- Schuster, J. M., Schvezov, C. E., & Rosenberger, M. R. (2015). Analysis of the Results of Surface Free Energy Measurement of Ti6Al4V by Different Methods. *Procedia Materials Science*, 8, 732–741.
- <https://doi.org/10.1016/j.mspro.2015.04.130>
- Servos, M. R., Liang, R., Hu, A., Hatat-Fraile, M., Zhou, N., Zhang, P., Li, Z., Tabe, S., Li, Y., & Seymour, M. (2014). Nanotechnology for Water Treatment and Purification. <https://doi.org/10.1007/978-3-319-06578-6>
- Sorlini, S., & Torretta, V. (2017). Overview of the Main Disinfection Processes for Wastewater and Drinking sustainability. *Sustainability*, 10(86).
- <https://doi.org/10.3390/su10010086>
- Świetlik, J., & Sikorska, E. (2006). Characterization of natural organic matter fractions by high pressure size-exclusion chromatography, specific UV absorbance and total luminescence spectroscopy. *Polish Journal of Environmental Studies*, 15(1), 145–153.
- Tchounwou, P. B., Yedjou, C. G., Patlolla, A. K., & Sutton, D. J. (2012). Heavy Metals Toxicity and the Environment. *National Institute of Health*, 101, 1–30.
- <https://doi.org/10.1007/978-3-7643-8340-4>
- Vatanpour, V., Faghani, S., Keyikoglu, R., & Khataee, A. (2020). Enhancing the permeability and antifouling properties of cellulose acetate ultrafiltration membrane by incorporation of ZnO @ graphitic carbon nitride nanocomposite. *Carbohydrate Polymers*, October, 117413.
- <https://doi.org/10.1016/j.carbpol.2020.117413>
- Wang, F., & Tarabara, V. V. (2008). Pore blocking mechanisms during early stages of membrane fouling by colloids. *Journal of Colloid and Interface Science*, 328(2), 464–469. <https://doi.org/10.1016/j.jcis.2008.09.028>
- Wang, S., Wang, Z., Xia, J., & Wang, X. (2021). Polyethylene-supported nanofiltration membrane with in situ formed surface patterns of millimeter size in resisting fouling. *Journal of Membrane Science*, 620, 118830.
- <https://doi.org/10.1016/j.memsci.2020.118830>
- Wenten, I. G. (n.d). Ultrafiltration in water treatment and its evaluation as pre-treatment for reverse osmosis system. *Institut Teknologi Bandung*.
- Zularisam, A. W., Ismail, A. F., & Salim, R. (2006). Behaviours of natural organic

matter in membrane filtration for surface water treatment — a review.

*Desalination*, 194(2006), 211–231. <https://doi.org/10.1016/j.desal.2005.10.030>



## CHAPTER 5

### **Investigation of the thermo-pneumatic properties of nanofluids made using copper oxide nanoparticles in pressure-based membrane filtration.**

---

#### **5.1 Introduction**

In the previous chapter, the proof of concept of the solar driven hydraulic pump using both nanofiltration and ultrafiltration membranes was demonstrated. Ultrafiltration membranes were shown to be more suitable for application on the solar pump than nanofiltration membranes. However, the ultrafiltration membranes fouled much more easily than the nanofiltration membranes. To reduce the effects of fouling, chemical cleaning was necessary, as it retained both ultrafiltration and nanofiltration membrane performances. The solar pump's performance was shown to be directly dependent on solar irradiation and air temperature. These factors directly affected the amount of heat that was transferred to the working liquid. It was evident that heat transfer to the working liquid was a great factor influencing the performance of the system. To improve heat absorption by the working liquid, it was thus necessary to find ways to increase the thermal conductivity of the working liquid. As such, in this chapter, focus was placed on improving the heat transfer processes within the working liquid using copper oxide nanoparticles. This was done through three stages which are: (i) synthesis and characterization of the nanoparticles, (ii) preparation of nanofluids as well as the analysis of their stability and thermal properties, and (iii) investigation of vapour pressure generation of the nanofluids. The copper oxide nanoparticles were synthesized through hydrothermal and chemical precipitation routes. The motivations behind the use of copper oxide nanoparticles were due to their desirable properties, mainly their high thermal conductivity of 69 W/mK as reported by (Okonkwo *et al.*, 2020), cheap cost, and high surface to volume ratio. These nanomaterials can be used to enhance the thermal conductivity of fluids by dispersing them in the base-fluids. The hydraulic pump used in this study operates by converting thermal energy into mechanical energy thus the efficiency of heat transfer is critical in its overall performance. As such, the synthesized nanoparticles were dispersed in the working fluid and their

enhancement of the thermal transfer properties of the working fluid were investigated and optimized. The effect of a change in thermal conductivity of the nanofluid on the operational pressure was also investigated. An increase in the operational pressure of the working liquid at the same temperature is beneficial as it results in an increase in the efficiency of diaphragm pumps.

## 5.2 Experimental

### 5.2.1 Materials and methods

This chapter used the same copper oxide precursors, solvents, and chemical reagents listed in **Chapter 3 Subsection 3.1** and methods described in **Section 3.7**. The aim of the different synthesis methods was to produce copper oxide nanoparticles of different shapes and investigate their thermal conductivity enhancements in the working fluid.

### 5.2.2 Preparation and characterization of $\text{Cu}_2\text{O}$ and $\text{CuO}$ nanoparticles.

Copper oxide ( $\text{CuO}$  and  $\text{Cu}_2\text{O}$ ) nanoparticles were prepared using a green chemical precipitation method and a hydrothermal method respectively, with  $\text{CuCl}$ ,  $\text{CuCl}_2$ , and  $\text{CuSO}_4$  as precursors as detailed in **Section 3.8**. As  $\text{Cu}_2\text{O}$  is oxidized to  $\text{CuO}$  when there is oxygen and high temperature (Gupta *et al.*, 2018), hence the calcination step was not done in this synthesis route. Yield calculations for the  $\text{CuO}$  and  $\text{Cu}_2\text{O}$  nanoparticles synthesized using the different methods were determined as outlined in **Section 3.8**. The nanomaterials were analysed using scanning electron microscopy (Jeol JSM IT300, Tokyo, Japan) for surface morphology and Energy Dispersive Spectroscopy (Jeol JSM IT300, Tokyo, Japan) for elemental composition as outlined in **Section 3.6.1**. The surface functionalities of the copper oxide nanoparticles were investigated using ATR-FTIR spectroscopy as outlined in **Section 3.8.1**. The zeta potential and size of the copper oxide nanoparticles were determined as described in **Section 3.8.1**. Uv-Vis spectroscopy (Lambda 650 S,

Perkin Elmer, United States of America) was also used to analyse the optical properties of the copper oxide nanoparticles as outlined in **Section 3.6.4**.

### **5.2.3 Preparation and testing protocols of prepared copper oxide-based nanofluids**

The copper oxide-based nanofluids were prepared and tested using two base fluids, i.e., deionized water and the pure working liquid. This was done to evaluate the properties of the copper oxide nanoparticles in different conditions. In one set of the copper oxide-based nanofluids, nanoparticles were dispersed in 20 ml volumes of the base fluid, i.e., deionized water and volatile working fluid. In the other set, 10mg of a dispersant, i.e., sodium dodecyl sulfate (SDS) was added to the nanofluid samples in addition to the nanoparticles and 20 ml of base fluid. As such, the stability of the nanoparticles in the nanofluid was investigated with or without the surfactant. All tests on the nanofluids were done only after sonicating the sample for a period of 30 minutes using an Elmasonic S-15H ultrasonic bath (Elma, Germany).

The agglomeration rate of the dispersed copper oxide nanoparticles was investigated as it is a measure of the stability of the nanofluids. Copper oxide nanoparticles were dispersed in deionized water at a concentration of 0,1% w/w at different pH values within the pH range of 2 to 12 with 1 pH unit differences. These nanofluid samples were immediately photographed after being sonicated for one hour using an Elma S-15H, Elmasonic sonicator (Elma, Germany). The samples were allowed to stand for 24 hours in a dark and cool area to prevent thermal and vibrational agitation. The samples were then photographed and the sedimentation level in each sample was visually identified. The pH values where the nanoparticles showed the highest stability were identified and the experiment was repeated but with the nanoparticles being dispersed in the volatile working fluid adjusted to these pH values. This was done to investigate how pH affected nanoparticle stability in the organic volatile base fluid whose pH was difficult to adjust due to immiscibility with water which affected pH adjustment by direct aqueous alkali or acid addition. The pH of the volatile organic nanofluid was altered by adjusting the pH of aqueous nanofluid samples then centrifuging and drying the sample. The dry nanoparticles

at different pH values were then added to the volatile organic base fluid and the excess alkali or acidic ions adsorbed on the nanoparticles produced nanofluids of different pH values from the pure base fluid.

#### 5.2.4 Heat transfer analysis in nanofluids

Heat transfer analysis in the copper oxide-based nanofluids was investigated through heating and cooling experiments. The rates of heat transfer were hypothesized to be proportional to the changes in temperature per unit and calculated using **Equation 5.1**.

$$q_r = \frac{\Delta T}{\Delta t} \quad \text{Equation 5.1}$$

Where:  $q_r$  is the heat transfer rate of the working liquid,  $\Delta T$  is the change in temperature, and  $\Delta t$  is the change in time.

The change in the rate of heat transfer was thus correlated to the differences in the changes in temperature per unit time of the pure working liquid (base fluid) and that of the nanofluid using **Equation 5.2**.

$$q_e = \frac{q_{r-nf} - q_{r-wl}}{q_{r-wl}} \times 100 \quad \text{Equation 5.2}$$

Where:  $q_e$  is the heat transfer rate enhancement,  $q_{r-nf}$  is the heat transfer rate of the nanofluid, and  $q_{r-wl}$  is the heat transfer rate of the pure working liquid.

The heating experiments on the copper oxide-based nanofluids were done through first allowing 20ml nanofluid samples to equilibrate to room temperature. The sample temperature was then measured using a thermocouple and the sample was transferred into a water bath at 80 °C as shown in **Figure 5.1**. The time taken between each 1 °C change in temperature was measured using a stopwatch and noted down until the sample achieved thermal equilibrium with the water bath then a graph of the temperature changes against time was plotted.



**Figure 5.1:** Image showing the setup used in the heating experiment for the determination of the thermal transfer enhancement of copper oxide nanoparticles.

The cooling experiments for the investigation of the rate of heat loss in the nanofluid samples were done through first heating 20ml samples in a water bath at 70°C until the sample achieved thermal equilibrium. The sample was then left to stand under ambient conditions out of the water bath and the temperature of the sample was noted at 5-minute intervals as shown in **Figure 5.2**. A graph of the temperature changes against time was then plotted.



**Figure 5.2:** Image showing the experimental setup used in the measurement of temperature change with time of nanofluids cooling under ambient temperature. The samples shown have (a) Deionized water, (b) 0,025%wt CuO, (c) 0,050%wt CuO, (d) 0,075%wt CuO, and (e) 0,10%wt CuO.

The thermal conductivity of the samples were correlated to the rate of temperature change of the sample per unit time after a specific amount of charge had been delivered through the sample using a hot wire. A custom variation of the Transient Hot Wire Method was adopted in this study and the apparatus used are show in **Figure 5.3**. To study the rate of heat transfer, 20ml aliquots of the nanofluid samples prepared using the volatile organic base fluid (working liquid) were put in glass tubes and allowed to thermally equilibrate in an ice bath. The temperature was lowered to increase the gap between the boiling temperature of the working liquid and the testing temperature hence reduce losses of the volatile liquid through evaporation under ambient conditions. The temperature of the sample was measured using a thermocouple held firmly at a 2mm separation from the hot wire immersed in the sample to the same depth of 4cm. A constant current was then passed through 4cm of an insulated nichrome wire (hot wire) for 15 seconds with the voltage and current

being measured using a digital multi-meter (DT92 Series). The time ( $t$ ) taken for each  $0.1^{\circ}\text{C}$  change ( $\Delta T$ ) was then noted using a stopwatch. A plot of the temperature change ( $\Delta T$ ) against the natural logarithm of the change in temperature  $\ln(\Delta t)$  was then made and the slope of this curve was used to estimate the rate of heat transfer within the sample. The experiment was repeated three times for each sample and the changes averaged to reduce experimental error while the time for each run was kept under a minute to reduce the error due to convection currents which aid in heat transfer (Özering, 2010). The same procedure was repeated for different nanofluids, and a comparative plot was made.

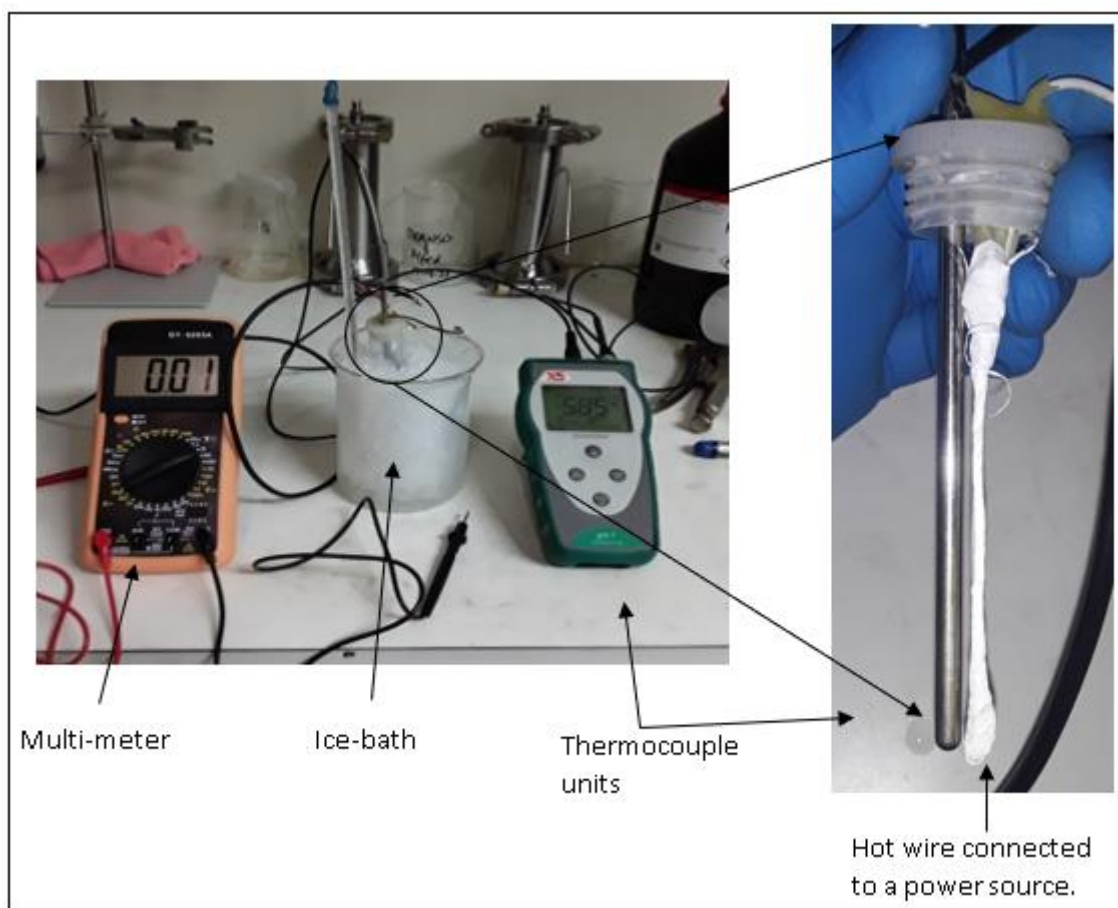


**Figure 5.3:** Images showing custom-made Transient Hot Wire Method apparatus for determining the rate of heat transfer in copper oxide-based nanofluids.

The development of equilibrium vapour pressure by the pure working liquid and the different nanofluids were studied through measuring the equilibrium pressure of the samples at isothermal conditions. The working fluid cylinder was prepared as

detailed in **Section 3.10.3** and was inserted into a water bath at room temperature. The time taken between insertion of the cylinder and that for the working liquid to reach a pressure of 20kPa on the pressure gauge was then noted using a stopwatch together with the time to reach subsequent pressure units until the equilibrium pressure was reached. The experimental procedure was done three times and the averages taken then repeated with a 20ml sample of 0,1% w/w CuO Working liquid samples.

#### **5.2.5 Analysis of pressure generation by the nanofluids**

The effect of nanoparticles on pressure generation was studied through an analysis of the pressure developed at different temperatures by the nanofluids. The pressure enhancement due to the nanoparticles was then investigated by comparing the pressure generated by the pure working liquid and the nanofluid at the same temperature. The test was first done through putting a 20 ml sample of the pure working liquid into the working liquid chamber of the cylinder then thermally equilibrating the cylinder in an ice bath at 1 °C. The cylinder was then put in a water bath at 25 °C and the pressure developed by the working liquid was closely monitored until an equilibrium pressure was reached as shown in **Figure 5.4**. The cylinder was then thermally equilibrated in an ice bath and the temperature of the water bath was increased by 5 °C and the procedure was repeated until the temperature of the water bath reached 60 °C. The experimental procedure was then repeated using a 0,1 % w/w. CuO working liquid.



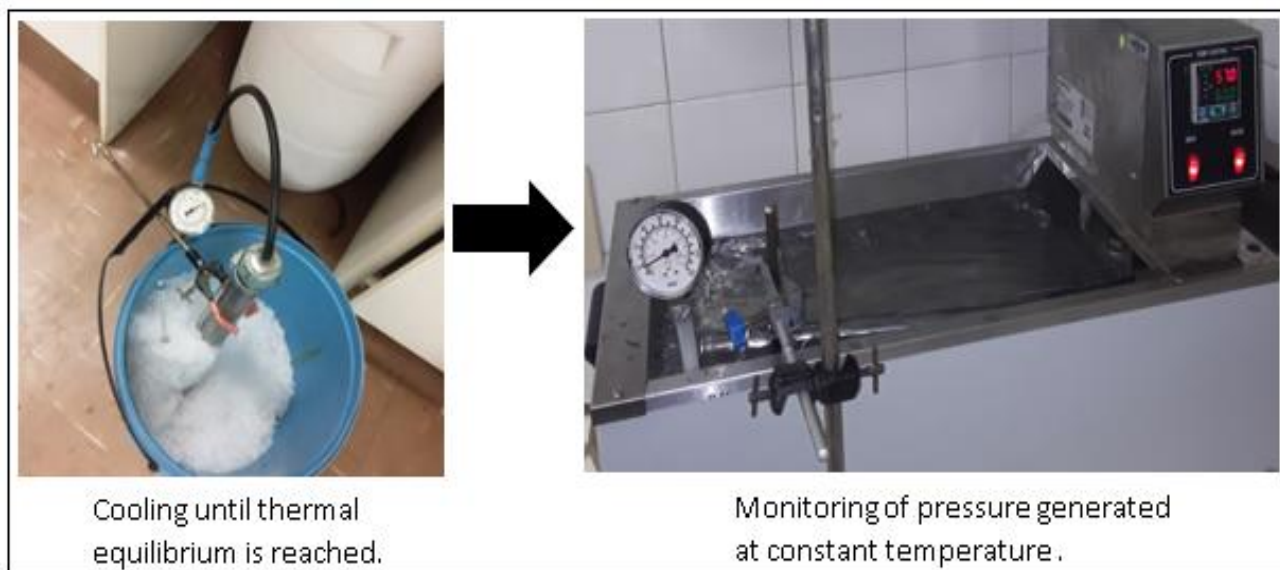


**Figure 5.4:** Images showing how the investigation of the relationship between temperature and pressure generated by the working liquid was carried out.

The latent heats of vaporization of the pure working fluid and the nanofluid were determined using the Clausius-Clapeyron equation (Rodgers & Hill, 1978) shown in **Equation 5.3**.

$$\ln \left( \frac{p_2}{p_1} \right) = \frac{\Delta H}{R} \left( \frac{1}{t_2} - \frac{1}{t_1} \right) \quad \text{Equation 5.3}$$

Where:  $\Delta H$  is the latent heat of vaporization ( $\text{J} \cdot \text{mol}^{-1}$ ),  $p_2$  and  $p_1$  is final and initial vapour pressures of the fluid in Pa (units of pressure should only be the same) while  $t_2$  and  $t_1$  are the final and initial temperatures of the fluid in Kelvins, and  $R$  is the ideal gas constant ( $8,314 \text{ J} \cdot \text{mol}^{-1} \cdot \text{K}^{-1}$ )

### 5.3 Results and discussion

#### 5.3.1 Preparation and characterization of CuO and Cu<sub>2</sub>O nanoparticles.

The synthesized copper oxide nanoparticles were visibly different with both CuO nanospheres and nanorods were black in colour while the Cu<sub>2</sub>O nanospheres and nanorods were brown as shown in **Figure 5.5**.

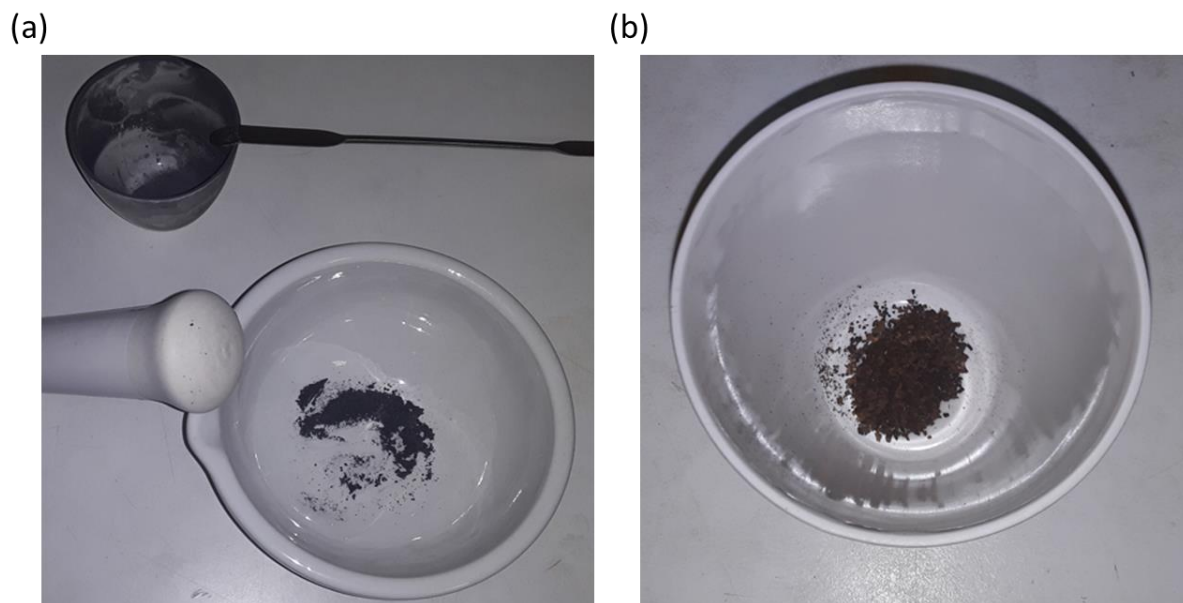


**Figure 5.5: Images of copper oxide nanoparticles showing (a) Black CuO nanoparticles and (b) Brown Cu<sub>2</sub>O nanoparticles.**

The yield of the Copper (II) oxide nanoparticles produced by the hydrothermal method was determined to be 86%. The low yield was attributed to losses of the nanoparticles during the washing phase as well as the particles adhering to the walls of the centrifuge tubes. The yield of copper (II) oxide by the chemical precipitation method was determined to be 90% as some of the product was lost in the washing process of the nanoparticles under vacuum filtration but these losses were lower than those in the hydrothermal synthesis. The chemical precipitation method is known to produce a high yield of CuO nanoparticles (Phiwdang *et al.*, 2013).

The differences in the morphology of the copper oxide nanoparticles prepared using the chemical precipitation and hydrothermal synthesis methods were identified through SEM images as shown in **Figure 5.6**. The chemical precipitation method produced copper oxide nanospheres which are evidently seen as small, agglomerated spheres in **Figure 5.6**. On the other hand, the hydrothermal synthesis method produced copper oxide nanorods seen in **Figure 5.6** as tiny rods.

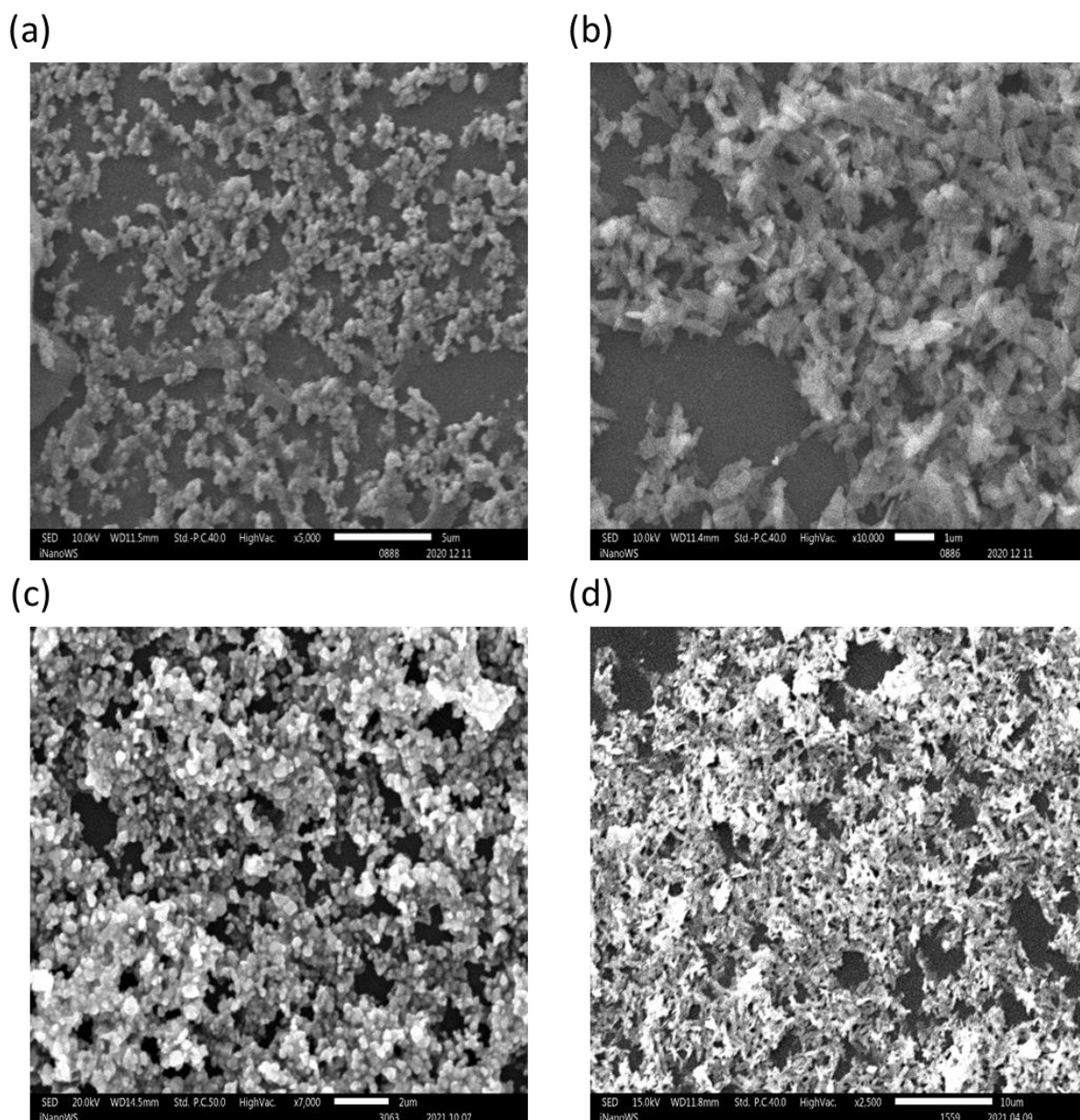


**Figure 5.6:** SEM images of copper (II) oxide nanoparticles showing (i) CuO nanospheres, (ii) CuO nanorods, (iii) Cu<sub>2</sub>O nanospheres, and (iv) Cu<sub>2</sub>O nanorods.

The copper oxide nanoparticles were confirmed to have an elemental composition with both copper and oxygen atoms as shown by the presence of copper and oxygen peaks in EDS spectra shown in **Figure 5.7**. The EDS spectra also has other peaks which were assumed to be from impurities not properly washed out in the synthesis steps like sodium hydroxide and trisodium acetate as well as gold used to coat the samples before EDS analysis. EDS analysis can also be used in the determination of a compound's formula through mean ratio analysis of the atomic composition

(Ren *et al.*, 2009). The atomic composition of the CuO nanospheres and nanoparticles shows mean ratios of Cu to O atoms of 1:0,93 and 1:0,87, respectively. These ratios all prove that the samples had an atomic composition of CuO. On the other hand, the mean ratios of Cu to O atoms in the Cu<sub>2</sub>O nanospheres and nanorods were found to be 1:1,92 and 2,38:0,50, respectively. The compound formula for the Cu<sub>2</sub>O nanospheres was thus determined to be CuO<sub>2</sub> but the compound formula for the nanorods could not be deduced directly from the presented data. This may have been due to the high temperature dual oxidation of Cu in alkaline solutions which occurs mainly through the formation of Cu<sub>2</sub>O or the formation of Cu(II)-oxide/ hydroxide (Keil *et al.*, 2007) in the hydrothermal synthesis method used. This also affected the chemical precipitation method as the same reactions can occur at room temperature. This is supported by the brown colour of the presumed Cu<sub>2</sub>O nanoparticles produced in both methods which are supposed to be red or reddish-brown in colour in their pure form. The compound formula of CuO<sub>2</sub> is formed when Cu<sub>2</sub>O crystallizes forming a metal two-coordinate structure in which a tetrahedron of copper atoms surrounds each oxygen atom (Ruiz *et al.*, 1997).

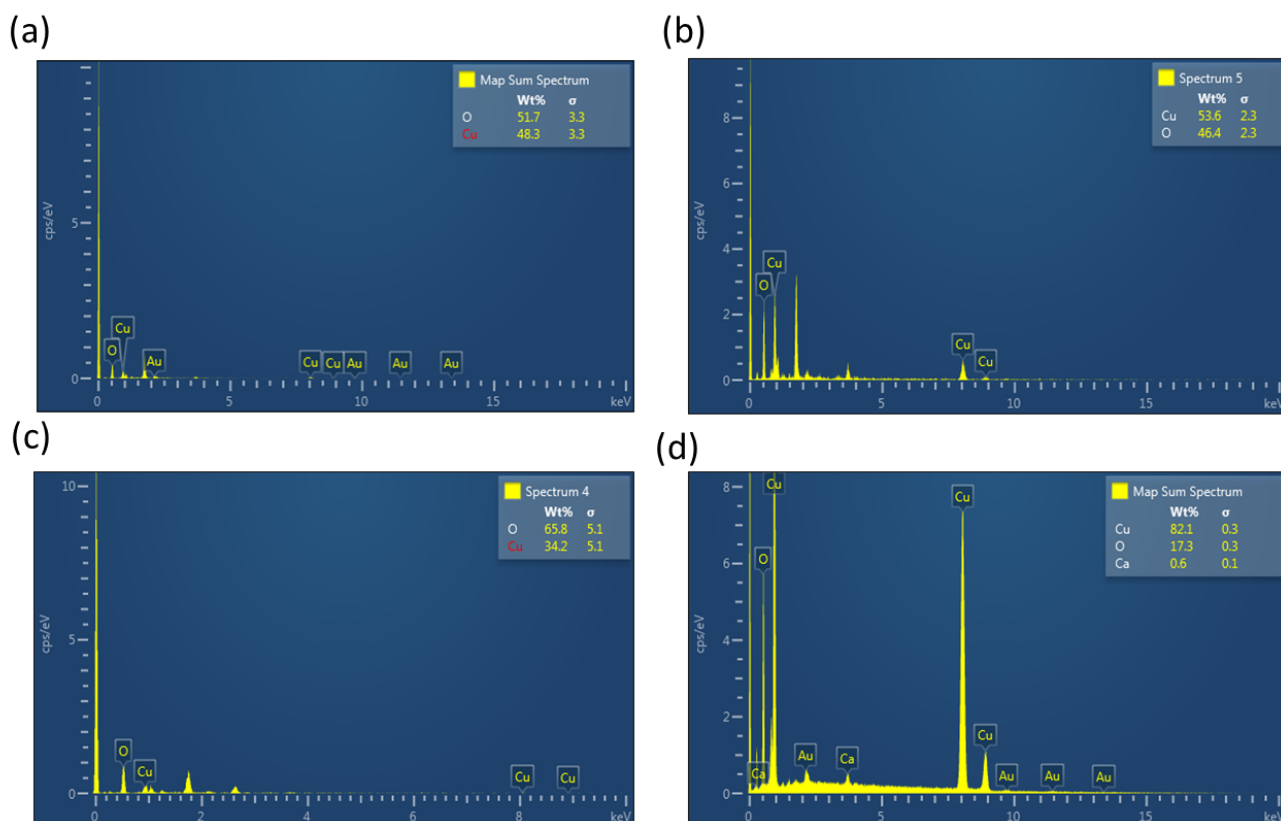


**Figure 5.7:** EDS spectra of (a) CuO nanospheres, (b) CuO nanorods, (c) Cu<sub>2</sub>O nanospheres, and (d) Cu<sub>2</sub>O nanorods.

FTIR spectroscopy was used to evaluate the surface functional units of the copper oxide nanoparticles and the ATR-FTIR spectra for Cu<sub>2</sub>O nanorods, CuO nanorods and CuO nanospheres are shown in **Figure 5.8**. Common characteristic vibrational peaks of CuO nanoparticles are shown in the spectra within the 700 cm<sup>-1</sup> – 500 cm<sup>-1</sup> region (Luna *et al.*, 2015) thereby confirming the elemental nature of the samples as CuO. Other characteristic peaks for the CuO and Cu<sub>2</sub>O nanoparticles are observed at (547 cm<sup>-1</sup>, 588 cm<sup>-1</sup>) and (497 cm<sup>-1</sup>, 609 cm<sup>-1</sup>), respectively, thereby confirming the successful synthesis of CuO and Cu<sub>2</sub>O nanoparticles.

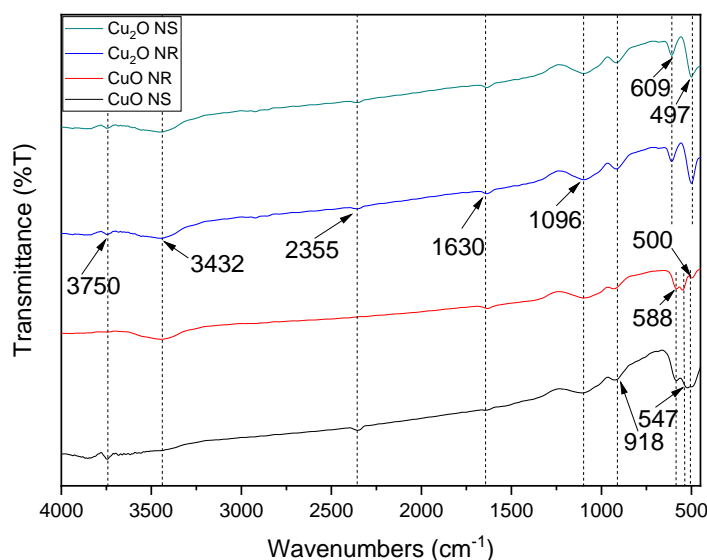


**Figure 5.8:** ATR-FTIR spectra of Cu<sub>2</sub>O nanospheres, Cu<sub>2</sub>O nanorods, CuO nanorods, and CuO nanospheres.

The main peaks in the ATR-FTIR spectra of the copper oxide nanoparticles were assigned to different functional units as shown in **Table 5.1**.

**Table 5.1:** Peak assignment for copper oxide nanoparticles' ATR-FTIR spectra.

Sample	Peak (cm <sup>-1</sup> )	wavenumber	Functional units band assignment
<b>Cu<sub>2</sub>O nanospheres and nanorods</b>		497	Main vibrational peak of Cu <sub>2</sub> O
		609	Main Cu <sub>2</sub> O vibrational mode
		1630	Cu-O symmetrical stretching
		3432	Hydroxy group, O-H stretch (from NaOH impurity)
<b>CuO nanospheres and nanorods</b>			
		547	Cu-O asymmetric stretching
		588	Cu-O wagging (Main Cu-O vibrational mode)
		1630	Cu-O symmetrical stretching
		3432	Hydroxy group, O-H stretch (from NaOH impurity)

### 5.3.2 Size and zeta potential of copper oxide nanoparticles

The thermal conductivity of a fluid is enhanced by dispersing nanoparticles in the fluid mainly due to the dispersed particles' surface charge (zeta potential) and size. However, there is a critical particle size below which, this thermal conductivity enhancement starts to decrease (Warrier & Teja, 2011). Zeta potential provides a measure of the surface charge of different particles and is critical in the formation of stable dispersions as agglomeration is lowered when the particles are highly charged and repel each other (Yu *et al.*, 2017). Hence, as the absolute surface charge of nanoparticles increases, there is a general increase in the stability of nanoparticle dispersions (Choudhary *et al.*, 2017). The zeta potential of the copper oxide nanoparticles were investigated using the Doppler technique in deionized

water with and without the SDS surfactant then in the working liquid with and without the SDS surfactant at neutral pH.

The particle sizes and zeta potentials of the copper oxide nanoparticles are shown in **Table 5.2**. It is important to note that dispersed nanoparticles have a range of sizes (Marcelino *et al.*, 2016) whose distribution is affected by many factors including the concentration of the nanoparticles and sonication time. The Cu<sub>2</sub>O nanospheres displayed the largest average particle size and absolute zeta potential. According to the zeta potential, the Cu<sub>2</sub>O nanospheres were thus expected to have a higher potential of forming the most stable dispersions at that pH. However, size is also a factor in nanofluid stability given the tendency to have faster sedimentation rates of bigger particles than smaller ones. This is supported by (Zhao *et al.*, 2018) who altered the sizes of silica nanoparticles in silica nanofluids by adjusting the pH and showed that the nanofluids increased stability with each decrease in size of the nanoparticles. As such the large size of the Cu<sub>2</sub>O nanospheres also adversely affected the stability of these nanoparticles in the nanofluid. On the other hand, the CuO nanospheres had the smallest average particle size and second largest absolute surface charge which implied that these particles were expected to have the largest stability.

Determination of the nanoparticle sizes in nanofluids with SDS as the dispersant was not possible as the dispersant quickly sedimented despite sonication. SDS is an anionic surfactant with amphiphilic properties derived from a sulphate group joined to carbon units and has the formula CH<sub>3</sub>(CH<sub>2</sub>)<sub>11</sub>OSO<sub>3</sub>Na (Figoli *et al.*, 2017). The SDS surfactant reduced the stability of the nanoparticles as the sodium in the surfactant is adsorbed on the nanoparticle's surface in the adsorbed layer which destabilizes the nanoparticle's surface charge thereby lowering the dispersion's stability. The surfactant also has high water solubility (Aksoy *et al.*, 2021), i.e., high hydrophilic-lipophilic balance (HLB) which also meant low solubility in non-aqueous base fluids like the volatile organic working liquid.

**Table 5.2:** Summary of the size and zeta potential values of the copper oxide nanoparticles at a pH of 7.

Sample	Base-fluid	Average Size (nm)	Zeta potential (mV)
<b>CuO nanospheres</b>	Water	17,43 to 21,43	23,1 to 23,8
<b>CuO nanorods</b>	Water	41,29	-5,15
<b>CuO nanospheres</b>	Water + SDS	Sedimented	-0,188 to – 0,290
<b>Cu<sub>2</sub>O nanorods</b>	Water	298,8	-4,38
<b>CuO nanospheres</b>	Base-fluid	Sedimented	-0,236
<b>Cu<sub>2</sub>O nanospheres</b>	Water	600	-42

The zeta potential of nanoparticles is affected by changes in the pH of the base fluid and this relationship was investigated by measuring the surface charge of the copper oxide nanoparticles at different pH values (2 – 12) as shown in **Figure 5.9**. As the pH increased, there was a general decrease in the surface charge of the copper oxide nanoparticles which is in line with results reported by (Younes *et al.*, 2012). The magnitude of zeta potential was generally high in alkaline conditions than in acidic ones and the zig-zag pattern in the change of zeta potential could not be explained. In general, the largest magnitude of surface charge for the CuO nanoparticles was observed to be at pH values of 8 and 10 while the smallest was in the range 2 to 4. On the other hand, the largest magnitude of zeta potential for the Cu<sub>2</sub>O was at pH values of 8 and 9 at pH values of 3 and 4. As nanoparticles with high surface charge have been shown to enhance heat transfer in nanofluids, (Lee *et al.*, 2006) it was thus expected that copper oxide nanoparticles with the largest magnitude of zeta potential would have the greatest thermal conductivity enhancement as well as stability. It is also important to note that the pH of the pure working liquid was measured to be 6,13 and at this pH the copper oxide nanoparticles were shown to have intermediate zeta potential. The copper oxide nanorods were also shown to generally have higher absolute values of zeta potential than the copper oxide nanospheres hence were expected to have higher stability. As such, the copper oxide nanorods were selected for further tests.



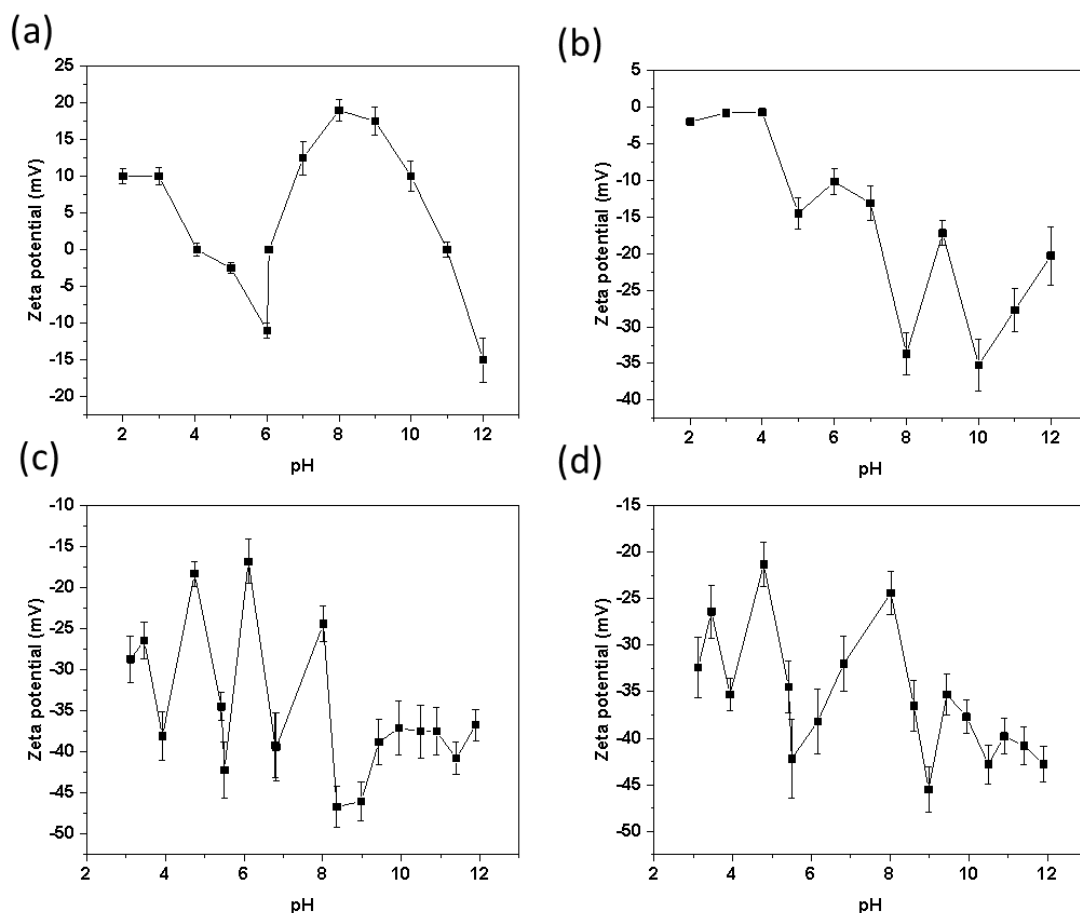


**Figure 5.9:** Change in surface charge of the nanomaterials with change in pH for (a) CuO nanospheres, (b) CuO nanorods, (c) Cu<sub>2</sub>O nanospheres, and (d) Cu<sub>2</sub>O nanorods.

The pH of the base fluid affects the size of dispersed nanoparticles. This was investigated using the hydrodynamic light scattering technique where the average size of the nanoparticles at different pH values in the pH range of 2 to 12 was plotted against the pH value as shown in **Figure 5.10**. The size of the copper oxide nanoparticles was observed to generally increase with the increase in the pH of the base fluid which tallies with results reported by (Lee *et al.*, 2006). (Lee *et al.*, 2006) varied the pH within a range of 3 to 12 for nanofluids prepared using CuO nanospheres dispersed water and found that the average size of the nanoparticles increased with an increase in pH. However, results by (Younes *et al.*, 2012) showed a general decrease in the hydrodynamic diameters (sizes) of CuO nanospheres suspended in water in the pH ranges of 3 to 12. The smallest average particle size

of the dispersed nanoparticles was found to be 500 nm and these particles were observed to be largely formed within the pH range of 4 to 8 for all the copper oxide nanoparticles. This led to the inference that stable copper oxide-based nanofluids would be formed in the pH range of 4 to 8 as the nanoparticles would have the smallest average particle size in this range. These results also supported the zeta potential results shown in **Figure 5.9** as the largest magnitude of zeta potential for the nanoparticles was observed to intersect with the smallest size at around a pH of 8.

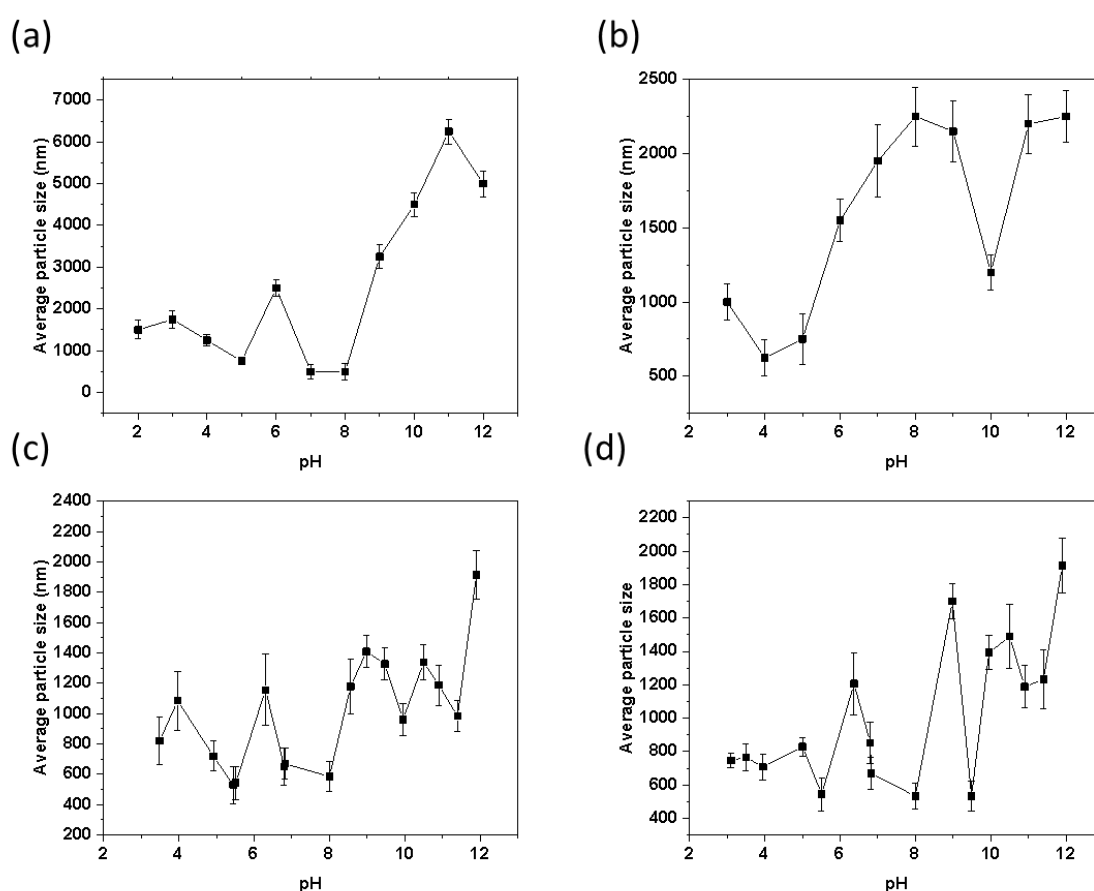


**Figure 5.10:** Change in particle size with pH of copper oxide nanoparticles showing (a) CuO nanospheres, (b) CuO nanorods, (c) Cu<sub>2</sub>O nanospheres, and (d) Cu<sub>2</sub>O nanorods.

### 5.3.3 Optical properties of copper oxide nanoparticles

The optical properties of the copper oxide nanoparticles were investigated using optical spectrometry and the Uv-Vis absorbance spectra are displayed in **Figure 5.11**. The spectra were used to determine the cut-off wavelengths by extending a tangent on the curve of the spectrum to the x-axis. The x-intercept value was taken as the cut-off wavelength which was then used to calculate the band-gap energy of the copper oxide nanoparticles. The band-gap energy values were then used to estimate the size of the average sizes of the nanoparticles as outlined in **Section 3.8.1**. As the calculate cut-off wavelength values are very close, this indicates that the nanoparticles have comparable band-gap energies.

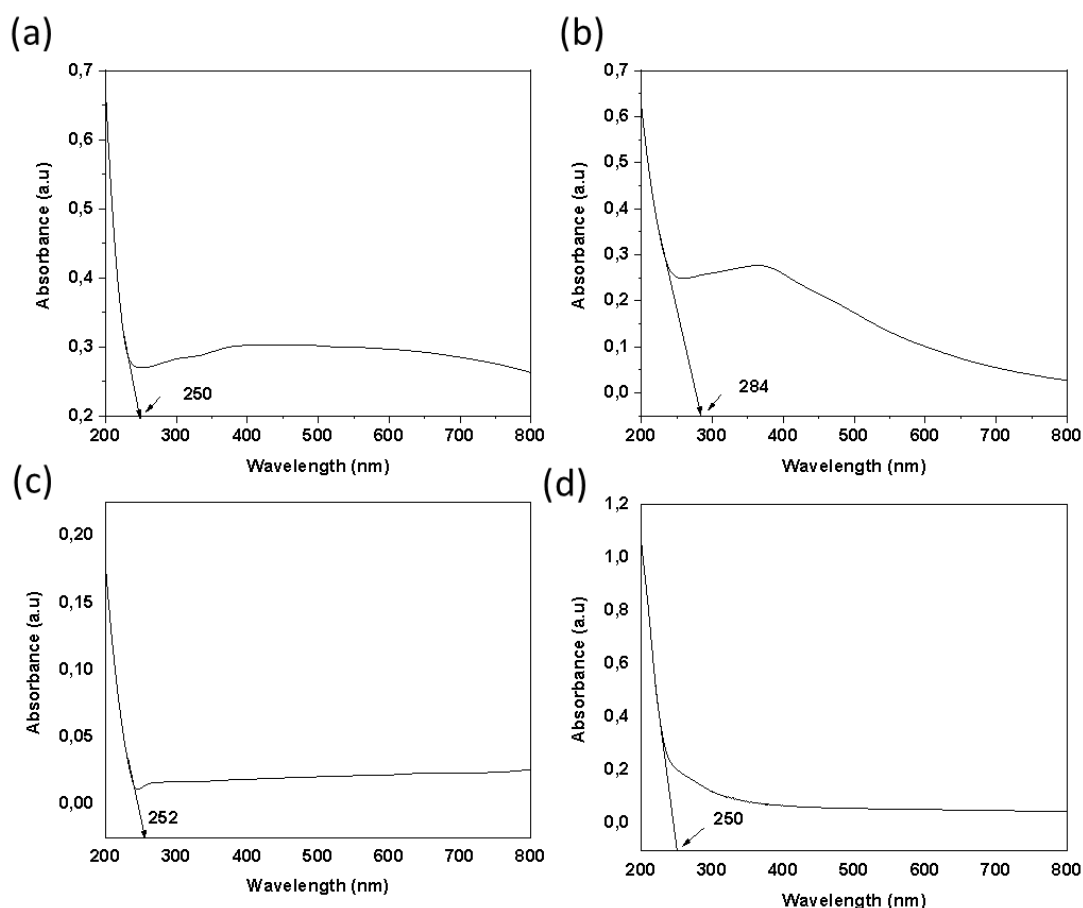


**Figure 5.11:** Optical properties of copper oxide nanoparticles showing the absorbance spectra of (i) CuO nanospheres, (ii) CuO nanorods, (iii) Cu<sub>2</sub>O nanospheres, and (iv) Cu<sub>2</sub>O nanorods.

A summary of the cut-off wavelengths, band gap energies and estimated sizes of the copper oxide nanoparticles is presented in **Table 5.3**. The experimentally determined band gap energies for CuO and Cu<sub>2</sub>O nanorods are the same as those reported by (Gupta *et al.*, 2018; Murali *et al.*, 2015). The Bohr exciton radius reported in literature for the copper oxide nanoparticles is in the range of 6,6 nm to 28,72nm (Talluri *et al.*, 2017). As the estimated radii of the copper oxide nanoparticles from the experimentally determined band-gap energies fall within the Bohr exciton radius range, the electron-hole pairs (exciton) for the nanoparticles will not experience quantum confinement (Makori *et al.*, 2017). Excitons will experience quantum confinement when the nanoparticle's size is smaller than their Bohr radius which results in increasing band-gap energy with a further decrease in the size of the nanoparticles (Arun *et al.*, 2015). However, the size estimates of the nanoparticles from Uv-Vis spectra were much smaller than those from the dynamic light scattering technique which might be explained by the time-dependent agglomeration of the nanoparticles in solution.

**Table 5.3:** Summary of copper oxide nanoparticles' optical properties (Gupta *et al.*, 2018).

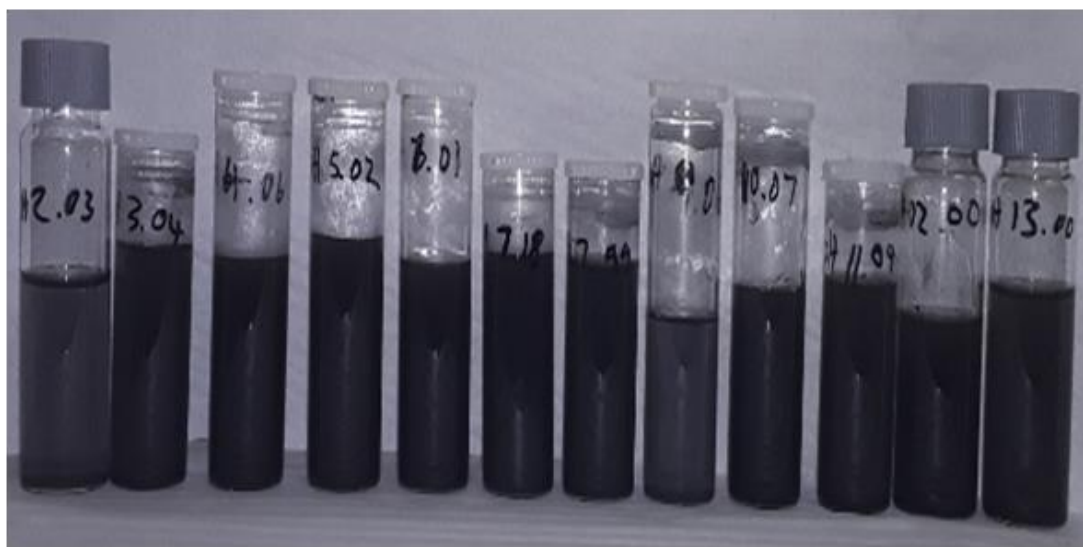
Sample	Cut-off wavelength (nm)	Experimental Band-gap energy (eV)	Theoretical band gaps energies (eV)	Size estimation (nm)
CuO nanorods	284	4,36	1,3 – 1,7	7,67 – 11,20
Cu <sub>2</sub> O nanorods	250	4,96	2 - 2,5	7,56 – 11,00
CuO nanospheres	250	4,96	2 - 2,5	7,56 – 11,00
Cu <sub>2</sub> O nanospheres	252	4,92	1,3 – 1,7	7,62 - 11,10

#### 5.4 Preparation and testing protocols of prepared nanofluids

#### 5.4.1 Stability and heat transfer of copper oxide nanofluids

Visual inspection of the sedimentation rate of nanoparticles in the nanofluid was used to assess the stability of the nanofluids. The addition of the SDS dispersant formed cloudy and unstable emulsions which quickly settled hence no further tests were done on the nanofluid samples with the dispersant. On the other hand, direct dispersion of the copper oxide nanoparticles in the volatile organic working liquid led to the formation of fairly stable dispersions. As shown in **Figure 5.12**, the nanofluid dispersions with concentrations of CuO nanospheres at 0,1% w/w in the pH range of 2 to 13 showed the most stable dispersion were at pH values of 4,06; 6,01 and 11,00 after standing for 24 hours. These pH values correspond well to the values with the highest surface charge and smallest particle size for the copper oxide nanoparticles as shown in **Figures 5.9 and 5.10**, respectively. It was thus hypothesized that the CuO nanorods would also show the same trend in stability as shown by the CuO nanospheres as both nanoparticle types showed the same trend in change of surface charge and particle size with pH.

(a)



(b)

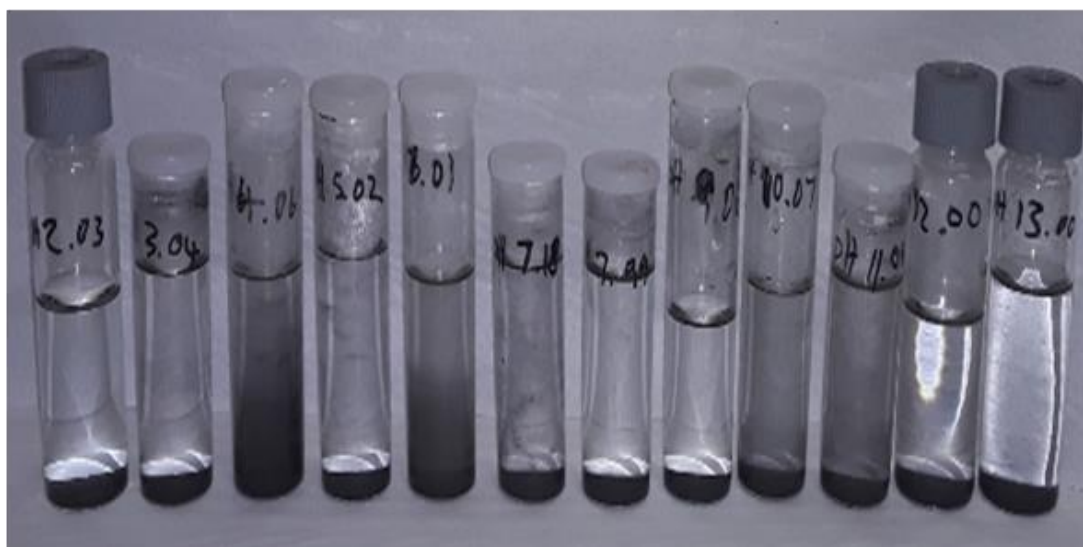


**Figure 5.12:** Images of 0,10 %w/w CuO nanospheres dispersed in water and prepared in the pH range 2 to 13 showing the samples (a) before and (b) after standing for 24 hours.

Further stability studies were then done at a pH value of 6 as this is the pH of the pure volatile working liquid. CuO nanorods were observed to have higher absolute values of zeta potential and smaller average particle sizes than CuO nanospheres at this pH value as shown in **Figures 5.9 and 5.10**, respectively, hence the possibility

of higher stability was evident. Generally nanoparticles with higher magnitudes of zeta potential form more stable nanofluid dispersions due to stronger electrostatic repulsions (Nia *et al.*, 2015) than those with lower zeta potentials. It thus follows that the CuO nanorods were then selected for testing in the volatile organic working liquid at the natural pH of the volatile organic working liquid which was a pH of 6. The CuO nanorods were then used to make nanofluids with different base fluids, i.e., water (pH = 6,06) and the volatile organic working liquid (pH = 6,13) and adjusting the pH to 6. In the other set, the pH of the samples was not adjusted and the nanofluids produced had pH values of 7,34 for the volatile organic working liquid and 8,40 for water as the base fluid. As shown in Figure 5.13, the pH adjusted nanofluids showed better stability for both base fluids hence it was determined that CuO nanorods formed stable nanofluids with the volatile organic working liquid at a pH of 6.

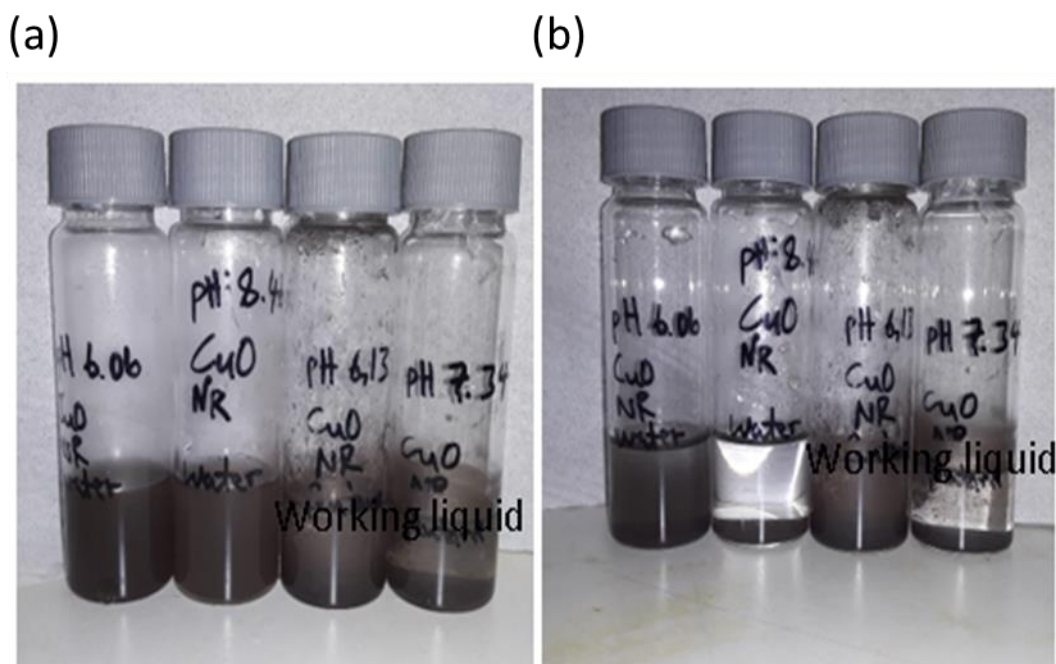


**Figure 5.13:** Images of nanofluid samples with concentration of 0,10% w/w CuO in water and 0,10% w/w CuO in the pure working liquid (a) before and (b) after standing for 24 hours.

Stability test with  $\text{Cu}_2\text{O}$  nanorods and nanospheres at a pH of 6 showed that these nanoparticles formed dispersions with the least stability while CuO nanospheres showed intermediate stability. The best stability was from CuO nanorod dispersions. The low stability of  $\text{Cu}_2\text{O}$  nanoparticles is due to them having larger grain sizes than CuO nanoparticles (Murali *et al.*, 2015). As such, the larger grains are heavier than the smaller grains and will sediment and agglomerate at a faster rate. This is also worsened by the fact that the  $\text{Cu}_2\text{O}$  nanoparticles were also shown to have smallest absolute values of surface charge.

The heat transfer properties of the nanoparticles were then assessed using deionized (DI) water as a base fluid. Deionized water was chosen as it is much less volatile than the pure working liquid used in this study hence the heat transfer effects of the nanoparticles could be much easily investigated over a wider temperature range. Results taken from the tests with water as the base fluid could then be generally related to the volatile base fluid. However, the thermal properties of a nanofluid are affected by the nature of the base fluid as well as the size and shape of the nanoparticles (Simpson *et al.*, 2019). A plot of time against temperature of the base fluid was developed as shown in **Figure 5.14** and shows that the CuO nanorods had the largest temperature change per unit time (largest slope) at a constant heating rate, which implies that it had the highest rate of heat transfer amongst all the tested samples. Dispersing nanoparticles in water was also confirmed to increase the rate of heat transfer in the water as shown by the higher heat transfer rates of the other nanofluids when compared to that of deionized water. This proves that the thermal conductivity of the base fluid is enhanced by suspending nanomaterials in it (Das *et al.*, 2007). This phenomenon has been proven by many researchers in literature (Chieruzzi *et al.*, 2013; Kabeel *et al.*, 2014; M. Liu *et al.*, 2011).



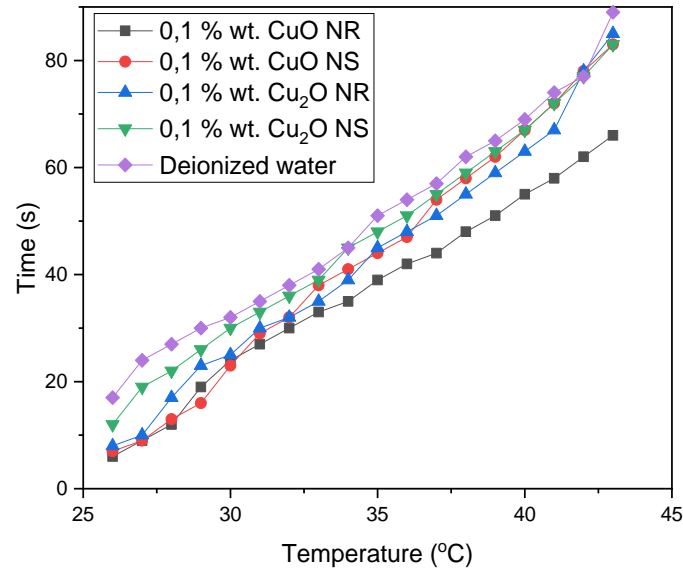


**Figure 5.14:** Heating curves of copper oxide nanofluids from 26°C to 45°C at a constant temperature of 70°C.

The average heat transfer rates for each sample over the heating period are 0,283 °C/s for CuO nanorods (NR), 0,224 °C/s for CuO nanospheres (NS), 0,220 °C/s for Cu<sub>2</sub>O NR, 0,239 °C/s for Cu<sub>2</sub>O NS and 0,236 °C/s for DI water. The heat transfer rates can be arranged in order of decreasing magnitude as follows: CuO NR > CuO NS > Cu<sub>2</sub>O NS > Cu<sub>2</sub>O NR. It is clear from the data presented in **Table 5.4** that the largest heat transfer rate was in the CuO NR while the least was in the DI water. The heat transfer rate was enhanced by 19,9% for the 0,1 %.w/w CuO NR than the pure DI water. This compares well with the reported value in literature of 12,4% thermal conductivity enhancement of CuO nanofluids when compared with deionized water (Luna *et al.*, 2015).

The cooling rates of the nanofluids were also investigated and a plot of time against temperature was used to make comparisons as shown in **Figure 5.15**. The cooling rate decreased as the temperature of the nanofluid got closer to room temperature as shown by the change in the steepness of the cooling curve. This decrease in cooling rate as the difference between the temperature of the surroundings and that of the substance is lowered is Newton's law of cooling (Shepherd, 2013). As

expected, the nanofluids had an enhanced rate of heat loss than the deionized water as evidenced by their steeper slopes. However, the differences in the rates of heat losses between the different nanofluids were imperceptible from the graph hence calculations of the rates of heat loss were thus necessary to perceive any differences.

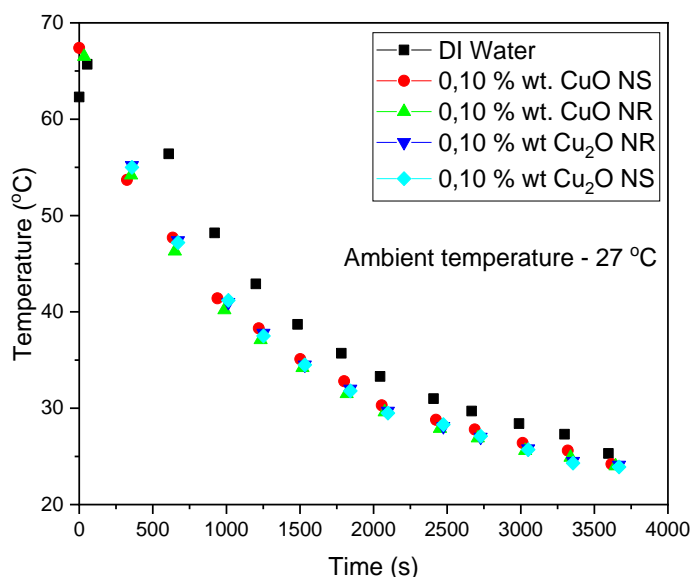


**Figure 5.15:** Cooling curves of copper oxide nanofluids within the temperature range of 68°C to 27°C at a constant air temperature of 27°C.

Heat transfer rates were then calculated for the different nanofluids and the values for the average cooling rates are 0,01191 °C/s for CuO NR, 0,01195 °C/s for CuO NS, 0,0118 °C/s for Cu<sub>2</sub>O NR, 0,01186 °C/s for Cu<sub>2</sub>O NS, and 0,01029 °C/s for DI water. The cooling rates can be arranged in order of decreasing magnitude as follows: CuO NR > CuO NS > Cu<sub>2</sub>O NR > Cu<sub>2</sub>O NS. As such, the CuO nanorods had the largest cooling rate value with the DI water having the least value.

From the previous experiments it is evident that nanoparticles enhanced both heat uptake and cooling rate to different extents as nanofluids with high heat uptake also showed high rates of heat loss. This implies that the thermal conductivity of the base fluid was enhanced to different extents by the nanoparticles. As such, the effect of different concentrations of nanoparticle dispersions on the rate of heat transfer was

thus investigated. The time taken for the nanofluids to change temperature was plotted against temperature and is shown in **Figure 5.16**. As expected, all nanofluids had larger cooling rates than deionized water. However, the differences in cooling rates of the nanofluids could not be identified from the graph hence calculations for the different rates of heat loss were thus warranted.

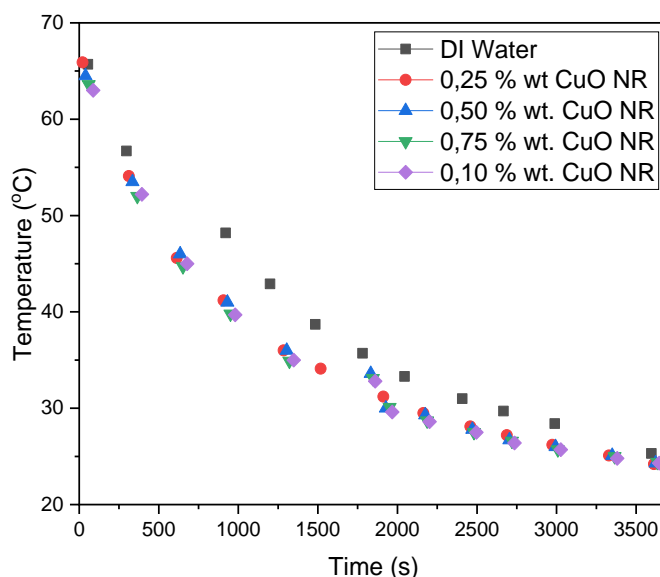


**Figure 5.16:** Cooling curves of copper oxide nanofluids from 68°C to 22,9°C at different concentrations under ambient air temperature of 22,9°C.

The average cooling rates of the different weight fractions of CuO nanorods dispersed in DI water were calculated and the values are 0,0095 °C/s for 0,10 wt.% CuO NR , 0,0091 °C/s for 0,075 wt.% CuO NR, 0,0089 °C/s for 0,0050 wt.% CuO NR, 0,0085 °C/s for 0,0025 wt.% CuO NR, and 0,0086 °C/s for DI water. It is thus evident that there was a general decrease in the rate of heat loss with a decrease in the concentration of the nanoparticles. The largest cooling rate was observed for the nanofluid with a concentration of 0,10 wt.% copper oxide nanoparticles which also means that it had the highest enhancement of heat loss. As the concentration of nanoparticles in a base fluid is increased, there is a corresponding increase in the thermal conductivity of the nanofluid (Thakur *et al.*, 2021). However, above a critical value of (Clary & Mills, 2011) 1% w/w nanoparticle concentration, there is reduced thermal conductivity enhancement.

The thermal conductivity enhancement of the copper oxide nanoparticles in the pure working fluid was investigated through a determination of the rate of temperature change under a constant amount of heat input from a hot wire. The nanofluid with the best heat transfer properties for the deionized water base fluid, i.e., 0,1% w/w CuO nanorods, was assumed to have transferable properties given a change in the base fluid nature. As such, the CuO nanorods were tested with the volatile organic working liquid as the base fluid. It is also important to note that the thermal conductivity of nanofluids with surfactants is lower than for that without. This was confirmed by (Younes *et al.*, 2012) who demonstrated that the thermal conductivity of 0,4 vol %  $\text{Fe}_2\text{O}_3$  and CuO nanofluids prepared with sodium dodecylbenzene sulfonate (NaDDBS) as a surfactant were lower than for the samples without the surfactant. As such, the preparation of nanofluids for enhanced heat transfer without a surfactant was thus further supported by this fact.

The thermal enhancement caused by nanoparticles dispersed in different base fluids is different with more enhancement observed for the base fluid with better thermal properties (Rahmatinejad *et al.*, 2021). As such, it was expected that the thermal conductivity enhancement by the copper oxide nanoparticles would be more for the volatile organic working liquid than for the deionized water.

A plot of time taken for temperature change against the temperature was made as shown in **Figure 5.17** and the steepness of this slope was related to the rate of heat transfer which is a measure of thermal conductivity enhancement. A change in the enhancement of the thermal conductivity between that of the base fluid and that of the nanofluids was shown by a change in the steepness of the slope. A decrease in the slope shows an enhancement in the thermal conductivity as a smaller amount of time is needed to increase the temperature by the same unit(s). An increase in the volume fraction of the nanoparticles resulted in a higher enhancement of the thermal conductivity of the base fluid. This is supported by literature as shown by the work of (Zhu *et al.*, 2018) and (Murshed *et al.*, 2005) who noted that there is a general increase in thermal conductivity enhancement with increase in volume fraction of the nanoparticles in the nanofluids they tested. The concentration of

nanoparticles in the nanofluid affects the osmophoretic motion of the particles, however, osmophoretic motion is of less significance than Brownian motion. Thermal conductivity of nanofluids depends strongly on temperature at which the measurements are taken (Mirmohammadi, 2012) hence measurements were made from a reference temperature of 1°C. This is attributed to a higher thermophoretic motion of nanoparticles in suspension at higher temperature which facilitates higher rates of heat transfer.

Several researchers have also proven that the nanoparticles with higher thermal conductivity will produce nanofluids of higher thermal conductivity in the same base-fluid when compared with nanoparticles of lesser thermal conductivity (Beck, 2008). However, the  $\text{Cu}_2\text{O}$  nanofluid showed the least thermal conductivity enhancement when compared to the  $\text{CuO}$  nanofluid of the same volume concentration as shown in **Figure 5.17**.

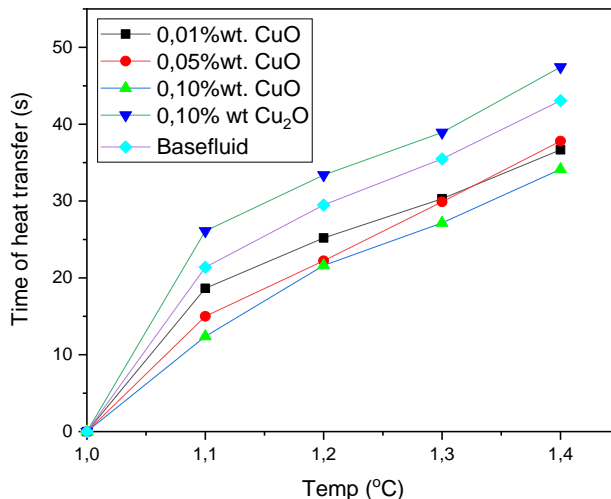


**Figure 5.17:** Temperature change with time after heat addition to the nanofluids of different weight fractions of  $\text{CuO}$  nanoparticles in 20 ml of the pure working liquid in an ice bath.

The rates of heat transfer for each working liquid are shown in **Table 5.4**. The highest rate of heat transfer is observed to be for the 0,1 %w/w  $\text{CuO}$  sample. As the measured temperature change was very small and a constant amount of heat

energy was transferred to each fluid over the same experimental times, the heat transfer values can be used to estimate the thermal conductivity enhancement of the nanoparticles. The  $\text{Cu}_2\text{O}$  nanorods were shown to have the least thermal enhancement despite having a high volumetric concentration in the base fluid whilst the  $\text{CuO}$  nanorods produced the highest thermal conductivity enhancement of 26,2% within the DI water base fluid. This value compared well to the thermal enhancement value of 23,8% that was determined by (M. Liu et al., 2011) in nanofluids prepared by dispersing Cu nanoparticles at 0,10 vol. % concentration.

**Table 5.4:** Rates of heat transfer of different copper oxide nanofluids.

Nanofluid	Pure working liquid	0,01% w/w $\text{CuO}$	0,05% w/w $\text{CuO}$	0,10% w/w $\text{CuO}$	0,10% w/w $\text{Cu}_2\text{O}$
Heat transfer rate (%/s)	0,00929	0,0109	0,0106	0,0117	0,00843
% Thermal conductivity enhancement		17,4	13,9	26,2	9,2

#### 5.4.2 Analysis of vapour pressure generation

Pressure driven membrane filtration systems rely on the generation of high operational pressures that lead to high flux. As such, the volatile nanofluid was expected to develop higher operational pressure than the pure volatile working liquid as it had higher thermal conductivity. It was also expected to have a lower evaporation point due to localized heating by the dispersed nanofluids at the liquid-vapour interface which enhanced evaporation rates (Nia *et al.*, 2015). As shown in **Figure 5.18**, there was a general increase in the vapour pressure developed by the volatile working liquids with an increase in temperature, as expected.

The 0.1 %wt. CuO NR working liquid generated a pressure of 20 kPa at a lower temperature (25 °C) than the pure working liquid (30 °C) but when the temperature was increased to 40 °C, both fluids gave the same equilibrium pressure. It was assumed that at temperatures above 40 °C the working liquid was completely vaporized into the gaseous state hence the nanoparticles did not offer additional benefit as they were in solid form and no longer in suspension. At 30 °C, the nanofluid produced pressure that was 100 % higher than that of the pure working liquid.

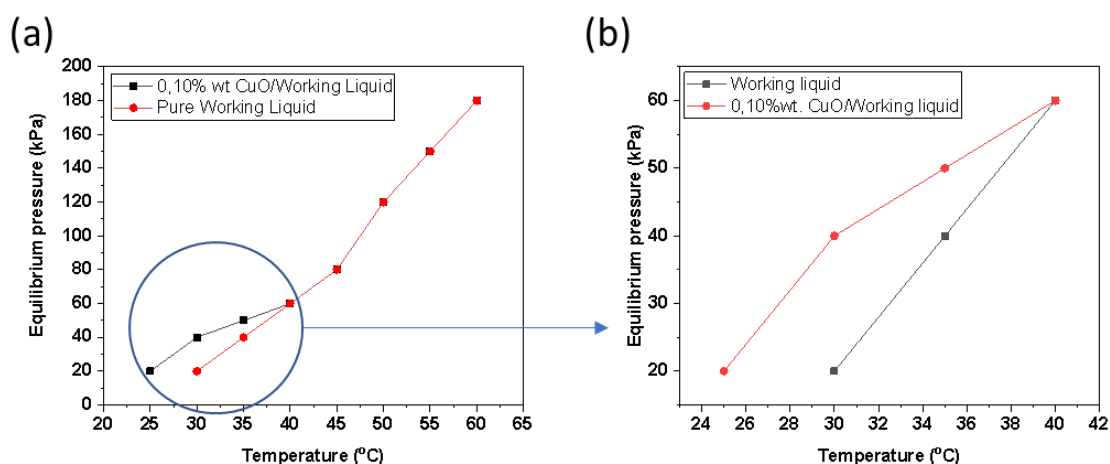


**Figure 5.18:** Variation of equilibrium pressure of working liquid with temperature change over the range of (a) 25° to 60° and (b) 25° to 40°.

The differences in the time taken to meet the equilibrium pressures by the pure working fluid and the nanofluid was investigated to determine the effect of the enhanced thermal conductivity on the generation of operational pressure. The nanofluid sample took a shorter time to reach the equilibrium pressure of 40 kPa in the temperature range of 35 – 60 °C as shown in **Figure 5.19** which supported that it had a higher thermal conductivity than the pure working liquid. The nanofluid attained the equilibrium pressure of 40 kPa at a rate that was almost 37 % faster on average than that of the pure working liquid.

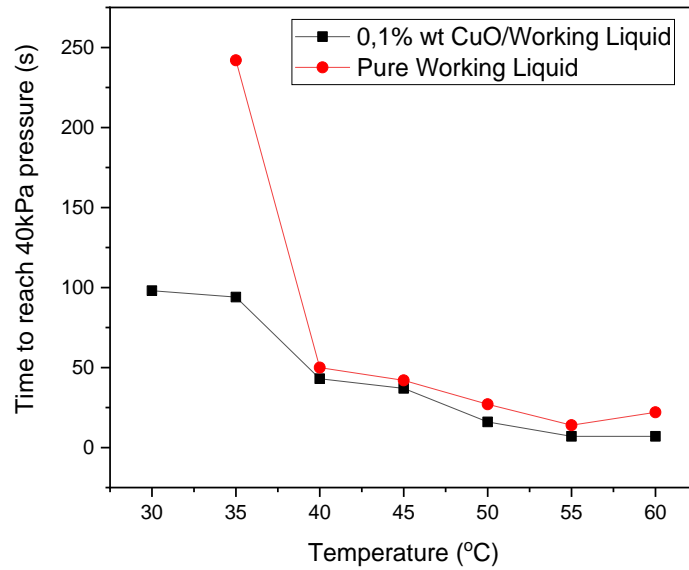


**Figure 5.19:** Comparison of the time taken to develop a pressure of 40kPa between pure working liquid and a 0,1 %.w/w CuO/Working Liquid.

The latent heat of vaporization is the energy absorbed by a liquid when it changes phase from liquid to a gas (Chaichan & Kazem, 2015) and liquids with lower heats of vaporization evaporate at lower temperatures. The latent heats of vaporization for the pure working fluid and the nanofluid were determined using the Clausius-Clapeyron equation shown in **Equation10** and are shown in **Table 5.5**. The experimentally determined value of the enthalpy of vaporization for the pure working liquid deviated from the theoretical value which showed that there were some errors in the measurements. However, both measurements of the enthalpies of vaporization for the pure working liquid and the nanofluid were assumed to have the same magnitude of errors, thus the figures can be compared. Given such a comparison, the 0,1 %.w/w CuO working liquid had an enthalpy of vaporization that was 15,7 % lower than that of the pure working liquid. This means that less heat energy was absorbed to vaporize an equivalent amount of the nanofluid than that required for the pure working liquid.



**Table 5.5:** Latent heat of vaporization of the working liquids.

Parameter	$P_2$ (Pa)	$P_1$ (Pa)	$T_2$ (K)	$T_1$ (K)	$\Delta H_{vap}$ (kJ/m ol) Experimental	$\Delta H_{vap}$ (kJ/mol) Theoretical
Pure Working fluid	180 000	20 000	333,15	303,15	61,440	25,79
0,1%.wt CuO/ Working fluid	180 000	20 000	333,15	298,15	51,793	

## 5.5 Conclusions

The preparation of copper oxide nanoparticles was successfully done through both chemical precipitation and hydrothermal synthesis routes and confirmed by elemental analysis using FTIR spectroscopy. Copper oxide nanorods were produced using the chemical precipitation method whilst hydrothermal synthesis produced nanospheres. As such, the synthesis method was confirmed to be one of the main factors in the determination of the shape of the nanoparticles. However,  $Cu_2O$  nanospheres could not be prepared in a pure form by the chemical precipitation method due to the oxidation of Cu to both  $Cu_2O$  and CuO hence a mixture of the products was synthesized. The copper oxide nanoparticles were characterized successfully using different techniques. From the characterization processes, it was found that nanorods had larger sizes than nanospheres. For the copper oxide-based nanofluids, the CuO nanorods had the best dispersion stability due to their higher magnitude of surface charge at the adjusted pH value of 6. As such, the objective of preparing and characterizing copper oxide nanoparticles and copper oxide-based nanofluids was achieved. This led to the next objective which was the investigation of the heat transfer properties and operational pressure generation capacity of the copper oxide-based nanofluids. It was observed that

increasing the weight fraction of the CuO nanoparticles in the nanofluids generally led to an increase in thermal conductivity enhancement but reduced stability of the nanofluid. The CuO nanorods were found to have the largest thermal conductivity enhancement amongst the prepared copper oxide nanoparticles at pH values in the range of 4 to 8. It was then determined that the nanofluid with a 0,1 %.w/w CuO/Water concentration had an optimum volumetric concentration, highest stability, and thermal conductivity amongst the copper oxide-based nanofluids. The 0,1 %.w/w CuO nanofluid with the pure working liquid as the base fluid had a 15,7 % lower enthalpy of vaporization and produced higher pressure at lower temperatures than the pure working liquid. Overall, the objectives of this chapter were thus successfully achieved.

## 5.6 References

- Aksoy, Y. T., Zhu, Y., Eneren, P., & Koos, E. (2021). The Impact of Nanofluids on Droplet / Spray Cooling of a Heated Surface : A Critical Review. *Ernegies*, 14(80), 1–34. <https://doi.org/>. <https://doi.org/10.3390/en14010080>
- Arun, K. J., Batra, A. K., Krishna, A., Bhat, K., Aggarwal, M. D., & Francis, P. J. J. (2015). Surfactant Free Hydrothermal Synthesis of Copper Oxide Nanoparticles. *American Journal of Materials Science*, 5(3A), 36–38. <https://doi.org/10.5923/s.materials.201502.06>
- Beck, M. P. (2008). Thermal conductivity of metal oxide nanofluids. *Georgia Institute of Technology*. In *October* (Vol. 129). <http://smartech.gatech.edu/handle/1853/26488>
- Chaichan, M. T., & Kazem, H. A. (2015). Water solar distiller productivity enhancement using concentrating solar water heater and phase change material (PCM). *Case Studies in Thermal Engineering*, April. <https://doi.org/10.1016/j.csite.2015.03.009>
- Chieruzzi, M., Cerritelli, G. F., Miliuzzi, A., & Kenny, J. M. (2013). Effect of nanoparticles on heat capacity of nanofluids based on molten salts as PCM for thermal energy storage. *Nano Express*, 8(448), 1–9. <https://doi.org/10.1186/1556-276X-8-448>
- Choudhary, R., Khurana, D., Kumar, A., & Subudhi, S. (2017). Stability analysis of

- Al<sub>2</sub>O<sub>3</sub> / water nanofluids. *Journal of Experimental Nanoscience*, 12(1), 140–151. <https://doi.org/10.1080/17458080.2017.1285445>
- Clary, D. R., & Mills, G. (2011). Preparation and Thermal Properties of CuO Particles. *The Journal of Physical Chemistry*, (115), 1767–1775. <https://doi.org/10.1021/jp110102r>
- Das, S. K., Choi, S. U. S., & Patel, H. E. (2007). Heat Transfer in Nanofluids — A Review Heat Transfer in Nanofluids —. *Heat Transfer Engineering*, 10, 3–19. <https://doi.org/10.1080/01457630600904593>
- Figoli, A., Hoinkis, J., Alsoy, S. A., & Bundschuh, J. (2017). Application of Nanotechnology in Membranes. *CRC Press*. <https://doi.org/10.1201/9781315179070>
- Gupta, D., Meher, S. R., Illyaskutty, N., & Alex, Z. C. (2018). Facile synthesis of Cu<sub>2</sub>O and CuO nanoparticles and study of their structural , optical and electronic properties. *Journal of Alloys and Compounds*, 743, 737–745. <https://doi.org/10.1016/j.jallcom.2018.01.181>
- Kabeel, A. E., Omara, Z. M., & Essa, F. A. (2014). Enhancement of modified solar still integrated with external condenser using nanofluids: An experimental approach. *Energy Conversion and Management*, 78, 493–498. <https://doi.org/10.1016/j.enconman.2013.11.013>
- Keil, P., Luetzenkirchen-hecht, D., & Frahm, R. (2007). Investigation Of Room Temperature Oxidation Of Cu In Air By Yoneda-XAFS. *AIP Conference Proceedings*, May 2014. <https://doi.org/10.1063/1.2644569>
- Lee, D., Kim, J., & Kim, B. G. (2006). A New Parameter to Control Heat Transport in Nanofluids : Surface Charge State of the Particle in Suspension. *J. Phys. Chem. B*, 110(9), 4323–4328. <https://doi.org/10.1021/jp057225m>
- Liu, M., Lin, M. C., & Wang, C. (2011). Enhancements of thermal conductivities with Cu , CuO , and carbon nanotube nanofluids and application of MWNT / water nanofluid on a water chiller system. *Nanoscale Research Letters*, 6(297), 1–13. <https://doi.org/10.1186/1556-276X-6-297>
- Luna, I. Z., Hilary, L. N., Chowdhury, A. M. S., Gafur, M. A., Khan, N., & Khan, R. A. (2015). Preparation and Characterization of Copper Oxide Nanoparticles Synthesized via Chemical Precipitation Method. *Open Access Library Journal*, August 2017. <https://doi.org/10.4236/oalib.1101409>

- Makori, N. E., Oeba, D. A., & Mosiori, C. O. (2017). Relationship between Band gap and particle size of Cadmium sulfide Quantum Dots. *Chemistry Research Journal*, 2(5), 15–21.
- Marcelino, E. W., Silva, D. D. O., & Riehl, R. R. (2016). A review on the influence of nanoparticle size in thermal enhancement of CuO-Water nanofluids and their characteristics. *Heat Powered Cycles Conference*.
- Mirmohammadi, S. A. (2012). Investigation on Thermal Conductivity, Viscosity and Stability of Nanofluids. *Royal Institute of Technology*.  
<https://www.google.com/url?sa=t&rct=j&q=&esrc=s&source=web&cd=&cad=rja&uact=8&ved=2ahUKEwj0vDots31AhUkmVwKHUROCHIQFnoECAQQAQ&url=https%3A%2F%2Fwww.divaportal.org%2Fsmash%2Fget%2Fdiva2%3A561791%2FFULLTEXT02.pdf&usg=AOvVaw2jDvYRIN1vLQqF5CbV8gLk>
- Murali, D. S., Kumar, S., Choudhary, R. J., Wadikar, A. D., Jain, M. K., & Subrahmanyam, A. (2015). Synthesis of Cu<sub>2</sub>O from CuO thin films : Optical and electrical properties. *AIP Advances*, 5(047143), 1–6.  
<https://doi.org/10.1063/1.4919323>
- Murshed, S. M. S., Leong, K. C., & Yang, C. (2005). Enhanced thermal conductivity of TiO<sub>2</sub> - Water based nanofluids. *International Journal of Thermal Sciences*, 44(4), 367–373.  
<https://doi.org/10.1016/j.ijthermalsci.2004.12.005>
- Nia, G., Miljkovica, N., Ghasemia, H., Huang, X., Boriskina, S. V., Lina, C.-T., Wang, J. J., Xua, Y., Rahman, M. M., Zhang, T., & Chen, G. (2015). Volumetric Solar Heating of Nanofluids for Direct Vapor Generation. *Nano Energy*. <https://doi.org/http://dx.doi.org/10.1016/j.nanoen.2015.08.021>
- Okonkwo, E. C., Wole, I., Ismail, O., Yasser, W. A., Tareq, M. A., Ansari, A., & Deionized, D. I. (2020). An updated review of nanofluids in various heat transfer devices. In *Journal of Thermal Analysis and Calorimetry* (Issue March). Springer International Publishing. <https://doi.org/10.1007/s10973-020-09760-2>
- Özerinç, S. (2010). Heat transfer enhancement with nanofluids. (Issue May). *Middle East Technical University*.  
[http://users.metu.edu.tr/dbaker/downloads/Sezer\\_Ozerinc\\_Thesis.pdf](http://users.metu.edu.tr/dbaker/downloads/Sezer_Ozerinc_Thesis.pdf)
- Phiwdang, K., Suphankij, S., & Mekprasart, W. (2013). Synthesis of CuO

- Nanoparticles by Precipitation Method Using Different Precursors. *Energy Procedia*, 34, 740–745. <https://doi.org/10.1016/j.egypro.2013.06.808>
- Rahmatinejad, B., Abbasgholipour, M., & Alasti, B. M. (2021). Investigating thermo-physical properties and thermal performance of  $\text{Al}_2\text{O}_3$  and CuO nanoparticles in Water and Ethylene Glycol based fluids. *Int. J. Nano Dimens*, 12(3), 252–271.
- Ren, G., Hu, D., Cheng, E. W. C., Vargas-reus, M. A., Reip, P., & Allaker, R. P. (2009). Characterisation of copper oxide nanoparticles for antimicrobial applications International Journal of Antimicrobial Agents Characterisation of copper oxide nanoparticles for antimicrobial applications. *International Journal of Antimicrobial Agents*, March, 1–5. <https://doi.org/10.1016/j.ijantimicag.2008.12.004>
- Rodgers, R. C., & Hill, G. E. (1978). Equations for vapour pressure versus temperature: Derivation and use of the antoine equation on a hand-held programmable calculator. *British Journal of Anaesthesia*, 50(5), 415–424. <https://doi.org/10.1093/bja/50.5.415>
- Ruiz, E., Alvarez, S., & Evarestov, R. A. (1997). Electronic structure and properties of  $\text{Cu}_2\text{O}$ . *The American Physical Society*, 56(12). <http://dx.doi.org/10.1103/PhysRevB.56.7189>
- Shepherd, P. J. (2013). Fundamentals of Thermodynamics. In *A Course in Theoretical Physics*. <https://doi.org/10.1002/9781118516911.ch5>
- Simpson, S., Schelfhout, A., Golden, C., & Vafaei, S. (2019). Nanofluid Thermal Conductivity and Effective Parameters. *Applied Sciences*, 1–56. <https://doi.org/10.3390/app9010087>
- Talluri, B., Prasad, E., & Thomas, T. (2017). Ultra-small ( $\leq 2$  nm), stable ( $> 1$  year), mixed valence copper oxide quantum dots with anomalous band gap. In *arXiv.org, e-Print Archive, Condensed Matter*. <http://arxiv.org/ftp/arxiv/papers/1706/1706.01261.pdf>
- Thakur, N., Sharma, D., Thakur, N., & Sood, S. (2021). Nanoparticles to nanofluids: A new fluid. In *Emerging Challenges for Human Health Sustainability and Interventions*.
- Warrier, P., & Teja, A. (2011). Effect of particle size on the thermal conductivity of nanofluids containing metallic nanoparticles. *Nanoscale Re*, 6(247), 1–6.

<http://dx.doi.org/10.1186/1556-276X-6-247>

Younes, H., Christensen, G., Luan, X., Hong, H., & Smith, P. (2012). Effects of alignment , pH , surfactant , and solvent on heat transfer nanofluids containing Fe<sub>2</sub>O<sub>3</sub> and CuO nanoparticles. *Journal of Applied Physics*, March.

<https://doi.org/10.1063/1.3694676>

Yu, F., Chen, Y., Liang, X., Xu, J., Lee, C., Liang, Q., & Tao, P. (2017). Dispersion stability of thermal nano fl uids. *Progress in Natural Science: Materials International*, 27(September), 531–542.

<https://doi.org/10.1016/j.pnsc.2017.08.010>

Zhao, M., Lv, W., Li, Y., Dai, C., Zhou, H., & Song, X. (2018). A Study on Preparation and Stabilizing Mechanism of Hydrophobic Silica Nanofluids. *Materials*. <https://doi.org/10.3390/ma11081385>

Zhu, D., Wang, L., Yu, W., & Xie, H. (2018). Intriguingly high thermal conductivity increment for CuO nanowires contained nanofluids with low viscosity. *Scientific Reports*, September, 1–12. <https://doi.org/10.1038/s41598-018-23174-z>

## CHAPTER 6

### EVALUATION OF THE PERFORMANCE OF THE SOLAR DRIVEN SYSTEM.

#### 6.1 Introduction

In previous chapters of this study, investigations were made into identifying the main influential parameters affecting the performance of the solar-driven membrane filtration system. These parameters included, thermal properties of the working fluid, type of membrane used, and cleaning procedures implemented in the membrane filtration process, as well as weather conditions. It was shown in **Chapter 4** that the field prototype without modification of the working liquid developed enough operational pressure to filter deionized water through a UF membrane when exposed to solar irradiation. In **Chapter 5**, an investigation into ways to improve the heat transfer and operational pressure generation ability of the working liquid was done with the introduction of copper oxide nanoparticles into the working fluid. The nanofluid with optimal thermal properties had a 0,1 % w/w copper (II) oxide nanorods concentration at a pH of 6. Against this background, this chapter aimed to optimize permeate production by the prototype in real-world application. The 0,1 % w/w CuO nanofluid was thus tested in the laboratory prototype within both laboratory and real-world application and its performance compared to that of the pure working liquid. The effects of weather conditions (solar intensity, wind speed, and air temperature) on permeate production were also evaluated to identify the most influential parameters and ways to mitigate or enhance their effects. Statistical analysis through an independent means t-test on the permeates produced by the laboratory prototypes with the two working fluids under the same real-world conditions, was used to determine the significance of the nanofluid flux enhancement. Heat transfer calculations were done to assess the effects of different heat loss mechanisms on the performance of the prototype to identify ways of further enhancing the performance of the prototype.

## 6.2 Experimental

### 6.2.1 Materials and methods

In this chapter, the same nanofluids prepared in **Chapter 3 Subsection 3.7** were used. The methods used in this chapter are described in further detail in the following sections.

### 6.2.2 Analysis of the effects of temperature and working liquid volume on pressure generation.

A minimum volume of the volatile liquid is required in the working chamber so that the volatile liquid will reach its largest vapour pressure possible. This minimum volume was determined as outlined in **Chapter 3 Subsection 3.8**. and other volumes of working liquid tested were above this value. The effect of changing the volume of the working liquid on the operational pressure generation was then investigated. Volumes tested were as follows: 2 ml, 5 ml, 10 ml, 20 ml, and 30 ml. The pump cylinder was cleaned and dried before an aliquot of the working liquid was pipetted into the working liquid chamber and the pressure meter attached as shown in **Figure 6.1**. The pump was then immersed into the water in the water bath at 40 °C. The system was then allowed to reach equilibrium pressure then the processes were repeated with different volumes of the pure working liquid while noting down the respective equilibrium pressures. The value of 20 ml for the volume working fluid was then chosen for pressure tests at different temperatures due to its ease of preparation and handling than other smaller volumes. In these experiments, 20 ml of the working liquid (pure working liquid and 0,1 % w/w. CuO working liquid) was put into the pump and the pump was heated in a water bath at set temperatures. The initial temperature of the water in the water bath was set at 25 °C and the temperature was adjusted by 5 °C increments until the temperature reached 60 °C.



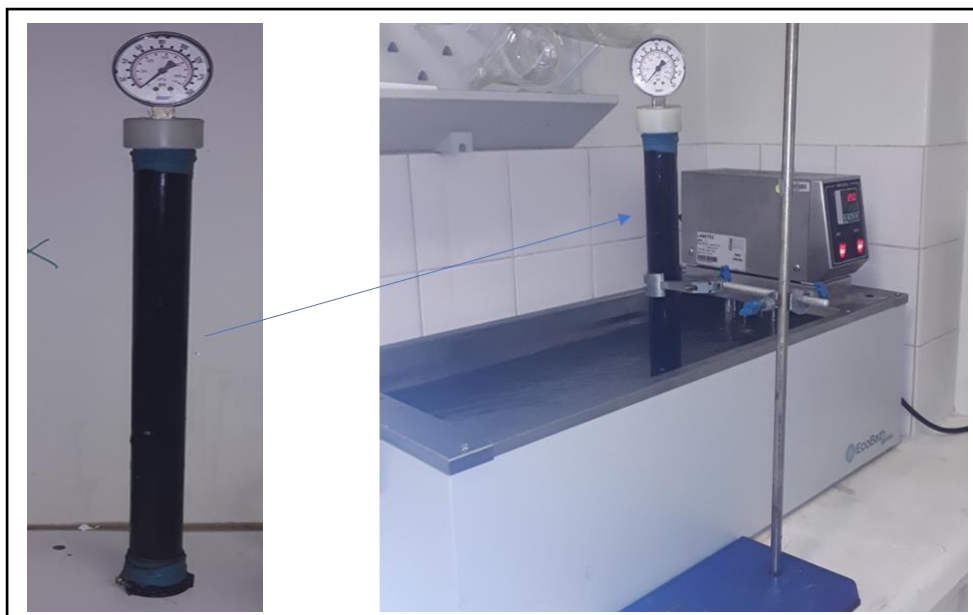


**Figure 6.1:** Images showing the measurement of the equilibrium vapour pressure with changes in the volume of the working liquid and temperature of the water bath.

The temperature of the gas produced by the working liquid was measured to determine its relationship to the ambient temperature. A thermocouple tip was inserted into the working liquid section of the pump. The point of contact between the thermocouple and the pump was insulated using Teflon and the thermocouple was secured tightly to avoid any gas leakage as shown in **Figure 6.2**. The same pump preparation procedure and testing used in the first part of **Section 6.2.2** was then used and the temperature of the water bath was set to 35 °C. The temperature readings of the thermocouple were then noted down when the working liquid reached the equilibrium pressure.

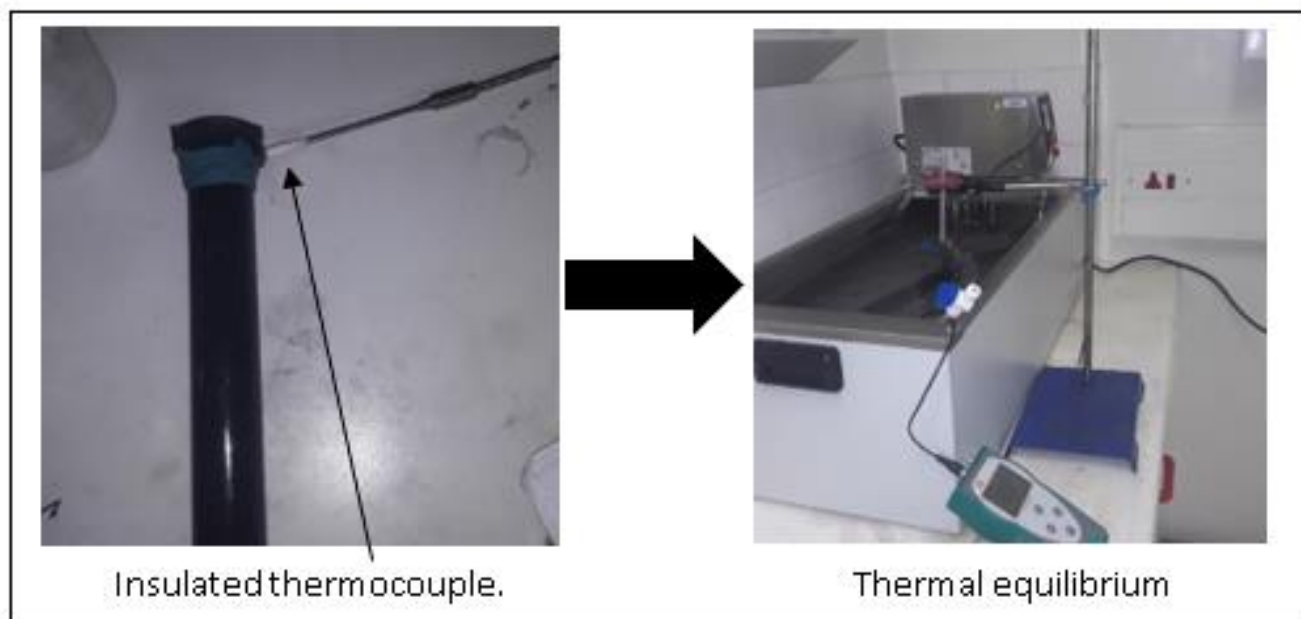


**Figure 6.2:** Images showing the procedure used in the determination of the relationship between the temperature of the pressurized working fluid and the temperature of the water bath.

### 6.2.3 Performance analysis of different working fluids in the generation of operational pressure.

The solar pumps (prototypes) were prepared for operation by placing 150 ml of DI water into the water compartments of the pumps and 20 ml of the pure working liquid into the working liquid chambers of one of the pumps while in the other, 20 ml of the nanofluid was placed. Thereafter, the performance of the working liquids was investigated using ultrafiltration and nanofiltration membranes. The pumps were then inserted into a water bath at 25°C as shown in **Figure 6.3**, and the permeate of each pump was measured every 5 minutes until constant volumes of permeate were obtained. The temperature of the water bath was then increased by 5°C and the measurements of permeate were taken as previously mentioned. This process was repeated until the temperature of the water bath reached 50°C and the permeate values were used to calculate the flux at each temperature. The highest air temperature recorded in South Africa is 50 °C hence was taken as the maximum

for ambient conditions as the experiment was a laboratory simulation of the real-world conditions.



**Figure 6.3:** Image showing how the permeate discharge of the filtration units with the pure working fluid and the nanofluid were monitored.

After laboratory testing on the performance of the prototypes with different working liquids, the same systems were tested in the real-world to demonstrate the translation of laboratory data to real-world application. The solar-driven pumps were prepared as outlined in the first part of **Section 6.2.3** and placed at an area exposed to the environmental elements, i.e., in the real world, at a location with the geographic coordinates (26°09'26.1"S 27°54'10.1"E) as shown in **Figure 6.4**. Both pumps were placed in an area where there were no obstructions of the Sun's rays to reach the prototypes and were in proximity to a weather station (Watchdog 2900 Professional) which was responsible for recording average hourly measurements of ambient air temperature, solar intensity, and wind speed data at that area. A thermometer was placed on the ground in the shade of the prototype to measure the ground temperature. The thermometer was placed in a shade to avoid it being heated directly by the Sun's rays through radiation. Permeate measurements were

taken on an hourly basis and used to calculate flux. The effect of each weather-related parameter on the flux produced by the two prototypes were then evaluated.

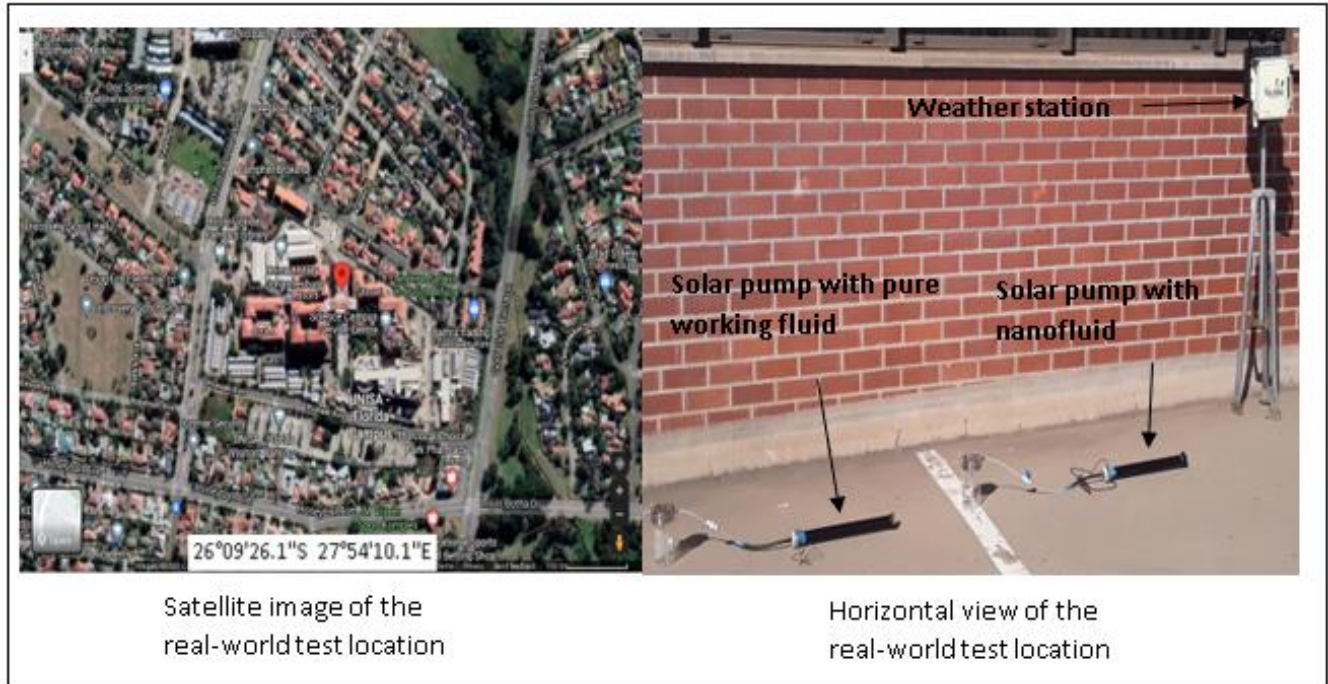


**Figure 6.4:** Images of satellite and horizontal illustrating the location of the prototypes and how they were tested under real-world conditions.

As the pumps were exposed to the same weather conditions simultaneously, their permeates could be directly compared. The comparison of the performance of the two working liquids was made through comparing the efficiencies of the two prototypes. The hydraulic efficiency of the diaphragm pump ( $\eta_{\text{exp}(h)}$ ) was calculated as the ratio of the hydraulic work ( $W_h$ ) done by the expanding gas to the solar irradiation ( $H_{\text{tot}}$ ) received that facilitated the positive displacement (Wong & Sumathy, 2000) in the given time, using **Equation 6.1**.

$$\eta_{\text{exp}(h)} = \frac{W_h}{H_{\text{tot}}} \times 100 \quad \text{Equation 6.1}$$

The hydraulic work done by the expanding gas is calculated using **Equation 6.2**.

$$W_h = p\Delta V \quad \text{Equation 6.2}$$

Where:  $p$  is the pressure of the working gas and  $\Delta V$  is the change in volume (permeate) in the measured time (hour).

The total solar irradiation incident on the working liquid chamber was calculated using **Equation 6.3**.

$$H_{\text{tot}} = I_s \cdot A_{\text{wc}} \quad \text{Equation 6.3}$$

Where:  $I_s$  is the solar intensity and  $A_{\text{wc}}$  is the Area of the working liquid chamber.

The nanofluid enhancement on the efficiency of the system was determined by comparing the efficiency of the pump using the nanofluid to the one using the pure working liquid which was calculated using **Equation 6.4**.

$$\% \eta_{\text{exp (e)}} = \frac{\Sigma m_{\text{nw}} - \Sigma m_{\text{pw}}}{\Sigma m_{\text{pw}}} \times 100 \quad \text{Equation 6.4}$$

Where:  $\% \eta_{\text{exp(e)}}$  is the experimental efficiency enhancement,  $m_{\text{nw}}$  is the average hourly mass of permeate from the pump using a nanofluid as the working liquid, and  $m_{\text{pw}}$  is the average hourly mass of permeate from the pump using the pure working liquid.

### 6.3 Heat transfer analysis

The order of magnitude of thermal losses due to radiative heat loss were estimated by calculating the net radiation loss through making several assumptions. It was assumed that the working liquid chamber was a black body, i.e.,  $\varepsilon = 1$  and the ambient temperature was used to estimate the sky temperature using **Equation 2.7**. The average solar intensity and working liquid chamber's wall temperature experimental data values were then used in the calculation of radiative heat loss using **Equation 2.6**

The order of magnitude of thermal losses due to convective heat loss were estimated by making assumptions on the wind speed, working liquid chamber's wall temperature and air temperature based on experimental data. The convective heat losses were then calculated using **Equation 2.2**.

#### 6.4 Statistical analysis of the system's performance

The fluxes produced by the two working liquids were different, but the significance of these differences had to be confirmed by statistical analysis. As such, an independent sample means t-test was used to compare the fluxes produced by the solar driven membrane filtration prototypes under real-world conditions using the following hypotheses (H):

$H_0$ : Mean permeate of pure working fluid = Mean permeate of nanofluid

$H_A$ : Mean permeate of pure working fluid  $\neq$  Mean permeate of nanofluid

The two-tailed t-test was performed with  $\alpha = 0,05$ .

### 6.3 Results and discussion

#### 6.3.1 Operational pressure test

The theoretical minimum volume of the working liquid was determined as 2,11 ml for the laboratory prototype working chamber. The change in vapour pressures generated by the different volumes of working liquid were then plotted against the operational temperature as shown in **Figure 6.5**. which shows that the isothermal changes in working liquid volume did not affect the generated equilibrium pressures. However, a volume of 20 ml was taken as appropriate for further tests as it provided a good working volume for the preparation and handling of the nanofluid given the high volatility of the pure working liquid. It was also assumed that a higher volume of working fluid would delay the complete vaporization of the liquid due to a higher saturation at temperatures close to the boiling point of the liquid hence allow for the

nanoparticles to remain dispersed in the remaining liquid. This would then allow the nanofluid to retain high thermal properties and improve performance.

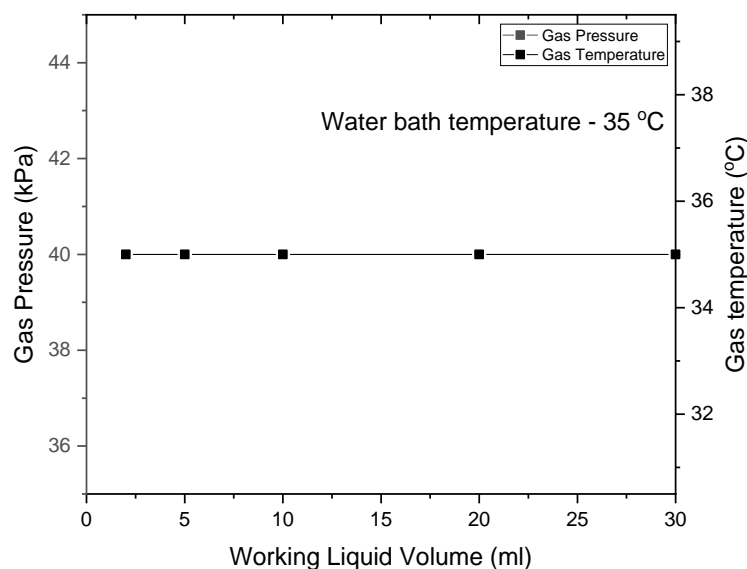


**Figure 6.5:** Changes in the gas pressure and temperature with change in the volume of the pure working liquid at a constant water bath temperature of 35 °C.

The temperatures of the equilibrium vapour generated by both the pure working liquid and the nanofluid were measured and found to be equal to the temperature of the water in the water bath which was set to 35 °C. The temperature of 35 °C was used as from the previous results presented in **Section 5.4.2** on the operational pressure generated by the pure working liquid and nanofluid had showed no difference in pressure at temperatures of 40 °C and above. The equality in temperatures at thermal equilibrium is supported by the Zeroth law of thermodynamics (Shepherd, 2013). It is also important to note that the droplet temperature of volatile organic compounds is assumed to be the same as the gas temperature and changes in the value of the droplet temperature is known to affect evaporation through the latent heat effect (Tsang *et al.*, 2007). It was assumed that the nanoparticles would promote an increase in the droplet temperature of the working liquid thus reducing the latent heat energy needed for evaporation. The effect of a reduction in the latent heat energy was shown by the higher vapour

pressure of the nanofluid than the pure working liquid at 35 °C shown in **Section 5.4.2**.

### 6.3.2 Performance of the different working fluids during membrane filtration

The permeate fluxes induced by the pure working liquid and that of the 0,1 % w/w CuO working liquid were compared as shown in **Figure 6.6**. The nanofluid produced its initial permeate at 25°C for the UF membrane and 30 °C for the NF membrane while the pure working liquid had its initial permeate at 35 °C and 40 °C, for the respective membranes. Permeate flux was induced at lower temperatures (25 °C and 30 °C) by the nanofluid revealed the enhanced thermal conductivity and volatility of the 0,1 %.w/w CuO working liquid. The lower temperatures for flux production for the nanofluid when compared to the pure working liquid shows that the nanofluid had better thermal conductivity hence enhanced volatility. There was an almost constant difference between the flux produced by the nanofluid and the pure working liquid in the temperature range of 35 °C to 45 °C then the two working liquids produced identical fluxes at 50°C. This was attributed to the complete vaporization of the working fluids at temperatures above 45 °C. As such, it was hypothesized that the volatile base fluid in the nanofluid would completely turn from liquid to gas state leaving behind the nanoparticles that would have aided in heat transfer thereby producing enhanced vapour pressure more than that produced by the pure working liquid. However, since both working liquid would now be completely in the gas state, there will thus produce same working pressure. This is supported by the data presented in **Section 5.4.2** that shows that both working liquids produce the same vapour pressure at temperatures above 40 °C. On average the nanofluid produced flux that was 35% and 45% higher than that produced by the pure working liquid for the over UF and NF membranes, respectively, over the tested temperature range of 25 °C – 50 °C.



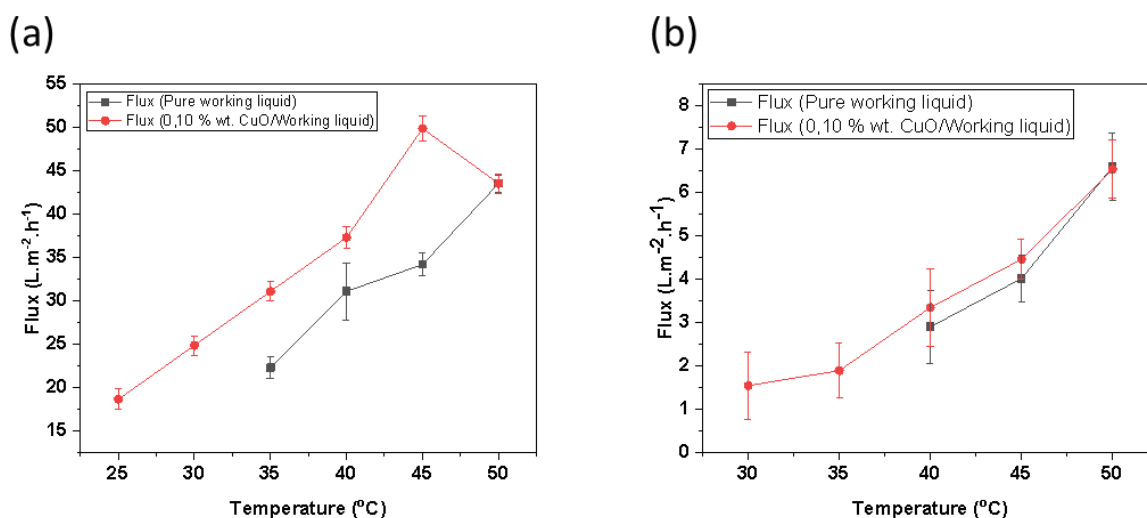


**Figure 6.6:** Comparison of flux generated by the pure working liquid and a 0,1% w/w CuO working liquid with changes in temperature while filtering DI water through (a) UF membranes and (b) NF membranes.

The effects of weather conditions (solar intensity, air temperature, and wind speed) on permeate flux of the prototype were then assessed under real-world conditions. The real-world comparison of the permeate fluxes generated by both working liquids were shown to be directly proportional to the solar intensity as shown in **Figure 6.7 (a)**. This observation supports/correlates/complements the trend of flux with solar intensity for the field prototype presented in **Chapter 4 Subsection 4.6** which showed the variation of flux during the day. The solar intensity gradually increased in the morning hours and reached a peak in the afternoon hours before steadily declining to zero in the evening hours. This variation in solar intensity was also reported by (Agrawal & Rana, 2019) who investigated the variation in distillate output of a modified solar still with change in daily solar radiation in India. It can be observed in **Figure 6.7 (b)** that flux was directly proportional to the ambient air temperature. The air temperature gradually increased from the morning hours and peaked during the afternoon hours then steadily declined afterwards. This trend closely followed that of solar intensity with an almost constant time lag which implied that the Sun was heating the air. The highest temperature was recorded at 1400 hrs while the highest solar intensity was recorded at 1200 hrs which shows a time lag of 2 hours. This time lag is due to the thermal inertia of air (Agrawal & Rana, 2019). The ground (concrete) temperature was higher than the air temperature for a greater

part of the day as it heated up much quickly than the air due to its higher thermal conductivity. It is evident that solar intensity and air temperature varied proportionally with permeate production. However, wind speed could not be correlated to permeate flux as shown in **Figure 6.7 (c)**. Marais (2018) also found that there was no relationship between wind speed and solar still performance. This can be explained by the fact that when wind speed is at zero, heat transfer between the air and an object (e.g., prototype) occurs through natural convection (Tiwari *et al.*, 2016) while at wind speeds higher than 0, heat transfer occurs through forced convection. This convective heat transfer can result in the wind either cooling or heating the object depending on the temperature difference between the object and the wind (Shitzer, 2006). The pump heated up at a higher rate than the ground (concrete) as it was made of steel which has a higher thermal conductivity (15 W/mK) than the concrete (2,25 W/mK). Given that the ground temperature was higher than the air temperature, it was thus assumed that the wind mainly cooled the prototype leading to thermal losses.

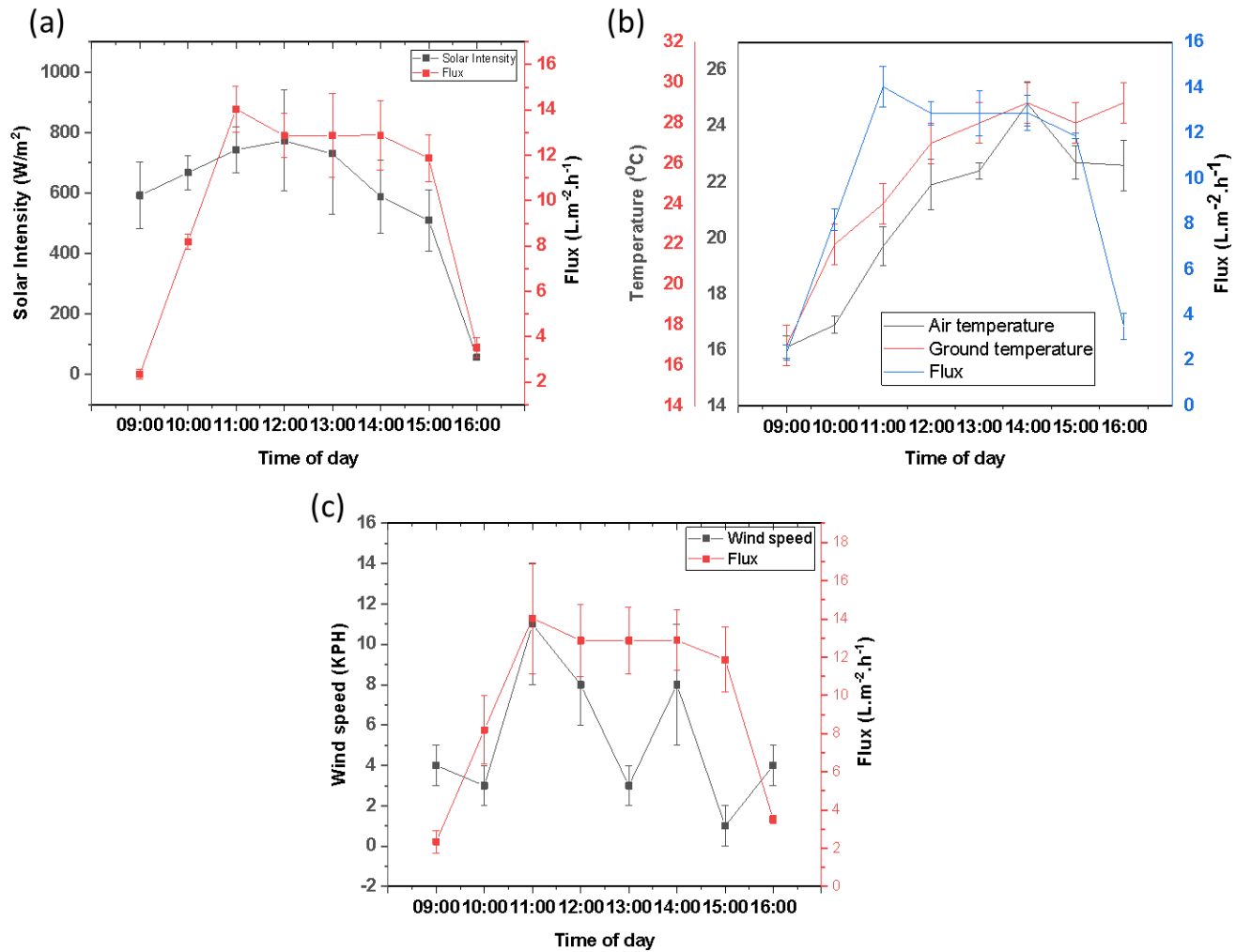


**Figure 6.7:** Evaluation of the effects of weather conditions: (i) Solar intensity, (ii) Air Temperature, and (iii) Wind speed, on flux production by the prototype using the pure working liquid.

The fluxes induced by the pure working liquid and nanofluid when using ultrafiltration and nanofiltration membranes in real-world application were determined and compared as shown in **Figure 6.8**. The nanofluid induced 13,6 % and 52,1% more flux than that produced by the pure working liquid using UF and NF membranes, respectively. The differences in flux between membranes are due to differences in selectivity which lead to the NF membrane having a higher minimum transmembrane pressure required for the filtration as compared to UF membranes. This lowest pressure at which a membrane starts to permeate is comparable to the bubble pressure point which is proportional to biggest pore size which offers the least resistance to hydraulic pressure (Shrestha, 2012). As such, an extensive

amount of applied pressure is required by the NF membrane before there is any flux. As shown in **Section 5.4.2**, the nanofluid induced higher vapour pressures than the pure working liquid at a faster rate and lower temperature. A similar case occurs in increasing discharge head when pumping water using diaphragm pumps. This was shown by (Wong & Sumathy, 2000) who demonstrated that for a higher discharge head (pressure), pump operation was delayed until the pump attained the required pressure which reduced the pump's operation time. A higher mass of the evaporated gas was needed to maintain the pressure to start pumping the water at a higher discharge head. On the other hand, for the UF membrane, the lower minimum pressure required meant that there was little difference in the fluxes produced by the pure working liquid and the nanofluid as both working fluids reached this operational pressure at comparable rates. The real-world flux enhancements are also comparable to those determined in laboratory tests. The maximum fluxes recorded were very close for both the nanofluid and pure working fluid for each membrane type. For ultrafiltration membranes the highest flux was determined as approximately  $45 \text{ L.m}^{-2}.\text{h}^{-1}$  at a solar intensity of  $775 \text{ W/m}^2$  while for the nanofiltration membranes it was  $6,6 \text{ L.m}^{-2}.\text{h}^{-1}$  at a solar intensity of  $1060 \text{ W/m}^2$ .under real-world conditions. As such, it was shown that water production by the prototype is highest when using UF membranes than NF membranes. The use of the nanofluid also enhanced flux production at lower temperatures which means that the system can be operated on cooler days.

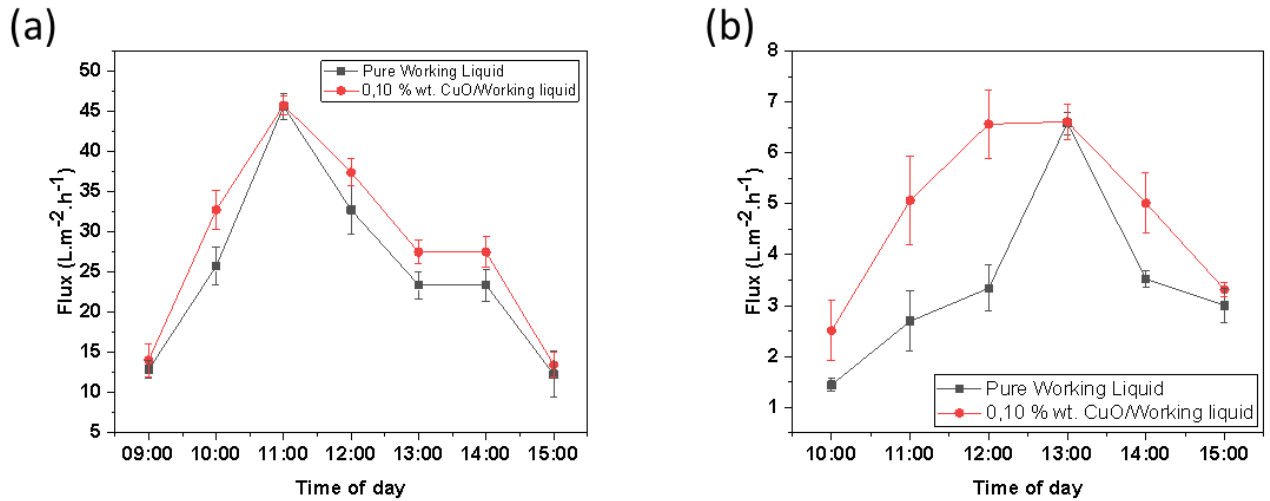


**Figure 6.8:** permeate flux graphs showing the comparison of the performance of the prototypes using the pure working liquid and 0,1 %.w/w CuO nanofluid filtering DI water through (a) UF membranes and (b) NF membranes in a real-world application.

#### 6.4 Heat transfer analysis in the system

Heat transfer calculations were made after making some assumptions derived from experimental data in which the wall temperature of the working liquid chamber was found to be generally 5 °C above the ambient temperature on days with a clear sky and wind speed under 1kph. The wall temperature of the working liquid chamber was taken as 30 °C (303,15 K) while the air temperature was taken as 25 °C (298,15 K). The ambient temperature was used to estimate the sky temperature using **Equation 2.8**.

The surface area of the working liquid chamber was determined using the dimensions in Section 3.6 and found to be equal to 0,0486 m<sup>2</sup>. Assuming that the solar radiation is 750 W/m<sup>2</sup> then the incident radiation on the working liquid chamber was assumed to be equal to 36,45 W. The radiative heat loss was then calculated using **Equation 2.7** and found to be equal to 6,882 W. Radiative heat loss was thus estimated to be at an approximate rate of 18,9 % of the total heat input which is much higher than the average radiative heat loss in most commercial Flat-Plate Collectors (FLC) used in solar domestic hot water (SDHW) systems (Tiwari *et al.*,

2016). Radiative heat loss is related to the fourth power of the temperature of the radiating surface hence a higher heat loss is observed at a higher temperature. Radiative heat loss can be minimized by insulating the unirradiated part of the absorber using glass wool (Taylor, 2011).

For the convective heat loss, it was assumed that the maximum wind-speed on a day was 2,5 m/s. The convective heat transfer coefficient of air at a speed of 2,5 m/s was determined to be 20 W/m<sup>2</sup>.K according to the Oszczewski (1995) curve (Shitzer, 2006), as shown in **Figure A1**.

The average temperatures of the wall of the working liquid chamber and the air temperature were taken as 303,15 K and 298,15 K, respectively. The convective heat loss was then calculated using **Equation 2.6** and found to be 4,86 W. Assuming solar radiation of 750 W/m<sup>2</sup>, the radiative heating of the sun on the working liquid chamber is calculated to be 36,45 W. This means that the convective heat loss is at an approximate rate of 13,3 % of the total heat input. Average convective heat losses in most Flat-Plate Collectors (FLC) used in solar domestic hot water (SDHW) systems have been found to be in the range of 22 – 30 % which is much higher than that determined in this study. Single or double glazing can be used to reduce convective heat transfer. However, at low temperatures, single glazing is more suitable as double glazing greatly reduces the amount of solar irradiation that reaches the solar absorber (Tiwari *et al.*, 2016).

#### 6.4 Evaluation of the efficiency of solar driven membrane filtration pump

The efficiencies of the different working fluids in the solar-driven membrane filtration pump were determined using data in **Table 6.1** and the value of the area of the working liquid chamber presented in **Section 3.4**. The hydraulic efficiency calculations for the prototypes using ultrafiltration and nanofiltration membranes with different working liquids were then calculated using **Equation 5.1**.

**Table 6.1:** Parameters used in the evaluation of the efficiency of the solar-driven prototypes using different membranes and working liquids.

Membrane Type	Average hourly solar intensity (W/m²)	Average Permeate volume (L)	hourly Operational pressure (Pa)	Operational time (s)	
		Pure Working Liquid	Nanofluid		
UF	945	0,0215	0,0242	178296	3600
NF	900	0,0037	0,0043	140267	3600

The efficiencies of the solar pump with the pure working liquid and nanofluid were determined to be 2,32 % and 2,61 %, respectively, when using ultrafiltration membranes. This meant that the nanofluid enhanced the efficiency of the diaphragm pump by 12,71 % on ultrafiltration. On the other hand, the efficiencies of the pure working liquid and nanofluid on the nanofiltration membranes were found to be 0,31 % and 0,40 %, respectively. This represented an enhancement in efficiency of 30,00% by the nanofluid over the pure working liquid. The efficiency values for the prototype during nanofiltration are comparable to those determined by (Kurhe *et al.*, 2017) who tested a membrane displacement operated at a working temperature of 85 °C using acetone as the working liquid. The researcher obtained efficiencies in the range of 0,25 % - 0,50 % for this pump. Wong & Sumathy (2000) also determined the efficiencies of a diaphragm pump and found the efficiencies to be 0,42 % and 0,34 % for ethyl-ether and pentane working liquids, respectively. The researchers showed that the efficiency changes with a change in the head of water lifted, which explains the differences in efficiencies between ultrafiltration and nanofiltration membranes as these membranes require different minimum operational pressures. The enhancement in efficiency of the prototype by using the nanofluid as the working fluid during nanofiltration was much greater (30,00 %) than for ultrafiltration (12,71). This greater difference was due to the reduced operation time of the prototype with the pure working liquid when compared with the nanofluid. The nanofluid was able to induce the minimum pressure needed for permeation through the nanofiltration membranes during the morning and evening hours when the solar

intensity was lowest as shown in **Section 6.3.2**. Overall, the efficiency of the prototype was increased by 21,30 % for both ultrafiltration and nanofiltration processes under real-world conditions.

## 6.5 Statistical analysis of system performance

The results of a statistical comparison of 60 flux values for both the pure working liquid and the nanofluid using both ultrafiltration and nanofiltration membranes are presented in **Table 6.2**. This test was done to investigate whether the copper oxide nanoparticles in the nanofluid had improved the thermal conductivity of the working liquid enough to significantly enhance the performance of the solar-driven pump. As was expected, the nanofluid induced a higher mean flux than the pure working liquid. The p-value of the F-test (0,092) was lesser than the alpha value ( $\alpha = 0,05$ ) of the t-test, hence equal variances were not assumed. The p-value (Sig. 2-tailed) of the t-test was lesser than the alpha value of the t-test, i.e.,  $0,025 < 0,05$ . It thus follows that the null hypothesis was rejected which meant that there was a significant difference between the mean of the pure working liquid flux and that of the nanofluid. This means that the thermal properties of the working liquid are an influential property in the performance of the solar-driven system. Significant improvement of the thermal properties of the working liquid can be achieved through the dispersion of copper oxide nanoparticles in the liquid.

**Table 6.2:** Independent sample means t-test comparison between the flux produced by the pure working liquid and that of the nanofluid.

Group statistics					
WL		N	Mean	Std. Deviation	Std. Error Mean
<b>Flux</b>	NF	60	33.2783	18.3644	2.3708
	PWL	60	26.3275	15.1089	1.9706
Independent Samples Test					



		Levene's Tests for Equality of Variances		t-test for Equality of Means		
		F	Sig.	t	Df	Sig. (2-tailed)
<b>Flux</b>	Equal variances assumed	2.8790	0.0920	2.2640	118.0000	0.0250
	Equal variances not assumed			2.2640	113.7760	0.0250

## 6.6 Conclusions

The equilibrium pressure generated by the working liquid was shown to be independent of the volume of working liquid when the volume was above the calculated minimum volume required for the working liquid chamber. As such, there was no benefit to enhancing the operational pressure by using a larger volume of the working fluid. This meant that performance enhancements of the solar-driven pump were influenced by other parameters which were then investigated. The temperature of the working liquid was then shown to directly impact flux. The air temperature and the solar intensity was then shown to contribute greatly to the temperature of the working liquid. The solar intensity and air temperature varied from the lowest values in the morning and peaked at noon, then declined back to minimum values in the evening hours. The permeate flux induced by the working liquids throughout the day closely followed the same pattern. The nanofluid induced an average amount of flux that was 13,35 % larger than that of pure working liquid in both ultrafiltration and nanofiltration. This showed that the use of the nanofluid improved the performance of the system, and an independent sample means t-test was done to investigate the significance of this difference. The independent sample means t-test showed that the difference of the means of the fluxes induced by the pure working liquid and the nanofluid on the diaphragm pump was statistically

significant. The overall enhancement in efficiency of the nanofluid was on average 21,30 % higher than that of the pure working liquid on both ultrafiltration and nanofiltration membranes. However, the solar-driven diaphragm pump was observed to still operate at low efficiencies of 2,61 % and 0,40 % for ultrafiltration and nanofiltration membranes, using the nanofluid. Heat loss estimations were thus carried out. Convective heat loss through the chilling effect of the wind was estimated to be at 13,3% of the total heat input while radiative heat loss was 18,9%. This showed that the loss of heat by convection and radiation were great factors that reduced the efficiency of the solar-driven membrane filtration system. Overall, the objective of evaluating the performance of the solar-driven membrane filtration system under laboratory and real-world conditions, was thus successfully achieved.

## 6.7 References

- Agrawal, A., & Rana, R. S. (2019). Theoretical and experimental performance evaluation of single-slope single-basin solar still with multiple V-shaped floating wicks. *Heliyon*, e01525. <https://doi.org/10.1016/j.heliyon.2019.e01525>
- Kurhe, N., Funde, A., Gokhale, P., Jadkar, S., Ghaisas, S., & Date, A. (2017). Development of Low Temperature Heat Engine for Water Pumping Application. *Energy Procedia*, 110, 292–297. <https://doi.org/10.1016/j.egypro.2017.03.142>
- Marais, H. L. (2018). Experimental Optimisation of a Simple Basin Solar Still : Improved Heat Loss Management and Evaporation Rate Experimental Optimisation of a Simple Basin Solar Still : Improved Heat Loss Management and Evaporation Rate. *University of Pretoria*. <https://repository.up.ac.za/handle/2263/71006>
- Shepherd, P. J. (2013). Fundamentals of Thermodynamics. In *A Course in Theoretical Physics*. <https://doi.org/10.1002/9781118516911.ch5>
- Shitzer, A. (2006). Wind-chill-equivalent temperatures : regarding the impact due to the variability of the environmental convective heat transfer coefficient. *Journal of Biometereology*. <https://doi.org/10.1007/s00484-005-0011-x>
- Shrestha, A. (2012). Characterization of porous membranes via porometry. *University of Colorado, Boulder*. <https://scholar.colorado.edu/downloads/vt150j670>

- Taylor, R. (2011). Thermal Energy Conversion in Nanofluids. *Arizona State University*.  
[https://keep.lib.asu.edu/\\_flysystem/fedora/c7/30050/Taylor\\_asu\\_0010E\\_10819.pdf](https://keep.lib.asu.edu/_flysystem/fedora/c7/30050/Taylor_asu_0010E_10819.pdf)
- Tiwari, G. N., Tiwari, A., & Shyam. (2016). Solar Water-Heating Systems Á Natural circulation Á Forced circulation Á Heat. <http://link.springer.com/10.1007/978-981-10-0807-8>
- Tsang, T. H., Cook, S. M., Marra, M. E., Tsang, T. H., Cook, S. M., & Marra, M. E. (2007). Dynamic Behavior of Condensation and Evaporation of Polydisperse Volatile Aerosols Dynamic Behavior of Condensation and Evaporation of Polydisperse Volatile Aerosols. *Aerosol Science and Technology*, 6826.  
<https://doi.org/10.1080/02786829008959354>
- Wong, Y. W., & Sumathy, K. (2000). Performance of a solar water pump with n-pentane and ethyl ether as working fluids. *Energy Conversion and Management*, 41, 915–927. [http://dx.doi.org/10.1016/S0196-8904\(99\)00167-3](http://dx.doi.org/10.1016/S0196-8904(99)00167-3)

## CHAPTER 7

### CONCLUSIONS AND RECOMMENDATIONS

---

## 7.1 Conclusions

The aim of this study was to optimize a novel solar-driven membrane filtration system developed for the production of clean drinking water for small, rural South African communities, from surface water sources without the use of electricity. To achieve this aim, the following objectives were successfully implemented: evaluation and comparison of ultrafiltration and nanofiltration membranes' suitability for application in the solar-driven filtration system, determination of the physicochemical properties of real water samples collected from a lake and a stream, preparation and characterization of Copper oxide nanoparticles and nanofluid, investigation of the heat transfer properties and operational pressure generation capacity of the copper oxide nanofluid, and evaluation of the performance of the solar-driven membrane filtration system under laboratory and real-world conditions.

The following conclusions were drawn from this study:

The surface water sources that were sampled were shown to be not suitable for direct water consumption without any water treatment techniques as some water quality parameters of these samples were outside the accepted range of South African National Standards (SANS) 241:2015 physico-chemical drinking water standards, e.g., turbidity, electrical conductivity, and Cd concentration. Permeate produced by both ultrafiltration and nanofiltration membranes was shown to be within the drinking water standards for all the tested parameters. This proved that either ultrafiltration or nanofiltration membranes could be used for drinking water treatment. As ultrafiltration requires a lower operational pressure with a higher flux, it was thus the more ideal membrane system for application on the prototype.

The characterization of the membranes revealed that the prepared membrane was classed as a tight ultrafiltration (UF) membrane. Fouling studies revealed that cake filtration was the dominant fouling mechanism in the UF membrane, whilst with the NF270 membrane, fouling was governed by pore constriction. The NF270 membrane had greater anti-fouling properties than the ultrafiltration membrane as

shown by its higher NFR (0,694) and FRR (97,9 %) values as opposed to 0,652 and 93,5 %, respectively. This meant that the ultrafiltration membrane fouled much more easily than the nanofiltration membrane thereby required more frequent cleaning to maintain a large flux.

Chemical cleaning of the membranes was shown to effectively retain flux in both the ultrafiltration and nanofiltration membranes. The effectiveness of chemical cleaning was shown with the changes in the contact angles and surface free energies (SFE) of the membranes before and after chemical cleaning. The contact angles of the UF (67,8°) and NF (51,6°) pristine membranes were smaller than those of the chemically cleaned UF (61,0°) and NF (49,9°) membranes. This meant that chemical cleaning with sodium hypochlorite altered the membranes' surfaces in addition to loosening and removing some foulants. It was also shown that the surface free energies of the fouled UF (51,9 mN/m) and NF (59,5 mN/m) membranes were lower than those of the pristine UF (45,2 mN/m) and NF (47,9 mN/m) membranes. Chemical cleaning reduced the SFE of the fouled UF membranes to 43,7 mN/m which was lower than that of the pristine UF membrane. On the other hand, the contact angle of the cleaned NF membrane was found to be 60,6 mN/m which was larger than that of the pristine NF membrane. The SFE results supported that the NF membrane had better antifouling properties than the UF membrane as there was a small difference between the SFE of the pristine and cleaned NF membranes.

The production of permeate by the prototype using the prepared UF membrane and commercially available NF270 membrane was shown to be proportional to the solar irradiation received by the working liquid as well as the ambient temperature. However, there was no correlation between flux and wind-speed. This showed that the main influential parameters on the performance of the prototype are solar intensity and air temperature.

The thermal properties of the working liquid were improved by dispersing copper oxide nanoparticles in the working liquid. The CuO nanoparticles that produced the most stable dispersion amongst the tested nanoparticles were the CuO nanorods. These CuO nanorods exhibited excellent stability when dispersed in aqueous media and had the best thermal properties at the optimal concentration of 0,10 %.w/w.

During optimization using controlled conditions, both the nanofluid and pure working liquid generated the same equilibrium pressure at the same temperature. However, the nanofluid had a faster pressure generation rate; its rate was improved by 37%. This means that the prototype would operate at a lower temperature thus increasing its water production time as the solar irradiation gradually increases in the morning hours and declines to zero in the evening hours of the day. It also means that water production can be achieved even on moderately warm days.

The volume of the working liquid was shown to have no significant effect on the generation of equilibrium pressure when the volume was above the calculated minimum volume. This therefore means that increasing the working liquid volume beyond the calculated minimum volume had no significant effect on permeate production. As such, changing the volume would not change the performance of the system since it is a pressure-based system. However, the volume should be at a certain level such that some nanofluid is present in liquid form within the solar-driven pump during expansion to allow the nanoparticles to absorb and dissipate heat in suspension.

The efficiency of the pump was enhanced by 21,30 % for both ultrafiltration and nanofiltration membranes. This increase in efficiency was translated into a 13.10 % increase in the flux of the system. The increase in flux was also shown to be statistically significant by use of an independent sample means t-test. It was thus demonstrated that improving the thermal properties of the working liquid through the dispersion of nanoparticles significantly improved the efficiency of the diaphragm pump. This meant that the aim of the study was achieved as the performance of the system was significantly enhanced through the optimization of different parameters.

However, there were several heat losses that were estimated to occur in the operation of the system. These heat losses were determined to be mainly through convection from the chilling effect of the wind and radiative heat loss which were estimated to be 13,3% and 18,9%, respectively. This means that the combined heat loss through these mechanisms was 32,2% and these greatly lowered the

performance of the system. This opens up opportunities for improving the efficiency of the prototype furthermore.

## **7.2. Limitations of the study**

The study was limited by seasonal changes in weather conditions which limited the time of study. The solar-driven system was only operated when weather conditions were conducive, and this was mostly done in summer which is the only time of the year when it is mostly sunny in the country. This also led to small sample sizes for each test due to the limited test time.

The diaphragm pump cannot be operated continuously without stopping it as the working liquid goes into the gas state during expansion. It remains in the gas state when the working chamber is being heated and this prevents addition of more raw water into the system during operation. This limited the number of operation cycles that could be done in a day to a maximum of 1 cycle.

## **7.3 Recommendations**

It was demonstrated in the study that the performance of the system could be significantly improved by improving heat transfer within the system. As such, it was established that heat transfer is one of the most influential factors in the operation of the diaphragm pump. Future studies could be extended to cover the following:

Investigation of the effect of different cleaning solutions and protocols on the properties of the membrane to improve cleaning efficiency.

Suspension of polymer-hybrid nanostructures in the working liquid. These polymer-hybrid nanostructures will be made from inorganic nanoparticles wrapped with polymers. The inorganic nanoparticles selected will have higher thermal conductivities than copper oxide nanoparticles thereby further enhancing the

thermal conductivity of the base fluid. On the other hand, the polymer envelope will improve the stability of the nanoparticles in suspension.

Thermal insulation of the working chamber will further enhance heat transfer in the system which will translate into a higher performance of the system.

Incorporation of a heat storage section using a phase change material (PCM), will also improve increasing the operation time of the system. The phase change material will melt when heated and store heat which will be transferred to the working liquid when it cools and solidifies in the evening hours.

Alternative working fluids which have lower boiling points will also help improve the performance of the system by enabling it to operate at much lower temperatures.

The volume of the working liquid should also be optimized to avoid complete vaporization of the working liquid. Further studies should be done on achieving this while maintaining a high vapour pressure generation by the working liquid.

Enhancement of the thermal transfer processes in the prototype through plasmonic heat transfer. This can be done by making the part of the absorber portion of the working liquid chamber transparent so that more radiative heat is captured by the nanoparticles.

The use of solar concentrators with tracking can be used to greatly improve the performance of the system as more radiation will reach the absorber part of the working liquid chamber.

.



## APPENDIX

**Table A1:** Pre- compaction fluxes of the ultrafiltration and nanofiltration membranes at a transmembrane pressure of 6 bars.

<b>Membrane Area (m<sup>2</sup>)</b>	0,001453									
<b>UF Membrane</b>	<b>Filtration Time</b>	59	68	82	91	100	105	108	116	121
	<b>Flux (LMH)</b>	474,950	447,416	419,883	392,350	371,700	357,933	351,050	351,050	337,283
<b>NF Membrane</b>	<b>Filtration Time</b>	17	25	35	42	51	59	68	82	91
	<b>Flux (LMH)</b>	15,487	15,487	15,487	15,487	15,487	20,650	15,487	16,520	15,487

**Table A2:** Permeability results for ultrafiltration and nanofiltration membranes.

<b>Membrane Area (m<sup>2</sup>)</b>	0,001453						
<b>UF Membrane</b>	<b>Transmembrane Pressure (bars)</b>	1	2	3	4	5	6
	<b>Flux (LMH)</b>						
		46,462	103,250	162,619	220,367	275,300	330,400
	<b>Permeability</b>						
		46,462	51,625	54,206	55,092	55,060	55,067
<b>NF Membrane</b>	<b>Flux (LMH)</b>						
		3,930	4,589	6,883	9,145	11,428	15,500
	<b>Permeability</b>						
		3,930	2,295	2,294	2,286	2,286	2,583

**Table A3:** DOC removal by UF and NF membranes with changes in the SUVA values of the feed water.

<b>UF</b>							
<b>Membrane</b>							
<b>SUVA</b>							
<b>L.mg<sup>-1</sup>.m<sup>-1</sup></b>	1,038	1,580	2,577	4,670	8,350	12,660	15,897
<b>DOC</b>							
<b>removal (%)</b>	37,055	42,870	53,688	56,780	60,560	64,660	68,388
<b>NF</b>							
<b>Membrane</b>							
<b>SUVA</b>							
<b>L.mg<sup>-1</sup>.m<sup>-1</sup></b>	1,038	1,580	2,577	4,670	8,350	12,660	15,897
<b>DOC</b>							
<b>removal (%)</b>	34,307	45,770	53,688	60,960	76,890	85,780	94,995

**Table A4:** Results of % DOC removal with filtration time for the filtration of Florida Stream and Florida Lake raw water samples through UF and NF membranes.

	UF membrane (FS)	UF membrane (FL)	NF membrane (FS)	NF membrane (FL)
Filtration Time (hours)	DOC removal (%)	DOC removal (%)	DOC removal (%)	DOC removal (%)
1	37,055	24,337	34,307	53,688
2	40,467	24,587	47,873	58,877
3	44,471	24,968	72,071	64,708
4	43,998	25,678	56,050	51,607
5	43,760	28,373	62,349	39,646
6	35,667	24,292	41,476	53,116

**Table A5:** Resistance values for UF and NF membranes.

Membrane resistance ( $\text{m}^{-1}$ )	$R_m$	$R_t$	$R_{if}$	$R_{rf}$	$R_t$
UF	1,96E-13	1,57E-14	8,00E-13	5,69E-13	1,57E-14
NF	1,44E-14	1,10E-15	4,70E-15	7,05E-14	1,44E-14

**Table A6:** Fouling mechanisms of ultrafiltration and nanofiltration membranes when fouling membranes using 50 ppm humic acid feed water.

Filtration Time (hours)	UF membrane fouling mechanism				NF membrane fouling mechanism			
	Cake filtration	Intermediate blockage	Pore constriction	Complete blockage	Cake filtration	Intermediate blockage	Pore constriction	Complete blockage
0	0	0	0	0	0	0	0	0
0,25	0,52964	0,23679	-0,10081	-0,21252	0,17361	0,08333	-0,03923	-0,08004
0,5	0,95866	0,39952	-0,1547	-0,33613	0,27788	0,13043	-0,05946	-0,1226
0,75	1,44663	0,56417	-0,20043	-0,44736	0,39669	0,18182	-0,08013	-0,16705
1	1,94309	0,71554	-0,23652	-0,53973	0,53288	0,23810	-0,10128	-0,21357
1,25	2,36303	0,83386	-0,26156	-0,60642	0,53288	0,23810	-0,10128	-0,21357
1,5	2,87971	0,9697	-0,28747	-0,67788	0,6900	0,30000	-0,12294	-0,26236
1,75	3,18388	1,04545	-0,30079	-0,71562	0,53288	0,23810	-0,10128	-0,21357
2	3,52529	1,12727	-0,31437	-0,75484	0,6900	0,30000	-0,12294	-0,26236
2,25	3,52529	1,12727	-0,31437	-0,75484	0,6900	0,30000	-0,12294	-0,26236
2,5	3,91025	1,21591	-0,32822	-0,79566	0,6900	0,30000	-0,12294	-0,26236
2,75	4,34651	1,31225	-0,34237	-0,83822	0,6900	0,30000	-0,12294	-0,26236
3	4,84361	1,41736	-0,35682	-0,88267	1,17071	0,47333	-0,17615	-0,38753

**Table A11:** Normalized fluxes of UF and NF membranes with chemical cleaning after fouling.

Area 0.001453 m <sup>2</sup>				
	UF membrane	Membrane cleaning	NF membrane	Membrane Cleaning
Filtration Time (hours)	Normalized Flux		Filtration Time (min)	Normalized Flux
0	1		0	0,9841
0,5	0,47222		30	0,63553
1	0,46667		60	0,40332
1,5	0,5		90	0,59154
2,5	0,47222		120	0,53776
3	0,4		150	0,87997
3,5	0,36667		180	0,9589
4	0,36667		210	0,74459
4,1	0,96889	Clean	240	0,74902
4,5	0,33333		270	0,6722
5	0,56667		300	0,60946
5,5	0,5		330	0,59437
6	0,5		360	0,99279
6,1	0,92667	Clean	390	0,78423
6,5	0,5		420	0,6739
7	0,46667		450	0,9841
7,5	0,43333		480	0,63553
8	0,91	Clean	510	0,40332
8,5	0,36667		540	0,59154
9	0,36667		0	0,53776

**Table A7:** Changes in flux with change in weather conditions during a specific period of the day.

NF Membrane Area – 0,000855					
Time of day	Solar intensity (W/m <sup>2</sup> )	Air temperature (°C)	Ground temperature (°C)	Wind speed (KPH)	Flux (L.m <sup>-1</sup> .h <sup>-1</sup> )
09:00	592	16,1	17	4	2,33955
10:00	667	16,9	22	3	8,18843
11:00	743	19,7	24	11	14,0373
12:00	773	21,9	27	8	12,86753
13:00	730	22,4	28	3	12,86753
14:00	588	24,8	29	8	12,88618
15:00	509	22,7	28	1	11,86753
16:00	56	22,6	29	4	3,50933

**Table A8:** Real-world results for flux induced by working fluids using both UF and NF membranes during a specific period of the day.

Time of day	UF membrane flux (L.m <sup>-1</sup> .h <sup>-1</sup> )		NF membrane flux (L.m <sup>-1</sup> .h <sup>-1</sup> )	
	Pure working liquid	0,1 %w/w CuO	Pure working liquid	0,1 %w/w CuO
25	-	18,66397	-	-
30	-	24,88529	-	1,548
35	22,3	31,10662	-	1,896
40	31,11	37,32794	4,018	3,34961
45	34,22	49,89009	6,591	4,463
50	43,55	43,54927	2,90549	6,538

**Table A9:** Laboratory results for flux induced by working fluids at different temperatures using both UF and NF membranes.

Temperature (°C)	UF membrane flux (L.m <sup>-1</sup> .h <sup>-1</sup> )		NF membrane flux (L.m <sup>-1</sup> .h <sup>-1</sup> )	
	Pure working liquid	0,1 %w/w CuO	Pure working liquid	0,1 %w/w CuO
09:00	12,8655	14,03509		
10:00	25,73099	32,74854	1,43959	0,589
11:00	45,61404	45,76608	2,69252	0,875
12:00	32,74854	37,4269	3,34124	0,678
13:00	23,39181	27,48538	6,58448	0,348
14:00	23,39181	27,48538	3,5223	0,598
15:00	12,2807	13,45029	3,00311	0,139

**Table A10:** Laboratory results of the vapour pressure induced by the pure working liquid and the 0,1 % w/w CuO nanofluid.

Temperature (°C)	Equilibrium vapour pressure (kPa)	
	Pure working liquid	0,1 % w/w CuO
25	20	
30	40	20
35	50	40
40	60	60
45	80	80
50	120	120
55	150	150
60	180	180

**Table A11:** Flux measurements for different working fluids in real world set-up under the similar weather conditions.

Membrane area – 0,000855 m <sup>2</sup>										
Working liquid type	Flux (L.m <sup>-1</sup> .h <sup>-1</sup> )									
Pure working liquid	12.87	25.73	45.61	32.75	23.39	23.39	12.28	31.11	37.33	49.89
0,1 % w/w CuO nanofluid	14.04	32.75	45.77	37.43	27.49	27.49	13.45	22.30	31.11	34.22
Pure working liquid	43.57	14.40	26.93	33.41	65.84	35.22	14.40	2.91	4.02	6.59
0,1 % w/w CuO nanofluid	43.75	25.08600	50.70	65.67	66.15	50.15	33.16	3.35	4.46	6.54
Pure working liquid	14,99	27,85	47,73	34,87	25,51	25,51	14,4	33,23	36,34	45,67
0,1 % w/w CuO nanofluid	16,16	34,87	47,89	39,55	29,61	29,61	15,57	33,23	39,45	52,01
Pure working liquid	41,72	13,27	25,8	32,28	64,71	34,09	13,27	1,78	2,89	5,46
0,1 % w/w CuO nanofluid	41,42	23,956	49,57	64,54	65,02	49,02	32,03	2,22	3,33	5,41



**Table A12:** Independent sample means t-test comparison between the flux produced by the pure working liquid and that of the nanofluid.

➔ **T-Test**

**Group Statistics**

	WL	N	Mean	Std. Deviation	Std. Error Mean
Flux	NF	60	33.2783	18.36442	2.37084
	PWL	60	26.3275	15.10893	1.95055

**Independent Samples Test**

		Levene's Test for Equality of Variances		t-test for Equality of Means						
		F	Sig.	t	df	Sig. (2-tailed)	Mean Difference	Std. Error Difference	95% Confidence Interval of the Difference	
Flux	Equal variances assumed	2.879	.092	2.264	118	.025	6.95080	3.07010	.87116	13.03044
	Equal variances not assumed			2.264	113.776	.025	6.95080	3.07010	.86882	13.03278

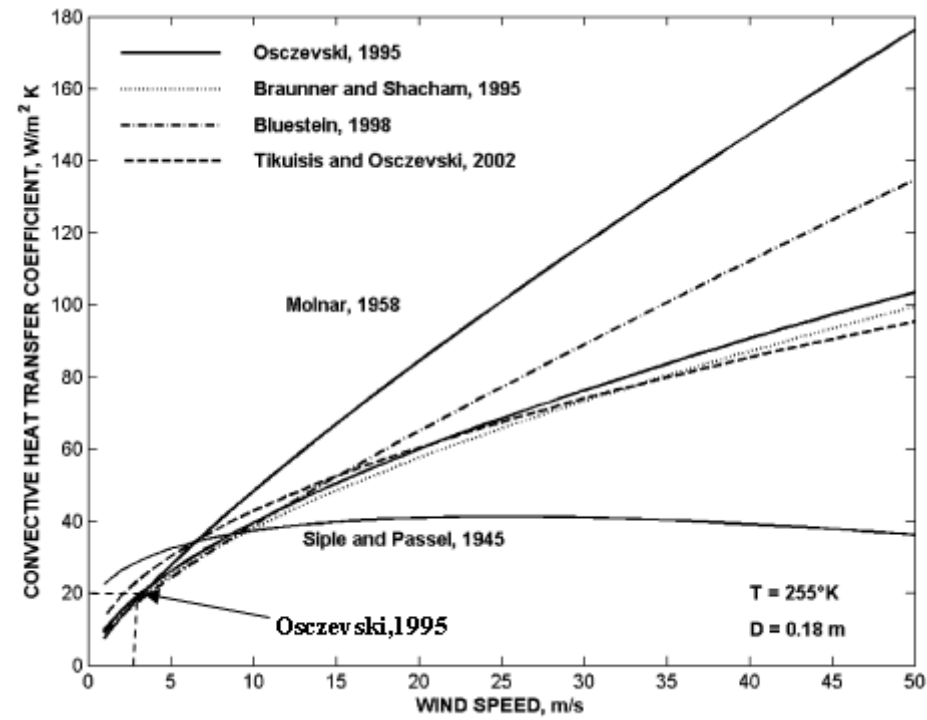


**Figure A1:** Convective heat transfer coefficient of wind at different speeds (Shitzer, 2006) showing the heat transfer conductive coefficient determination according to the Osczevski, 1995 curve at a wind speed of 2,5 m/s.